



TECHNISCHE
UNIVERSITÄT
WIEN

Vienna University of Technology

DISSERTATION

APPLICATION OF NEUTRON RADIOGRAPHY TO FUEL CELLS, HYDROGEN FILLED MICRO HOLLOW SPHERES, BORON MICRO-INHOMOGENEITIES AND TO PLATE HEAT EXCHANGERS

ausgeführt zum Zwecke der Erlangung des akademischen Grades einer
Doktorin der Technischen Naturwissenschaften unter der Leitung von

Ao.Univ.Prof. Dipl.-Ing. Dr.techn. Helmuth Böck

Mit wirkender Assistent: Ass.-Prof. Dipl.-Ing. Dr. Michael Zawisky

TU- Wien Atominstitut

Eingereicht an der Technischen Universität Wien,

Fakultät für Technische Physik

von

Eva Dyrnjaja

MAT.No 0127379

Ausstellungsstrasse 47/9 1020 Wien

Wien, am 23 May 2016

To
My parents Lejla and Bujar Dyrnjaja
My Prof. Fatos Klosi and
to my Peter, my endless love

I couldn't have started and finished without their LOVE support and encouragement.

I'm grateful for the beautiful times and dreams we shared making true few of them.

For them I lack words to express my gratitude.

I'm so lucky to have them in my life

I'm grateful to loving people who stepped in my life and shaped it the way it is now!

I'm grateful to them till the rest of my life!

"I have found it to be true that the older I've become the better my life has become"

Doris Lessing

Acknowledgements

To all who have contributed to the successful completion of this work I would like to warmly thank.

First of all I would like to thank Dr. Michael Zawisky for the opportunity he gave me in his scientific experimental group. His dynamical, energetic, sometimes very loud discussions were so fruitful for me for my further motivation. I want to thank him for his tireless enthusiasm and motivation permanently in my experimental and evaluation data.

I would like to warmly thank Prof. Helmuth Böck who encouraged me to proceed finally with my PhD, for his interest in my work. I appreciate this very much. I would like thank you most warmly for your support at Atominstitut.

Deep, deep thanks go to my best friend Robert Schöppl. Thank you so much for your help and support in all this years. Thank you for taking the time to discuss with me not only scientifically topics, listening to my sorrows, my daily problems. I want you to know how much I appreciate your friendship. It is rare to find such kind friend like you, especially ones who you can call at the last minute. Thanks for being such a great friend.

Warm thanks to my former and present colleagues, Robert Schoppl, Dr. Katharina Durstberger, Thomas Stummer, Dr. Erwin Jericha, Mario Villa, Gertrude Konrad, Andreas Musilek, Hanno Filter, Matthias Heumesser, Wilfried Mach, Tobias Rechberger, Marcela Cagnazzo, Peter Kregsamer, Laura Stöber, Stefan Hummel, Marie-Theres Smolle, Johannes Hecher for their friendly conversations, spending nice time while drinking long coffees and their helps to improve my German language. I could express my gratitude for the friendly and unique atmosphere created at the Atominstitut where the enduring memories are made of.

I would like to give my thanks to Prof. Eberhard Lehmann for his support. I appreciate very much his role in this study. My special thanks go also to Nikolay Kardjilov for our scientific discussions even in far distance.

The performance of this PhD would not be possible without the high quality education offered in the Physics Faculty of the Tirana University. For basics in Physics and Nuclear Physics I want to acknowledge Prof. Fatos Klosi. He supported me permanently in all this long way. He had and still has a very strong positive influence on me. Teaching me the most important thing in life: That only hard working, making big efforts you will reach everything in your life, so in few words: Never give up..... If you work really, really hard over a long period of time, it will pay off.

My family, my parents they always wanted the best for me. They could to the impossible only for me. They always believed in me

Content

Abstract	7
Introduction	11
Chapter 1 Neutron Source	14
1.1 Thermalized Neutron Source	14
1.2 Neutron Spectra	17
1.3 Neutron Collimator	19
1.4 Neutron Interaction with Matter	20
1.5 Neutron Radiography	23
1.6 Basic Experimental Set-Up of Neutron Radiography	27
1.7 Neutron Beam Line	28
1.8 Mathematical and Physical Foundations of Neutron Radiography	29
1.9 Neutron Tomography NT (3-D imaging)	32
Chapter 2 Neutron detectors	34
2.1 Neutron Detectors Types	34
2.2 Characterization of the Detectors	35
2.3 Neutron Detection with ⁶ Li-Scintillator	36
2.4 Imaging Plate Neutron Detector (IP-ND)	42
2.5 Transmission Experiments with IP-ND	44
2.6 Neutron Irradiation Experiments with IP-ND; Linearity and Reproducibility	46
2.7 ND&M Neutron Camera	49
2.8 Summary	52
Chapter 3 Investigation of Boron Steel and Monte Carlo Method	53
3.1 MCNPX –Boron Micro in-homogeneities	53
3.1.1 Physics	54
3.1.2 Neutron Physics in MCNPX	54
3.2 Neutron Source Simulation	55
3.3 Geometry Description: Simulated Collimator	56
3.4 Detector Design in Simulations	59
3.5 Heterogeneous Structure Modelling of Boron in Steel Alloy	63
3.5.1 Model 1	65
3.5.2 Model 2	66
3.5.3 Model 3	66
3.5.4 Model 4	67

3.6	The Absorber Fluctuation Effect	69
3.7	Applications: Transmission Experiments on Boron Steel Plates.....	70
3.8	Exponential Attenuation	73
3.9	Transmission Experiment with ^6Li Scintillator Detector.....	74
3.10	Experimental Setup – Background Correction	76
3.11	Transmission Experiment with IP-ND Detector.....	78
3.12	Results and Comparison of the Experiment with Simulated Data.....	81
3.13	Rescaling Effect.....	83
3.14	Isotopic Ratio Diagrams	85
3.15	Simulated Neutron Scattering inside the Sample	86
3.16	The Background Estimation	87
	Boron Polyethylene Transmission Experiments with ^6Li Detector	87
3.17	Summary.....	89
Chapter 4	Hollow Glass Micro-spheres	91
4.1	Introduction	91
4.2	Hollow Glass Microspheres HGM	92
4.3	Hydrogen Storage.....	92
4.4	HGM for Hydrogen Transport.....	93
4.5	Storage Capacity.....	95
4.6	Filling HGM with Hydrogen	96
4.7	The Neutron Radiography Method.....	98
4.7.1	Theoretical Considerations	99
4.8	Experimental Data and Results.....	100
4.9	Summary.....	104
Chapter 5	Fuel Cell Radiography.....	105
5.1	Introduction	105
5.1.1	Design.....	105
5.1.2	Proton Exchange Membrane Fuel Cells	106
5.1.3	Gas Diffusion Electrodes (GDE).....	109
5.1.4	Theoretical Maximum Efficiency.....	109
5.1.5	Basics and Motivation	110
5.2	Neutron Imaging System	111
5.3	Water Visualization	112
5.4	Image Normalization; Quantification Analysis	113
5.5	Radiography Measurements with Scintillator	114

5.6	Image Processing and Analysis - Results	117
5.7	Fuel Cell - humidity 90% (2A und 6A applied current)	119
5.8	Fuel Cell - humidity 30% (2 and 6 A applied current)	122
5.9	Fuel Cell - humidity 30% (2 and 8.5A applied current)	123
5.10	Fuel Cell - humidity 90% (0 and 2 A applied current)	129
5.11	Fuel Cell - humidity 90% (0 and 6 A applied current)	130
5.12	Quantification and Visualization with IP-ND Detector	136
5.13	Fuel Cell - humidity 90% (6 and 8.5 A applied current)	138
5.14	Summary	141
Chapter 6	Heat Exchanger Radiography	143
6.1	Introduction	143
6.2	Design of Plate and Frame Heat Exchangers	143
6.3	Heat Pump	146
6.4	Neutron Radiography of a Plate Heat Exchange	146
6.5	Results and Discussion	147
6.6	Summary	149
Chapter 7	Conclusions	150
Chapter 8	References	152
Chapter 9	Appendix A	160
A-1	MCNPX 2.4.0 version	160
A-2	Cell Card	160
A-3	Surface Card	160
A-4	Data Card	161
A-5	SDEF – General Source Card	161
A-6	Tallies	161
A-7	Material Specification	162
A-8	How to Run MCNPX	162
A-9	Detector Modelling	163
A-10	Collimator Modelling	164
A-11	Boron Steel in-Homogeneity Modelling	165
A-12	Neutron Source design in simulations.	167
A-13	Material Modelling	168
Chapter 10	Appendix B	168
B-1	Transmission Experiments with Monochromatic Beam	168

Abstract

This thesis presents neutron imaging as a technique that can be used to reveal the presence of chemical composition in the materials, their structure, and the presence of the in homogeneities within the sample. Because the neutrons are very sensitive to small amounts of hydrogen this method makes possible the visualisation of water in a very accurate way.

Most of the experimental results were obtained using the neutron radiography NR station II at Atominstitut, which possesses a Triga Mark II research reactor. The reactor has a maximum power of 250 kW. The neutron radiography instrument set-up utilises a thermal flux of 1.3×10^5 neutrons/(cm²s) and is capable of producing high quality images. Meanwhile the neutron beam has a diameter of 9 cm, with a divergence of 0.44 degrees (7.6 mrad), equivalent to the beam length to diameter ratio $L/D \sim 130$ achieving a spatial resolution of ~ 150 μm with a thin plate ⁶Li scintillator detector. The imaging instruments include also an imaging plate neutron detector, which has a nominal scanner resolution of 50 μm , and make this method ideal for obtaining real time images in two dimensions, and in three dimensions as well. In this thesis, we analyse the strengths and limitations of each detector in the field of neutron radiography and tomography, and demonstrate that high resolution digitized images down to the 50 μm scale can be accomplished with such a low neutron flux, if appropriate measures are taken in appropriate exposure time.

It has been shown that with these properties, the neutron radiography method is the best method for highly absorbing and relatively thick samples on a reasonable time-scale and in a wide range of scientific fields. Interesting materials used in nuclear technology such as Boron steel materials used in nuclear shielding were studied together with MCNPX simulations. The neutron transmission through thick and strong absorbing steel sheets is slightly enhanced due to boron micro-in-homogeneities. This effect was estimated by means of MCNPX in details. The transmission data have been analysed by applying different models of micro-in-homogeneities in the range of 20 μm , and in all cases these models demonstrate an elevated transmission. It has been shown, that including the microstructure in the analysis provides a more suitable modelling for neutron transmission through strong absorbing materials.

Hollow microspheres are promising candidates for future hydrogen storage technologies. Hollow micro-glass spheres filled with hydrogen were investigated under different conditions. Although the physical process for hydrogen diffusion through glass is well understood, measurements of static quantities such as hydrogen pressure inside the spheres as well as dynamic properties such as the diffusion rate of hydrogen through glass are still difficult to handle due to the small size of the spheres ($d \approx 15$ μm). For diffusion rate measurements, the long-term stability of the experiment is mandatory due to the relatively slow diffusion rate. In this work,

we present an accurate and long-term stable measurement technique for static and dynamic properties, using neutron radiography method.

Neutrons are ideal for imaging of hydrogen fuel cells because of their sensitivity to hydrogen-containing compounds such as water. Neutron imaging was performed to visualize the water distribution and movement at flow channels in operating proton exchange membrane fuel cell. According to operation conditions, inlet humidity and density current, the phenomenon of water distribution was investigated. The real-time radiography image were analysed to quantify the water amount in the membrane electrode assembly MEA inside the fuel cell. However, the mechanism of the membrane is not completely understood, because of the difficulty of measuring the water distribution during the operation of the fuel cell. Knowing where liquid water accumulates with more certainty helps us to understand the water transport in proton exchange membrane of the fuel cell.

Experimental techniques were developed to visualize liquid flows inside a heat exchanger by the neutron radiography method. The air–water two-phase brazing plate heat exchanger was visualized by the thermal neutron radiography method as a non-destructive method in order to clarify the water distribution. Heat transfer characteristics of the heat exchanger are dominated by the characteristics of fluid movement and it is essential to understand the two-phase regime in heat exchangers. It was shown that it is possible to visualize these two - phase regimes in a plate heat exchanger by neutron radiography.

These applications show that neutron imaging can be performed at the low power research reactor and is a suitable non-destructive technique in various scientific disciplines and other application in oriented fields.

Kurzfassung

Die vorgelegte Arbeit präsentiert Neutronenbildgebung als Technik zum Finden der Zusammensetzung von Proben, deren Grobstruktur und möglicher Verunreinigungen. Neutronen wechselwirken stark mit geringsten Mengen von Wasserstoff, weshalb Wassergehalte leicht sichtbar gemacht werden können.

Die meisten Experimente wurden an der Neutronen-Radiographie Station II am Atominstytut (TRIGA Mark II Forschungsreaktor, 250 kW thermische Leistung im Dauerbetrieb) durchgeführt. An diesem Strahlrohr wird ein Fluss von 1.3×10^5 Neutronen/(cm²s) - thermisch - erreicht, was für qualitativ hochwertige Abbildungen ausreicht. Der Neutronenstrahldurchmesser am Austritt beträgt 9 cm, mit einer Divergenz von 0.44 Grad (7.6 mrad), gleichbedeutend zu einem Verhältnis Strahllänge zu Durchmesser von $L/D \sim 130$. Mit einem dünnen ⁶Li Szintillationsdetektor kann eine Auflösung von ~ 150 μm erreicht werden. Weiteres kann ein imaging plate Neutronendetektor mit einer nominellen Scanner-Auflösung von 50 μm eingesetzt werden. Insgesamt ist diese Methode ausgezeichnet zur 2- und 3- dimensionalen Bildgebung in Echtzeit geeignet. In dieser Arbeit werden die Stärken und Schwächen der jeweiligen Detektoren im Felde der Neutronenradiographie und Tomographie ausgelotet. Es wird weiter gezeigt, dass trotz des relativ geringen Neutronenflusses, dass hochauflösende Bildgebung bis in den 50 μm Bereich in akzeptabler Messzeit erreicht werden kann, wenn geeignete Maßnahmen ergriffen werden.

Es konnte gezeigt werden, dass diese Methode für ein breit gestreutes Feld von Anwendungen bestens geeignet ist für stark absorbierende und relativ dicke Proben. Bor-Stahl, der in der Nukleartechnik als Absorber verwendet wird, wurde vermessen und in Verbindung mit MCNPX Simulationsrechnungen erstellt. Eine vom theoretisch erwarteten Verhalten abweichende Transmission durch dicke, stark absorbierende Stahlproben konnte auf Bor – Mikroinhomogenität im Bereich von 20 μm zurückgeführt werden. Es konnte gezeigt werden, dass, durch die Einbeziehung verschiedener Mikrostrukturmodelle in die MCNPX Berechnungen, eine bessere Übereinstimmung mit den realen Messwerten zu erzielen ist.

Hohle Mikro-Glaskugeln stellen vielversprechende Kandidaten zur Wasserstoff-Speicherung dar. Derartige hohle Mikro-Glaskugeln wurden unter verschiedenen Bedingungen vermessen. Obwohl der physikalische Vorgang der Wasserstoff-Diffusion gut verstanden ist, sind z.B. der innere statische Wasserstoff-Druck, als auch die dynamische Diffusionsrate relativ schlecht zugänglich; Dies liegt an der geringen Größe der Mikro-Glaskugeln ($d \approx 15$ μm). Für die Messung der relativ langsamen Diffusion ist die Langzeitstabilität der bildgebenden Experimente von entscheidender Bedeutung. In dieser Arbeit wird eine genaue und langzeitstabile Messtechnik zur Erfassung statischer und dynamischer Eigenschaften mittels Neutronenradiographie vorgestellt.

Neutronen sind ideal geeignet zur Bildgebung von Wasserstoff-Brennzellen wegen der Empfindlichkeit gegenüber Wasserstoff. Dieses Verfahren wurde eingesetzt, um die Wasserverteilung und Bewegung in den internen Kanälen einer operativen Protonen-Austausch-Membran Brennstoffzelle zu verbildlichen, wobei

verschiedene Einflussparameter, wie Feuchtigkeit und Strom variiert wurden. Echtzeit-Aufnahmen über das Verhalten im Inneren konnten so erhalten werden, da etwa die Wasserverteilung an den Membranen im Betrieb noch nicht ausreichend verstanden ist. Diese Methode verbessert das Verständnis der Wasserverteilung / Akkumulation an den Membranen innerhalb der Brennstoffzellen.

Experimentelle Methoden, unter Zuhilfenahme der Neutronenradiographie, wurden entwickelt, die Flüssigkeitsverteilung im Inneren von Wärmetauschern zu verbildlichen. Ein 2-Phasen Luft-Wasser Wärmetauscher wurde zerstörungsfrei untersucht, um die Wasserverteilung besser zu verstehen. Die Wärmeübergangscharakteristik eines solchen Wärmetauschers wird dominiert durch die Flüssigkeitsbewegung im Inneren, welche mittels der Neutronenradiographie dargestellt werden konnte.

Die dargelegten Anwendungen zeigen, dass Neutronenradiographie durchaus an einem Niederleistungsforschungsreaktor durchgeführt werden kann. Diese ist ein geeignetes, zerstörungsfreies Verfahren für verschiedenste wissenschaftliche Disziplinen als auch anwendungsorientierte Bereiche.

Introduction

At the Atomic Institute, Vienna, neutron imaging has a long tradition with a 250kW TRIGA MARK II reactor. In the framework of this thesis, the experimental set-up at Neutron Radiography station II has been used to perform several experiments.

At the neutron radiography station NR II we have characterised and improved the existing detection system. The NR II station provides a neutron scintillator in combination with a CCD camera and an imaging plate neutron detector IP-ND. Each of our detectors has specific features and fields of applications. The selection of the detectors is determined by beam intensity and intended applications. We analysed the strengths and limitations of each detector in the field of neutron radiography and tomography, and demonstrated that high resolution digitized imaging down to the 50 μm scale can be accomplished with weak beam intensities of $1.3 \times 10^5 \text{ n}/(\text{cm}^2\text{s})$, if appropriate measures are taken for the inevitable extension of measurement times.

The neutron interaction with matter principle has been employed in investigations of boron steel materials used in the nuclear industry, for studying hydrogen storage in hollow micro-spheres and in the field of engineering and in many research topics e.g. neutron radiography of fuel cells and heat exchangers.

Boron element, especially the B-10 isotope, is a strong neutron absorber used for neutron screens, advanced neutron converter detectors, and in nuclear engineering as reactor shielding, fuel storage and transportation baskets. The realization of uniform boron distribution is an important property for these applications in order to homogenize and minimize neutron transmission.

Neutron transmission is a well-suited method for inspection of in-homogeneities of the materials. The transmission data have been analysed by designed models, using Monte Carlo Neutron Transport (MCNPX) code modelling materials with inhomogeneities. The transmission through boron polyethylene plates was accurately background corrected. The main objective of this work was to investigate the effect of micro-inhomogeneities on neutron transmission, in order to obtain additional information about the absorber distribution even beyond the detector resolution. The Böhler Bleche GmbH Company, which produces boron steel, has supplied us with sample plates. Monte Carlo simulations were performed for better understanding and interpretation of the obtained experimental results. In this part of the thesis, we focused on the secondary effects, considering: energy distribution, beam hardening, the background effect, and finally the analysis of absorber inhomogeneities.

Hydrogen due to its usage in fuel cells is seen as an important alternative renewable energy source. Most research into hydrogen storage is focused on storing hydrogen as a lightweight, compact energy carrier for mobile applications.

The concept of using hollow glass microspheres as a hydrogen storage medium has been known for some time. Hollow glass microspheres (HGM) can be used for controlling storage and release of hydrogen. Hydrogen diffuses through the thin wall of the HGM at elevated temperatures and pressures.

The hydrogen diffuses through the microsphere membranes, equilibrating the internal and external pressures and filling the spheres. The gas is then trapped upon cooling to room temperature. The ability of HGM to safely store compressed hydrogen gas is a major advantage.

We are presenting a method for pressure and diffusion rate measurements based on neutron radiography. Based on the hydrogen sensitivity, which is very high, high scattering cross-section of hydrogen yields high detection sensitivity by neutron radiography. This property has been used to study the transport and storage of hydrogen filling the hollow micro spheres. For this experiment we used S38HS microspheres with an average diameter of approximately 15 μ m. The hollow microspheres were filled with hydrogen gas under different pressures. The attenuation is dominated by the hydrogen presence in the samples.

Neutron transmission measurements of hydrogen filled microspheres are the first step quantifying microspheres and their filling process. These data are necessary to optimize the complete system regarding storage pressure and long-term stability. The next steps are the optimization of the filling process and testing different types of microspheres. The outcome of this fundamental research can further be used to optimize hydrogen filled microspheres for energy related applications, e.g. safety hydrogen storage system for fuel cells.

A Fuel cell is a device that converts the chemical energy from a fuel into electricity via a chemical reaction with oxygen or another oxidizing agent. Hydrogen is the most common fuel.

Oxygen and hydrogen react at the gas diffusion electrodes, to form water, while converting the chemical energy into electrical energy.

Fuel cells are used to power vehicles, including automobiles, buses, forklifts, airplanes, boats, motorcycles and submarines. There are many types of fuel cells, but they all consist of an anode (negative side), a cathode (positive side) and an electrolyte that allows charges to move between the two sides of the fuel cell. Electrons are drawn from the anode to the cathode through an external circuit, producing direct current electricity.

A proton exchange membrane fuel cell or electrolyte membrane (PEMFC) is a semi permeable membrane generally made from ionomers and designed to conduct protons while being impermeable to gases such as oxygen or hydrogen. This is their essential function when incorporated into a membrane electrode assembly (MEA) of a proton exchange membrane fuel cell or of a proton exchange membrane electrolyser: separation

of the reactants and transport of protons. Liquid water comes into the fuel cell by humidification of the supplied gases. Only with a humid membrane the proton conductivity of the membrane – which is essential for the function of a PEMFC - is warranted.

Neutron imaging was used to investigate the water distribution inside the membrane of a stationary fuel cell, under different applied current density and under different humidity conditions. This method has proven to be a valuable tool to visualize operating stationary fuel cells and to detect and quantify water created inside the fuel cells.

The NR II station at ATI has provided images with spatial resolution of 200 μm for ^6Li scintillator with CCD camera and 50 μm for imaging plate neutron detector IP-ND of a fuel cell during operation. Knowing where liquid water accumulates with more certainty helps us to understand the water transport inside membrane in fuel cells.

A heat exchanger is equipment built for efficient heat transfer from one medium to another. Heat exchanger and heat pumps are an important and promising technology to decrease energy consumption regarding heating and cooling and therefore increase overall efficiency of industrial processes. To further develop these technologies it is important to understand two phases (liquid, gas) flow regimes in heat exchangers, in particular plate heat exchangers. For that an experiment was carried out at the NR II station, where a small plate heat exchanger was analysed by neutron radiography to visualize the process.

The difference of a water filled or air filled heat exchanger is clearly visible as well as the inner structure of the heat exchanger. Visualization had been successfully obtained from images with high spatial resolution imaging plate neutron detector IP-ND.

Chapter 1 Neutron Source

A nuclear reactor produces free neutrons via fission reaction with high energies; therefore neutrons have to be thermalized. Neutrons are moderated to have a thermalized neutron flux described by Maxwellian distribution. Thermal neutrons have a high absorption cross section in the thermal energy range. Therefore the total neutron absorption principle is used in neutron radiography and tomography techniques. These techniques enable us having in this way information about internal structure of materials of interest.

1.1 Thermalized Neutron Source

For neutron transmission experiments usually thermal ($v_{thermal} = 2200 \text{ m/s}$) and cold ($v_{cold} = 700 \text{ m/s}$) neutrons are used, because most of the investigated materials have a higher attenuation for low neutron energies. But also the detection sensitivity for slow neutrons is higher. This allows us to use very thin detectors with high resolution. Free neutrons, which are necessary in a neutron transmission experiment, are produced via nuclear reactions at the Triga Mark-II reactor at ATI (Atominstut der Österreichischen Universitäten) (figure. 1.1.1) [Buchberger, 1986].

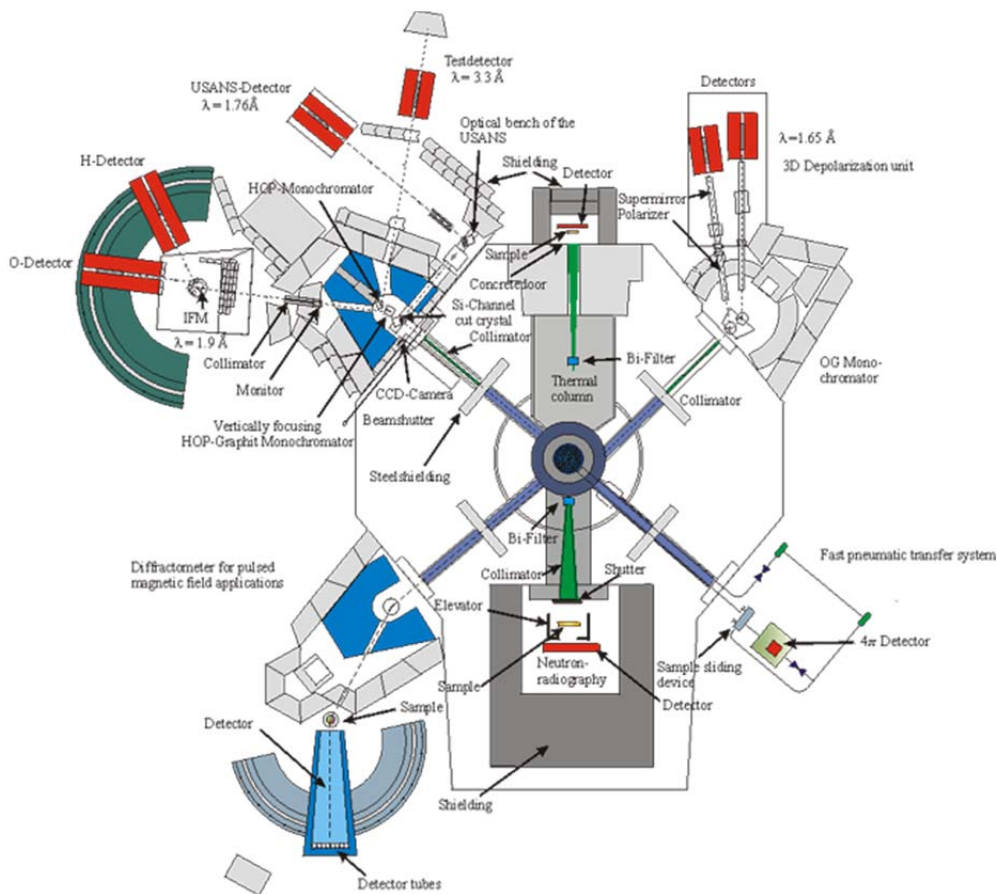
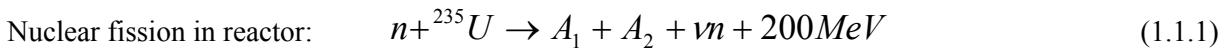


Figure 1.1.1 The four neutrons beam lines at the Triga Mark-II reactor near ATI.

It is a swimming-pool type that is used for training, research and isotope production.



where nuclear fission is mainly initiated by thermal neutrons and where $\nu \cong 2.4$ neutrons are released. A continuous source of neutrons is provided by a chain reaction. A_1 and A_2 denote the various fission fragments. The Triga MARK II reactor has a maximum continuous output of 250 kW. The reactor core consists of some 80 fuel elements. Figure 1.1.2 shows the core map. The fuel is in the form of a uniform mixture of 8 wt% uranium (U), 1 wt% hydrogen (H) and 91 wt% zirconium (Zr), as zirconium-hydride, being the main moderator. The reactor is controlled by three control rods, which contain boron carbide as absorber material.

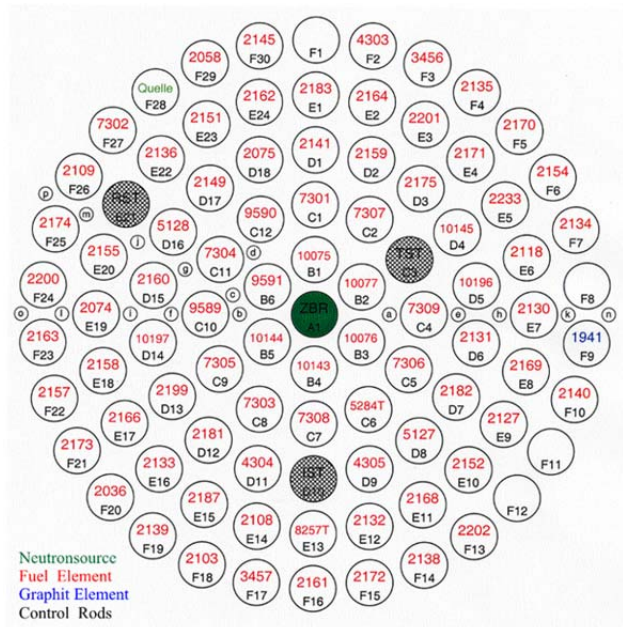


Figure 1.1.2 The core map of the ATI Triga MARK II reactor.

As a research reactor the Triga Mark-II is equipped with one neutron radiography facility and with one thermal column, which is filled with graphite to slow down the neutrons. In this case it is working as a moderator for free neutrons coming from the core. By applying elementary laws of mechanics the mean energy loss ΔE in the laboratory system for scattering from nuclei of mass number A has the form:

$$\Delta E = \frac{E}{2} \frac{4A}{(A+1)^2} \quad (1.1.2)$$

In the case of graphite, around 114 collisions and a time of about 159 μs are necessary for moderations. Fission takes place in any of the heavy nuclei after capture of a neutron. However, low-energy or thermal neutrons are able to cause fission in ${}^{235}\text{U}$ isotopes of uranium. The probability that fission will occur is

described by the neutron cross-section for that reaction. In such as ^{235}U , the fission cross-section becomes very large at the thermal energies of slow neutrons like is shown in figure 1.1.3.

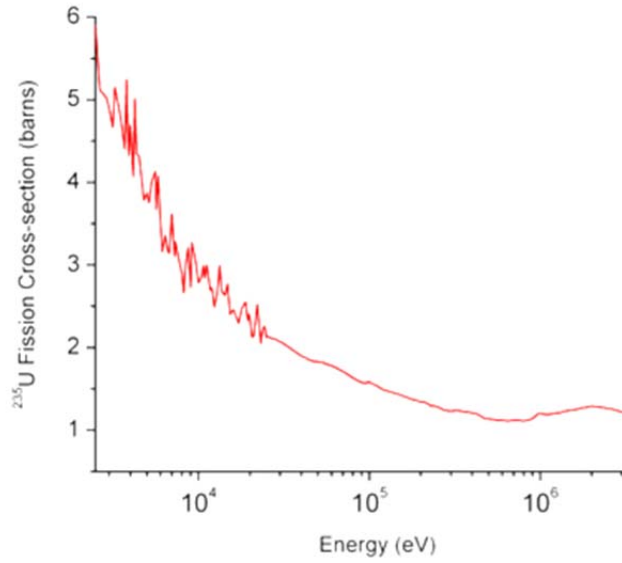


Figure 1.1.3 Cross section (in barns) as a function of neutron energy for ^{235}U , showing increases in fission probability with lower neutron energy.

As soon as the neutrons reach the energies comparable to the thermal energy of moderator atoms, there are in thermal equilibrium corresponding to the Maxwell-Boltzmann energy distribution. The thermalized neutrons are extracted from the moderator through beam tubes. Kinetic energy E can be related to temperature T via [Zawisky, 2006]:

$$E = \frac{1}{2}mv^2 = \frac{3}{2}k_B T \quad (1.1.3)$$

Where k_B - Boltzmann constant, m is neutron mass and v is neutron velocity. The energy distribution of the neutron flux can be written approximately as:

$$\Phi(E) = \Phi_{th} \frac{E}{(k_B T)^{3/2}} e^{-E/k_B T} \quad (1.1.4)$$

Where Φ_{th} - thermal neutron flux. The values for the thermal energy, velocity wavelength can be derived using the relationship [Zawisky, 2006]:

$$E_{th} = k_B T = \frac{mv_{th}^2}{2} = \frac{h^2}{2m\lambda_{th}^2} \quad (1.1.5)$$

Where h is Planck constant.

1.2 Neutron Spectra

With Bonner Sphere Spectrometry (BSS) it is possible to measure the spectral distribution of the neutron fluence rate at the thermal column of the Triga reactor [Hajek, 2001]. This method makes use of a detector for thermal neutrons in the centre of polyethylene moderating spheres. Polyethylene $(CH_2)_n$ is employed, because it is an ideal moderating material for neutrons due to its high concentration of elements like hydrogen and carbon which have a low atomic number and high scattering probability. Depending on the diameter of the sphere, a fraction of the neutrons gets moderated until they reach the thermal equilibrium with the moderator atoms and the detector placed in the centre of the sphere detects these neutrons. The detector in BSS used for this type of measurements was a $^6Li(EU)$ -scintillation counter optically coupled to a photo multiplier tube with connected pre-amplifier. The LiI-scintillator measures the density of the thermalized neutron inside the Bonner spheres. Thermal neutrons will have a Maxwellian energy distribution such that the number of neutrons dn per volume element with energies between E and $E + dE$ is [Hajek, 2001]:

$$dn = n(E) = \frac{2\pi n}{(\pi k_B T)^{3/2}} \exp(-E/k_B T) \sqrt{EdE} \quad (1.2)$$

From the figure 1.2.1 it is clearly visible that the energy spectrum emitted at the reactor beamlines can approximately described by three parts: a Maxwellian distribution around thermal energies, followed by $1/E$ -spectrum for intermediate energies and again a Maxwellian spectrum for the fast neutrons. These theoretical were used as input into measurements data.

From the plot in the figure 1.2.2 the neutron energy spectrum at the thermal column at The Triga Mark II reaserch reactor at ATI can be well described by a Maxwellian distribution function.

The contribution of the fast neutrons to the total flux is negligible. Values are calculated for a thermal power of 250 kWh with the assumption of a linear flux/power relationship. BSS measurements have been carried out at a distance of 35 cm from the graphite surface, behind the concrete door.

For fully thermalized neutron spectra at room temperature we have: $E_{th} = 0.0253 \text{ eV}$, $v_{th} = 2200 \text{ m/s}$, $\lambda_{th} = 0.18 \text{ nm}$ [Sears, 1992].

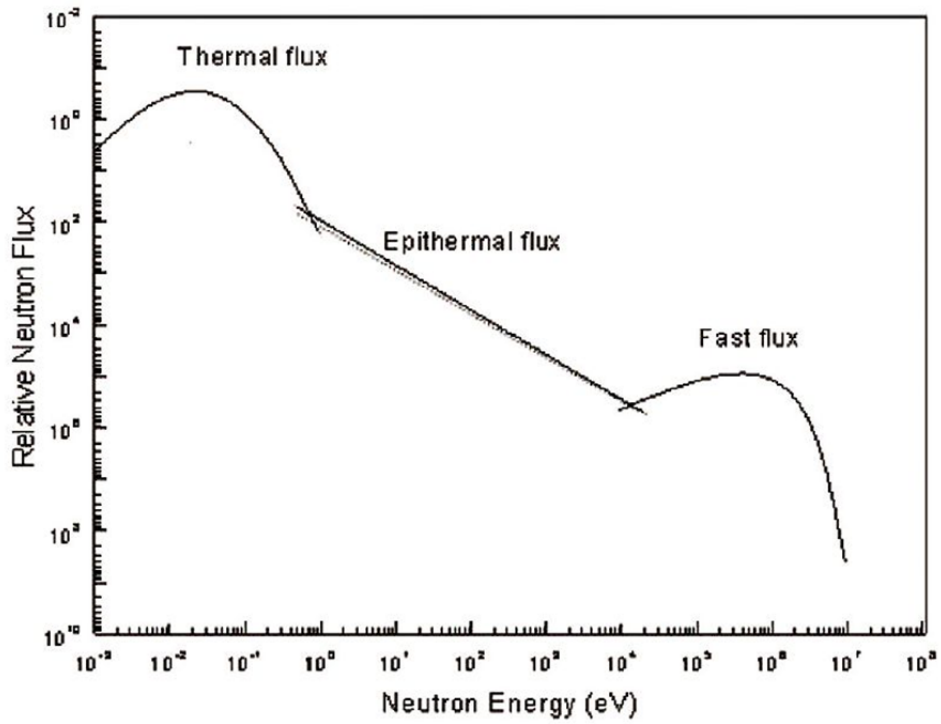


Figure 1.2.1 Default reactor spectra used for spectra deconvolution [Hajek, 2001].

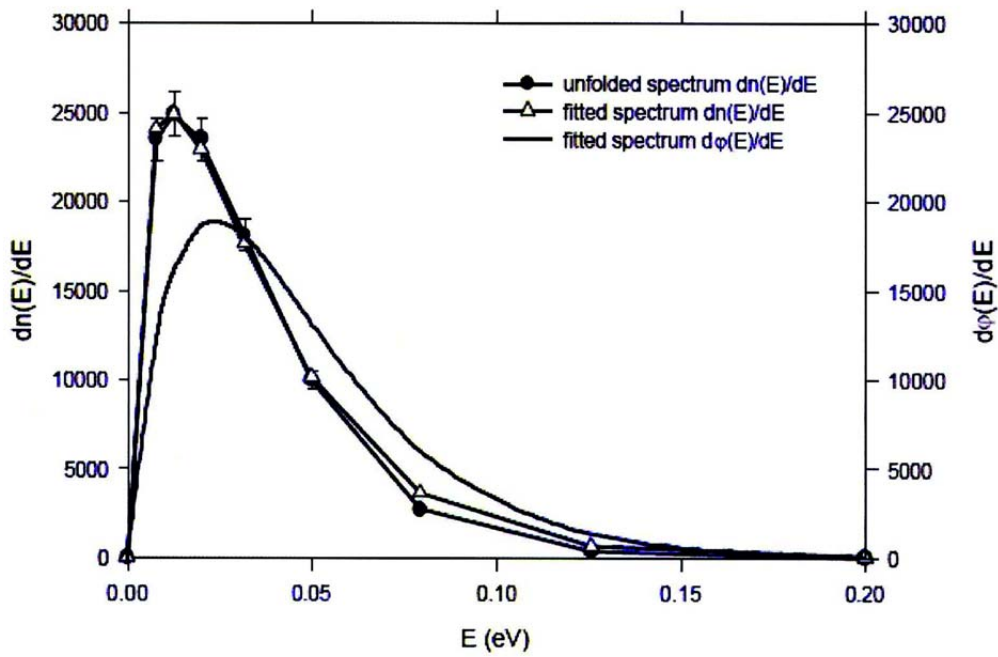


Figure 1.2.2 Unfolded and fitted neutron spectra at the thermal column of the TRIGA Mark-II research reactor at ATI [Hajek, 2001].

1.3 Neutron Collimator

When the neutrons are in a thermal equilibrium with the moderator, the collimator selects the neutrons flying in the same direction towards the sample and the detector. The collimator at the NR-II facility has two sections as shown in figure 1.3.1. The first section is conical and the second section is cylindrical.

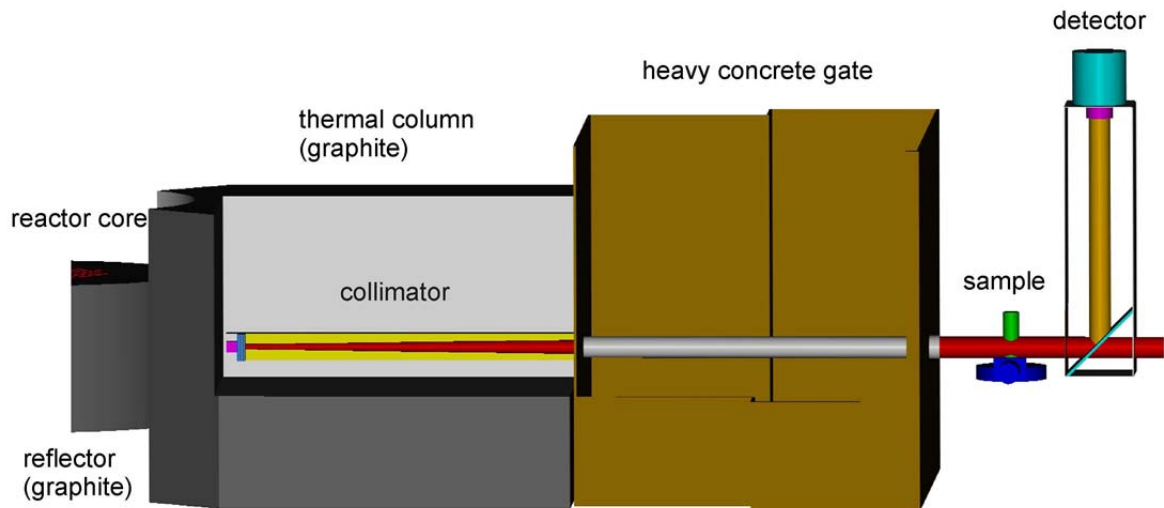


Figure 1.3.1 The NR-II station at ATI in Vienna [Zawisky, 2006].

The conical part is installed in the thermal column and consists of two concentric cones, where the innermost has an aperture of 2 cm and an outlet of 9 cm at a length of 130 cm. Each is about 3 mm thick.

The inner cone is the borated epoxy compound also coating the outer cadmium cone (see figure 1.3.2). The cylinders are shielded at their outside of the thermal column by borated polyethylene out to a diameter of 20 cm. After this comes the cylindrical part which is attached to the movable heavy concrete door and has a length of 130 cm, (innermost has a diameter of 9 cm). It has a similar cross section as the cone [Koerner, 2000], [Bastuerk, 2003].

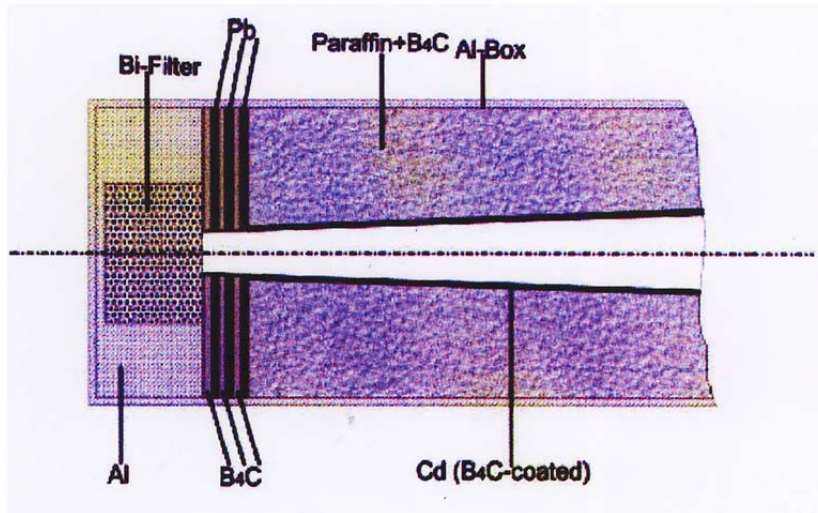


Figure 1.3.2 The composition of the conical part of the collimator at NR-II station.

After the moderation, the directions of the neutron velocities are approximately isotropically distributed. By collimation we can say, that the neutron beam reaching the sample can be considered as being parallel. The existence of the graphite block makes possible a homogeneous neutron energy distribution. If the z-axis is aligned with the neutron beam and assuming to be quasi parallel, the inevitable divergence is described by the L/D-ratio, where L is the length of the collimator and D the diameter of the aperture. Typical value for L/D at our NR-II station is 130, which corresponds approximately to a maximum divergence angle of 0.44 degrees.

1.4 Neutron Interaction with Matter

The neutron is a subatomic particle with no electric charge and a mass slightly larger than that of a proton: $m_n = 939.565379(21) \text{ MeV}/c^2 = 1.67492716 \times 10^{-27} \text{ kg}$ [PDG, 2015].

Neutrons passing the sample can react with atomic nuclei and possible reactions are absorbing or scattering events. The probability for a reaction depends on the neutron energy and is described by the microscopic cross section $\sigma(E)$. For slow neutrons the cross section σ is exactly proportional to $1/v$: ($\sigma(E) \approx \frac{1}{v}$, Fermi's Law) - where v is neutron velocity. The total cross section σ_t is usually measured in transmission experiments. A thin sample, with thickness dx is placed in front of the monochromatic parallel neutron beam, with an intensity I_0 and a detector is placed behind the sample. The intensity of the beam will decrease by the number of neutrons that have interacted in the thin sample [Lamarsh, 1969]:

$$-dI(x) = N\sigma_t I(x)dx \quad (1.4.1)$$

where N is the atom density of the target. After integration, we have:

$$I(x) = I_o e^{-N\sigma_t x} \quad (1.4.2)$$

The intensity after interaction decreases exponentially with distance inside the target. This equation is known as *Beer's law*.

The product of the atomic density and the cross section is called the macroscopic cross section. In particular the product: $N\sigma_t = \Sigma_t$ is called *the macroscopic total cross section*.

In terms of Σ_t the equation (1.4.1) can be written as [Lamarsh, 1969]:

$$-dI(x) = \Sigma_t I(x)dx \quad (1.4.3)$$

Dividing this expression by $I(x)$ gives:

$$-\frac{dI(x)}{I(x)} = \Sigma_t dx \quad (1.4.4)$$

The quantity $dI(x)/I(x)$ is the fraction of the neutrons that have penetrated the distance x into the target without interacting, which subsequently interact in the infinitesimal length dx . Thus from equation (1.4.4)

$\Sigma_t dx$ is the probability that a neutron interacts in dx , and it follows that Σ_t is the *probability per unit path length* that a neutron will undergo some sort of interaction. Returning to equation (1.4.2), it should be noted that in view of the fact that $I(x)$ refers to those neutrons that have not interacted in penetrating the distance x , the ratio [Lamarsh, 1969]:

$$\frac{I(x)}{I_o} = e^{-N\sigma_t x} = e^{-\Sigma_t x} \quad (1.4.5)$$

is equal to the probability that a neutron can move through this distance without interacting. Now let the quantity $p(x)dx$ be the probability that a neutron will have its first interaction in dx in the neighbourhood of x . Since Σ_t is the probability of interaction per path length, $p(x)dx$ is given by:

$$p(x)dx = e^{-\Sigma_t x} \times \Sigma_t dx = \Sigma_t e^{-\Sigma_t x} dx \quad (1.4.6)$$

For instance, the probability $P(a, b)$ that a neutron will have its first interaction between: $x = a$ and $x = b$ is simply the integral of $p(x)dx$ between these limits. That is:

$$P(a, b) = \Sigma_t \int_a^b e^{-\Sigma_t x} dx = e^{-\Sigma_t a} - e^{-\Sigma_t b}. \quad (1.4.7)$$

In particular, the probability that a neutron will interact at least once in an infinite medium is obtained by placing $a = 0$ and $b = \infty$ thus:

$$P(0, \infty) = \int_0^{\infty} p(x) dx = 1 \quad (1.4.8)$$

as would be expected.

The distance that a neutron move between interactions is called a *free path*, and the average distance between interactions is known as the *mean free path*. This quantity, which is usually denoted by the symbol λ , is equal to the average value of x , the distance traversed by a neutron without interaction, over the interaction probability distribution $p(x)$, that is,

$$\lambda = \int_0^{\infty} xp(x) dx = \frac{1}{\Sigma_t} \int_0^{\infty} xe^{-\Sigma_t x} dx = \frac{1}{\Sigma_t} \quad (1.4.9)$$

The sum of the cross section of all possibilities interactions is known as the total cross section:

$$\sigma_t = \sigma_s + \sigma_i + \sigma_\gamma + \sigma_f + \dots \quad (1.4.10)$$

where elastic scattering is described by the elastic scattering cross section, σ_s ; inelastic scattering by the inelastic scattering cross section σ_i ; the (n, γ) reaction (radiative capture) by the capture cross section σ_γ ; fission by the fission cross section, σ_f ; etc.

In this way the total cross section measures the probability of all absorption reactions. The difference between the total σ_t and elastic cross sections σ_s is called the “inelastic cross section”:

$$\sigma_{ne} = \sigma_t - \sigma_s \quad (1.4.11)$$

The sum of cross section over all absorption reactions is called absorption cross section:

$$\sigma_a = \sigma_\gamma + \sigma_f + \sigma_p + \sigma_\alpha + \dots \quad (1.4.12)$$

where σ_p and σ_α are the cross sections for the (n, p) and (n, α) reactions.

Besides absorption also the elastic neutron scattering on crystals is of major importance. For low energies neutron the so-called *Bragg scattering* describes the reflection of the beam on crystal planes (see figure 1.4.1), [Lamarsh, 1969].

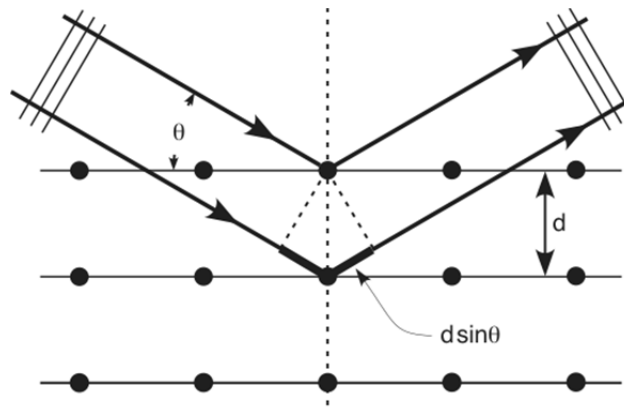


Figure 1.4.1 Bragg reflection from three crystal planes.

Neutrons will be reflected from these planes scattered through 2θ , provided the neutron wavelength λ satisfies the relation:

$$n\lambda = 2d \sin\theta \quad (1.4.13)$$

Where $n = 1, 2, 3, \dots$ and d is the distance between adjacent Bragg planes. According to this equation there is a maximum wavelength above which Bragg scattering cannot occur. By placing: $\theta = \pi/2$ and $n = 1$, this wavelength, λ_{\max} , is found to be:

$$\lambda_{\max} = 2d \quad (1.4.14)$$

Since λ increases with decreasing neutron energy, it follows that here is a minimum energy, called the *Bragg cutoff*, below which Bragg scattering cannot occur. More in details this principle is discussed in Appendix B: Transmission with Monochromatic Beam [Lamarsh, 1969].

1.5 Neutron Radiography¹

Neutron transmission radiography (NR) is based on the application of the universal law of attenuation of radiation passing through matter (equation 1.4.2). Because different materials have different attenuation behaviour the neutron beam passing through a sample can be interpreted as signal carrying information about the composition and structure of the sample. By measuring the intensity variations in the beam that passes through an object, a two-dimensional neutron image is achieved. Neutron radiography provides a very efficient tool for investigations in the field of non - destructive testing as well as for many

¹<http://www.ati.ac.at/~neutropt/experiments/Radiography/radiography.html>

applications in fundamental research. A neutron beam penetrating a specimen is attenuated by the sample material and detected by a two-dimensional imaging device. The image contains information about material and structure inside the sample because neutrons are attenuated according to the basic law of radiation attenuation. Contrary to X - rays, neutrons are attenuated by some light materials, as i.e. hydrogen, boron and lithium, but penetrate many heavy materials. Neutrons are able to distinguish between different isotopes and neutron radiography is an important tool for studies of radioactive materials. At the Atominstitut (ATI) neutron radiographic investigations are performed for more than 35 years. The detectors mainly used are converter/film assemblies. However, these detectors are limited regarding their sensitivity, dynamic range and linearity. Due to rapid development of detector and computer technologies as well as advances in the field of digital image processing, new technologies are available which have the potential to improve the performance of neutron radiographic investigations enormously. Therefore, the aim of this work is to identify and develop two and three-dimensional digital image processing methods suitable for neutron radiographic and tomographic applications, and to implement and optimize them within data processing strategies. Figure 1.5.1 shows a basic neutron radiography setup: it consists basically of a neutron beam, a collimator and a two-dimensional position detector system. The figure provides a graphical demonstration of the three components in NR. The sample is placed between neutron beam and detector, which measures the transmitted neutrons. Here we represent these two digitized imaging instruments used during transmission measurements of boron alloyed steel plate samples. The NR I and NR II are two beam lines at ATI that are dedicated to neutron imaging.

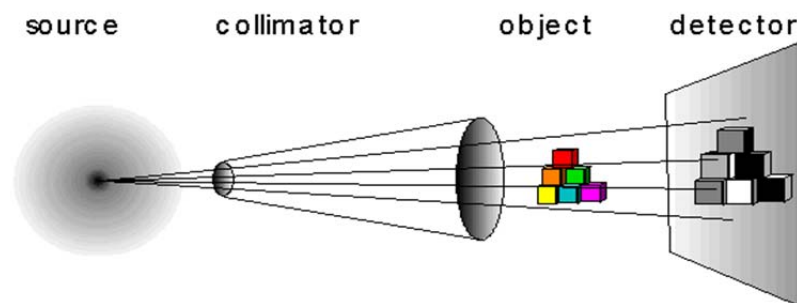


Figure 1.5.1 *The basic experimental set-up for neutron imaging.*

The NR station I is based on the film/converter method. The NR station I¹ at the Atominstitut is located at a radial thermal beam channel of the TRIGA (reactor figure 1.5.3). The collimator assembly penetrates into the reactor pool, leaving only a thin layer of water between the graphite moderator of the reactor and the

¹<http://www.ati.ac.at/~neutropt/experiments/Radiography/radiography.html>

collimator entrance. The background emitted by the reactor is reduced by a bismuth filter, which is mounted at the collimator entrance. The size of the entrance aperture (D) is 5 cm. The collimator continues as a divergent conical space with walls lined with boron carbide. Part of the collimator can be filled with water to close the beam channel. At the beginning of operation, this water is pumped out of the channel. The length of the collimator (L) is 250 cm. Therefore the L/D -ratio of this facility is 50.

The NR station II at the Atominstitut is located at the thermal column of the TRIGA reactor (figure 1.5.3). This is a cube of nuclear grade graphite with dimensions of about 1.2 m at each side. A collimator is mounted inside this cube with an aluminum shell of the dimensions $(10 \times 10) \text{ cm}^2$. The conical collimator inside this shell is made of cadmium sheet metal. The space between the collimator and its shell is filled with a polycrystalline material consisting of paraffin and boron carbide (figure 1.3.2). The diameter of the aperture blend is: $D = 2 \text{ cm}$. It is a sandwich construction made of 5 mm thick lead and boron carbide layers. A 4 cm thick bismuth crystal is used to reduce the γ -background emitted from the reactor. The second part of the collimator is mounted inside the concrete door in front of the thermal column. This part of the collimator has a cylindrical shape and a steel shell. This collimator design (2 parts) was chosen to enable access to a high flux irradiation position at the end of the thermal column. The total length of the collimator is: $L = 260 \text{ cm}$. Therefore the L/D -ratio of this facility is 130. The beam diameter at the collimator exit is: $d = 9 \text{ cm}$ (see figure 1.5.2). Both parts of the collimator are lined with boron carbide to absorb neutrons. Reasonable exposure times in the thermal column with the thermal flux $1.3 \times 10^5 \text{ neutrons}/(\text{cm}^2\text{s})$ can get as low as 20 s per image. This means, that it is possible to perform a set of measurements necessary for neutron tomography (about 200 images) within several hours. Therefore, in a second working step, an entirely automated neutron tomography facility has been built at the Atominstitut with this detector.

Table 1.1 summarizes the parameters for NR I & II stations at ATI.

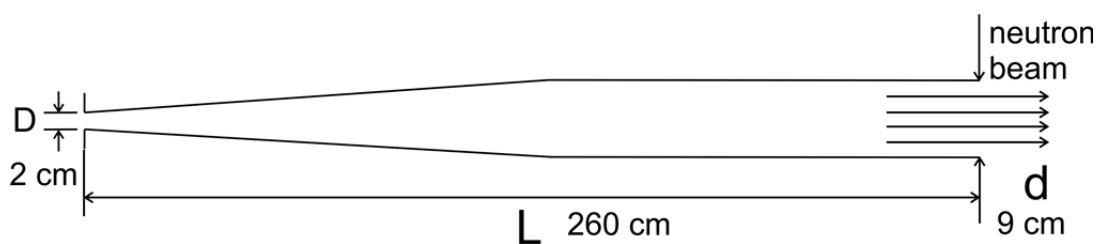


Figure 1.5.2 The L/D ratio, which is a characteristic parameter of the neutron collimator at NR II station at Atominstitut.

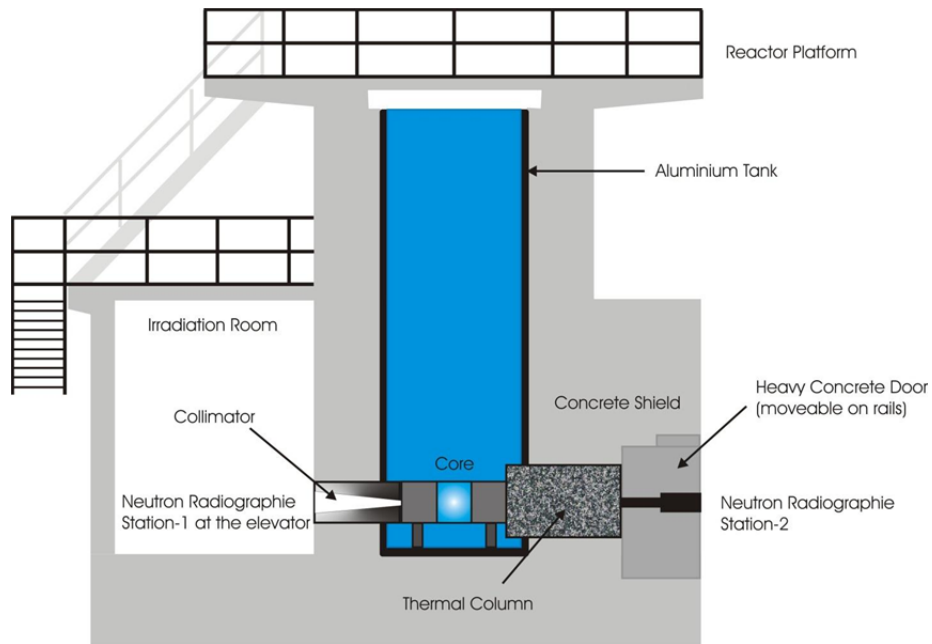


Figure 1.5.3 NR Station I & II at TRIGA Mark II research reactor at ATI.

	NR I Facility	NR II Facility
Neutron flux ($\text{cm}^{-2} \text{s}^{-1}$)	3×10^5	1.3×10^5
L/D (collimation) ratio	50	130
Cd-ratio	3	20
Beam diameter (cm)	40	9
Gamma background (Sv/h)	0.4	0.045
Source strength (n.s^{-1})	3.8×10^8	7.0×10^6
Facilities	NR	NR and NT
Detection system	X-ray film/ Converter	Scintillator/CCD camera IP-ND

Table 1.1 Basic characteristics of NR facilities at ATI.

1.6 Basic Experimental Set-Up of Neutron Radiography¹

In neutron radiography (NR), a neutron beam is recorded on a two dimensional integrating position sensitive detector after penetrating a sample. The output of the detector is an image representing the macroscopic structure of the sample interior, as the neutron beam is attenuated depending on the sample material and geometry according to the attenuation law:

$$\Phi(x, y, E) = \Phi_o(x, y, E)e^{-\Sigma(x, y, E)d} \quad (1.6.1)$$

- $\Phi_o(x, y, E)$ flux density behind the collimator in [$\text{cm}^{-2}\text{s}^{-1}$]
- $\Phi(x, y, E)$ flux density transmitted through the object in [$\text{cm}^{-2}\text{s}^{-1}$]
- d - thickness of the sample in [cm]
- Σ - total macroscopic neutron cross-section of the sample in [cm^{-1}]

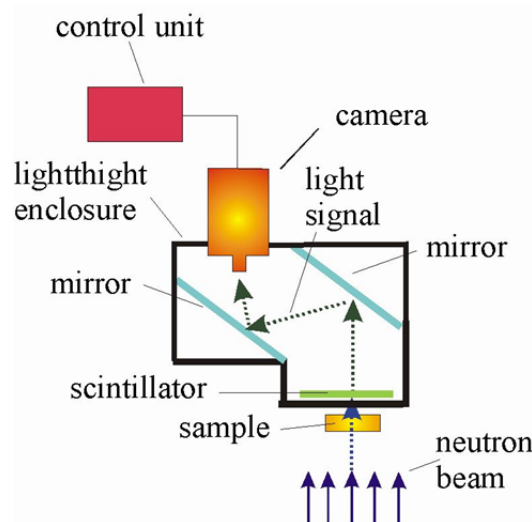


Figure 1.6.1 Scintillator with CCD camera system available at NR station II at Atominstytut¹.

Because the interaction takes place with the nucleus of the atom, the cross-section depends not only on the chemical element, but also on the specific isotope. Cross-sections of isotopes of the same element may vary over several orders of magnitude. For a chemical element consisting of a mixture of several isotopes, the overall macroscopic cross-section is the sum of the cross-sections of the isotopes weighted with their mass fractions, and for a material consisting of several chemical elements; the overall cross-section is the sum of

¹<http://www.ati.ac.at/~neutropt/experiments/Radiography/radiography.html>

the cross-sections Σ_{Ele} of the component elements designated by an index Ele , weighted with their mass-fractions p_{Ele} :

$$\Sigma = \sum_{Ele} p_{Ele} \Sigma_{Ele} \quad (1.6.2)$$

As mentioned above, the Σ of any isotope or element also depends on the neutron energy, i.e. the material of a sample interacts differently with neutrons of different energies from a typical polychromatic NR beam. The NR II is located at the thermal column of the TRIGA reactor, as shown in figure 1.5.3. The digitized neutron imaging is installed at NR II (figure 1.6.1). It has a lower neutron flux and a smaller beam diameter, and has easy access to the sample position during reactor operation.

1.7 Neutron Beam Line¹

The basic experimental layout of NR consists of a neutron source, of a collimator functioning as a beam formatting assembly, of a detector and of the object of study, which is placed between the exit of the collimator and the detector.

A neutron beam line consists of all components from the neutron source to the exit of the collimator. The following performance criteria are most relevant:

- the flux density
- the spatial resolution achievable with the beam
- the energy spectrum of the neutrons, including the Cd - ratio
- the spatial flux density distribution at the exit of the beam line, i.e. the homogeneity of the beam profile
- the size of the beam area (A)
- the gamma (γ) background.

These characteristics depend on the nature of the source and of the beam formatting assembly, and are also partly correlated. From these performance criteria the strength of the source (S) and a parameter (Q), representing the quality of the beam line can be defined:

$$S = \Phi A \quad (1.7.1)$$

and

$$Q = S \left(\frac{L}{D} \right)^2 \quad (1.7.2)$$

¹<http://www.ati.ac.at/~neutropt/experiments/Radiography/radiography.html>

At stationary NR facilities, neutron sources are usually fission reactors or accelerator / target assemblies, including neutron spallation sources. In all of these sources, neutrons are generated with high initial energies, between 2 MeV (mean value in nuclear reactors) and several 100 MeV (in spallation sources). For other materials (i.e. thin layers), the use of cold neutrons provides the most suitable technique. But nevertheless, thermal NR is the most frequent technique because thermal neutrons provide good contrasts for a large number of elements, and they are more easily available at most large neutron sources (in a thermal reactor neutrons have to be moderated to maintain the chain reaction).

1.8 Mathematical and Physical Foundations of Neutron Radiography

Neutron Radiography is an imaging technique, which provides images following the same principle to X-ray radiography. The neutron and X-ray interaction give us significantly different information. While X-ray attenuation is directly dependent on atomic number, neutrons are efficiently scattered or absorbed by the number of nuclide in a given volume unit.

Neutron imaging has long been known to provide complementary, non-destructive imaging capabilities to X-ray and gamma ray imaging methods [Anderson, 2009]. For radiography and tomography apertures or collimator systems to reduce the range of directions in which the neutrons propagate in order to obtain a defined point-to-point image collimate neutrons. Figure 1.8.1 represents the basic elements of the neutron radiography system: source of neutrons, beam conditioning and shaping, neutron and detection, and sampling and signal generation.

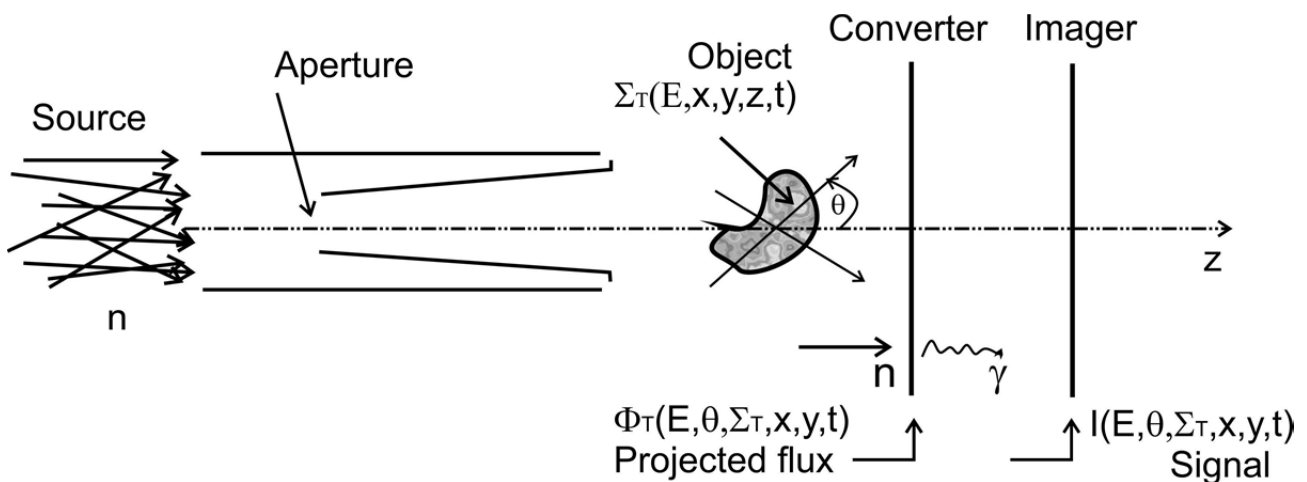


Figure 1.8.1 Basic elements of a neutron radiography-imaging environment. A source of neutron is typically shaped and collimated, interacts with the material constituents of a 3D object and is projected onto a 2D imaging array [Anderson, 2009].

The imaging system, the image of a given point in a sample, can be described by the so-called point spread function (PSF) because it involves not only the interaction with the sample but also the detector resolution

(pixel size), the spread of radiation due to divergence and scintillation (detection) processes, and optical systems (CCD cameras) [Anderson, 2009]. Referring to [Anderson, 2009] the spatial 2D resolution of a system is best measured by determining its modulation transfer function (MTF). The MTF can be derived from the Fourier Transform (FT) of the PSF (The Fourier Transform is an important image processing tool which is used to decompose an image into its sine and cosine components):

$$|MTF| = FT\{PSF(x, y)\} \quad (1.8.1)$$

So the measured intensity image $I(x, y)$ is the convolution of the 2D PSF with the 2D projection of the object function $O_p(x, y)$ (the 2D Radon transform of the 3D object), plus background (b_g), normalized to the pixel-efficiency $\varepsilon_{pixel}(x, y)$ of the detector:

$$I(x, y) = \{PSF(x, y) \otimes O_p(x, y) + b_g(x, y)\} \bullet \varepsilon_{pixel}(x, y) \quad (1.8.2)$$

Because of different efficiencies of the detector pixel and background, these two parameters must be determined very accurately to achieve definite images or reconstructions. They are derived from flat field and background images, the first obtained without the sample in the beam and the second when the beam shutter is closed.

The goal of image analysis can be formulated as one of measuring the interaction cross-section of the materials in the imaged object: Σ_t – total macroscopic cross section. Direct measurements of Σ_t provide indirect information about material properties because [Anderson, 2009]:

$$\Sigma = N\sigma \quad (1.8.3)$$

where

$$N = \frac{\rho N_A}{A} \quad (1.8.4)$$

where σ is the microscopic cross-section, N is the number of atoms per cm^2 , ρ is the material density, N_A is Avogadro's number, and A is the atomic weight.

Referring to Tobin in [Anderson, 2009] the interaction of the neutron beam Φ_o produces a total of 2D field at the converted plane Φ_T that can be decomposed into the uncollided flux, Φ_u , and the scattered flux, Φ_s , as:

$$\Phi_T = \Phi_u + \Phi_s \quad (1.8.5)$$

To understand the dependencies of the scattered flux on the image formation process, we introduce a buildup factor as: B (has a value of $B \geq 1$). It is a dependent on the composition and geometry presented by the object:

- Resolution modeling
- The effect of the neutron aperture D
- The optical diffusion response of a scintillator δ (the optical component)
- Sampling at the sensor, Δs

These effects of these systems are fundamentally described through the system impulse response $h(x)$. System impulse response $h(x)$ will be expressed as [Anderson, 2009]:

$$h(x) = h_D(x) * h_\delta(x) * h_{CCD}(x) \quad (1.8.6)$$

(corresponding to the neutron beam aperture, scintillator, and CCD sensor, respectively).

For modeling purposes, figure 1.8.2 represents an idealized radiography system containing the basic elements described earlier in figure 1.8.1. To realize a point-to-point image, the size of the source and or the beam divergence must be kept small L/D ratio where L is the distance of the point from the source and D the source aperture [Anderson, 2009].

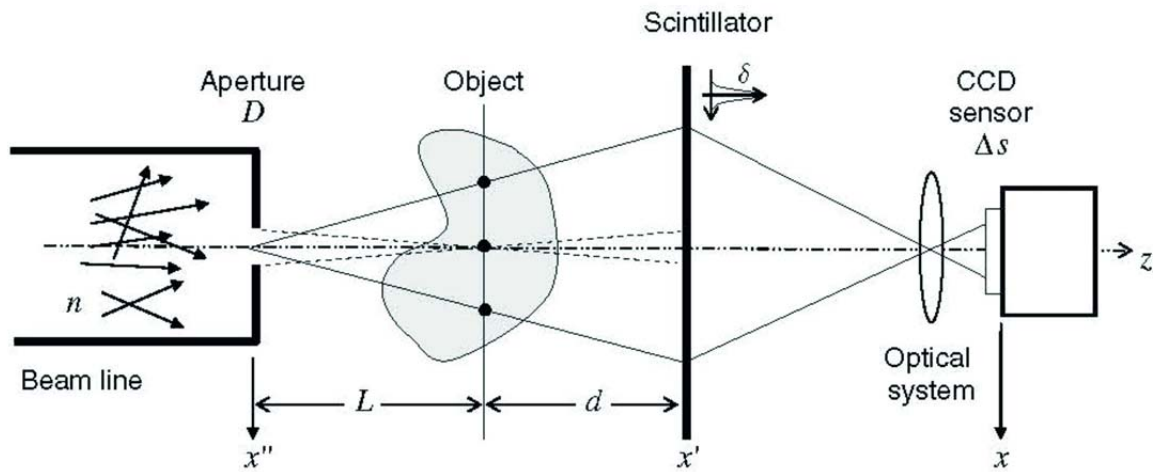


Figure 1.8. 2 Representation of a basic radiographic image formation system used to estimate resolution performance during the design stage. Model accounts for geometry, aperture size, scintillator resolution, and optical system resolution [Anderson, 2009].

The most common collimator design is a divergent collimator with a small entrance aperture and a larger exit. This maximizes the neutron flux and permits a larger field at the image plane. The angular spread of the emerging beam is dependent upon the ratio of the collimator tube length (L) to its aperture diameter (D), referred to as the L/D ratio. A large L/D ratio corresponds to a small beam divergence.

If $L/D \rightarrow \infty$ will improve the resolution also as $d \rightarrow 0$ as the object moves closer to the detection plane resolution also improves where d is the distance between the sample and the detector [Anderson, 2009].

For a system with $L/D = 150$ with beam aperture 25 mm and magnification factor $M_{CCD} = 0.25$ resolution is $= 60 \mu\text{m}$ at the CCD imaging plate.

If, hypothetically we take for a radiography system: $L/D = 750$, corresponding to a beam aperture of $D = 5$ mm at a distance of 3.75 m from the object, the resolution of such system would be $14 \mu\text{m}$ at the sensor, moving from the macro-analysis scale to the microscopy scale. Reducing the beam aperture from 25 mm to 5 mm this will increase system resolution by a factor of 4. This indicates the strong effect of L/D factor has on

the resolution of a radiography system. L/D ratio can be increased by moving farther from the beam aperture or by reducing the size of the aperture, also if the object sample moves closer to the detection as plane $d \rightarrow 0$ (see figure 1.8.2), the resolution also improves [Anderson, 2009].

1.9 Neutron Tomography NT (3-D imaging)

If we rotate an object into 180 degrees, and taking neutron radiography images at all angular positions, a 3-Dimensional image of the object is taken. The technique is based on the Filtered Back Projection Algorithm.

The methodological computed tomography, the tomography reconstruction problem is to obtain a tomographic slice image from a set of projections. A projection is formed by drawing a set of parallel rays through the 2D object of interest, assigning the integral of the object's contrast along each ray to a single pixel in the projection. A single projection of a 2D object is one-dimensional. To enable computed tomography reconstruction of the object, several projections must be acquired, each of them corresponding to a different angle between the rays with respect to the object [radon_transform.html]. A collection of projections at several angles is called a sinogram, which is a linear transform of the original image according to: [Smith, 2003], [Kharfi, 2013], [Rehacek, 2002], [Treimer, 2009], [Anderson, 2009].

The inverse Radon transform is used in computed tomography to reconstruct a 2D image from the measured projections (the sinogram). A practical, exact implementation of the inverse Radon transform does not exist, but there are several good approximate algorithms available.

As the inverse Radon transform reconstructs the object from a set of projections, the (forward) Radon transform can be used to simulate a tomography experiment. The Radon transform simulate a tomography experiment and reconstructs the input image based on the resulting sinogram formed by the simulation. One method for performing the inverse Radon transform and reconstructing the original image is: The Filtered Back Projection (FBP).

An object $O(x, y, z)$ is considered as a superposition of n layers of the same thickness along z -axis, all located in planes parallel to the plane (x, y) and perpendicular to z (figure 1.9.1). The intensity of the transmitted beam is recorded like a translation function of the position parameter. The transmitted intensity is given by, Beer-Lambert's law given by the following expression [Kharfi, 2013], [Treimer, 2009]:

$$I(x, y) = I_o \exp\left(- \int_{path} \mu(x, y) ds\right) \quad (1.9.1a)$$

One can define a so-called projection $P_\theta(t)$:

$$P_\theta(t) = \ln\left(\frac{I_o}{I}\right) = \int_{path} \mu(x, y) \cdot ds \quad (1.9.2b)$$

The set of all projections $P_{\theta}(t)$ of $\mu(x, y)$ is called the Radon transform of $\mu(x, y)$. From these projections, a 2D image can be reconstructed using the “Fourier slice theorem”.

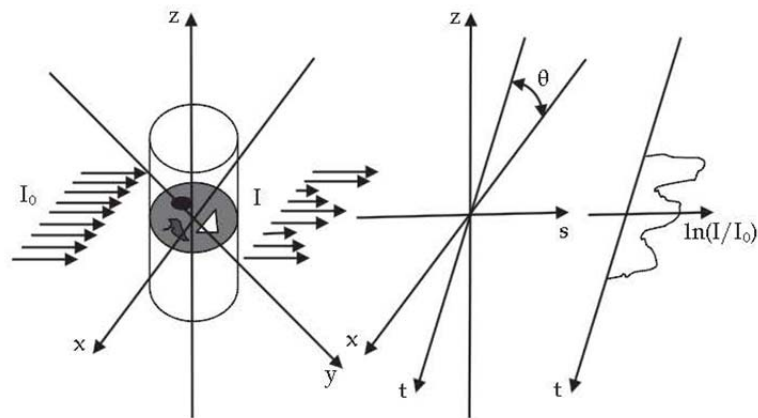


Figure 1.9.1 The geometry of a studied object scanning in the $\{x, y, z\}$ coordinates system. A layer in the plane (x, y) is scanned along the angle θ and the transmitted intensity is stored in a system (t, s) of rotational coordinates [Smith, 2003], [Treimer, 2009].

Chapter 2 Neutron detectors

Neutrons are fundamental particles, which have a mass m_n , but they are free of charge. Neutrons are not able to ionize the detector and therefore they cannot be directly detected. Neutron detectors are based on secondary processes in which secondary charged particles are produced. These particles then could be directly detected and show the presence of the neutron in the detectors. In this chapter, we give an overview of the neutron reactions with the ${}^6\text{Li}$ and ${}^{\text{nat}}\text{Gd}$ elements that are widely used for neutron detection. Detector characteristics like detector spatial resolution, efficiency, linearity, layer thickness, intrinsic noise/pixel, noise contributions, reproducibility, neutron sensitivity, low gamma sensitivity, background are analysed in detailed.

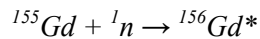
2.1 Neutron Detectors Types

Neutrons are electrically neutral particles. Because they interact only by the hadronic interaction with matter, neutron radiation is extremely penetrating into material thickness. For detection neutrons have to be converted into charged particles by nuclear reactions. For detection neutrons have to be converted into charged particles by nuclear reactions [Smith, 2002], [Sears, 1992]:

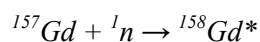
- i) Reactions that have cross sections that decreases as the square root of the neutron energy.



- ii) Reactions that are (n,γ) resonances in which γ -ray emission is inhibited and energy is transferred to the orbital electrons.



Main electron energies are 39 and 81 KeV



Main electron energies are 29, 71, 78 and 131 KeV

The created particles produce common signals in radiation detectors and this principle is used in the ${}^6\text{Li}$ scintillator screen in combination with a CCD camera and Imaging Plate Neutron Detector (IP-ND). These two are major detector systems used in neutron radiography (NR) and neutron tomography (NT) at ATI.

In a low-power reactor the signal-to-noise ratio becomes a major factor for neutron imaging [Zawisky, Dyrnjaja, 2008]. The distance between the radial tube of the NT station and the reactor core is only 3 m; therefore a 40 μm thick bismuth filter is placed at the collimator entrance for gamma reduction. The neutron beam has a 9 cm diameter and is well thermalized by a graphite wall of the thermal column of the TRIGA

reactor. The detector selection is determined by the beam intensity and the intended application. The following items have to be taken into account:

- High detection efficiency, low background noise, as well as high signal-to-noise ratio;
- Good linearity and reproducibility for tomographic investigations;
- High dynamic range to achieve sufficient image gradation and sensitivity;
- High spatial resolution;
- The detectors should be commercially available at reasonable cost.

It is clear that one detector alone cannot fulfill all these requirements. Previous studies by the ISNR (International Society for Neutron Radiology) community [Lehmann, Vontobel, 2004], [Schillinger, 2006], [Pleinert, 1997] have shown that scintillation detectors coupled with a slow-scan CCD system represent the best choice for tomography due to superior linearity, reproducibility, and weak gamma sensitivity. Integrating image intensifiers are preferably utilized for fast and periodic processes, which are, however, not typical applications for a low intensity beamline.

Our first 400 μm scintillator plate did not provide sufficient spatial resolution; therefore, we installed a 100 mm thin plate scintillator, which is now commercially available at a reasonable price [Zawisky, Dyrnjaja, 2008]. Our second detector, the ND&M camera is also commercially available. It is a scintillation detector coupled to a micro-channel plate with 50 μm resolution, high efficiency and extremely low intrinsic noise. The ND&M camera was originally used for beam alignment and tomography with monochromatic neutron beams at ILL in Grenoble [Dubus, 2005]. Its application in neutron imaging is restricted to weak beams with small cross-section and small objects

The third detector is intended to replace our Gd converter films. We have chosen neutron imaging plates Imaging plate Neutron Detector with a nominal scanning resolution of 25 μm . With this ensemble of digitized detectors we have recently started a routine operation with the upgraded instrument [Zawisky, Dyrnjaja, 2008].

2.2 Characterization of the Detectors

All three detectors are suitable for high resolution imaging beyond the resolution of 340 μm with the old scintillator [Koerner, 2001], [Williams, 2012]. The spatial resolution is primarily limited by the collimation ratio $L/D = 130$, i.e., the ratio of the collimator length $L = 2600 \text{ mm}$ and the aperture $D = 20 \text{ mm}$. To achieve better resolution it is necessary to minimize the sample-to-detector distance L_{S-D} and thereby the geometric unsharpness U_g :

$$U_g = L_{S-D} \left(\frac{D}{L} \right) \quad (2.2.1)$$

The second, blurring effect is the intrinsic unsharpness in the sensitive layer. A thin layer narrows the spread of secondary radiation in the converter, thereby reducing the detector blurring at the cost of detection efficiency. To compare the spatial resolutions a sharp edge fabricated of a 25 μm thick gadolinium foil with 5.1% neutron transmission was placed directly on the scintillator or the imaging plate. The measured edge spread function (ESF) and its derivative, the line spread function (LSF), can be approximated by a Lorentzian model if image blurring predominantly emerges in the converter [Harms, 1972].

The ESF parameters p_1 - p_3 and λ are fitted to the measured edge profile with the resolution parameter λ as a result:

$$\text{Edge spread function: } ESF(x) = p_1 + p_2 \cdot \arctan(x(\lambda(x - p_3))) \quad (2.2.1a)$$

$$\text{Line spread function: } LSF(x) = \frac{d}{dx} ESF(x) \quad (2.2.1b)$$

$$\text{Resolution: } FWHM(x) = \frac{2}{\lambda} \quad (2.2.1c)$$

In the following sections we compare the full-width at half-maximum FWHM resolutions, the absorption probabilities in the neutron sensitive layers, and the inhomogeneities in the beam profiles.

Table 2.1 gives an overview of some key detector characteristics for NR/NT applications.

The neutron-to-gamma ratio was determined by comparing the intensities with open and closed boron beam shutter. The intrinsic noise was measured several hours after reactor shutdown with beam and camera shutters closed.

detector	sensitive area (cm^2)	layer thickness (μm)	spatial resolution (μm)	n/ γ ratio	intrinsic noise/pixel
^6Li thin-plate	10 x 15	100	150	500	300+(0.4/s)
^6Li – ND&M	5	400	50	40	$3 \times 10^{-7}/\text{s}$
Gd IP - ND	20 x 25	135	40	50	$4 \times 10^{-5}/\text{s}$

Table 2.1 An overview of some key detector characteristics of Neutron Radiography NR and Neutron Tomography applications NT [Zawisky, Dyrnjaja, 2008].

2.3 Neutron Detection with ^6Li -Scintillator

NR detectors are generally plane integrating position-sensitive imaging devices containing material with a high neutron cross-section functioning as neutron converter and a recorder, which has the task of collecting the signal emitted by the converter during exposure. After the measurement the detector signal is read out and maybe digitized. In the context of the neutron radiographic measurement the output of the

detector will be called the detector signal or radiography image, whereas the terms signal and image are considered equivalent.

Typical NR-detectors are:

- X-ray film/converter plate assemblies
- track-etch films
- imaging plates
- scintillator/camera
- amorphous silicon (a-Si) or flat panel detectors

CCD-camera/scintillator systems of a NR detector consists of a neutron sensitive scintillator screen which has the task of converting the neutrons in photons, and a camera, which is the recording device for the light emitted by the scintillator. The camera produces a digitized image as illustrated in figure 2.3.1. Typical scintillator materials are $\text{ZnS}(\text{Ag})\text{-}^6\text{LiF}$ or $\text{ZnS}(\text{Cu})\text{-}^6\text{LiF}$.

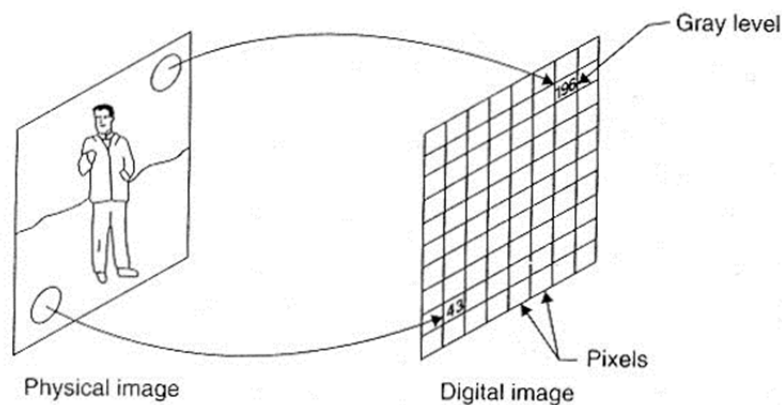


Figure 2.3.1 Illustration of image digitization¹.

Cooling can enhance the performance of a CCD-camera, which can be done with liquid nitrogen (approximately between -120°C and -130°C). The cooling reduces the dark current and therefore enhances the signal to noise ratio. Especially for applications requiring longer exposure times (several minutes), the optimal temperature of the CCD-chip is in the range -130°C , which can be achieved only with liquid nitrogen cooling. To avoid radiation damage of the semiconductor material of the CCD-chip the camera has to be placed outside of the direct neutron beam. Therefore the light emitted by the scintillator is reflected to

¹<http://www.ati.ac.at/~neutropt/experiments/Radiography/radiography.html>

the camera by one or several mirrors. CCD cameras with Peltier cooling are widely used in radiography techniques as well.

Advantages of these detectors are: An excellent linearity, high sensitivity, easy handling (readout of information and digitization do not cause additional working steps), good reproducibility (for the use of a cooled CCD-camera) and the possibility of real-time measurements (for the use of an adequate camera with high repetition rate and sensitivity). Disadvantages are the high costs of the detector system and the lower spatial resolution compared to film and image plate detectors. The spatial resolution of the CCD-camera depends on the chosen chip size to image size ratio and scintillator thickness. Components of the detector of the ATI at the Station II:

- Nitrogen cooled slow scan CCD-camera

Chip: SITE SI502A/T 512 x 512 pixels, 24 x 24 μm^2 pixel size,
Quantum efficiency QE: up to 90 %.

- 16 bit digitalization \leftrightarrow 65535 gray-level

Lenses: Nikon NOKT 58 mm F 1,2

Nikon NOKT 180 mm F 2,8

- Scintillator

Levy Hill: $\text{ZnS}(\text{Ag})\text{-}^6\text{LiF}$

- Mirror: 2 mm thick glass plate coated with Al and TiO_2

- Al-Box, light tight

Area of the object projected on one pixel:

58 mm Lens F 1,2 : 410 x 410 μm^2

180 mm Lens F 2,8 : 80 x 80 μm^2

Image size:

58 mm F 1,2 : 21 x 21 cm^2

180 mm F 2,8 : 4 x 4 cm^2

Actually the NR-station II possesses a 100 μm thin-plate scintillator and an old scintillator plate with 400 μm thick layers. The old 400 μm scintillator did not provide sufficient spatial resolution; therefore we installed a 100 μm thin plate scintillator which is available at relatively low price. To compare these scintillators, the layers (400 μm and 100 μm thick) were exposed at a low neutron beam flux of $1.3 \times 10^5 \text{ n/cm}^2\text{s}$ and the transmission through these layers was measured. From the acquired transmission T the effective detector efficiency ϵ_{ff} (absorption probability) was estimated by: $\epsilon_{ff} \approx 1 - T$.

The overall detection efficiency depends on the ${}^6\text{Li}$ -density, scintillator thickness, composition of the activators (ZnS, Ag) [Litvin, 2009], self-absorption of the generated photons in the scintillator, optical lens, and, finally, the photon detection efficiency in the CCD-camera [Eijk, 2003], [Barmakov, 2002]. Experimentally, we have compared the neutron transmissions through the old 400 μm scintillator plate, $T = 68.7\%$ (absorption probability $\epsilon_{\text{ff}} = 31\%$), and the new 100 μm scintillator, $T = 86.8\%$ (absorption probability $\epsilon_{\text{ff}} = 13\%$) (see figure 2.3.2). Thus, the detection efficiency of the 100 μm scintillator is lower by at least a factor of two, and the exposure time increases by that factor to achieve similar image gradation. The weight percent of the ${}^6\text{LiF}$ of our scintillators is 30% of total weight and the ${}^6\text{Li}$ isotope content of the LiF is more than 90%.

From transmission data, we could calculate the ${}^6\text{Li}$ density for both thicknesses knowing the total absorption cross section of the ${}^6\text{Li}$ isotope for the thermal neutron region:

$\rho_{\text{Li-100}\mu\text{m}} = 0.150 \text{ g/cm}^3$ and $\rho_{\text{Li-400}\mu\text{m}} = 0.102 \text{ g/cm}^3$, where the total absorption cross section of the ${}^6\text{Li}$ isotope for thermal neutrons is given by:

$$\sigma_{\text{Li-6}} = 940 \frac{\lambda}{1.8} \text{ barns} \quad (2.3a)$$

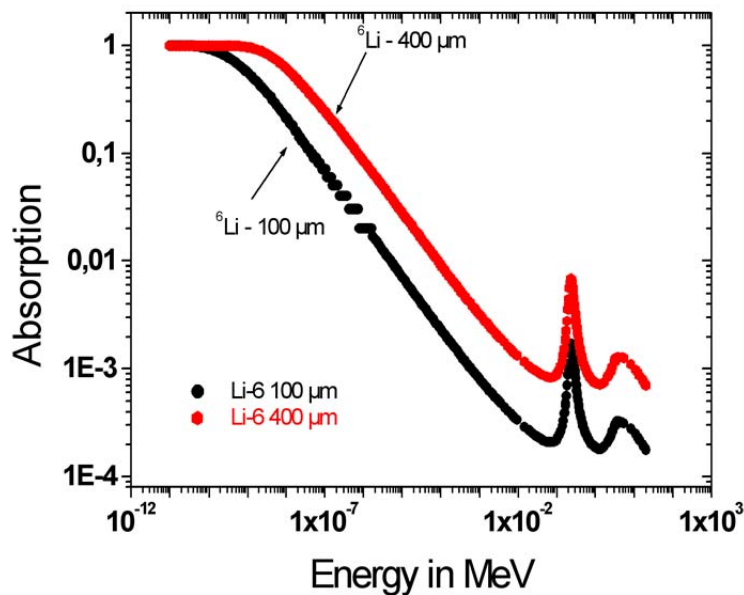


Figure 2.3.2 The absorption of the ${}^6\text{Li}$ isotope for two different thicknesses. The energy data are extracted from ENDF-VI library using MCNPX 2.4.0 version software [Zawisky, Dyrnjaja, 2008].

The spatial resolution predicted by the manufacturer is 170 μm for the 100 μm scintillator and 340 μm for the 400 μm scintillator. We obtained the best resolution of 150 μm for the new scintillator layer (100 μm), quite well in agreement with the manufacturer's data.

The sensitive area of the 100 μm layer is 10 x 15 cm^2 , coated on a 1.5 μm thick plate of pure aluminum. From the data sheet provided by the company the relative light output is peaked at 100 μm . An alternatively available 50 μm scintillator would be inefficient for weak beam intensities. The spatial resolution predicted by the manufacturer is 170 μm for the 100 μm scintillator and 340 μm for the 400 μm scintillator. With our standard lens, $f = 105 \mu\text{m}$ (Nikon f/1.8, Nikon), we are limited by the optical resolution of $200 \times 200 \mu\text{m}^2$ (CCD pixel size $24 \times 24 \mu\text{m}^2$). Therefore, we have repeated the ESF measurement with larger focal length ($f = 180 \text{ mm}$, f/2.8) and $80 \times 80 \mu\text{m}^2$ optical resolution (see figure 2.3.3). We obtained as best resolution 150 μm for the 100 μm plate, well in agreement with the manufacturer's specification.

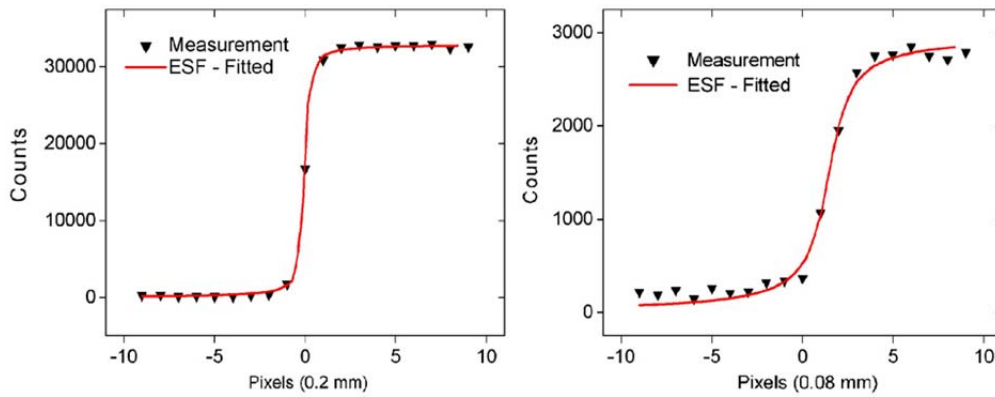


Figure 2.3.3 Edge Spread Function ESF measurements with different lenses. The pixel size denotes the optical resolution of the lenses; **Left:** $f = 10 \text{ mm}$, **Right:** $f = 180 \text{ mm}$. The fit yields $\lambda = 1.1(1)$ and $145 \pm 13 \mu\text{m}$ resolution in the right plot.

Figure 2.3.4 reveals different open beam inhomogeneities in the two ${}^6\text{Li}$ layers. As a measure for such intensity variations, the standard deviation σ of the illuminated pixels are computed for the whole beam, and intensity profiles are plotted for the central region within the line markers. Given a uniform beam profile and ${}^6\text{Li}$ distribution, σ approaches the square root of the average pixel intensity ($\sigma \approx \sqrt{N_{\text{average}}}$). In reality, this ideal limit is not reached, and therefore the resulting inhomogeneities have to be eliminated by pixel-wise open beam correction [Zawisky, Dyrnjaja, 2008]:

The scintillator-CCD unit has several noise contributions: gammas absorbed in the scintillator, white spots caused by bad (“hot”) pixels whose position remains unchanged, dark current and readout noise. Surprisingly, we see very little difference in the dark images with the reactor on/off; only a few multipixel events occur due to gamma or neutron tracks. This shows that direct interactions of gammas and neutrons hitting the CCD chip are negligible at the detector site. Cooling the CCD chip down to -130°C with liquid nitrogen minimizes the dark current; it increases linearly with time if a constant readout offset is added

(figure 2.3.5, left). In transmission experiments the transmission T is calculated by applying 2.3b formula given below:

$$\text{Transmission } T = \frac{N_{\text{sample}} - N_{\text{background}}}{N_{\text{open}} - N_{\text{background}}} \quad (2.3b)$$

The readout noise depends on the readout speed of the CCD chip, where the best signal-to-noise ratio is obtained at the lowest speed. The gamma sensitivity is derived by, comparing beam intensities with open and closed boron beam shutter, which is transparent to gamma rays (figure 2.3.5, right).

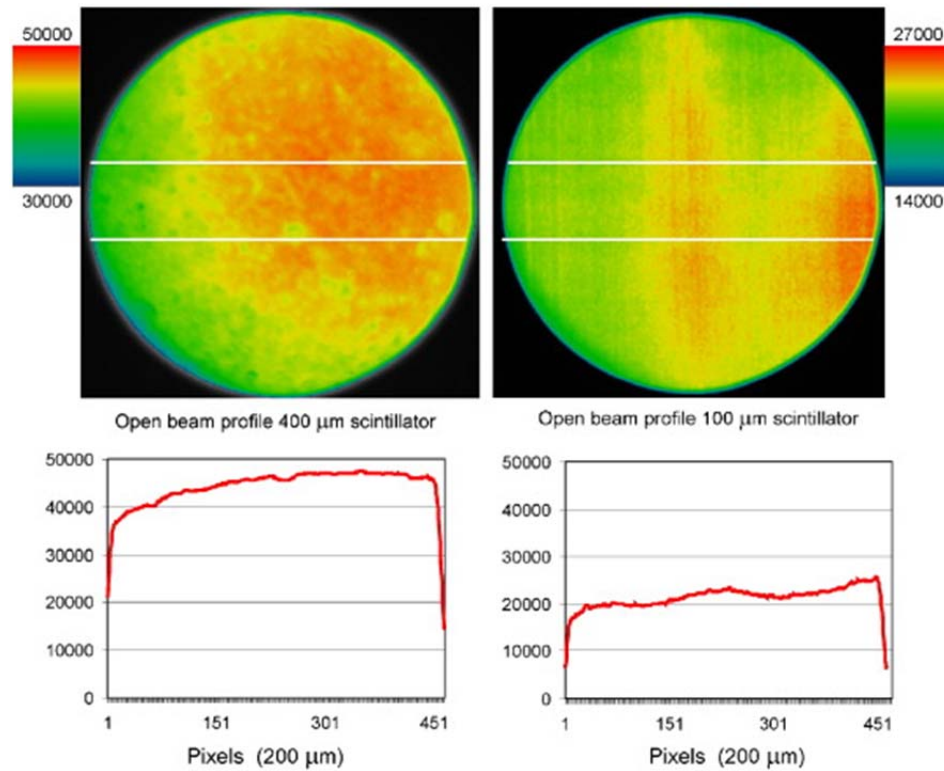


Figure 2.3.4 Inhomogeneities in the open beam profile. **Left:** 400 μm scintillator, overall intensity variance, $\sigma = 13 \times \sqrt{N_{\text{average}}}$ maximum intensity difference in the area between the two marked lines $(N_{\text{max}} - N_{\text{min}}) / N_{\text{average}} = 17\%$. **Right:** 100 μm scintillator, $\sigma = 11 \times \sqrt{N_{\text{average}}}$, maximum intensity difference 22% [Zawisky, Dyrnjaja, 2008].

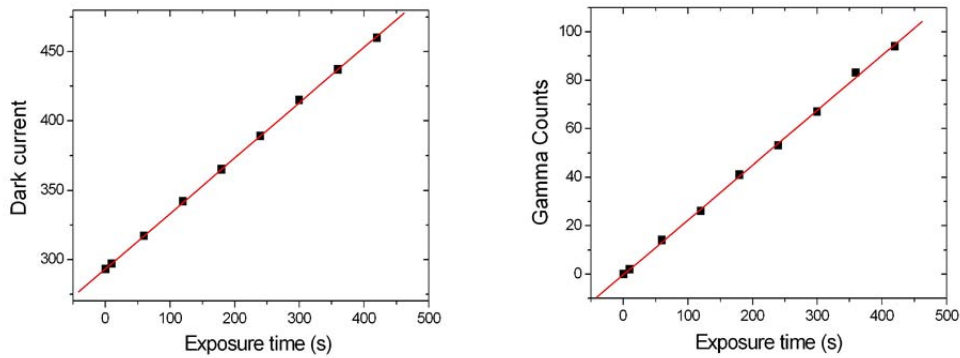


Figure 2.3.5 Comparison of the dark noise. **Left:** camera-shutter close and gamma noise. **Right:** beam shutter closed. The dominating dark noise increases with: $N_{Dark} = 293 + 0.4 \times \text{time (s)}$ and the gamma background with $N_{Gamma} = 0.23 \times \text{time (s)}$ [Zawisky, Dyrnjaja, 2008].

2.4 Imaging Plate Neutron Detector (IP-ND)

Imaging Plates IP are intensively used as neutrons detector, and described as “ii” type of reaction group given above (see section 2.1, chapter 2), where neutron converters like natural Gd_2O_3 are mixed with photo stimulated luminescence materials (BaFBr:Eu).

The images created by irradiation of the IP are usually read out by measuring the Eu luminescence at a wavelength of 633 nm from 390 nm He-Ne laser scanner.

In the first step of the neutron detection process, neutrons irradiate the gadolinium converter particles that are uniformly dispersed in the (BaFBr:Eu) layer. The gadolinium converter particles emit secondary radiation that excites the (BaFBr:Eu) to a metastable state, where electrons are trapped. In the second step, red light from a He-Ne laser (633 nm) is irradiated on the surface of the photo stimuable phosphor layer of the BAS-ND imaging plate and trapped electrons are further excited. These electrons cause luminescence of blue light. The blue light is detected in a photomultiplier tube (PMT) within a BAS-5000 scanner to produce the two-dimensional digitized images on a computer display. Since 2007 the Atominstitut possess an IP-ND with 25 μm scanning resolution with 135 μm $^{nat}Gd_2O_3$ thick layer. Figure 2.4.1 shows the neutron imaging plate used during the irradiations with thermal neutrons. Figure 2.4.2 shows the BAS-5000 scanner and the eraser set-up at NR station II. The detection principles are presented in figure 2.4.3.

A key advantage of image plates is their mechanical flexibility, among other advantages, such as:

- no accumulation of intrinsic dark signals during the exposure
- no limitation in the count or dose rate
- a high dynamic range

- high efficiency
- high resolution
- no limitation of the detection area



Figure 2.4.1 The 25 x 20 cm² imaging plate inserting in the BAS-5000 scanner.



Figure 2.4.2 The BAS-5000 scanner and the eraser device at NR-II station at Atominstytut.

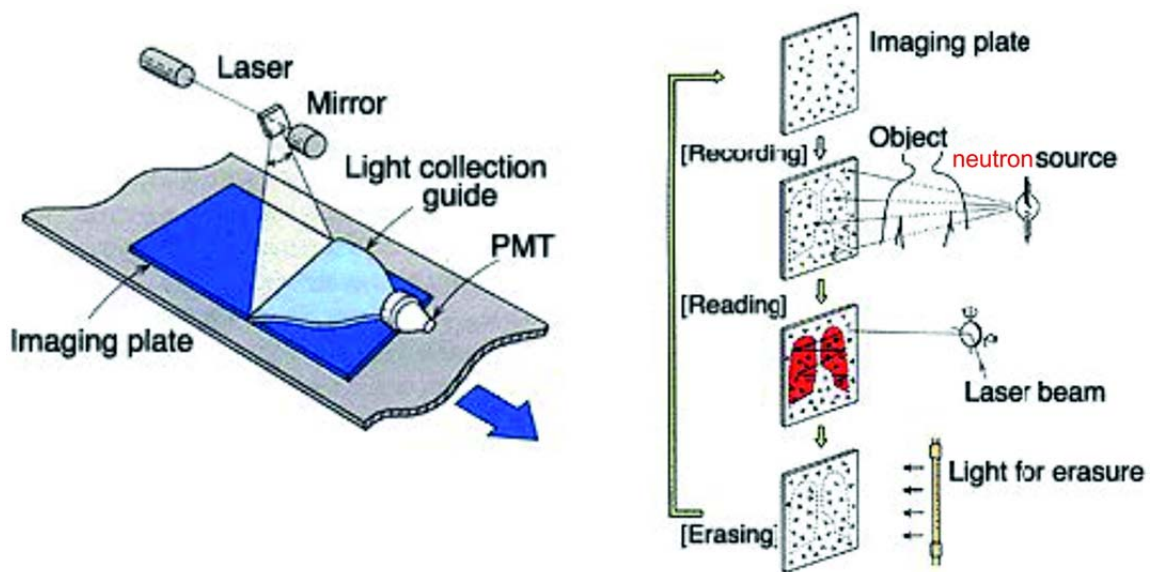


Figure 2.4.3 *Left: Principle of reading the radiation image from the imaging plate. Right: Process of recording, reading, erasing and reusing the radiation image by the Imaging Plate method [Fuji, 2010].*

2.5 Transmission Experiments with IP-ND

The neutron absorption of the IP is controlled by the absorption coefficient of the neutron converter, which in this case is $^{natural}\text{Gd}_2\text{O}_3$ with the natural abundance of the isotopes ^{155}Gd (14.8%) and ^{157}Gd (15.7%). The IP detector is sensitive to γ -ray. The absorption cross-section of Gd (n, γ), (61.100 barns in thermal region, $\lambda=1.8 \text{ \AA}$) and a phosphor layer thickness of $135 \mu\text{m}$ is sufficient to absorb 80% of the neutrons. The measured transmission value for a $135 \mu\text{m}$ Gadolinium photostimulable layer (density of 0.124 g/cm^3) plus $370 \mu\text{m}$ polymer support is: $T_{\text{Gd-135}\mu\text{m}} = 0.19\%$, which indicates a high detection efficiency of (absorption probability) $\approx 80\%$ (figure 2.5.1).

Another advantage of the Image Plate-Neutron Detector IP-ND is the wide range linearity. Figure 2.5.2 shows the relation between the photostimulated photons (PSL) linearity and neutron capture efficiency.

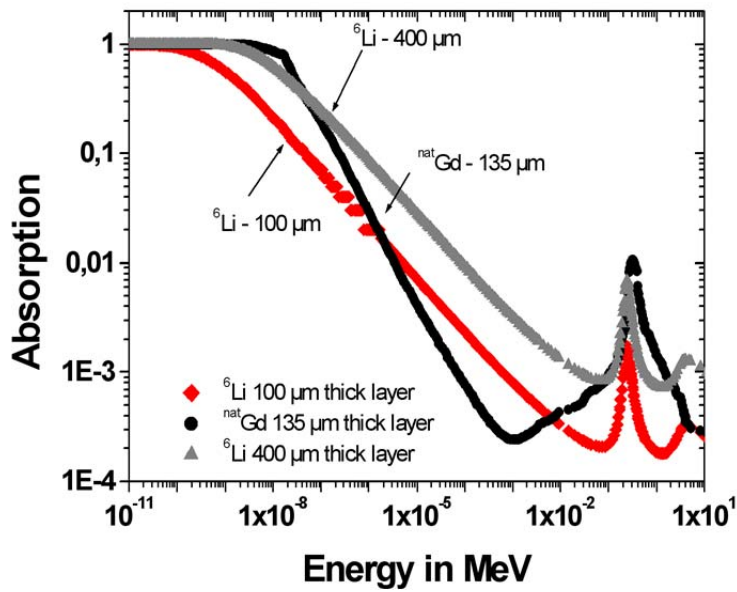


Figure 2.5.1 The energy dependence of the ${}^6\text{Li}$ and Gd detector layers for different mixture and thicknesses. The energy data are extracted from ENDF library using MCNPX 2.4.0 version software. Selecting a typical reactor spectrum from ENDF library, the MCNPX simulation yields an absorption probability of 80% of the Gd-layer, and 13% of the ${}^6\text{Li}$ -layer. These values have been confirmed in our transmission experiments [Zawisky, Dyrnjaja, 2008].

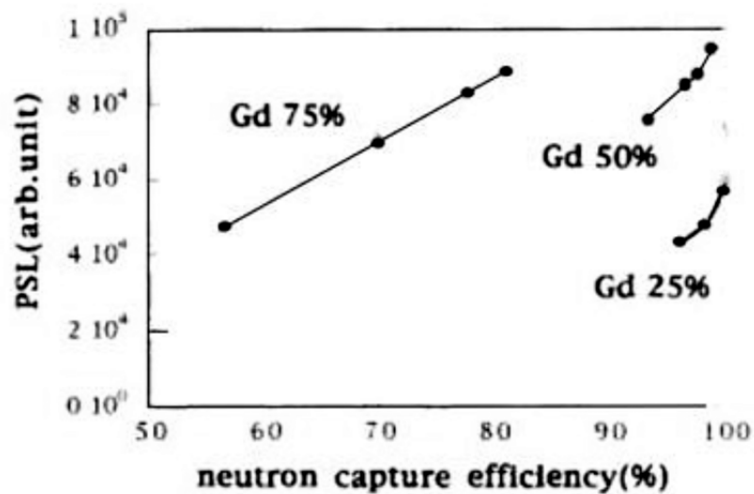


Figure 2.5.2 Linearity between PSL intensity and neutron capture efficiency [Karasawa, 1998].

2.6 Neutron Irradiation Experiments with IP-ND; Linearity and Reproducibility

A disadvantage of the IP-ND is high gamma sensitivity due to the heavy elements on the plate [Massalovich, 2002]. The neutron-gamma ratio was determined by comparing the intensities of the images of open beam with closed shutter. A neutron-to-gamma ratio of 50 was derived. The IP-ND linearity was confirmed between 1 and 60 min exposure time (figure 2.6.1). For IP-ND the dynamic range of neutron detection depends on the storage capacity of the storage phosphor and the intrinsic background of the detector, which is negligible in the case of optimized IP detectors compared to the natural background radiation.

After erasing the IP-ND image, the intrinsic noise is only 0.3 counts per $25 \times 25 \mu\text{m}^2$. The intrinsic noise increases from 0.3 to 11 per pixel after three days deposition in light-tight box outside the reactor building.

Another disadvantage of this kind of detectors is the bad reproducibility. The neutron irradiation experiments have been carried out Neutron Radiography Station NR II at the 250 kW TRIGA reactor at ATI, where a thermalized neutron beam is available. The IP-ND was placed 30 cm from neutron source beam collimator, which has a diameter of 9 cm. To estimate the statistical fluctuation of PSL counts and the stability the IP-ND is exposed to open beam for 10 min, then 10 min waiting after exposure (cooling time) followed by 10 min scanning time ($25 \mu\text{m}$ pixel size). The manufacturer recommended this procedure.

For the first set of IP-ND measurements, the reproducibility of open beam intensities, repeated under identical experimental conditions and read-out parameters, was not as what we expected. The PSL counts at 10 min exposure at 10 min exposure time varied between 7000 and 11000, far beyond the 3 % of statistical fluctuations [Zawisky, Dyrnjaja, 2008]. According to our supplier recommendations we decided to wait something like 10 min after exposure time before scanning in order to stabilize the latent image. We decided to wait 10 min before we scan all images and the reproducibility is improved according to the figure given above. We have chosen a 10 min waiting interval for all subsequent IP-ND scans and the reproducibility has improved like is shown in figure 2.6.2).

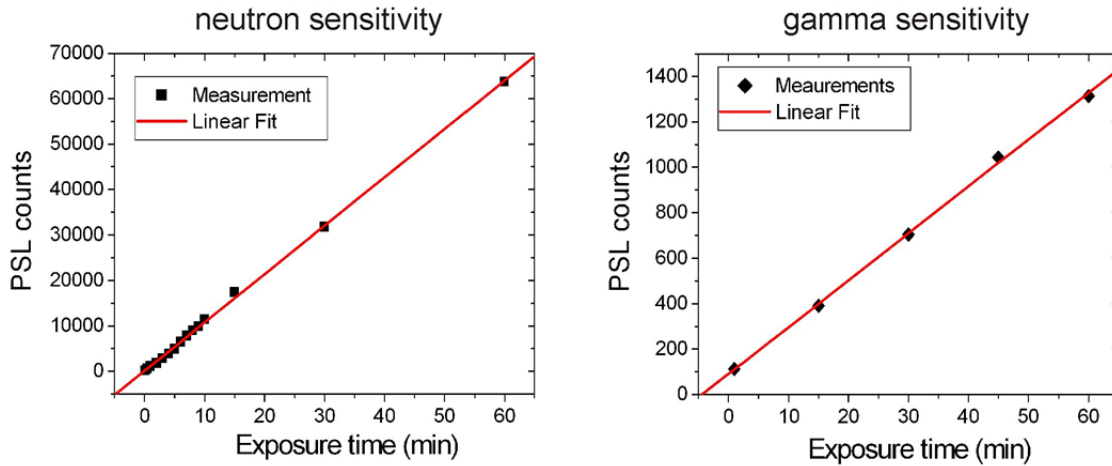


Figure 2.6.1 Linearity of the NIP counts numbers at 25 μm pixel resolution. **Left:** IP-ND in the open neutron beam, $\text{PSL}/\text{pixel} = 169 + 1064 \times \text{time (min)}$. **Right:** IP-ND with beam. Shutter closed, $\text{PSL}/\text{pixel} = 91 + 21 \times \text{time (min)}$ [Zawisky, Dyrnjaja, 2008].

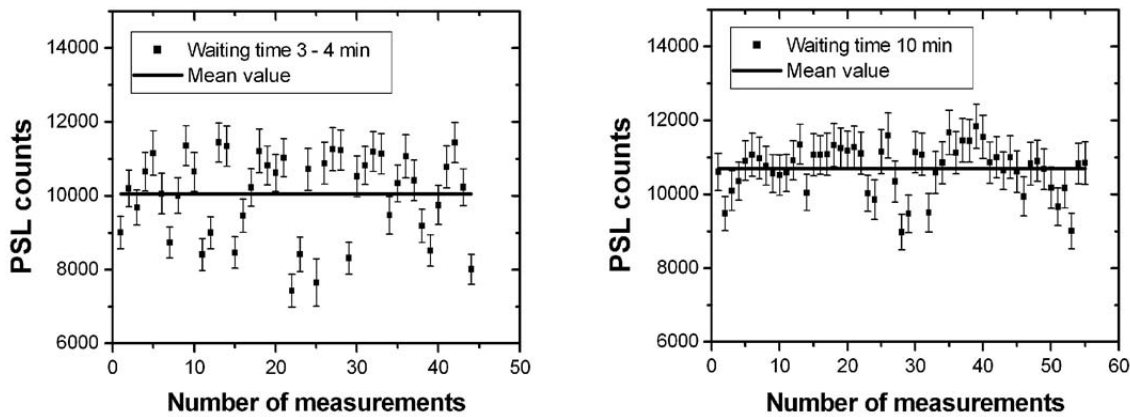


Figure 2.6.2 The reproducibility of the IP-ND intensities by repeating always the identical measurements procedure: 10 min exposure time \rightarrow waiting time \rightarrow scanning \rightarrow 30 min erasing time. **Left:** 3-4 min waiting interval, $\text{Mean} = 10050 \pm 1150$. **Right:** 10 minutes waiting interval, $\text{Mean} = 10700 \pm 650$ [Zawisky, Dyrnjaja, 2008].

As scanning parameters with the best signal-to-noise ratio at 25 μm resolution we choose the highest gradation (16 bit) and sensitivity S4000 at level L5. The scanned images are stored as Fuji-image file format and then further processed with Image-Pro Plus 6 (MediaCybernetics); the logarithm of the detected PSL signals is converted to unsigned 16 bit data yielding a full image size of 160 Mb. After erasing the IP the intrinsic noise is only 0.3 counts per 25 x 25 μm^2 . The intrinsic noise increases from 0.3 to 11 per pixel after three days depositing in a light-tight box outside the reactor building. The open beam image confirms, except for a few scratches in the layer a uniform Gd distribution (figure 2.6.3). Unfortunately a microscopic pattern

of dark spots 150-200 μm in size appears in the image, yielding 25% reduced PSL intensity. A similar pattern was found when scanning the NIP with 50 and 100 mm resolution, and also on the X-ray sensitive SR imaging plate. Such microstructural artifacts enhance the intensity variance in detector pixels and impede the investigation of inhomogeneities in materials [Zawisky, Dyrnjaja, 2008]. In figure 2.6.3 we also recognize disturbing horizontal line structures from the scanning process, which can be removed by a low-pass filter.

The Gd-edge directly attached onto the IP-ND yields 60 μm resolution horizontally and 40 μm vertically see figure 2.6.4.

Table 2 gives an overview of detector performances for Neutron Radiography (NR) applications [Lima, 2007], [Hameed, 2008].

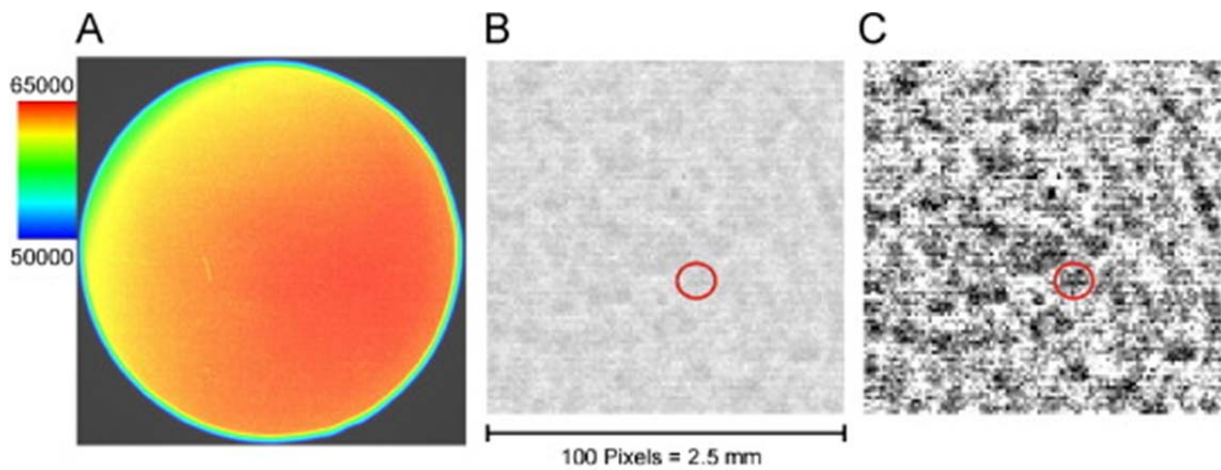


Figure 2.6.3 Open beam intensity variations and NIP artefacts. (A) Intensity variance in the open beam $\sigma = 12 \times \sqrt{N_{\text{average}}}$, maximum intensity variation 17%. (B) Random pattern of dark spots (150-200 μm) with reduced PSL intensity (unprocessed). (C) Same artefacts contrast enhanced [Zawisky, Dyrnjaja, 2008].

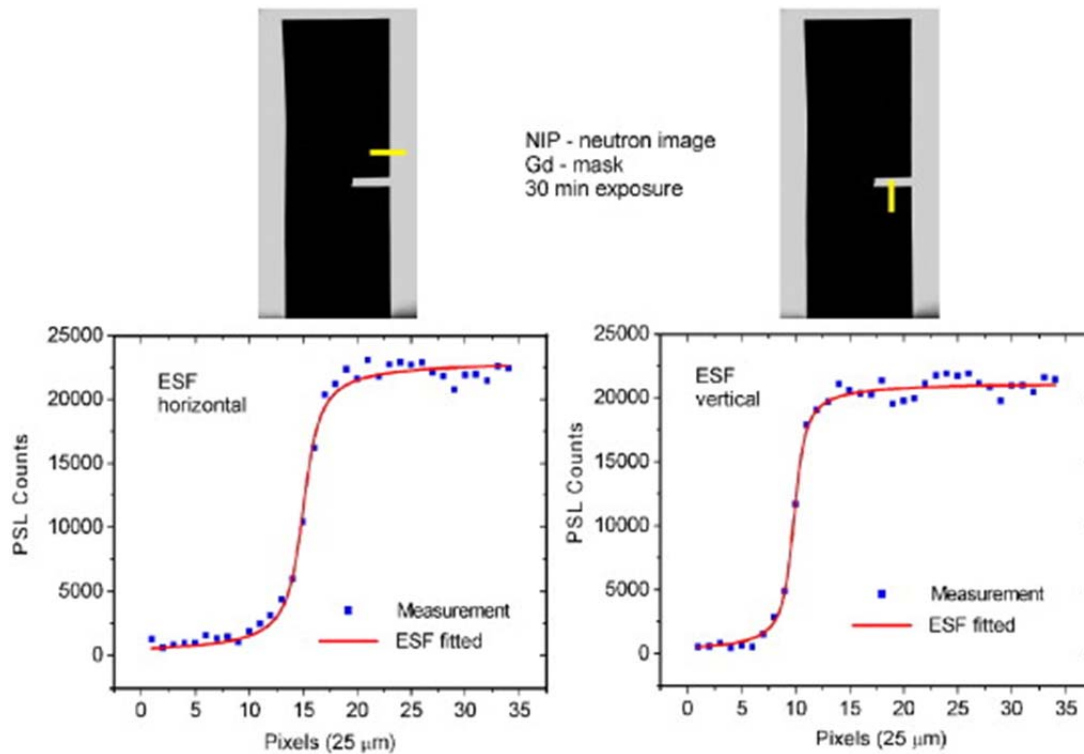


Figure 2.6.4 ESF-resolutions with the NIP; the ticks in the neutron images mark the positions of the edge profiles. The fits yield $\lambda = 0.8(2) \Rightarrow 60 \pm 15 \mu\text{m}$ horizontal and vertical resolution $\lambda = 1.25(20) \Rightarrow 40 \pm 7 \mu\text{m}$ [Zawisky, Dyrnjaja, 2008].

	Thin plate scintillators	IP- ND detector
Advantages	<p>Reproducibility</p> <p>Low gamma sensitivity</p>	<p>High efficiency;</p> <p>High resolution;</p> <p>Homogeneous profile;</p>
Disadvantages	<p>Lower efficiency;</p> <p>Medium resolution;</p> <p>Inhomogeneous beam profile;</p>	<p>Poor position reproducibility;</p> <p>Micro- artefacts;</p> <p>Higher sensitivity to gammas and scattered radiations;</p>

Table 2 Detectors performances and applications fields at NR II station near ATI in Vienna.

2.7 ND&M Neutron Camera

The ND&M is a compact neutron detector, which consists of a hand monitor and a readout unit. Gadolinium converter film detectors, despite their superior spatial resolution of up to $20 \mu\text{m}$, have been widely replaced by digitized scintillator and imaging plate detectors [Feigl, 1968], [Bruckner, 1968]. The

hand monitor contains the $^6\text{LiF-ZnS(Ag)}$ scintillator coupled to a micro-channel plate image amplifier with 25 μm opening, the output of which is projected to a phosphor screen (see figure 2.7.1). The hand monitor can be used as a stand-alone device for beam alignment. For quantitative imaging it is attached to a readout unit, which consists of a mirror, a high speed lens, and a low noise CCD camera with 512 x 512 pixels and 11 x 11 μm^2 resolution. The readout unit is connected to the ND&M real time centroiding processor in the host PC. Special features of this detector are single neutron counting and a high optical resolution of 50 μm , realized by an electronic centroiding procedure of the light spots on the screen. Single neutron counting is accomplished by the high readout rate of the CCD frames, thereby avoiding an overlap of the light spots on the single digitized image; frames with overlapping spots are discarded. Each digitized video frame runs through a two-dimensional convolver where the frames are correlated with idealized mode

A demonstration of the efficient electronic noise suppression and the homogenous intensity profile in the central beam area is shown in figure 2.7.2. From ESF data we fitted 50 μm horizontal and 80 μm vertical resolutions (see figure 2.7.3). The neutron-to-gamma sensitivity is 40. A severe limitation for neutron imaging is the maximum acceptable count rate of approx. 3000 n/s in the whole detector field to avoid overlapping light spots on the phosphor screen. This limit counteracts the high efficiency of approximately 40%, because the beam has to be attenuated by a factor of 100 to be applicable at this beam line. But due to its effective noise suppression and high efficiency the ND&M camera is suitable for NR/NT applications with weak beams of 10^3 - 10^4 n/s.

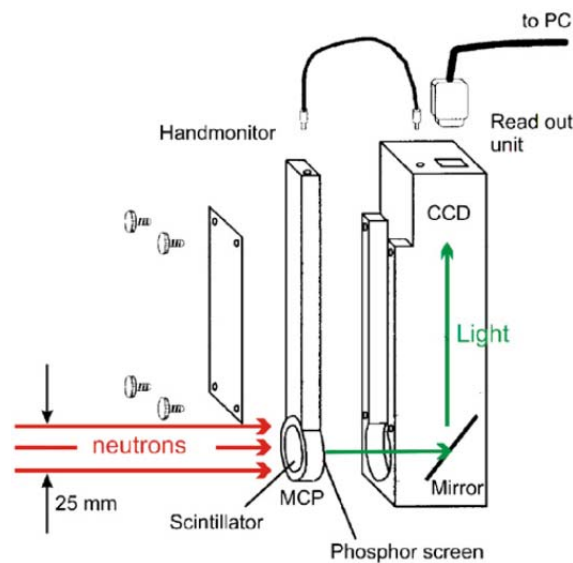


Figure 2.7.1 Outline of the ND&M micro-channel scintillation detector [Zawisky, Dyrnjaja, 2008].

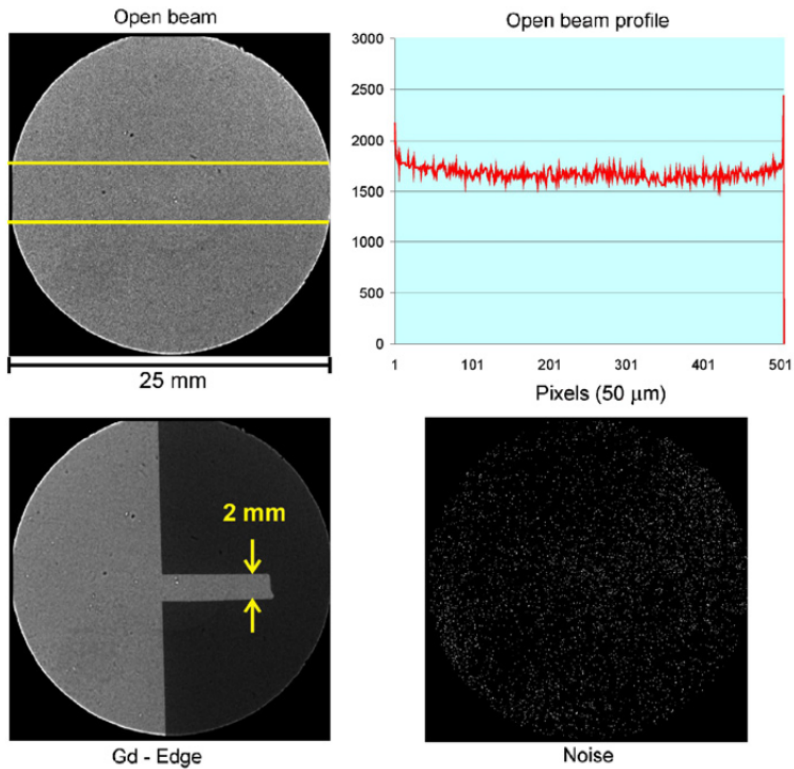


Figure 2.7.2 The ND&M open beam analysis yields a rather homogeneous profile with intensity variance: $\sigma = 1.2x\sqrt{N_{average}}$. The measured intrinsic noise was 8200 counts in 28 hours on the whole sensitive area after reactor shut-down [Zawisky, Dyrnjaja, 2008].

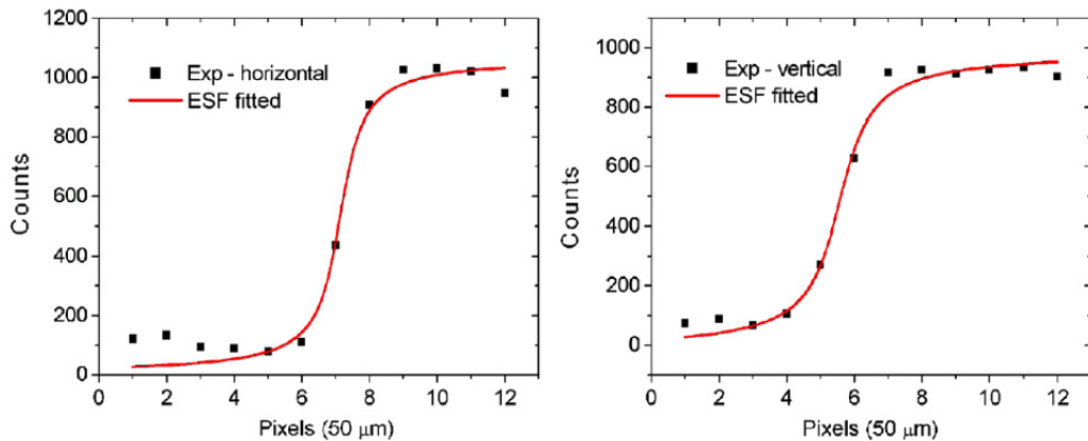


Figure 2.7.3 ESF resolution with the ND&M camera. The fits yield FWHM resolutions of 50 ± 15 mm horizontally and 80 ± 15 mm vertically [Zawisky, Dyrnjaja, 2008].

Finally, we have compared the Gd-edge resolution with a recently developed gadolinium test mask consisting of a Siemens star, with spoke periods from 500 to 40 μm , and a square grid with line widths of 150, 100, and 50 μm [Grünzweig, 2007]. The 50 μm grid lines are easily resolved in figure 2.7.4 A, whereas

the resolution of periodic spoke structures lies between the two innermost concentric radial markers of 100 and 50 μm . Here again the intrinsic granularity affects the detection of line pairs and periodic structures (figures. 2.7.4 B, C).

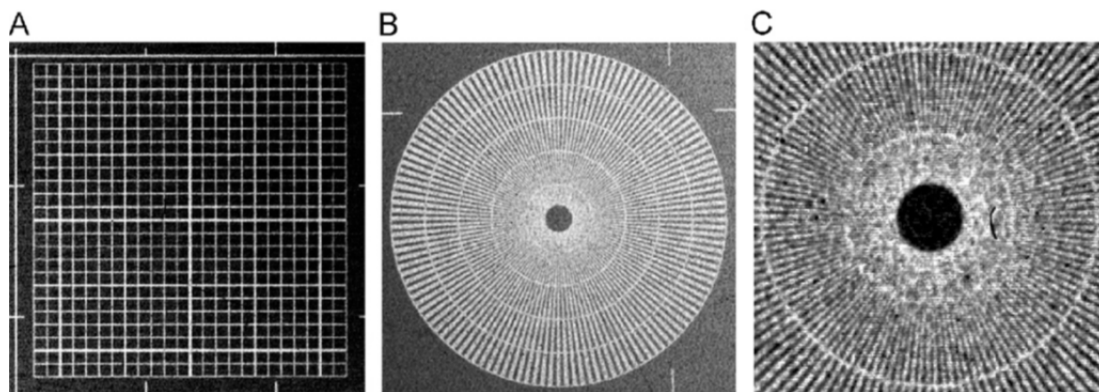


Figure 2.7.4 *Imaging of the PSI Gd test mask with the NIP. (A) The fine grid lines with 50 μm line width are clearly visible in the square. (B) Siemens star with radial markers at 500, 400, 300, 200, 100, and 50 μm line pair resolution. (C) The visibility of the periodic spokes becomes blurred between 100 and 50 μm resolution [Zawisky, Dyrnjaja, 2008].*

2.8 Summary

Each of our detectors has specific advantages and preferential applications fields. The 100 μm scintillator is more preferably to be used for tomography and radiography for different materials due to low gamma sensitivity, stable position and good reproducibility. The imaging plate neutron detector offers a very high resolution, detection efficiency and image gradation among other detectors.

Specific features and applications fields of our digitized detectors are summarized in the table below. The 100 μm scintillator offers high positions and intensity reproducibility which allows either sequential imaging in dynamic neutron radiography and tomography or to increase statistically accuracy and sensitivity by repeated measurements. The spatial resolutions cannot compete with imaging plates but in many cases, e.g. thick and scattering samples, this disadvantage is of no practical consequence. Imaging plates offers best resolution and higher efficiency but our set-up does not allow repetitive imaging. Granular artefacts in the plates are very disturbing in the inspection of material in-homogeneities.

We have shown that high spatial resolution down to the 50 μm regime is practicable with weak intensities of approximately $10^5 \text{ n/cm}^2 \text{ s}$. With the new detectors we have reached the limits of spatial resolution and image gradation at this beamline; a further enhancement of optical resolution would entail unrealistic exposure times and degrade the signal-to-noise ratio. Considering the constraints imposed by the collimation ratio and scattering artifacts, a 50 μm resolution can only be exploited with thin and weakly scattering samples mounted directly on the detection plate.

Chapter 3 Investigation of Boron Steel and Monte Carlo Method

The neutron Transmission imaging experiment is a method based on the interaction of neutron beam with a material thickness. Therefore, this method allows us to have information about internal structure of the given material. The neutron interaction beam is attenuated passing through the thickness plate sample, interacting with nuclide volume. With neutron transmission experiment we have investigated boron steel sample, which often are used in nuclear shielding. The neutron beam is mostly absorbed in the sample thickness due to the presence of the ^{10}B element which has a high absorption cross section. The results, which, are presented are based on direct transmission experiment and analysis to transmission imaging.

3.1 MCNPX –Boron Micro in-homogeneities

MCNPX is a general purpose Monte Carlo transport code that tracks all particles and photons at all energies, that includes 3-D geometry, continuous-energy transport for neutrons in the energy interval 10^{-11} MeV to 150 MeV, 1 KeV to 100 GeV for photons and 1 KeV to 1 GeV for electrons; transport of 34 different particles. Applications of the code are quite broad and constantly developing. Include the design and shielding of accelerators and reactors, medical therapies, dosimeter, imaging, space radiation, plasma transport, nuclear physics, detector design. *Monte Carlo* methods are very different from *deterministic transport* methods. *Deterministic methods* solve the transport equation for the average particle behaviour.

Monte Carlo does not solve an explicit equation, but rather obtains answers by simulating individual particle/photons and recording some aspects of their average behaviour. No transport equation needs ever be written to solve a transport problem by the Monte Carlo method. Monte Carlo solves a transport problem by simulating particle histories rather by solving an equation.

The probability distributions governing these events are statistically sampled to describe the total phenomenon. The statistical sampling process is based on the selection of random numbers – analogous to throwing a dice in gambling casino- hence has the name *Monte Carlo*.

Referring to [MCNPX, 2004] the Monte Carlo method consists of following each of particles or photons from the source throughout its life to “death”.

Probability distributions are randomly sampled using transport data to determine the outcome at each step of its life. MCNPX uses continuous energy nuclear and atomic data libraries. The primary sources of nuclear data are evaluations from the Evaluated Nuclear Data File (ENDF), Evaluated Nuclear Data Library (ENDL) and the Activation Library (ACTL) [MCNPX, 2004].

3.1.1 Physics

The physics of neutrons and other particles is the very essence of MCNPX. When a particle is generated from the source, a particle track is created. If the track is split in two out of splitting surface, a second track is created and there are now two tracks from the original source particle. If one of the tracks has (n, 2n) reaction, one more track is started for a total of three. A track refers to each component of a source particle during its history. Tracks crossing surfaces are used to calculate fluence, flux and pulse-height energy deposition. Within a given cell of fixed composition, the method of sampling a collision along the track is determined using the following theory:

The probability $p(l)$ of a first collision for a particle between l and $l+dl$ along its line is given by [MCNPX, 2004]:

$$p(l)dl = e^{-\Sigma_t l} \Sigma_t dl \quad 3.1.1$$

where Σ_t the macroscopic total is cross section of the medium and is interpreted as the probability per unit length of a collision. Setting ξ the random number on $[0,1)$ to be:

$$\xi = 1 - e^{-\Sigma_t l} \quad 3.1.2$$

it follows that:

$$l = -\frac{l}{\Sigma_t} \ln(1 - \xi) \quad 3.1.3$$

because $1 - \xi$ is distributed in the same manner as ξ , $1 - \xi$ may be replaced by ξ , we obtain the well-known expression for the distance to collision:

$$l = -\frac{1}{\Sigma_t} \ln(\xi) \quad 3.1.4$$

If there are n different nuclides forming the material in which the collision occurred, and if ξ is a random number on the unit interval $[0,1]$, then the k^{th} is chosen as the collision nuclide, if:

$$\sum_{i=1}^{k-1} \Sigma_{t_i} < \xi \sum_{i=1}^n \Sigma_{t_i} \leq \sum_{i=1}^k \Sigma_{t_i} \quad 3.1.5$$

where Σ_{t_i} is the macroscopic total cross section of nuclide i .

3.1.2 Neutron Physics in MCNPX

MCNPX uses interaction tables when simulating neutrons. The data on the interaction include cross sections and other relevant information, like the total absorption cross-section and the angular distributions of scattered neutrons. The nuclear data tables for neutrons are divided into five classes, continuous-energy

neutron interaction data, discrete reaction neutron interaction data, neutron dosimetry cross section data, neutron thermal data and multi-group neutron data. When MCNPX runs, the particle tracks are computed event by event. If a particle collides with a nucleus, a standard sequence always occurs, which in the case is as follows:

1. MCNPX identifies the collision nuclide by considering the total cross section, σ_T .
2. Neutron capture is modelled with consideration of the absorption cross section, σ_a .
3. If thermal treatment is not used, either elastic scattering or inelastic reaction including is selected, and the new energy and direction of the outgoing tracks are determined.
4. If the energy of the neutron is low enough and an appropriate thermal table is present, the collision is modelled by the thermal treatment instead following step 3.

The selection of elastic scattering is based on the probability:
$$\frac{\sigma_{el}}{\sigma_{in} + \sigma_{el}} = \frac{\sigma_{el}}{\sigma_T - \sigma_a}$$

Whereas the probability for inelastic scattering is:
$$\frac{\sigma_{in}}{\sigma_T - \sigma_a}$$

where σ_{el} is the elastic scattering cross section, σ_{in} is the inelastic cross section, σ_a is the absorption cross section and σ_T is the total cross section:
$$\sigma_T = \sigma_{el} + \sigma_{in} + \sigma_a$$

The directions of excited and emitted particles are determined by sampling angular distribution tables from the cross section files. The direction of the particles, when elastic scattering appears, is sampled from angular distribution tables and the excited energy is determined by two-body kinematics. There are many types of inelastic scattering reactions. The energy of the excited particles is determined from scatterings laws that are sampled independently from cross section files for each excited particles as referred to MCNPX code collection, 2.4.0 version [MCNPX, 2004]:

3.2 Neutron Source Simulation

The ATI in Vienna operates a TRIGA-II 250 kW thermal research reactor. It is a swimming pool type and the reactor core consists of some 80 fuel elements, which are arranged in an annular lattice. There are four neutron beam holes and two thermal columns, which are used to extract a thermal neutron spectrum. The space between reactor core and the hall is filled with graphite to slow down the neutrons. At the NT II station neutrons are collimated inside the collimator. The collimator consists of a concentric cone at a length of 130 cm, followed by a 130 cm long cylindrical section. The neutron beam at the end of the cylinder has a diameter of 9 cm and the neutron flux density is approximately 3×10^5 n/(cm²s). The cone and cylinder (see

figures 1.3.1 and 1.3.2, chapter 1) are shielded outside by borated polyethylene material. The neutron source with a certain energy and direction is simulated using the **SDEF** card [Stummer, 2005], [Wallin, 2005], [Shultis, 2006]; the neutrons can be scattered or absorbed in the sample (in this case in boron steel alloy plates) and finally are detected in the detector. As we mentioned before the neutron energy spectrum at the thermal column at NR station II is well described by a Maxwellian distribution function. The Maxwell spectrum is directly used as an input file parameter, at given energies (or temperatures), in this case: $2.93 \cdot 10^{-9}$ MeV, $1.31 \cdot 10^{-8}$ MeV, $2.53 \cdot 10^{-8}$ MeV, $4.45 \cdot 10^{-8}$ MeV, which corresponds to 5.244, 2.5, 1.8, 1.38 Å neutron wavelength respectively. The neutron source in simulation generates thermal neutrons which have the Maxwell distribution having the syntax: $f(e) = c \cdot \text{sqrt}(e) \cdot \exp(-e/a)$ where “c” is the normalization factor and parameter “a” takes the energy values given above.

For each energy value as input parameter in simulations the calculated neutron flux is inserted in the diagram in figure 3.2.1. (the probability distribution of source variable energy, the energy function is a Maxwell (fission) spectrum, referring to source card, see Appendix A).

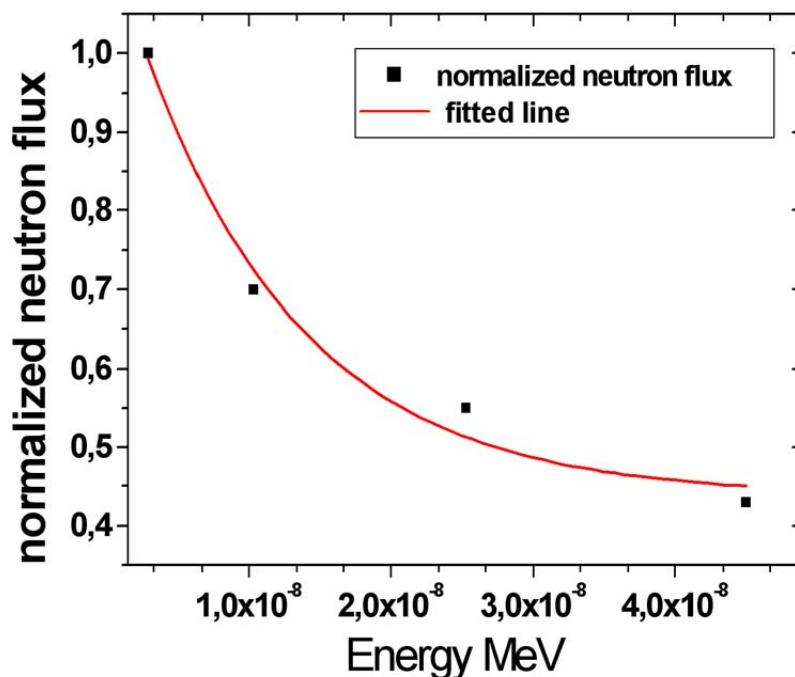


Figure 3.2.1 Simulation of the neutron spectrum (using Maxwell distribution) at different energies (or temperature). Data libraries were taken from ENDF-VI evaluated nuclear data file.

3.3 Geometry Description: Simulated Collimator

Monte Carlo simulations are suitable tool, for calculating neutron radiographs results. [Hassanein, 2005]. The particle transport is simulated with pseudo-random decisions about the origin of the neutrons and

their interactions with matter, starting with the source of the neutrons and their interactions with the sample and finally being counted in the simulated detector. Using MCNPX it is possible to simulate the whole transmission experiment and to describe the boron distribution within a steel sample. During this thesis the Monte-Carlo software version 2.4.0 has been used. With this version all ENDF libraries for the cross sections for almost all isotopes are available. It is possible to reconstruct geometries, including micro-inhomogeneities of the sample and it provides a variety of statistical evaluations. With the MCNPX software, it is possible to reconstruct the geometry needed for the transmission experiment. The input geometry for the simulation consists of the neutron source, collimator (concentric cones and cylinders) and the sample positioned between collimator and the detector. Because of very high absorption at the walls of the collimator and the sample itself, the relatively small number of neutrons led to very poor statistics. Therefore the **SSW** and **SSR** cards were used [Stummer, 2005]. However, all neutrons are directed parallel to the z-axis with a very low divergence (see collimator part, figure 3.3.1). From the collimator walls absorbed neutrons were calculated with flagged tallies. The neutrons at the collimator exit are directed to the sample plate and counted in the detector like illustrated in figure 3.3.2. To reduce the statistical error and to improve the results due to loss of neutrons in the collimator walls and the sample the input file was modified by dividing the sample plates into several plans and increasing the neutron importance in each cell by a factor of two (see input file in appendix A). Of course the input geometry for the simulation is considerably simplified compared to the existing facility (figure 3.3.2). It is assumed that the simplified geometry configuration of the reactor doesn't influence the results. All the graphs and geometry were plotted with X- Deep/32 program (see appendix A).

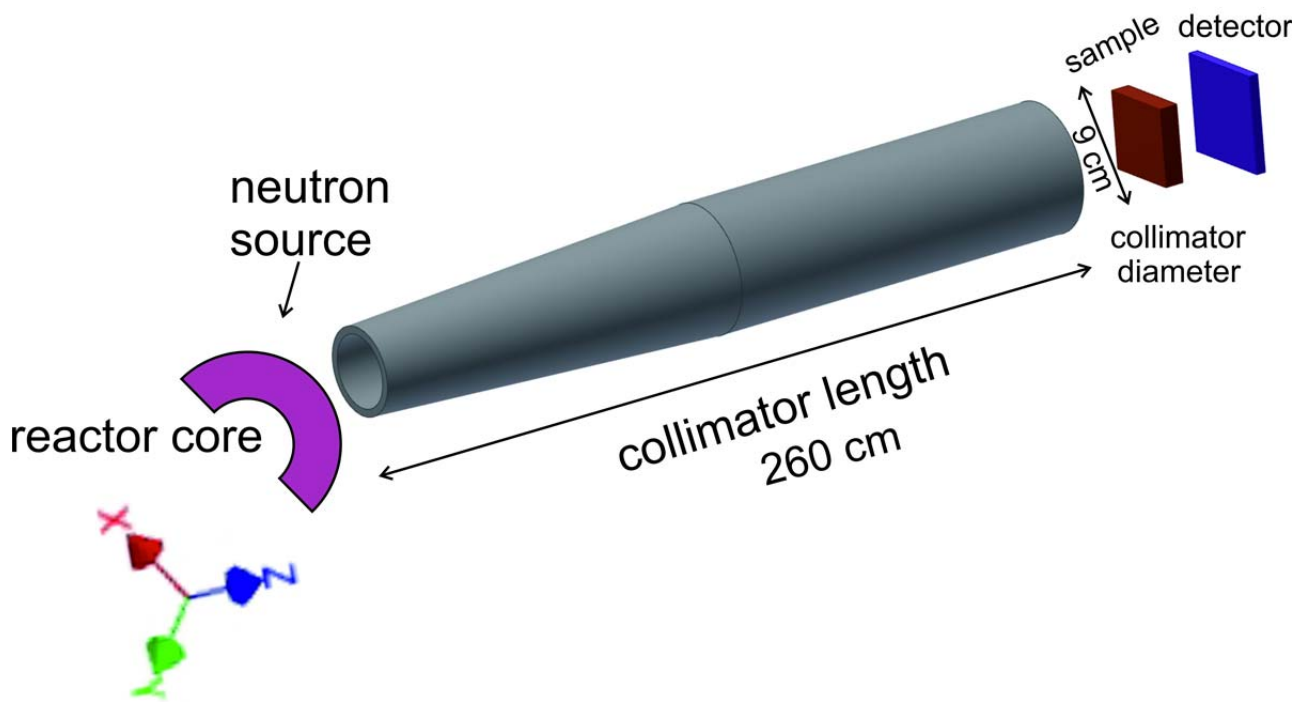


Figure 3.3.1 Collimator geometry using MCNPX 2.4.0 version software.

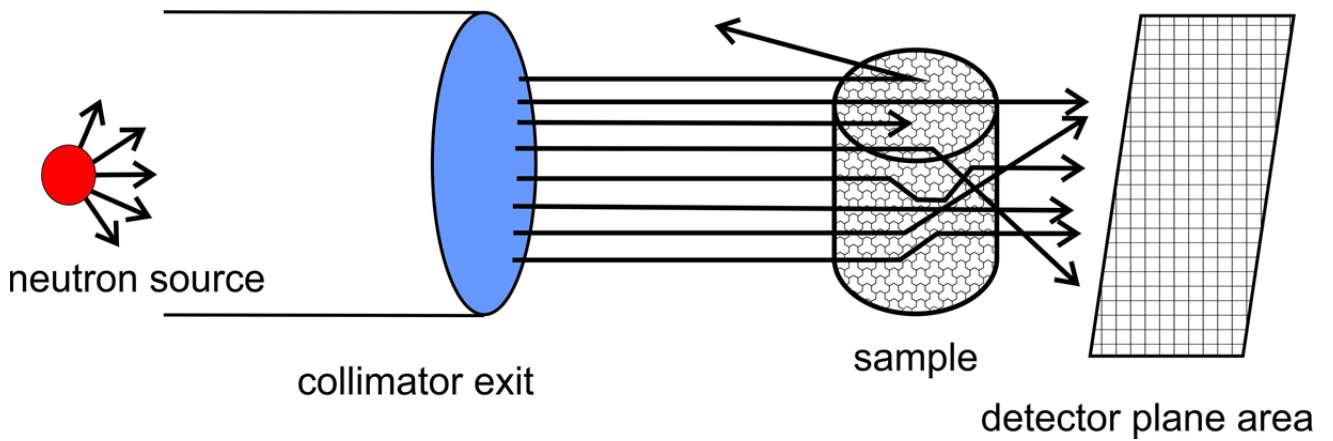


Figure 3.3.2 The three components for the Monte-Carlo simulation for neutron radiography. The neutrons coming from the source, being collimated passing through the sample can be absorbed or scattered and finally are detected in the detector.

3.4 Detector Design in Simulations

Considering that the neutron beam is parallel to the z-axis the attenuated flux is given:

$$\Phi = \Phi_o \cdot \exp\left(-\Sigma_{sample} \cdot d_{sample}\right) \quad (3.4.1)$$

where: Φ_o - the initial flux, Φ - the attenuated flux, Σ_{sample} - the total attenuation coefficient of the sample and d - sample thickness (see figure 3.4.1). In simulations the neutron flux simulated has the units: *particles/cm²*. The detector system detects the neutron flux $\Phi(E)$, behind the sample which represents the measured intensity for a given time interval, where E is the neutron energy [Hassanein, 2006].

All types of detectors for thermal neutrons have a thin neutron absorbing layer. This layer is energy dependent on the macroscopic absorption cross-section $\Sigma_{det}(E)$. Thus the absorption of the detector layer is given by:

$$A_{det} = 1 - \exp(-\Sigma_{det} \cdot d_{det}) \quad (3.4.2)$$

Where: d_{det} - the detector layer thickness. The scattering effect in this case is ignored. Using the formula 3.4.1 the detected neutron flux behind the sample is:

$$\Phi_{det} = \Phi \cdot A_{det}^{abs} dE \quad (3.4.3)$$

$$\Phi_{det} = \Phi_o \cdot \exp(-\Sigma_{sample} \cdot d_{sample}) \cdot (1 - \exp(-\Sigma_{det} \cdot d_{det})) \quad (3.4.4)$$

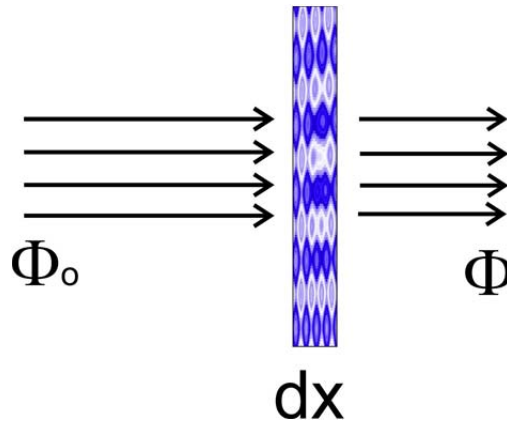


Figure 3.4.1 The initial flux Φ_o passes through the sample and reacts with the nuclides of the sample with thickness dx . Φ value represents the attenuated flux.

The simulated neutron transmission for the ⁶Li detector and IP-ND was calculated by using the **F2** tally, measuring the flux of the neutrons before and after the detector layer by taking the ratio to obtain the absorption of the neutrons:

$$A_{det}^{sim} = \frac{\Phi}{\Phi_o} = \frac{n_{arrived} - n_{absorbed}}{n_{arrived}} \quad (3.4.5)$$

Φ_o - the calculated neutron flux, which arrives at the detector without sample;

Φ - the calculated flux at the detector with the sample between the neutron source and detector;

$n_{arrived}$ are the number of neutrons which arrive at the detector;

$n_{absorbed}$ are the number of neutrons absorbed inside the detector volume.

In the simulated detector no physical processes are taken into account except for the total absorption of the neutrons in the Gd or Li layer. Although MCNPX offers different tallies, usually the cell tallies **F2** and **F4** has been used to calculate the flux over the detector surface or volume. The detector surface is divided into multi bins into a rectangular grid that corresponds to the detector pixels. Figure 3.4.2 shows the neutron detector simulated with the MCNPX program.

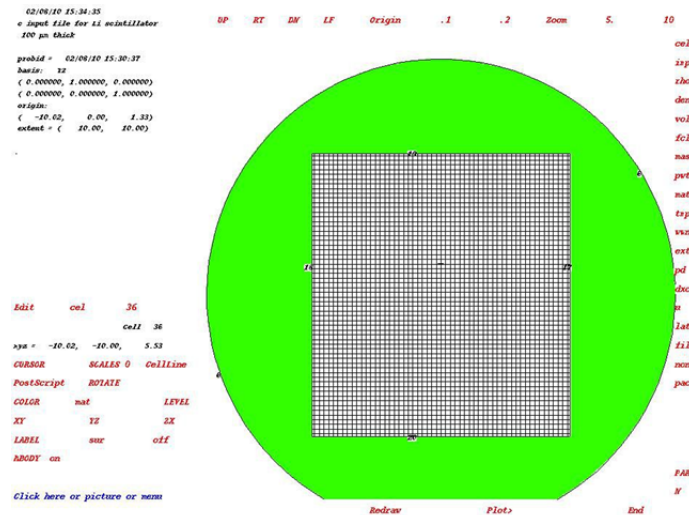


Figure 3.4.2 Geometry configuration of the simulated detector.

MCNPX allows using an energy dependent tally multiplier **EMn**. The absorption values are calculated for ^{nat}Gd and ^6Li thick layer using Equation 3.4.2. The cross section data for ^{nat}Gd and ^6Li were taken from the Evaluated Nuclear Data Files (ENDF). This numerical data were directly used as a tally energy multiplier in the input file during the simulations.

With **F4** tally one can calculate the neutron flux over the cell detector volume, which is filled with Li material. Another very accurate tally, which was used often in the simulations, was the **FMn** Tally Multiplier Card together with the **F4** tally.

During simulations, these two tallies calculate the neutron flux, which is absorbed inside the detector.

It has a form like for the attenuator set: $Attenuator\ set = C -I\ m\ px$

where C = multiplicative constant
 $-I$ = flag indicating attenuator
 m = material number identified in the Mm card
 px = density times thickness of the attenuating material

Evaluated Nuclear Data Files ENDF for ${}^6\text{Li}$ isotope allows having the cross section data for neutron capture.

The **F4** tally is modified by the factor, $e^{-\sigma_{abs}px}$ which, in reality is the attenuation factor px .

The density of Li, which is given in the input file, is in atomic density units: $\rho_{atomic} = 0.01504$ atoms/(barns·cm); in the **F4** tally particles/cm² units are employed.

Thus **FM4** has the form: **FM4** → C -1 m9 exp (-0.01504·0.01· $\sigma_{totalLi}$).

Indeed the total absorption cross section of ${}^6\text{Li}$ isotope is: $\sigma_{absLi} = 940$ barns, atomic weight: $A = 6.015$, density: $\rho_{Li} = 0.1504\text{ g/cm}^3$ and $d = 0.01$ is scintillator thickness in cm. The detector macroscopic cross section (detector layer) is calculated by the total microscopic absorption cross section: $\Sigma_{det} = N \cdot \sigma_{absLi}$,

where N is the number of nuclides per volume: $N = \frac{\rho_{Li} \cdot N_A}{A}$; N_A is Avogadro number. Finally **m9** is the material card for ${}^6\text{Li}$ isotope (used in the input file, see Appendix A).

Another syntax of this tally is: *the Multiplier Set* which has a form: **C m type of reaction**

For a ${}^6\text{Li}$ scintillator layer with 0.01 cm (100 μm) thickness the tally multiplier card has the form:

FM4 → (0.01504·0.01) m9 -2
m9 → 3006.60c

The syntax **-2** means, that only absorption of neutrons is taken to the account and **m9** is the material card for ${}^6\text{Li}$ isotope (used in the input file), where the absorption cross section data are taken and **C** is the attenuation factor. A thin layer is assumed so that formula 3.4.2 is fully valid. Setting this multiplier as absorption coefficients for neutrons yields an accurate model of the detector properties during the simulations. This is shown in figures 3.4.3 and 3.4.4 where most of the neutron flux is distributed in the centre of the detector. Figure 3.4.5 shows the decrease of neutron flux caused by the one sample plate (0.137 cm thick) measured in the designed detector.

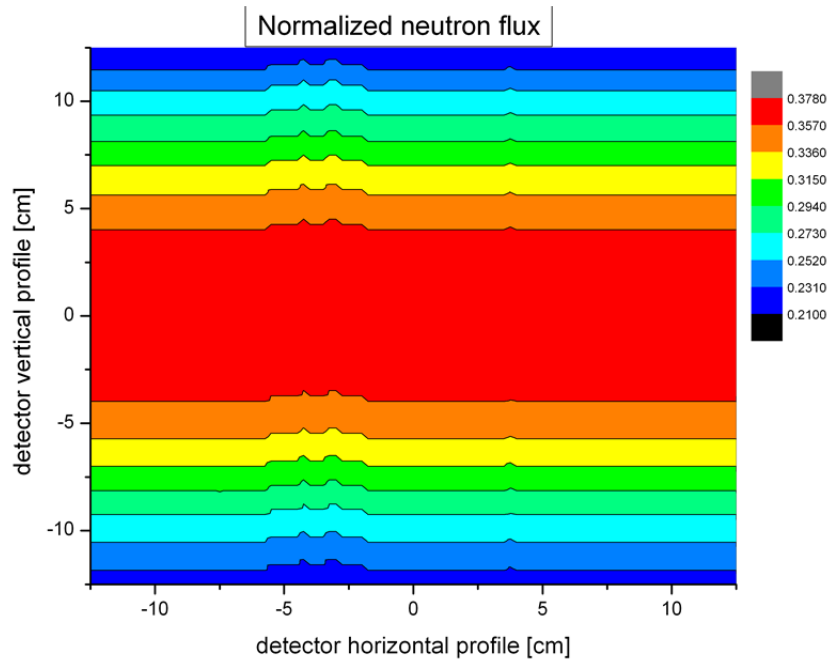


Figure 3.4.3 The contour plot shows that the neutron flux has a maximum (vertical direction-red colour) at the centre of the detector.

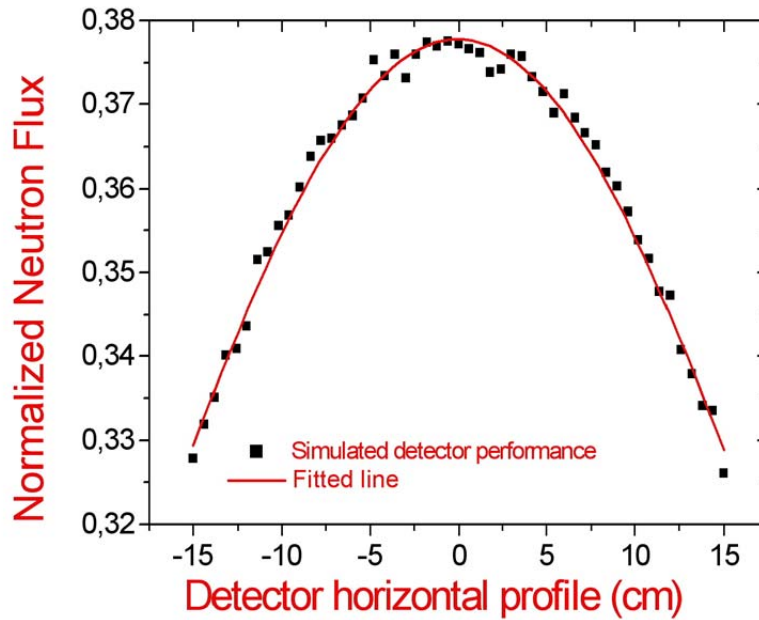


Figure 3.4.4 The simulated neutron flux calculated, at the simulated detector where the detector itself is a simple array with pixel size 200 μm , (the dimensions are given in the input file), which is covered by F4 tally.

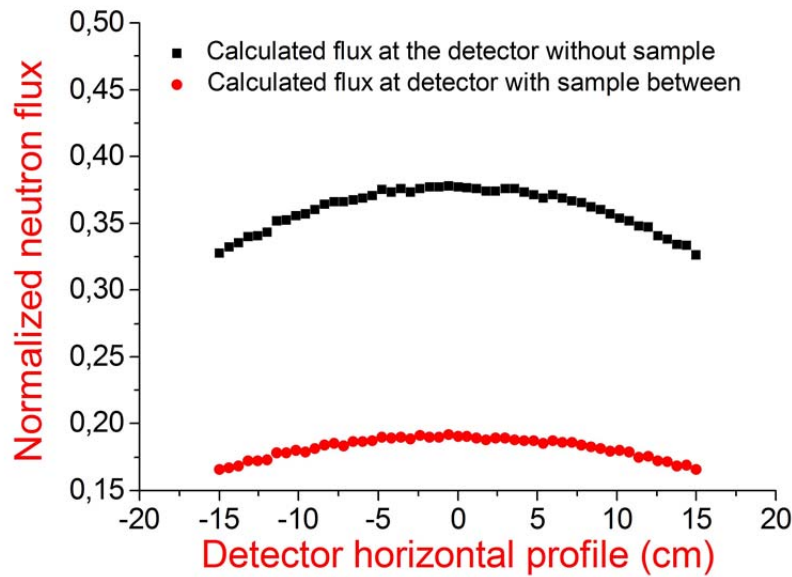


Figure 3.4.5 The change of the simulated neutron flux caused by the boron steel sample plate (in this case thickness $d = 0.137$ cm).

3.5 Heterogeneous Structure Modelling of Boron in Steel Alloy

As a first step a homogeneous distribution of Boron in steel was assumed, but this assumption was not in a good agreement with the transmission experiment. The enhanced transmission measured in experiments could be related to considerable secondary effect namely material heterogeneity. We developed an analytical model on the basis of the SEM (Scanning Electron Microscope) inspection, and USANS (Ultra-Small-Angle Neutron Scattering) done at ATI, which are proposing an inhomogeneous boron distribution inside the steel matrix at the range of $20 \mu\text{m}$ (figure 3.7.1).

Simulations of homogenous model were done with a density of $\rho_{B\text{-steel}} = 7.695 \text{ g/cm}^3$, filling the whole volume of the sample plates. This work was based on the technique introduced by M. Bastürk, [Bastürk, 2003], [Bastürk, Kardjilov 2005], [Bastürk, Arztmann 2005] using the heterogeneous model used in MCNPX simulations to describe the structure of boron-alloyed steel plates and did not find agreement with the transmission results from the experiment.

The scope of this project was a comprehensive analysis of neutron transmission data for quality assurance, thereby considering energy distribution, detector response, beam hardening, background, and finally, as a new tool in the analysis, absorber inhomogeneities. Hypothetic macroscopic absorber homogeneity could be directly verified by high-resolution neutron imaging, [Zawisky, 2004], [Zawisky, Bastürk, 2003], [Bastürk, Kardjilov, 2005], [Bastürk, Arztmann, 2005] and [Zawisky, Dyrnjaja, 2008, 2010], [Dyrnjaja, 2015] however, micro-structures reveal themselves only in strong absorbing materials, i.e., transmission

probabilities of 10^{-2} and below, which requires an efficient background shielding [Zawisky, Dyrnjaja, 2010], [Dyrnjaja, 2015]. The main objective of this work was to investigate the effect of micro-inhomogeneities on neutron transmission, in order to obtain additional information about the absorber distribution beyond the detector resolution. The overall material composition was taken from the manufacturer; MCNPX combines the cross section data for all isotopes to compose a certain material. (Note that during the simulations, free gas approximation is used, the atoms are not combined to molecules, which change the scattering cross section values). The first attempt in this work was to create a unit cell with two different densities which both contain boron-steel ($\rho_{B-steel}$), keeping the total weight percent of natural boron constant in the sample. After several sequences of simulations for different sample thicknesses the results were not promising. In fact, our model was approaching the homogeneous model because the density difference between steel (ρ_{steel}) and steel containing boron is very small ($\rho_{B-steel}$), in this case it is less than 1%. According to the manufacturer's data, the density of pure 100% steel is: $\rho_{steel} = 7.80 \text{ g/cm}^3$ and of boron steel $\rho_{B-steel} = 7.695 \text{ g/cm}^3$. As boron is not homogeneously distributed inside the steel matrix, the sample was modelled by geometric equations like is shown below in order to create a non-homogeneous material. Boron, and especially the ^{10}B isotope, is a strong neutron absorber used for neutron screens, advanced neutron converter detectors [Zeitelhack, 2012], and in nuclear engineering as reactor shielding, fuel storage and transportation baskets. Some related cross sections are listed in Table 3.5 [Dyrnjaja, 2015].

Boron material	Total microscopic cross section σ (cm^{-2})	Total macroscopic cross section Σ (cm^{-1})	Density ρ_{B10} (g/cm^3)
Steel		1.16	
Elemental boron	$7.72 \cdot 10^{-22}$		
^{10}B isotope	$3.838 \cdot 10^{-21}$		
Natural boron alloyed steel 1.88 wt% boron 0.35 wt% ^{10}B		7.3	0.00377 g/cm^3
Borolene 10.3 wt% boron		15	0.023 g/cm^3

Table 3.5 The neutron cross-sections for steel, B-alloyed steel and borolene [Dyrnjaja, 2015].

The realization of a uniform boron distribution is an important property for these applications in order to homogenize and minimize neutron transmission.

Micro-heterogeneity can play a big role in the transmission through strong absorber materials. The best agreement with experimental data and MCNPX simulations was found with the assumption of an inhomogeneous composition like hexagonal lattice cell model, which is being described below.

3.5.1 Model 1

The first model used; Model 1-consists of a hexagonal lattice cell model where the hexagon has a density of $\rho_{steel} = 7.80 \text{ g/cm}^3$ and a sphere inside the hexagon which contains boron and steel with a density of $\rho_{B-steel} = 7.695 \text{ g/cm}^3$. This model describes the heterogeneity at the range of $20 \text{ }\mu\text{m}$. The material is a build-up of hexagonal lattice cells. One hexagonal lattice cell is composed of two homogeneous sub-cells where one these sub-cells are the hexagon, contains only steel (light grey region), while the sphere, inside the hexagon, contains boron and steel (dark grey regions), as depicted in figure 3.5.1a, b & c.

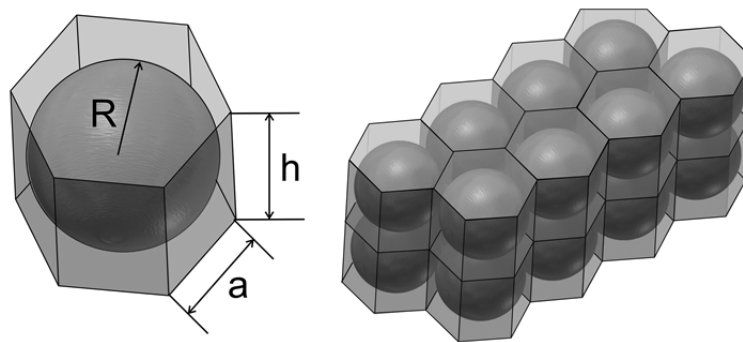


Figure 3.5.1.a In model 1 it is assumed that boron is filling the spheres in the centre of the hexagon. Typical simulation parameters radius of the sphere: $R \sim 10 \text{ }\mu\text{m}$, height of the hexagon: $h \sim 20 \text{ }\mu\text{m}$, side of the hexagon: $a \sim 10 \text{ }\mu\text{m}$.

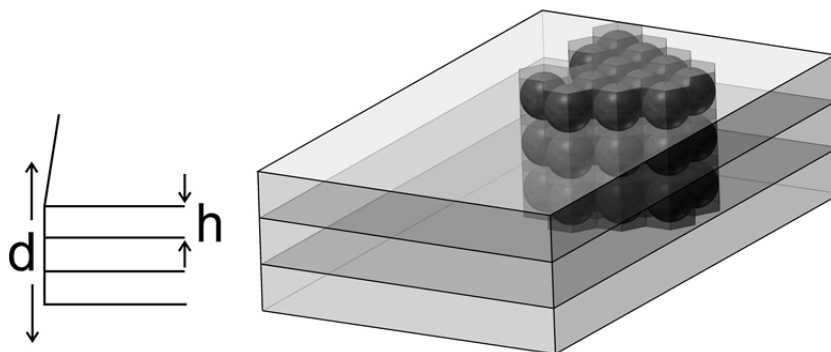


Figure 3.5.1.b The two different materials cell fills the volume of the boron steel plate. The distribution of boron powder, with a size $20 \text{ }\mu\text{m}$, is concentrated at the centre of the hexagon, always keeping constant the total weight percent of 1.88 wt % of natural boron in the sample.

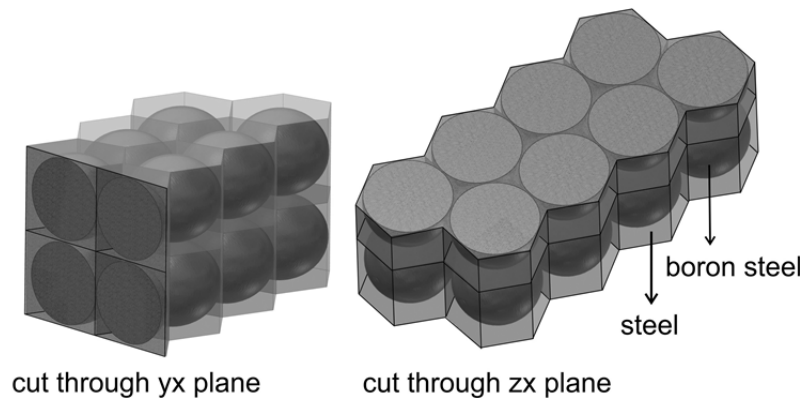


Figure 3.5.1.c The modelled micro-heterogeneity of the material. The sample is modelled by geometric equations and material composition, density for the different volumes. The dark colour shows the volume filled with boron steel (neutron-absorbing material) while the rest of the hexagon is filled with steel only (light grey colour).

3.5.2 Model 2

Model 2 is a slight modification of model 1 (figure 3.5.2). It contains a cube (with parameter “a”) filled with boron-steel. The rest of the hexagon volume is filled with steel material only. Volume ratio: $Vol_{B\text{-steel}}/Vol_{steel}$ is 90 %. Material density of the cube is: $\rho_{B\text{-steel}} = 7.695 \text{ g/cm}^3$ Again the density, which fills the rest of the hexagon volume is: $\rho_{steel} = 7.80 \text{ g/cm}^3$.

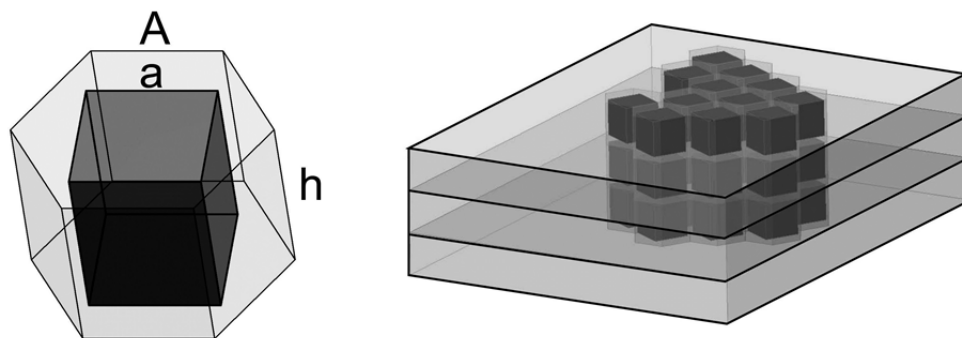


Figure 3.5.2. The material inhomogeneity created by a cell in which the hexagon (contains steel only) is filled with boron steel (inner cube). The dark colour shows the volume filled with boron steel (neutron-absorbing material) while the rest of the hexagon is filled with steel only (light grey colour).

3.5.3 Model 3

Model 3 is composed of two coaxial cubes: the outer cube with the length parameter “A” and the inner cube with parameter “a”. Model 3 was chosen to study the transition when, boron-free channels get

closed by flattening the inner cube (see figures 3.5.3). The parameters used in the simulations of figure 3.5.3 are listed in Table 3.5.3.

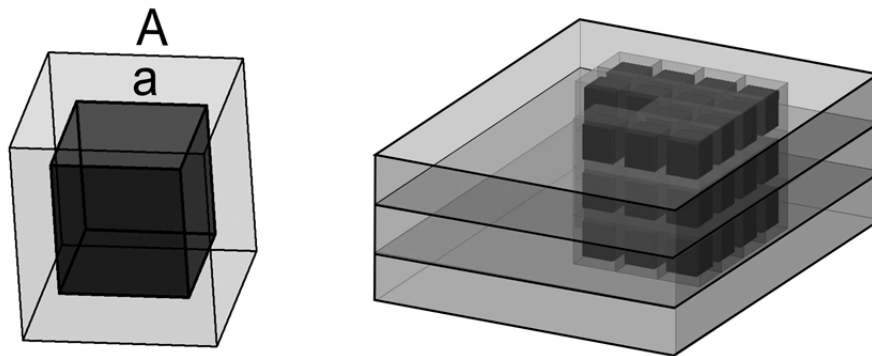


Figure 3.5.3. Two coaxial cubes filling the volume of the sample plate. The dark colour shows the volume filled with boron steel (neutron-absorbing material) and the rest of the hexagon is filled with steel only (light grey colour).

Model	Parameters		
	A (μm)	a (μm)	Volume Ratio %
3	21	20.37	91
	21	20.28	90
	21	20.18	88

Table 3.5.3 The parameters (used in the input file) for model 3[Dyrnjaja, 2015].

3.5.4 Model 4

Model 4 is another attempting to create another non-homogeneous model for this given material where the micro-structure created from different geometric equations has no effect in neutron transmission experiments (see section 3.12 Results and Comparisons Data).

Model 4 assumes two hexagons, where the cell size is in the range of 20 μm . The cut through different planes illustrate the micro homogeneity, which fills the volumes created by geometrical equations using MCNPX. Figure 3.5.4 shows the simulated model 4, which has other geometrical equations to describe the inhomogeneity of boron in steel.

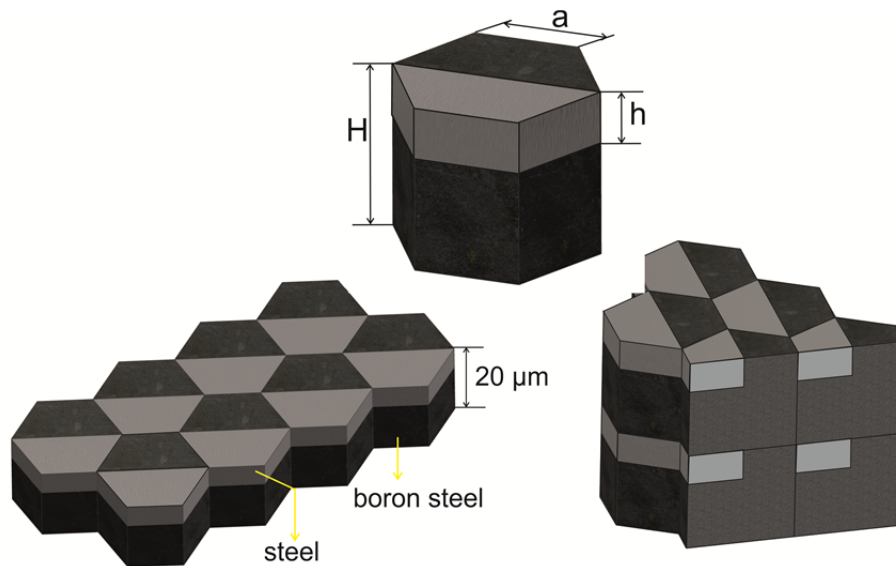


Figure 3.5.4. The geometry model is describing a non-homogeneous distribution of boron-steel and steel. Two hexagons, which intersect each other, represent this non-homogeneity.

In all models we kept the parameters of the geometry in the range of 20 μm . Boron steel investigations with SEM from Böhler Bleche Company and with USANS method at ATI indicate a range of 20 μm dimensions of B micro-structure. The total B amount is kept constant at 1.88 wt% and density 7.695 g/cm^3 . Every neutron track through the sample experiences a slightly different amount of boron, and Monte Carlo simulations (MCNPX) are able to estimate an averaged transmission of a large number of stochastic paths, thereby considering the Maxwellian energy spectrum at our beamline, multiple scattering, absorption probabilities of the ^6Li scintillator [Zawisky, Dyrnjaja 2008], and as a new feature in our analysis: different models for the absorber structure. In the absence of macroscopic inhomogeneities, the models focus on the microstructure as indicated by SEM and USANS measurements. Figure 3.5.5 summarizes four artificial lattice models containing alloys of boron plus steel (dark regions) concentrated in the center of the steel hexagon cells. The light gray parts of the cells contain only steel without boron. As reference serves the homogeneous model where boron is uniformly distributed in the whole volume of the sample (density, $\rho = 7.695 \text{ g}/\text{cm}^3$). The total amount of boron (weight fraction 1.88 (3) wt %), provided by the manufacturer and confirmed by TOF (Time of flight) transmission measurements [Zawisky, 2004], has been preserved in all simulations.

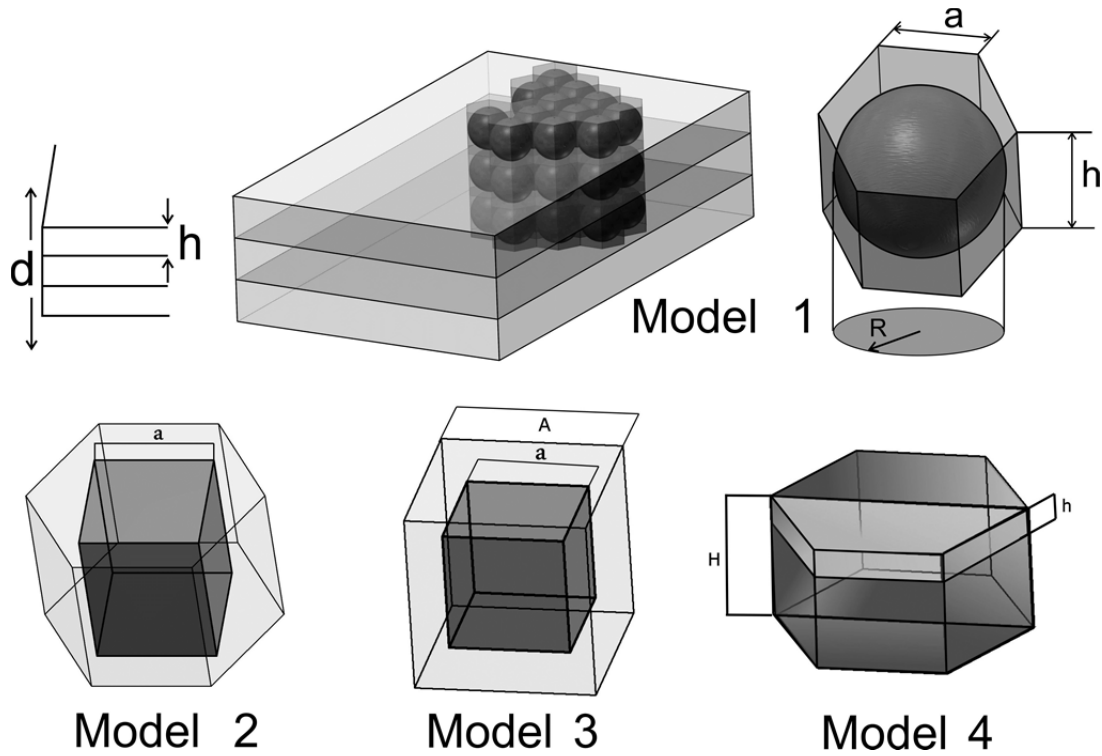


Figure 3.5.5 Different lattice models for the simulation of boron absorber inhomogeneity in steel alloyed plates: **Model 1:** Hexagon lattice cells filled with spheres; **Model 2:** Hexagons filled with cubes; **Model 3:** coaxial cubes; **Model 4:** two hexagons which intersect with each other. Only the dark shaded volumes ($V_{B\text{-steel}}$) contain the absorber [Dyrnjaja, 2015].

3.6 The Absorber Fluctuation Effect

An exponential law describes the transmission of monochromatic, collimated neutrons through a thin and perfectly homogeneous material:

$$T = \exp\left(-d \frac{\lambda}{\lambda_{th}} \sum_i (\sigma_{th} \cdot N)_i\right) \quad (3.6.1)$$

where: d = thickness, λ = neutron wavelength, λ_{th} = thermal wavelength (= 0.18 nm), σ_{th} = total microscopic thermal cross section, N = nuclear density and i = isotope index.

However, secondary effects like beam hardening, scattering and absorber fluctuations always enhance the neutron transmission. Another source of enhanced transmission is the background of scattered neutrons by passing the sample [Zawisky, 1999]. This background effect has to be eliminated experimentally by appropriate sample and detector shielding. The most interesting effect is the absorber fluctuation because even micro-heterogeneities below the imaging resolution can reveal themselves by a slightly elevated neutron transmission. This effect can be explained by the exponential nature of the transmission law where

particle density fluctuations (δN) to smaller densities have a greater effect than to higher densities. Assuming a Gaussian absorber fluctuation the transmission enhancement reads [Zawisky, 1999]: However, equation (3.6.2) provides only a qualitative understanding, for a comprehensive modeling of the stochastic transmission processes MCNPX simulations are used.

$$T(\delta N) \approx T(0) \times \exp \left[\left(d \sum_i \sigma_i \delta N_i \right)^2 / 2 \right] \quad (3.6.2)$$

3.7 Applications: Transmission Experiments on Boron Steel Plates

The Böhler Bleche GmbH Company, offering stainless steel grades with different boron contents, provided the boron steel alloy plates. These satisfy requirements such as: largest possible thermal absorption cross-section, toughness, resistance to corrosion and ease of welding. Such materials are of high interest as they are used in nuclear shielding or for radioactive waste disposal equipment, such as:

- Components for compact storage racks
- Transportation baskets, etc.

The neutron absorption in these samples depends on the content of boron and mostly of ^{10}B isotope which has an absorption cross section in the thermal region of 3840 barns as shown in figure 3.7.2. Among all elements having large absorption cross-sections for thermal neutrons, up to now only boron is of importance for steelmaking. The reason is that the production of shielding materials is affected by economical consideration of availability in industrial volumes and metallurgical problems. Natural boron consists of about 19.9% of ^{10}B isotope. The Böhler Bleche GmbH Company has developed a fabrication technology, which allows any mixture between natural boron and enriched boron, (figure 3.7.1). The resulting boron-steel is hard, resistant against oxidation and chemical attack and resistant against corrosion attack under environmental conditions of a nuclear power station. The cross sections of the alloying elements C, Si, Mn, S, Cr, Mo, Ni, Fe (mostly of chromium, molybdenum and nickel) are considerably smaller and may be disregarded for the evaluation of neutron absorption (see tables 3.7a and 3.7b).

elements	density ρ_i [g/cm ³] $\rho_i = \rho * m_i / m$	atomic weight A	number of atoms per unit volume N $N = \rho * N_A / A$	cross section σ ($\sigma_{total} = \sigma_{sc} + \sigma_{abs}$) barns	Macroscopic cross section Σ cm ⁻¹
Fe	0,66116320	12,0107	2,00E+20	5,55E-24	1,11E-03
C	0,0004835	28,0855	8,56E+20	2,34E-24	2,00E-03
Si	0,0048350	54,938049	1,57E+21	1,55E-23	2,43E-02
Mn	0,0174060	32,065	3,00E+20	1,56E-24	4,66E-04
S	0,0019340	51,9961	1,64E+22	6,54E-24	1,08E-01
Cr	0,1720293	95,94	1,35E+21	8,19E-24	1,11E-02
Mo	0,0261090	58,6934	9,83E+21	2,30E-23	2,26E-01
Ni	0,1160400	55,845	5,59E+22	1,42E-23	7,93E-01
Total Σ_{steel}					1,16 cm⁻¹

Table 3.7a The chemical composition of the elements in steel plates produced by Böhler Bleche GmbH.

elements	density ρ_i [g/cm ³] $\rho_i = \rho * m_i / m$	atomic weight A	number of atoms per unit volume $N = \rho * N_A / A$	cross section σ ($\sigma_{total} = \sigma_{sc} + \sigma_{abs}$) barns	Macroscopic cross section Σ cm ⁻¹
Fe	0,638882	12,0107	2,00E+20	5,55E-24	1,11E-03
C	0,00048845	28,0855	8,56E+20	2,34E-24	2,00E-03
Si	0,0048845	54,938049	1,57E+21	1,55E-23	2,43E-02
Mn	0,0175842	32,065	3,00E+20	1,56E-24	4,66E-04
S	0,0019538	51,9961	1,64E+22	6,54E-24	1,08E-01
Cr	0,1738882	95,94	1,35E+21	8,19E-24	1,11E-02
Mo	0,0263763	58,6934	9,83E+21	2,30E-23	2,26E-01
Ni	0,117228	55,845	5,59E+22	1,42E-23	7,93E-01
B-10	0,003743	10,01293	1,74E+21	3,8381E-21	6,68E+00
B-11	0,014972	11,0093	6,33E+21	5,7755E-24	3,66E-02
Total Σ_{boron_steel}					7,3 cm⁻¹

Table 3.7b The chemical composition of the elements in boron steel sample produced by Böhler Bleche GmbH.

The theoretical calculated macroscopic cross section for boron steel alloy: $\Sigma_{boron-steel} = 7.3 \text{ cm}^{-1}$.

The theoretical macroscopic cross sections for steel alloy only plates: $\Sigma_{steel} = 1.16 \text{ cm}^{-1}$ (see table 3.5).

The cross section's data were taken at neutron energies of 2.52×10^{-8} MeV (thermal region).

For transmission experiments in this work, seventeen identical boron steel alloy plate were available, each having a thickness of $d = 0.137$ cm, density $\rho = 7.695$ g/cm³ and containing 1.88 wt% of natural boron. There is a practical upper limit for alloying boron into a steel matrix of about 1.90%. This is due to the tendency of boron to lower melting eutectic points together with iron and accompanying elements. Boron alloyed stainless steel has a heterogeneous structure. The size and distributions of boron in the steel matrix depend on the technological cooling process of the manufacturer. Scanning Electron Microscope (SEM) investigations exhibit an inhomogeneous boron distribution where the boron particles with a diameter of 50 to 20 μm (figure 3.7.1) are embedded inside the steel matrix.

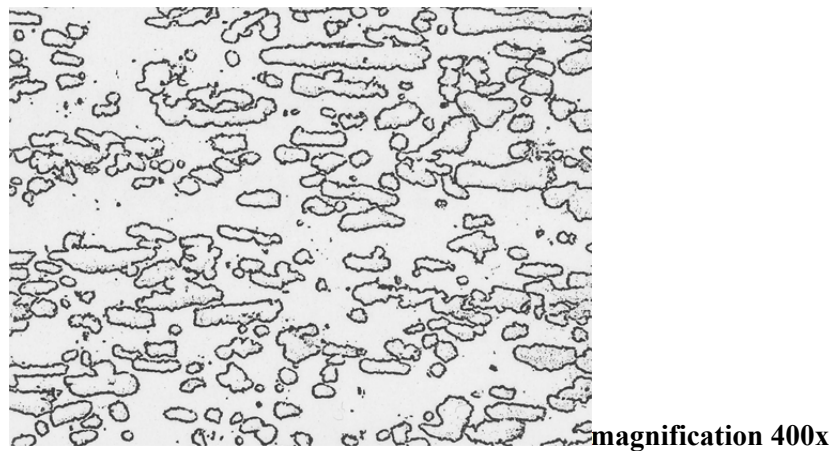


Figure 3.7.1 A slice image, which shows the distribution of boron in steel matrix; the image was taken by SEM analysis; 1 mm is magnified by factor of 400 [Böhler Bleche, 2001].

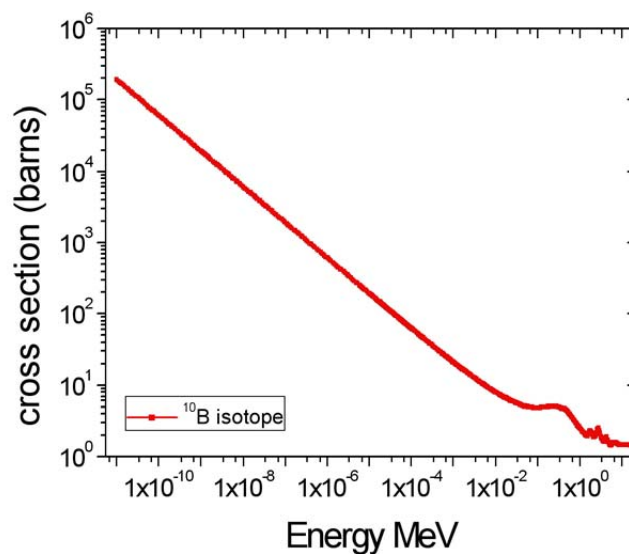


Figure 3.7.2 Cross section in barns as a function of neutron energy for ¹⁰B, showing that in the thermal region the absorption cross section is very high (data are taken from ENDF-IV, MCNPX).

3.8 Exponential Attenuation

For thin plates, monochromatic and well-collimated neutron beam, the exponential attenuation law is given by (referring to the Beer attenuation law (1.4.2) equation):

$$T_{cal} = \exp\left(-\left(\Sigma_{abs,^{10}B} + \Sigma_{abs,steel}\right) \cdot \frac{\lambda_{neutron}}{\lambda_{thermal}} \cdot d_x\right) = \exp\left(-\Sigma_{^{10}B,steel} \cdot \frac{\lambda_{neutron}}{\lambda_{thermal}} \cdot d_x\right) \quad (3.8a)$$

Here d_x is the thickness of the plate and $\Sigma_{^{10}B,steel} = N \cdot \sigma_{abs}$ is the macroscopic absorption cross section where N is the number of nuclides per volume, σ_{abs} is the nuclear absorption cross section. The attenuation coefficient, $\Sigma_{^{10}B,steel}$, is considered for a homogeneous mixture of defined parts of B and Fe atoms and of course other elements present in steel at neutron energies of 2.53×10^{-8} MeV which corresponds to 1.8\AA neutron wavelength. Theoretically the effective macroscopic cross section does not change, if we increase the thickness of the plate, but experimental results do not agree with theoretical results like shown in figure 3.8.1. Experimentally the attenuation coefficient at the given sample thickness d is obtained by the following:

$$\Sigma_{^{10}B,steel} = -(\ln T) / d \quad (3.8b)$$

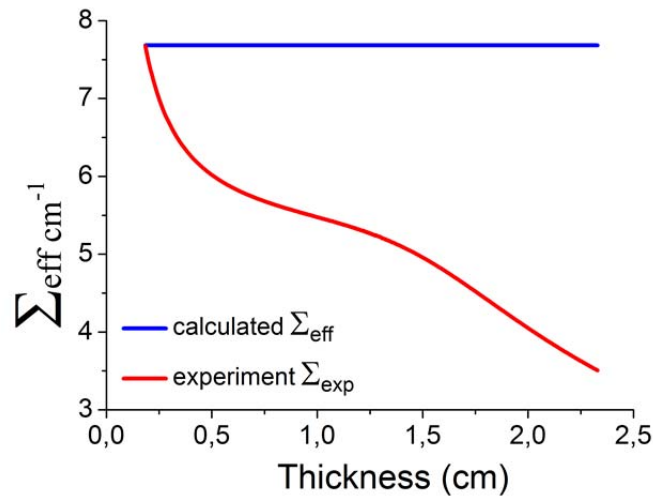


Figure 3.8.1 Calculated and experimental comparison of the effective macroscopic cross section values between 1.88 % wt natural boron in alloy steel plates as a function of thickness.

This deviation between theory and experiment is related mainly to other contributions. We consider that the inhomogeneities of the boron distribution in steel, the background contribution, beam hardening effect, resulting in transmission enhancement especially for strong neutron absorption and thick samples. The

macroscopic cross section values were calculated from the transmission values through boron steel plates with different thicknesses.

3.9 Transmission Experiment with ^6Li Scintillator Detector

Experimentally, the transmission is derived from the count numbers. Count numbers have a determined pixel-wise or preferably averaged over larger areas to reduce the statistical uncertainty:

$$T = \frac{N_s - N_b}{N_o - N_b} \quad (3.9)$$

N_s and N_o are the count numbers behind the sample and in the open beam respectively and N_b represents the background. Ideally, the background is measured by replacing the sample by an ‘infinite’ strong absorber with the same dimensions (in practice 5 cm thick borolene is used on our beam line due to the fact that the transmission would be smaller than the measured background).

The transmission experiments have been carried out at Neutron Radiography Station NR II in combination with scintillator and CCD camera (figure 3.9.1). The read out noise depends on the readout speed of the CCD chip, where the best signal-to-noise ratio is obtained at lowest speed and an overall signal-to-noise ratio of 60 had been obtained after the maximum exposure time of 7 minutes. However, there are two noise components: read out noise which is independent of exposure time; thermal and radiation noise which depends on the exposure time. On the other hand a thin scintillator causes a poor signal-to-noise ratio due to the small neutron reaction rate [Dyrnjaja, 2015]. Certainly there are limitations of transmission measurements while reaching the noise limit level. The transmission experiments have been done with 100 μm thick scintillators layer with 150 μm spatial resolution having a 10 x 15 cm^2 detection area. Because the light is not produced directly by the neutrons, but by secondary particles the blurring effect increases with detector thickness. On the other hands a thin scintillator causes a poor signal-to-noise ratio due to the small neutron reaction rate. The efficiency of the ^6Li scintillator depends on ^6Li density, scintillator thickness, composition (ZnS, Ag), self-absorption of the generated photons in the scintillator, optical lens used, and the photon detection efficiency in the CCD-camera. The transmission of a 100 μm scintillator layer is $T_{exp} = 86.8\%$ (absorption probability $\approx 13\%$) [Zawisky, Dyrnjaja, 2010].

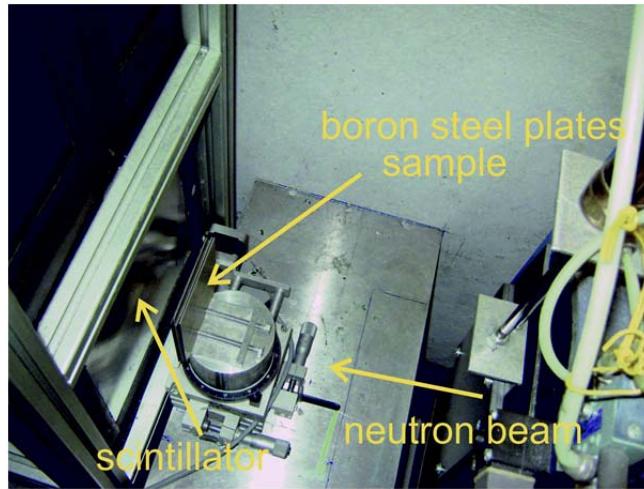


Figure 3.9.1 The experimental set-up with six plates, 0.822 cm thick, placed in front of the detector at thermal column, NR-II station.

To minimize the dark current, the CCD camera was cooled to -130°C with liquid nitrogen. The cooling process was checked every 30 and 45 min and all the data were kept at experimental book. Exposure time was 200 seconds and, “no black removal” and “whole CCD camera” option with format 16 bit (dynamic range) was chosen for every image. The images were saved in the TIF - file format and processed with Image-Pro Plus 6 (Media Cybernetics) program. The gammas absorbed in the scintillator, the so-called white spots (cause by bad “hot” pixels whose position remains unchanged) were removed by using median filters (7x7 median filters). Together with dark current and readout noise these factors are representing the electronic noise contribution at the scintillator-CCD camera unit.

The goal of this experiment was the verification of uniform boron distribution to evaluate the melting and milling processes and the quantification of neutron attenuation [Zawisky, Dyrnjaja, 2010]. At first, 17 boron steel plates with 0.137 thicknesses have been investigated. Within the scintillator’s resolution no statistically significant regions of reduced boron content were found. A selected sample image plate is shown in figure 3.9.2, left. The variance of pixel counts δN was less than $3 \times \sqrt{N_{average}}$ for all sheets. Within the scintillator’s resolution no statistically significant regions of reduced boron were found in the material. Assuming a uniform beam profile and ${}^6\text{Li}$ distribution, σ approaches the square root of the average pixel intensity ($\sigma \approx \sqrt{N_{average}}$) [Zawisky, Dyrnjaja, 2010]. Employing a ND&M camera continued the search for a hypothetical boron microstructure. Nine images were taken of the same steel area in order to separate statistical fluctuations from reproducible structures in this plate. The statistical analysis yielded low intensity variances of $\sigma = 1.4 \times \sqrt{N_{average}}$ in the individual images; furthermore, the sum of pixel intensities yielded an

even lower variance of only $1.2 \times \sqrt{N_{average}}$, [Zawisky, Dyrnjaja, 2010]. Hence, there was no evidence for absorber microstructures in the ND&M measurements (figure 3.9.2, right).

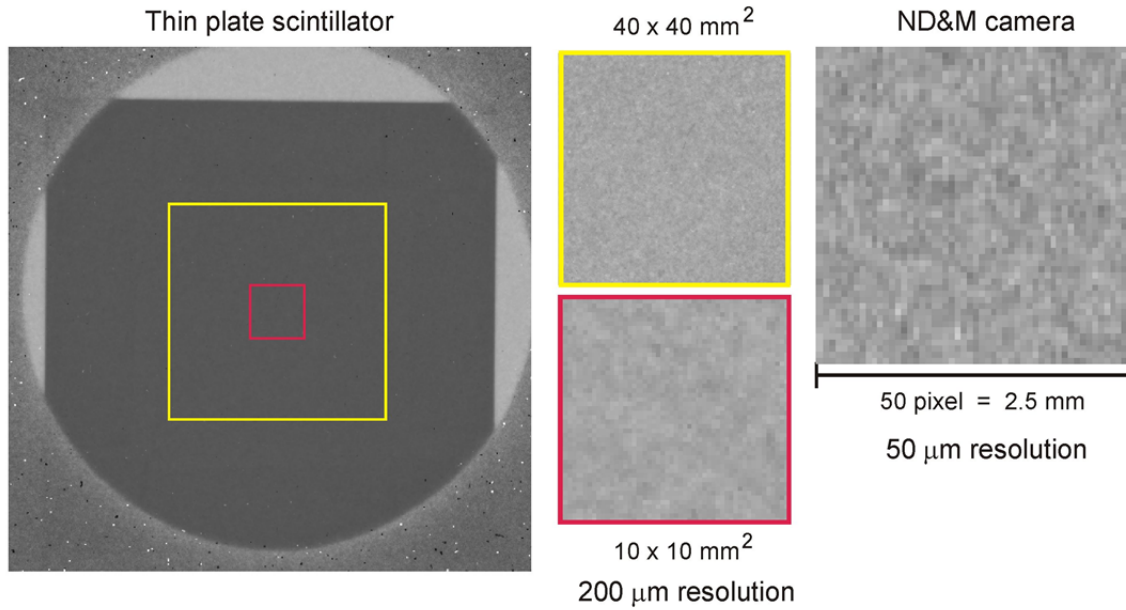


Figure 3.9.2 Transmission images of a 0.137 cm thick boron alloyed steel plate. The intensity variance is $2.3 \times \sqrt{N_{average}}$ in the scintillator, and $1.4 \times \sqrt{N_{average}}$ in the ND&M image. We detected an intensity contrast of $(I_{max} - I_{min}) / (I_{max} + I_{min}) = 23\%$ in the ND&M pixel counts but there is not enough statistical evidence for boron-free zones in the steel [Zawisky, Dyrnjaja, 2010].

3.10 Experimental Setup – Background Correction

Referring to Hassanein the neutrons scattered by the sample are spatially smoothly distributed on the detector. The amount of scattered neutrons in each detector pixel depends not only on the sample thickness, but also on the distance between sample and detector [Hassanein, 2005], [Hassanein, 2006].

Neutron scattering in the sample depends on the material composition, neutron energy spectrum, the density of the sample and sample thickness.

The total cross section σ is dominated by ^{10}B isotope (table 3.7b). Material composition has dependence, which correlates to the contribution to the total cross section: $\frac{\sigma_{abs}}{\sigma_{total}}$ where $\sigma_{total} = \sigma_{^{10}\text{B}} + \sigma_{steel}$.

Sample scattering is not the only disturbing neutron contribution in neutron images. The background scattering contribution has big influence, especially for transmission experiment of strong absorber materials. Neutrons that directly could not reach the detector can be scattered at the shielding or at the borders of the

camera box and hit the detector, [Hassanein, 2006]. This background effect is corrected by using a boron polyethylene mask (borolene with 20 wt% boron), 10 mm thick, which has an aperture of 1x1 cm² regular at the centre of the beam. The transmission experiments with this mask were done using ⁶Li scintillator with 300 seconds exposure time (see figure 3.10.1, right and figure 3.10.3). This mask is designed in a way to reduce the scattered neutrons, which aren't penetrating inside the sample (figure 3.10.2) [Dyrnjaja, 2015]. After finishing this experiment we repeated this experiment with a polyethylene mask of 2x2 cm² aperture, keeping the same condition as for the first mask (figure 3.10.3). These experiments were repeated two more times. In total were 6 sets of transmission experiments through boron steel plate samples (see figure 3.10.1, left). The sample plates were placed between the neutron beam source and scintillator at a distance 3 cm from it. The neutron beam has a 9 cm diameter and the beam shutter has 10x10 cm² dimensions.

Within the scintillator's resolution no statistically significant regions of reduced boron were found. A selected sample image is shown in figure 3.10.2. The lowest detectable transmission level of our beam line, when approaching the noise limit level, is: $T_{\min} \geq 5.0 \times 10^{-5} \pm 2.0 \times 10^{-5}$ (figure 3.10.1 at maximum thickness $d = 2.3$ cm). The resolution is mainly limited by the statistical fluctuation due to the low count numbers and the unavoidable flux of neutrons circumventing the steel plate samples.

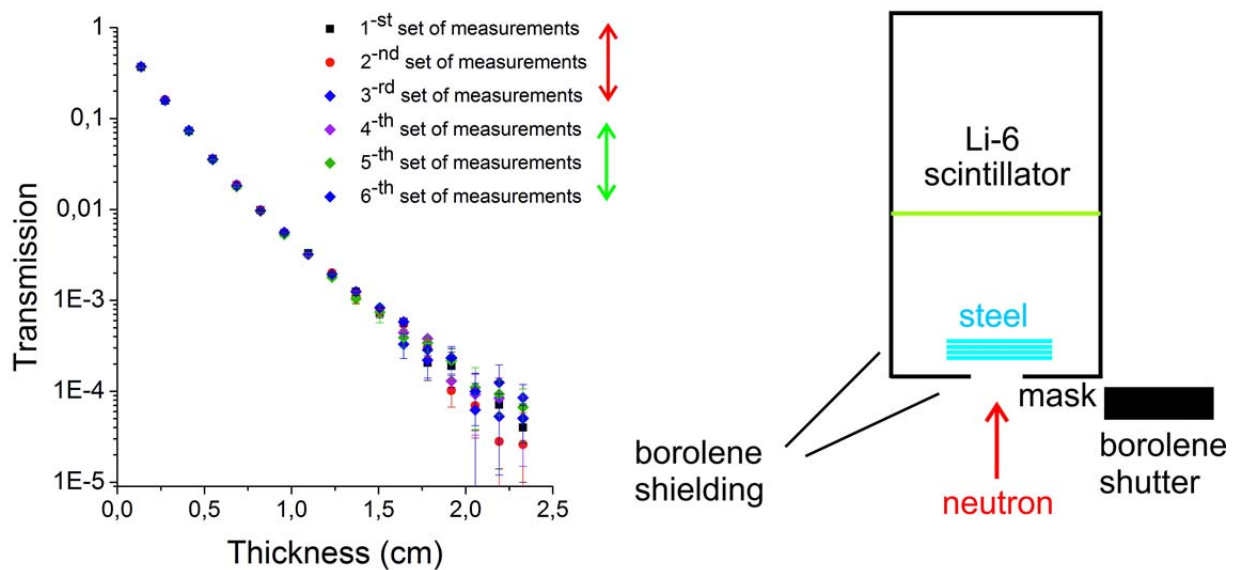


Figure 3.10.1 **Left:** The diagram shows the transmission boron steel alloyed plates versus thickness (for 17 plates) with ⁶Li 100 μm thick scintillator layer. These transmission measurements were repeated 6 times under the same conditions with two polyethylene apertures or masks 1x1 and 2x2 cm². The uncertainty is very high for thick samples. **Right:** The sample was masked with 10 mm thick borolene in order to guarantee that all detected neutrons pass the 1 cm² sample area [Dyrnjaja, 2015].

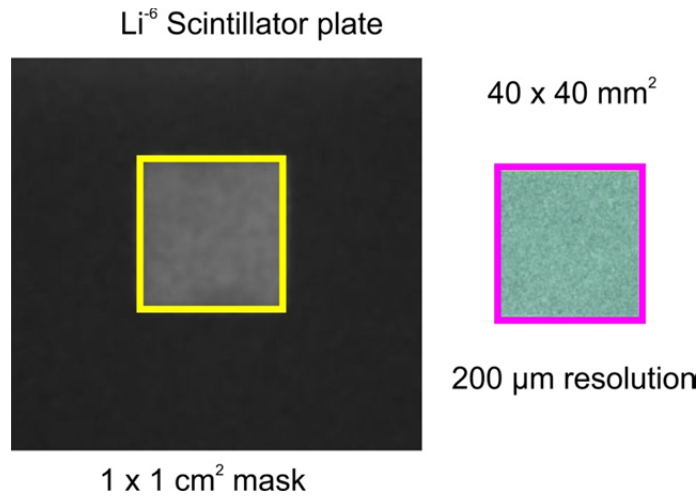


Figure 3.10.2 Transmission image of a 0.137 cm thick boron alloyed steel plate taken with a 100 µm thick scintillator layer using 1x1 cm² boron polyethylene mask at NR II station. Contrast is enhanced only for presentation [Dyrnjaja, 2015].

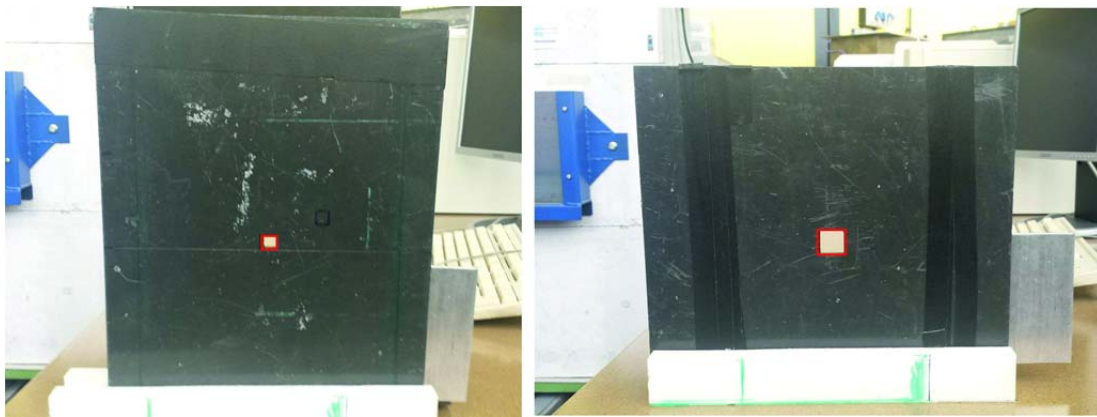


Figure 3.10.3 Boron polyethylene masks used in transmission measurements of boron steel plates. **Left:** aperture of 1x1 cm². **Right:** Aperture of 2x2 cm² in the centre of the neutron beam.

3.11 Transmission Experiment with IP-ND Detector

Finally, we investigated the steel homogeneity with a neutron imaging plate neutron detector IP-ND, using a BAS-5000 readout scanner with 25 µm nominal resolution. The plates were placed directly in front of the IP-ND at 3cm distance, with 40 µm vertical and 60 µm horizontal effective resolution. For each plate N_b and N_o were measured repeatedly. During all measurements a thin aluminium foil shielded the IP-ND, in order to avoid mechanical damage. The exposure time was 50 min followed by a cooling time of 10 minutes after exposure and 10 minutes scanning time for 25 µm pixel size. Between the neutron beam and the

sample, a boron polyethylene mask (10 mm thick) was placed at the centre of the beam, with an aperture of $1 \times 1 \text{ cm}^2$. To achieve the best signal-to-noise ratio at $25 \text{ }\mu\text{m}$ resolution, the highest gradation (16 bit) and sensitivity S4000 at level L5 scanning parameters were chosen. The scanned images were stored as Fuji-img file format and then further processed with Image-Pro Plus 6 (Media-Cybernetics) program. The transmission experiments were repeated systematically for each plate thickness. Due to the poor reproducibility of the IP-ND, the uncertainty reaching the background limit is even higher as compared to the measurements done with the ^6Li scintillator detector.

In the IP-ND detector, gamma radiation is the main background contribution. Because of this the background counts N_b were determined by closing the boron beam shutter and therefore reducing the gamma rays contribution for N_b . Unfortunately, the IP-ND's intrinsic granular micro-structure complicates the analysis of absorber inhomogeneities. To correct for the granularity, the plate has to be adjusted in exactly the same position for open beam correction. Figure 3.11.1 gives an example of a steel inspection image; besides the intrinsic IP-ND artefacts, no significant boron inhomogeneities were found in the steel plates. The IP-ND artefacts and steel inhomogeneities are expected on a similar scale.

The transmission was averaged in an area of 1 cm^2 in order to reduce statistical uncertainties: where N_b represents the background by closing the open mask area with 10 cm thick borolene (see figure 3.11.2 right). The neutron intensity surrounding the mask was confirmed to be uniform and reached the background level with closed mask. This confirms that backscattered neutrons have no influence on the transmission measurements using the setup shown in figure 3.11.2, right. N_b has a great effect on low transmission experiments when N_s approach N_b ; it depends mainly on detector noise [Zawisky, Dyrnjaja, 2010], [Karasawa, 1999] and scattered neutrons, which reach the detector without passing the sample. With the imaging plate detector the background limit, $N_s \approx N_b$, was reached at the 15-th plate (1.781 cm thick) [Zawisky, Dyrnjaja, 2010] see figure 3.11.2 and, considering their poor position reproducibility, the scintillation detectors are the better choice for steel inspections. N_b has a great effect on low transmission experiments when N_s approaches N_b ; it depends on several factors, e.g., sample composition and thickness, the sample-to-detector-distance, intrinsic detector noise, scattered neutrons, gamma radiation, as well as readout noise. Thus, the IP-ND in the present setup is not optimal for such investigations).

Despite the experimental difficulties it can be concluded that no evidence has been found so far for a non-uniform boron distribution in the boron alloyed steel samples down to $50 - 100 \text{ }\mu\text{m}$ detector resolution [Zawisky, Dyrnjaja, 2010].

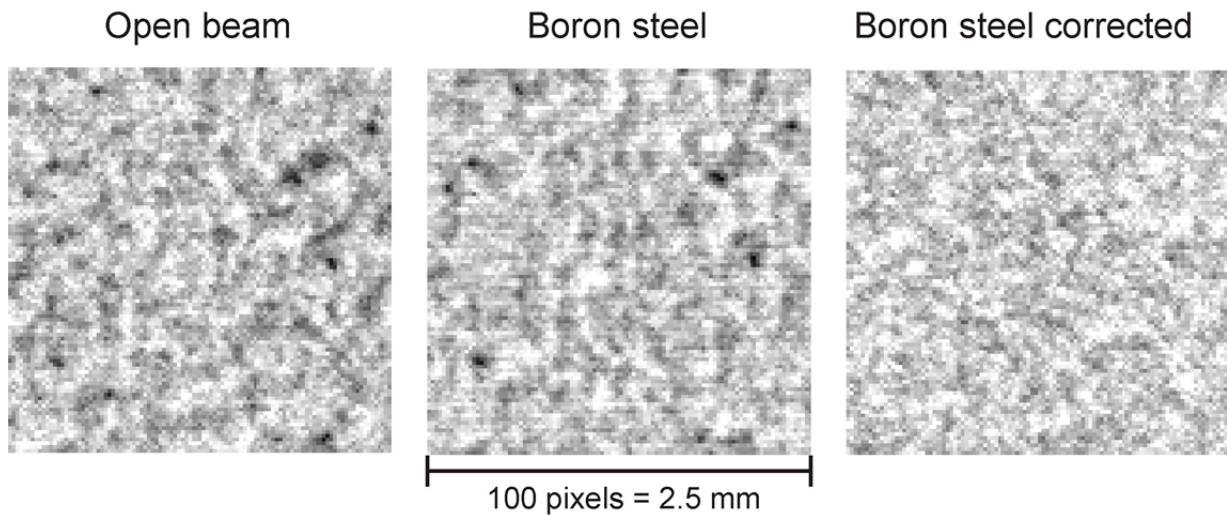


Figure 3.11.1 *Left:* Steel inspection with the neutron imaging plate detector, 25 μm nominal and 40 μm optical resolution. The search for inhomogeneities in boron-alloyed steels is complicated by the intrinsic granular structure of the IP-ND. The transmission image of the steel samples is superposed by the IP-ND granularity (*middle*). *Right:* After open beam correction (*right*) no significant inhomogeneities remained: $(I_{\text{max}} - I_{\text{min}}) / (I_{\text{max}} + I_{\text{min}}) \approx 10\%$ (images contrast enhanced only for presentation) [Zawisky, Dyrnjaja, 2010].

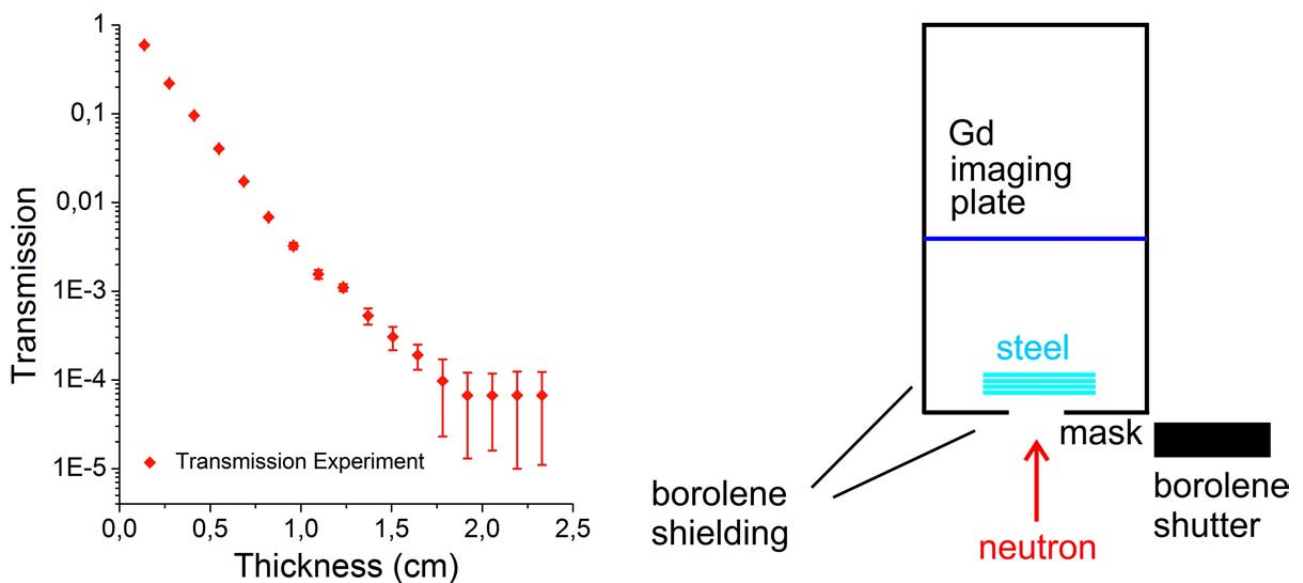


Figure 3.11.2 *Left:* Neutron transmission in strong neutron absorbing steels with $\Sigma = 7.3\text{ cm}^{-1}$ macroscopic attenuation cross section taken with imaging plate IP-ND. *Right:* The sample was masked with 10 mm thick borolene in order to guarantee that all detected neutrons pass the 1 cm^2 sample area [Dyrnjaja, 2015].

3.12 Results and Comparison of the Experiment with Simulated Data

The simulations shown in figure 3.12.1 left indicate (increasing the thickness, number of the plates) that the details of the lattice models have practically no effect, only the volume ratio determines the transmission. All inhomogeneity models can be well adapted to the experimental data; only the assumption of homogeneous absorber distribution yields systematic derivations at low transmission.

As an example, a good agreement with transmission data was obtained with parameters $R \approx 10 \mu\text{m}$, $h \approx 20 \mu\text{m}$, $a \approx 10 \mu\text{m}$ in model 1 (figure 3.12.1). By modeling the geometric parameters one is able to adapt the volume ratio $Vol_{B\text{-steel}}/Vol_{steel}$ to the transmission data (figure 3.12.2).

Only in the extreme cases like: model 3a (no boron free channels) and model 3b (free channel created) one perceives a slight effect on the simulated transmission is observed. By “squeezing” the inner cube in model 3, one approaches a homogeneous layer model where all boron-free paths are closed (model 3a in figure 3.12.3). In this model only the parameter “c” is changed by, keeping the volume ratio constant (90%). The opposite case is model 3b. The parameter “a” changes and defines the channel width.

The parameters for model 3, 3a and 3b are listed in Table 3.12; Volume ratio $Vol_{B\text{-steel}}/Vol_{steel}$ remains always constant at about 90%.

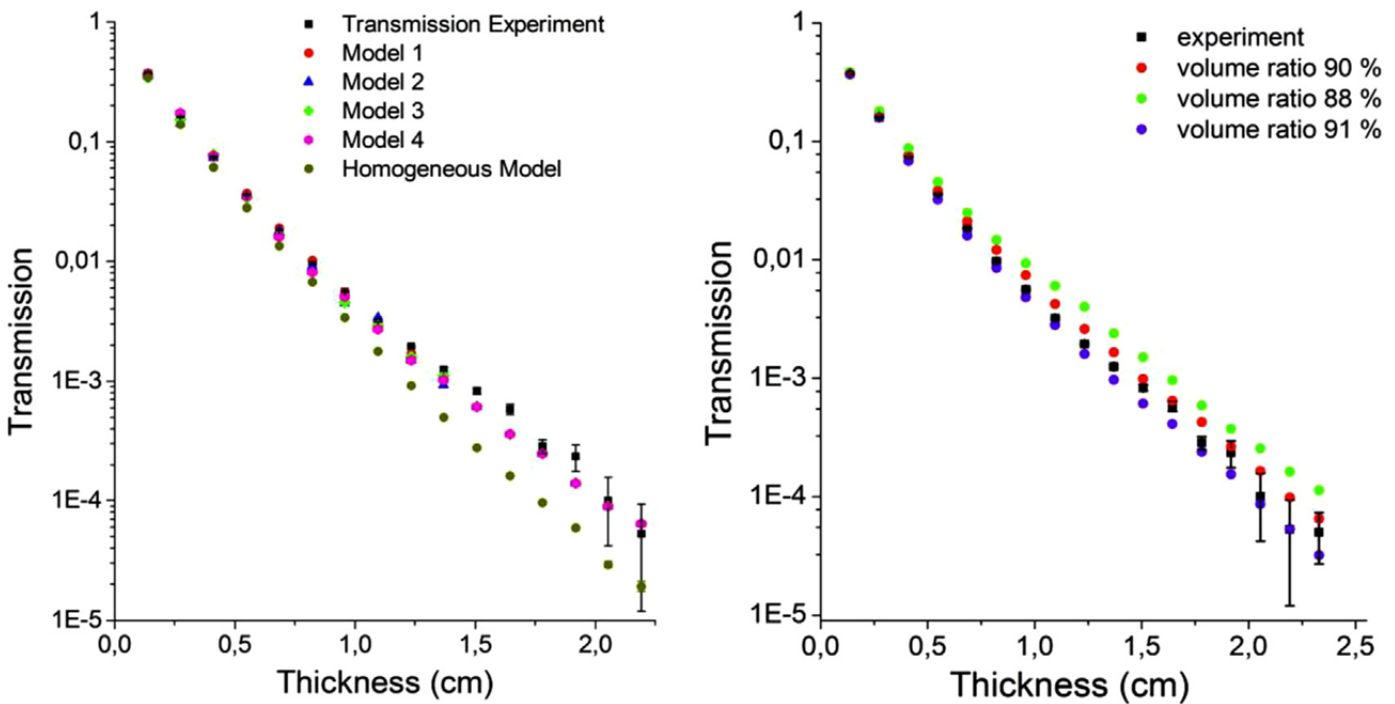


Figure 3.12.1 *Left: Adaption of different MCNPX models to the measured transmission of boron-alloyed steel yielding a volume ratio $Vol_{B\text{-steel}}/Vol_{steel}$ of 90%. Right: Effect of different volume ratios $Vol_{B\text{-steel}}/Vol_{steel}$ in the simulations (model 3) [Dyrnjaja, 2015].*

Models	Parameters			
	A (μm)	a (μm)	b (μm)	c (μm)
3	21	21	21	21
3a	21	21	21	18.9
3b	21	18.9	21	21

Table 3.12 The parameters for models 3, 3a and 3b used in figure 3.12.3.

From the diagram in figure 3.12.3 (blue points) we notice that the transmission from model 3a is decreased, thus we have higher absorption because all neutrons are penetrating the absorber region A (surface A of the outer cube). On the other hand, transmission through absorber free-channels created in model 3b increases the transmission. Referring to diagram in figure 3.12.1, the model 3 fits better to the experimental data. Although we assume, that in the boron alloyed steels the existence of boron-free trajectories are very unlikely, but for other materials the modelling of boron-free channels might be successful. In this diagram, we clearly see that the transmission for model 3b is increased due to channels created in it (green points, figure 3.12.2).

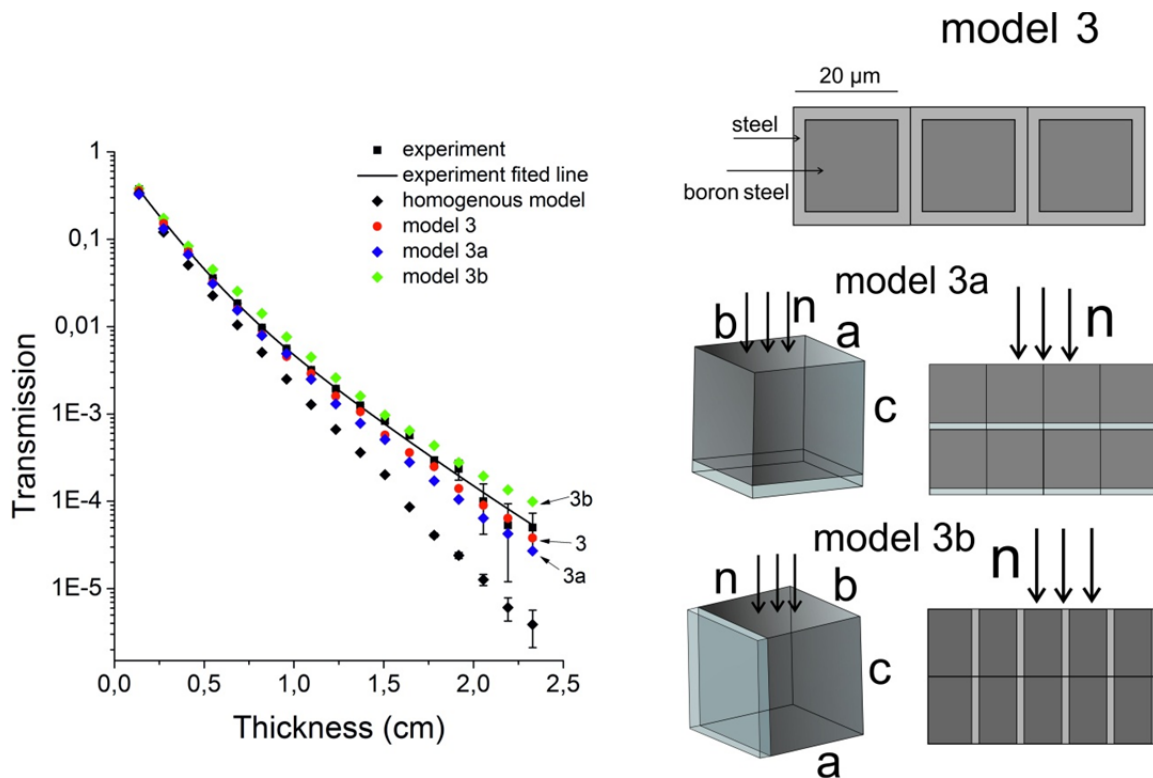


Figure 3.12.2 **Left:** Transmission diagram for models 3, 3a and 3, for 90% volume ratio. The error bars for the simulated models represent the statistical relative errors for each calculated flux. **Right:** Model 3: Transition from the “layer” model 3a to “channel” model 3b, realized by flattening or stretching the inner cube. The parameters of the cell are given in the Table 3.12 [Dyrnjaja, 2015].

The diagram in figure 3.12.3 shows the relative error of the transmission ΔT .

The calculated errors for: $T_{sim(model3a)}$, $T_{sim(model3b)}$, T_{exp} , T_{fit} , and $T_{sim(model3)}$ were estimated by means of the square-root-sum error propagation approach.

$$\left(\frac{\delta T}{T}\right)^2 = \left(\frac{\delta T_{sim3a}}{T_{sim3a}}\right)^2 + \left(\frac{\delta T_{sim3}}{T_{sim3}}\right)^2 \quad (3.12)$$

The uncertainties for the experimental data increase with sample thickness, but still one can see that model 3 fits the experimental data (red points, figure 3.12.2) and lies within the confidence interval of the experimental data fit (black line, figure 3.12.2).

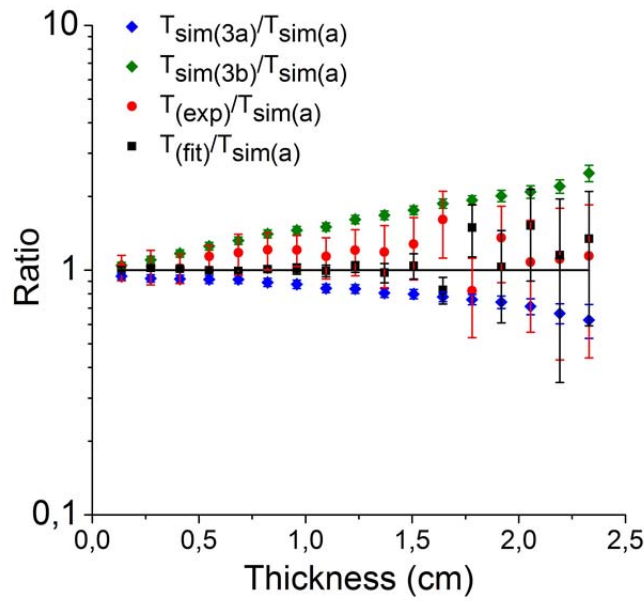


Figure 3.12.3 Ratio between $T_{sim(model3a)} / T_{sim(model3)}$, $T_{sim(model3b)} / T_{sim(model3)}$, $T_{exp} / T_{sim(model3)}$, $T_{fit} / T_{sim(model3)}$ for model 3, 3a, 3b and experimental data [Dyrnjaja, 2015].

3.13 Rescaling Effect

The question arises, if a rescaling of the cell structure or better to say the size of the cell structure affects the neutron transmission. From equation (3.6.2) one would expect no influence, because δN is not restricted to microscopic scales or parameters. For each model we have calculated the neutron transmission through sample plate for all simulated cells, rescaling the whole cell from (increasing the parameters of the outer and the inner cube respectively, keeping the volume ratio constant: $Vol_{B-steel} / Vol_{steel} = const$) $\sim 20\mu\text{m}$, $\sim 30\mu\text{m}$, $\sim 50\mu\text{m}$, $\sim 100\mu\text{m}$, to $200\mu\text{m}$, increasing the size (see figures 3.13.1, 3.13.2 and 3.13.3).

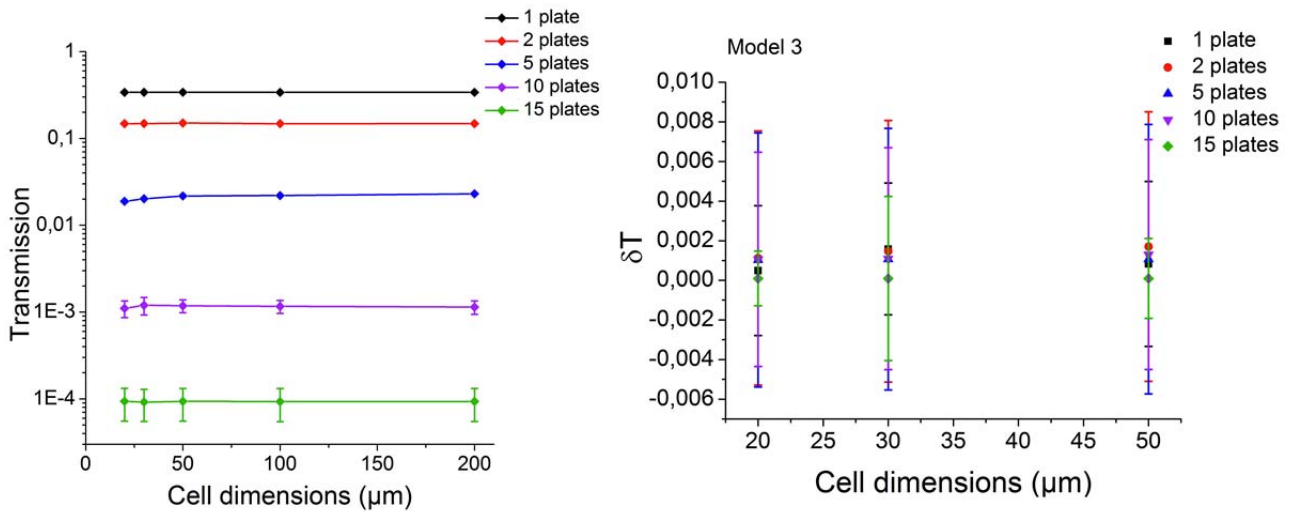


Figure 3.13.1 *Left:* The dimensions of the cell (coaxial cubes) have been increased in several steps by maintaining the relative cell structure constant referring to model 3. **Right:** The rescaling of the cell structure yields no significant effect on transmission. For each plate we have calculated ΔT for the transmission value $T_{20\mu\text{m}}$,

$T_{30\mu\text{m}}$, $T_{50\mu\text{m}}$ applying the formula $\Delta T = \frac{T_i - T_j}{T_i}$ where T_i for example correspond to $T_{20\mu\text{m}}$; T_j correspond to

$T_{30\mu\text{m}}$ [Dyrnjaja, 2015].

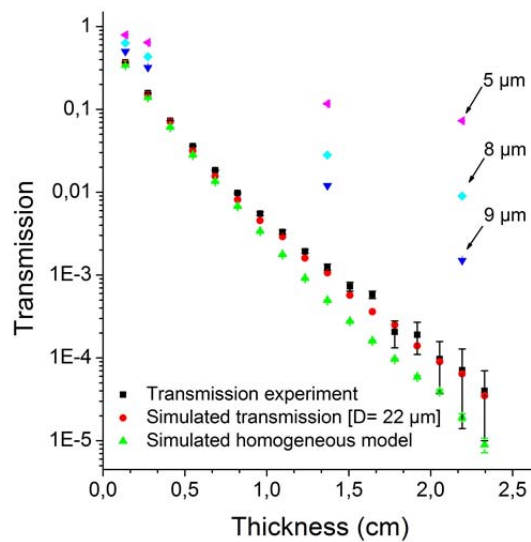


Figure 3.13.2 *A slightly enhanced transmission was observed with 100 μm thick scintillation layer. Neutron transmission in strong absorbing steels with $\Sigma = 7.3 \text{ cm}^{-1}$ macroscopic attenuation cross section compared with different MCNPX models. By increasing the boron spheres (model 1; $R =$ average grain radius in μm) one approaches the homogeneous model, contrary, by reducing the sphere radius the transmission is enhanced [Zawisky, Dyrnjaja, 2010].*

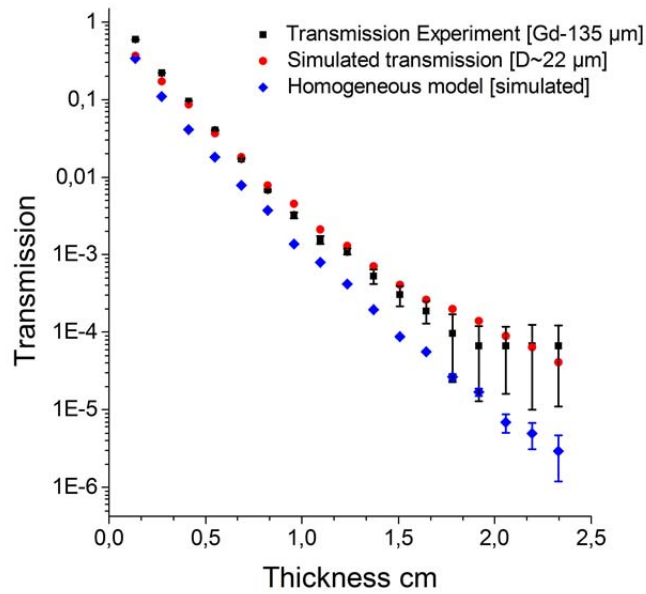


Figure 3.13.3 A slightly enhanced transmission was observed with imaging plate neutron detector due to micro-inhomogeneities of the boron distribution in the steel (model 1) [Zawisky, Dyrnjaja 2008].

3.14 Isotopic Ratio Diagrams

The natural abundance of ^{10}B is 20 wt% and of ^{11}B is 80 wt%. Referring to figure 3.7.2, boron enriched with B^{10} considerably increases the neutron absorption even in heterogeneous models. For systematic analysis increasing the ^{10}B fraction changed the isotopic ratio. The simulations yield a sensitivity of approximately $\Delta(^{10}\text{B}) \approx 1\text{wt}\%$ but reducing the statistical errors in the data and simulations as well can further increase this resolution. As shown in figure 3.14.1 the neutron transmission is very sensitive to the volume ratio as well.

Figure 3.14.2 compares the two effects; the influence of the volume ratio of ^{10}B in steel and the isotopic ratio $^{10}\text{B}/^{11}\text{B}$. In thin steel boron steel ($d = 0.137\text{ cm}$) the sensitivities are similar. But the thicker the material and the stronger the absorption, the more the neutron transmission is dominated by the absorber structure, expressed by the volume ratio.

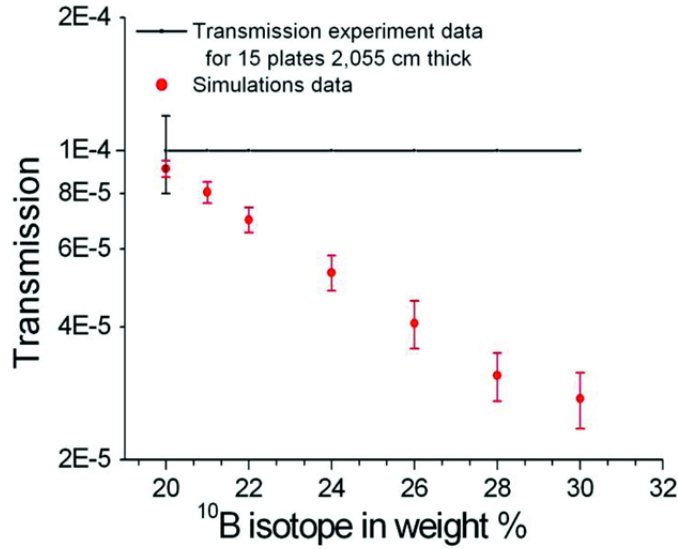


Figure 3.14.1 Influence of the volume ratio and the isotopic B^{10}/B^{11} ratio for a 2.055 cm thick absorber. (For a systematic analysis the isotopic ratio was changed by increasing the B^{10} fraction in steps of 1 wt% of).

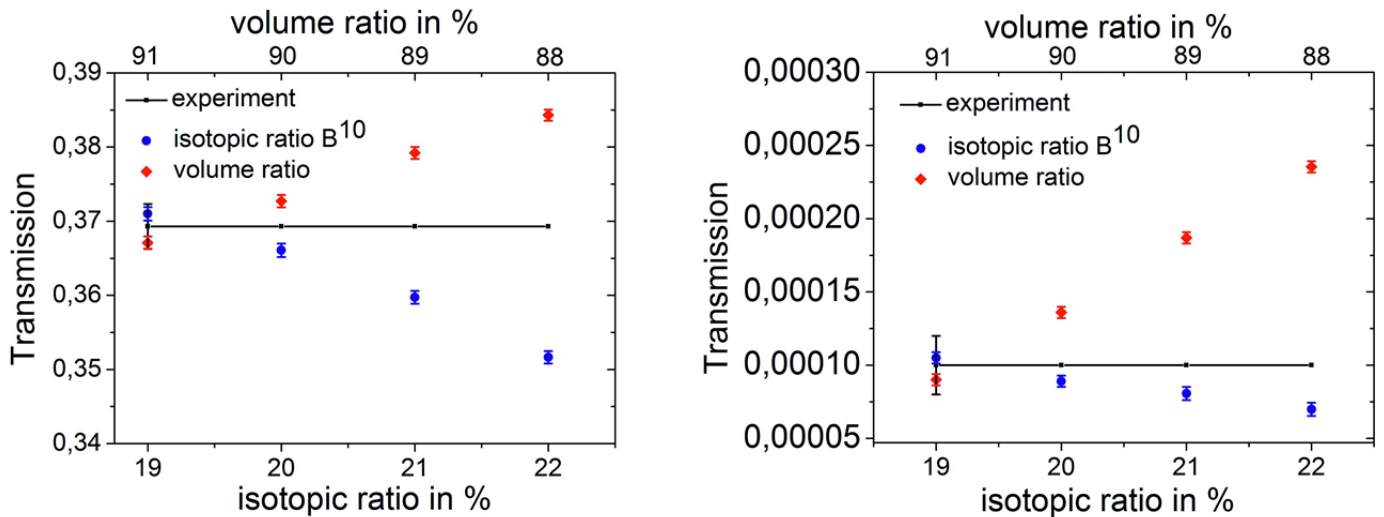


Figure 3.14.2 **Left:** Sensitivities for a thin 0.137 cm boron steel sheet (1 plate). **Right:** Influence of the volume ratio and the isotopic $^{10}\text{B}/^{11}\text{B}$ ratio for a 2.055 cm thick absorber (15 plates).

3.15 Simulated Neutron Scattering inside the Sample

MCNPX also allows an estimation of multiple scattering inside the sample. In thick and strong absorbing materials the probability for multiple scattering becomes large, because more absorption and scattering events occur [Hassanein, 2006], [Sears, 1989]. All elements present in steel (Fe, C, Si, Mn, S, Cr, Mo, Ni) have a small scattering total macroscopic cross section of $\Sigma_{steel} = 1.16 \text{ cm}^{-1}$ referring to table 3.7a

(neutron scattering cross sections are very small for these elements referring to all ENDF data libraries) [Sears, 1975].

Considering the (simulated) inner structure, with boron free channels or closing the channels we can estimate the scattering effect inside the sample. The simulated neutron flux reaches the sample and the neutrons scattered by the sample are distributed on the detector. Figure 3.15.1 represents the neutron flux, which arrives to the detector versus scattering events (the number of neutrons scattered several times).

In thick samples like in a boron alloyed steel with thickness $d = 2.055 \text{ cm}$ from the homogeneous model the multiple scattering events have a smaller probability to happen and more absorption events occur as compared with the inhomogeneous model 3a; (blue and green line in figure 3.15.1, right). Referring to the model 3b (channel model, figure 3.12.2, right) the probability for multiple scattering becomes large, absorption decreases due to the free boron channels in the model. Neutrons passing through a steel volume have a higher probability for multiple scattering (purple line in figure 3.15.1).

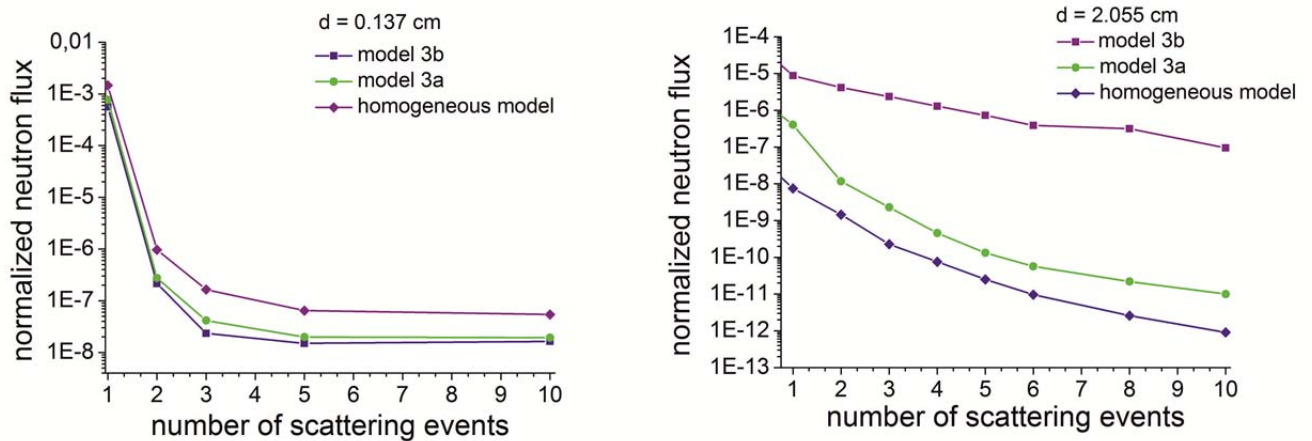


Figure 3.15.1 *Left: Multiple scattering effects for a single plate (0.137 cm thick). Right: Multiple scattering effects in a thick absorber (15 plates, 2.055 cm thick). Multiple scattering is increasingly suppressed when approaching the homogeneous case.*

3.16 The Background Estimation

Boron Polyethylene Transmission Experiments with ^6Li Detector

The best correction of the neutron scattering at the surroundings of the sample is to avoid it [Hassanein, 2006]. This is achieved by putting an additional boron polyethylene mask 10 mm thick with an aperture $1 \times 1 \text{ cm}^2$ between sample and detector (see figure 3.16.1) The smaller the aperture the less neutron contribution and the thicker the boron polyethylene plate the less neutrons contribute to the scattering background. This contribution is measured by transmission of 10 boron polyethylene plates, (the first plate

has 2.5 mm thickness, the second plate has 5 mm thickness, the third plate has 7.5 mm thickness) each plate with 20% boron content, 5 mm thick. These experiments were carried out at NR station II. The neutron spectra can be well described by a Maxwellian distribution. From the beam line profile we extract intensity values, (from images done with scintillator detector) therefore we are trying to extract the signal from the noise.

The lowest experiment transmission value for these plates is only about $2 \cdot 10^{-5}$ including the scattered neutrons. This value is in the order of the detection limit of the 16-bit scintillator detector. Ideally the boron polyethylene plates have the same size and shape as the boron steel plate's samples (see figure 3.16.2). We measured flat transmission behaviour of different borolene stacks, (figure 3.16.1). The uncertainty in the experimental data is, due to the strong absorption in boron polyethylene, reaching the background level. The transmission through boron polyethylene plates shows that borolene behave completely differently, while some transmission through boron steel is possible; the steel material still enables some neutron penetration through steel channels created.

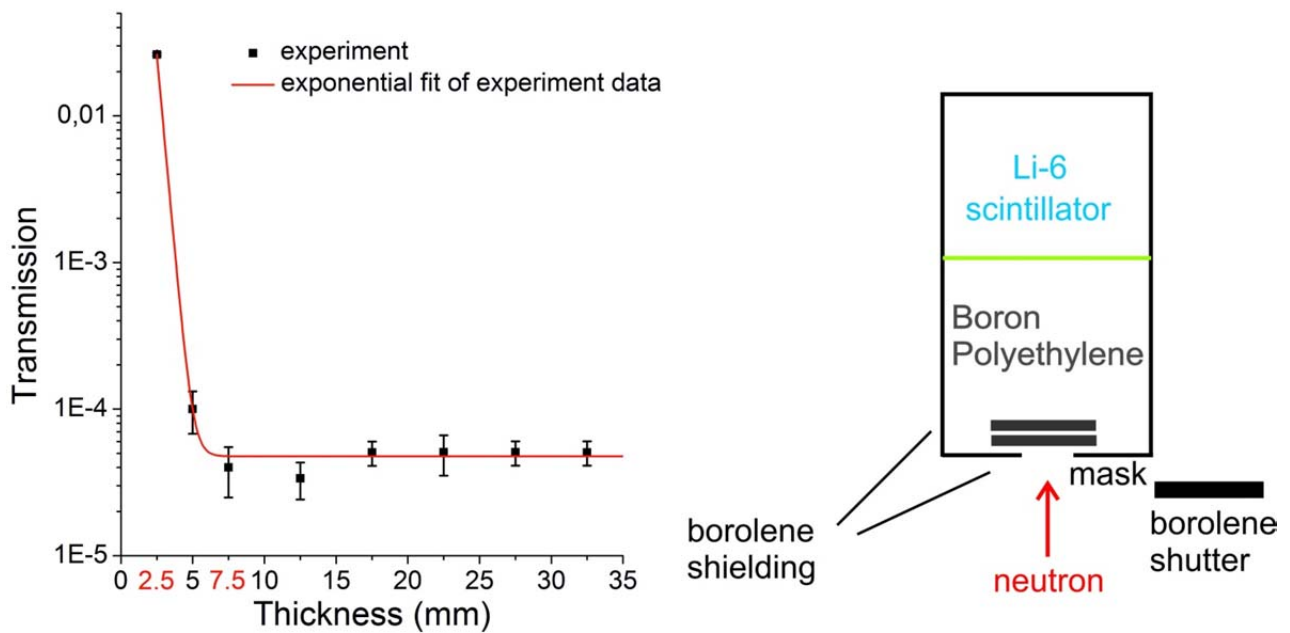


Figure 3.16.1 **Left:** Transmission measurements through boron polyethylene (borolene) plates. The first point represents a transmission through the first plate with 0.25 cm thickness, the second point represent transmission through 2 plates with 0.5 cm thickness; **Right:** The illustration of the boron polyethylene shielding during boron polyethylene transmission plates experiment.

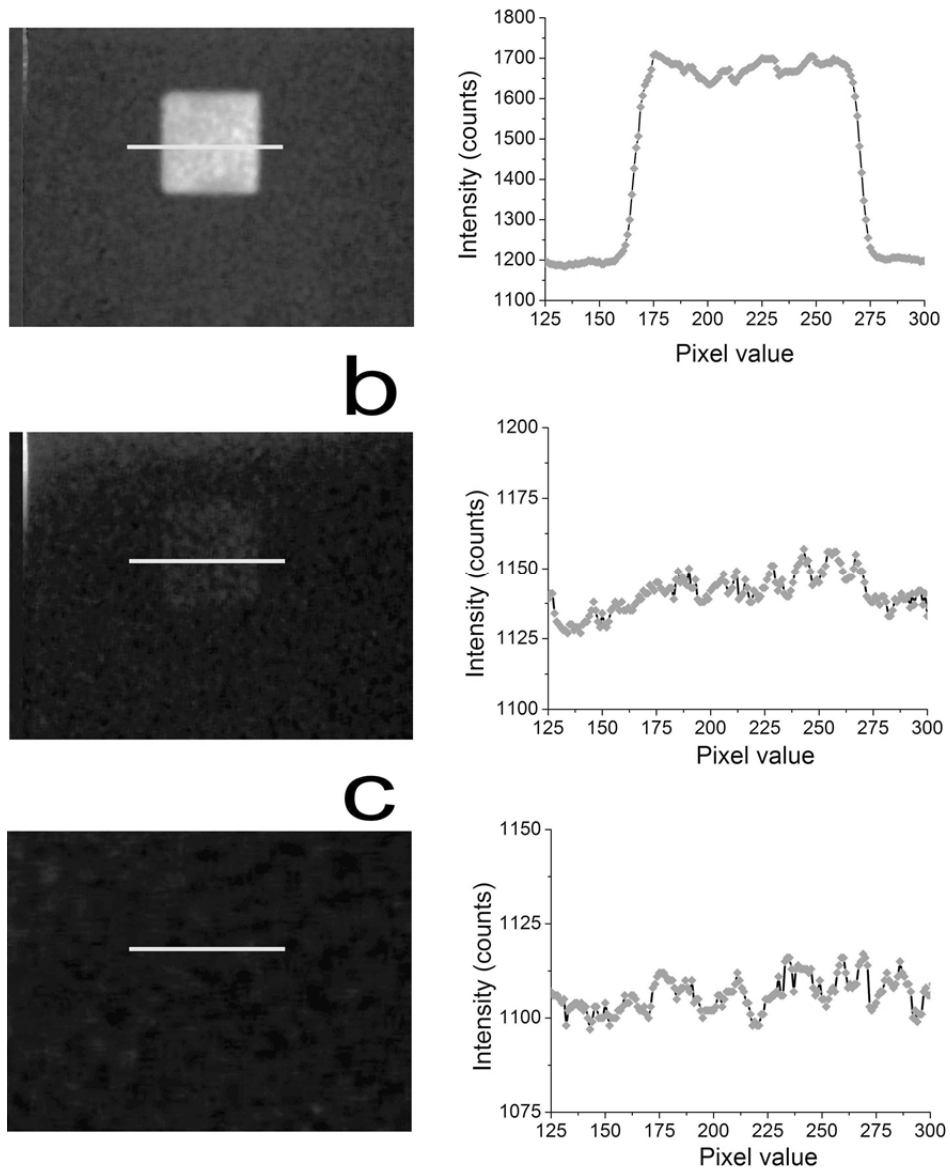


Figure 3.16.2 The radiography image of the boron polyethylene plates with boron polyethylene $1 \times 1 \text{ cm}^2$ mask placed in the front of the sample: **a)** Radiograph of boron polyethylene 2.5 mm thick plate (1 plate). **b)** Radiography of boron polyethylene 5 mm thick plate (2 plates). **c)** Radiograph image of boron polyethylene 12.5 mm thick plate (3 plates) where the contrast is not large enough to overcome the image noise. Contrast is enhanced only for presentation.

3.17 Summary

Thick and strong absorbing boron steel alloy plates have been investigated at the ATI neutron radiography facility. It was evaluated how integral transmission measurements, assisted by Monte Carlo simulations, and is able to detect micro-inhomogeneities independent of the spatial detector resolution. The

slightly enhanced neutron transmission of thick boron-alloyed steels revealed a micro heterogeneity of the ferro-borides. The MCNPX simulations further show that the neutron transmission do not depend on the absolute scale of the absorber fluctuations; only the volume ratio and the existence of absorber-free channels affect the transmission. Hence, such microstructures become detectable far below the detectors' imaging resolution. It is shown that microstructure has an influence for the transmission analysis and these models are needed for accurate prediction of the transmission. Boron steel plates (with 1.88 wt% of boron content) with a maximum thickness of 2.3 cm can be examined, for greater thicknesses the background fluctuations will not permit qualitative nor quantitative statements. For this working range recommendations for the boron-steel production and material specifications can be provided. We have shown that corrections to the transmission data are recommended in the transmission range specified in Table 3.17.

<i>Transmission</i>	$T_{effective}/T_{homogeneous}$	$d_{effective}$ (cm)	$d_{homogenous}$ (cm)
0.1	1.09	0.34	0.30
0.01	1.36	0.82	0.68
10^{-3}	2.5	1.42	1.14
10^{-4}	3.4	2.02	1.65

Table 3.17 Derived transmission corrections for boron alloyed steels (1.88 wt % boron content). $T_{effective}$ is the expected (experimental) transmission enhanced by the microstructure of this material. $T_{homogeneous}$ denotes the ideal transmission of a perfectly homogeneous material with the same boron content while; $d_{effective}$ is the recommended thickness in order to achieve the transmission T [Dyrnjaja, 2015].

Chapter 4 Hollow Glass Micro-spheres

Hydrogen is the most abundant element in the universe. Hydrogen can be produced in high amount from other energy sources and renewable energy. Hydrogen has some specific characteristics for examples hydrogen can be converted into electric current producing energy like in the case of the fuel cell. Hydrogen is stored in the form of a gas using micro hollow spheres as hydrogen storage. This characteristic can be used in fuel cell application in proton exchange membrane to produce current inside the fuel cell. The amount of hydrogen inside the micro spheres depends on pressure before and after loading, temperature, shell's thickness and sphere's material. Using Neutron Radiography NR method we would be in able to quantify hydrogen filling the hollow micro spheres under different filling conditions.

4.1 Introduction

Glass microspheres are microscopic spheres of glass manufactured for a wide variety of uses in research, medicine, consumer goods and various industries [https://wiki/Glass_microsphere]. Glass microspheres are usually between 1 to 1000 micrometres in diameter, although the sizes can range from 100 nanometres to 5 millimetres in diameter (see figure 4.1). Hollow glass microspheres, sometimes termed micro balloons, or glass bubbles have diameters ranging from 10 to 300 micrometres.

Glass microspheres are made by heating tiny droplets of dissolved water glass in a process known as *ultrasonic spray pyrolysis*.

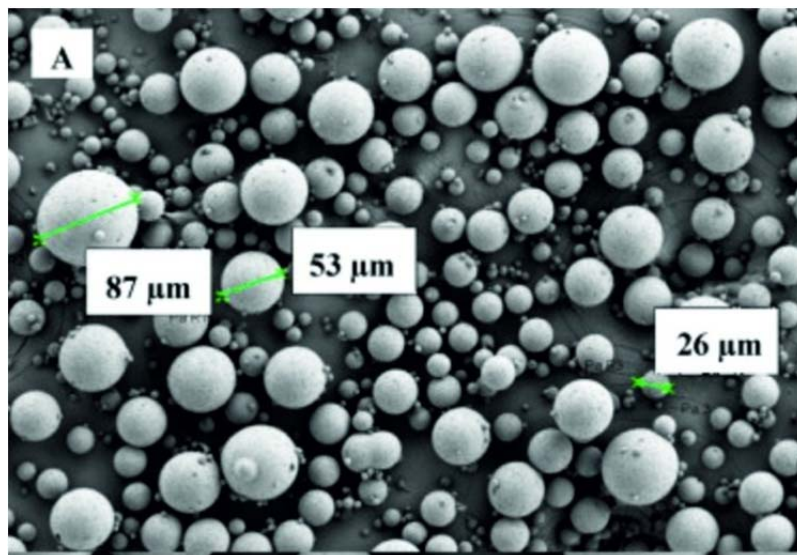


Figure 4.1 SEM image of the Hollow Glass Microspheres.

4.2 Hollow Glass Microspheres HGM

A hollow glass microsphere has a diameter in the range of 1 to 200 microns, a density between 0.2 to 0.60 g/cm³, a porous-wall structure having wall openings defining an average pore size of between 10 to 1000 angstroms. The spheres can be used as hydrogen storage material. The porous-wall structure facilitates the entrance of hydrogen as storage material into the interior of the hollow glass microsphere. Thereafter, a barrier coating may be applied and/or the microspheres are processed to alter or reduce the effective pore size. In this manner, the hollow glass microsphere can provide a membrane for the transport of hydrogen through the porous walls of the microsphere, the small pore size preventing gaseous or liquid contaminants from entering the interior of the hollow glass microsphere referring [Shelby, 2005], [Shelby, 2006].

4.3 Hydrogen Storage

Most research into hydrogen storage is focused on storing hydrogen as a lightweight, compact energy carrier for mobile applications [Shelby, 2006]. Liquid hydrogen or slush hydrogen may be used, as in the Space Shuttle. However, liquid hydrogen requires cryogenic storage and boils around 20.268 K (-252.882°C) [https://wiki/Glass_microsphere]. Hence, its liquefaction imposes a large energy loss (as energy is needed to cool it down to that temperature). The tanks must also be well insulated to prevent boil off. Insulation by design for liquid hydrogen tanks is adding costs for this method. Liquid hydrogen has less energy density *by volume* than hydrocarbon fuels such as gasoline by approximately a factor of 4. This highlights the density problem for pure hydrogen: there is actually about 64% more hydrogen in 1 liter of gasoline (116 grams hydrogen) than there is in 1 liter of pure liquid hydrogen (71 grams hydrogen). The carbon in the gasoline also contributes to the energy of combustion. Compressed hydrogen, in comparison, is quite different to store. Hydrogen gas has good energy density by weight, but poor energy density by volume versus hydrocarbons; hence it requires a larger tank to store. A large hydrogen tank will be heavier than the small hydrocarbon tank used to store the same amount of energy, all other factors remaining equal (figure 4.3.1, left). Increasing gas pressure would improve the energy density by volume, making for smaller, but not lighter container tanks (see hydrogen tank). Compressed hydrogen will require 2.1% of the energy content to power the compressor. Higher compression without energy recovery will mean more energy lost to the compression step.

Compressed hydrogen storage can exhibit very low permeation referring to [Shelby, 2005], [Shelby, 2006]. Figure 4.3.1 (left) represents the hydrogen stored in a bottle under 200 bar pressure and figure 4.3.1 (right) shows the hydrogen stored in micro glass hollow spheres under 40 bar pressure at Atominstitut. General data for Hollow Glass Microspheres (HGM) are given in the table 4.1.



Figure 4.3.1 *Left: Hydrogen stored in bottles under 200 bar pressure. Right: Hydrogen stored in HGM under 40 bar pressure.*

Diameter	10 – 200 μm
Wall thickness	1 – 10 % diameter
Density	0.2 to 0.6 g/cm^3
Compressive strength	200 to 30.000 psi
Composition	Soda lime silica, borosilicate, high silica etc.

Table 4.1 *Hollow Glass Microspheres (HGM) characteristics.*

4.4 HGM for Hydrogen Transport

Hydrogen is by far the most promising energy carrier of the future. Due to its usage in fuel cells, where the efficiency is very high and still increasing, and it's practically limitless availability on earth, hydrogen might be the most important energy carrier for alternative, renewable energy sources.

The concept of using hollow glass microspheres (HGM) as a hydrogen storage medium has been known for some time. Hollow glass microspheres can be used as a solid medium for the controlled storage and release of hydrogen. The spraying of a glass frit inside a flame is one of the commercial procedures to make HGMs.

Different chemical agents such as sulfur or urea must be added to the glass frit in order to cause the frit to blow outward and form the hollow spheres.

In 1981, Teitel, [Sherif, 2014] was the first person to propose the use of HGM's as hydrogen storage media [Rambach, 1995]. The characteristics of so-called super high-strength micro-balloons towards hydrogen storage and extraction in comparison to other known methods have also been investigated referring to [Lim, 2010].

However, one of the main concerns with regard to the use of HGM for hydrogen storage purposes is their strength. If the HGMs were made of engineered glass, which can be up to 50 times stronger than normal glasses, the amount of hydrogen capable of being stored in the microspheres can be increased remarkably. This would lead to an increase in the energy density per unit volume by over an order of magnitude resulting in the advancement of hydrogen energy technology and in the improvement of the hydrogen market as a renewable energy source via cheaper and safer hydrogen storage [Lim, 2010], [Nelson, 2013].

HGM can be utilized for controlled storage and release of hydrogen like is shown in figure 4.4.1. Hydrogen diffuses through the thin wall of the HGM at elevated temperatures and pressures. The gas is then trapped upon cooling to room temperature. The ability of HGM to safely store compressed hydrogen gas is a major advantage. However, a traditional limitation of HGM has been the poor thermal conductivity of a packed bed of HGM; poor conduction of heat translates to unsuitably low release rates of hydrogen gas [Shelby, 2005], [Sherif, 2014].

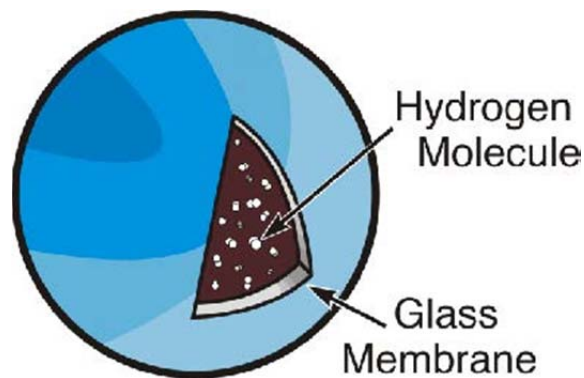


Figure 4.4.1 Hydrogen filled hollow microsphere [Shelby, 2005].

Advantages of HGM

- Cheap, plentiful raw materials
- Established technology
- Made from recycled glass
- Readily used for many cycles

- Light-weight
- High strength (high pressure)
- Safety
- Flow like liquids
- High separation ratio ($>10^6$)
- High H₂/volume
- Low mass/H₂ content

Modern Applications for Hydrogen-Filled HGM

- Hydrogen storage
- Hydrogen separation and purification
- Radiation shielding for manned space flight [Shelby, 2006]

4.5 Storage Capacity

These spheres, shown in figure 4.1 have diameters of 15 to 200 μm and membrane thicknesses of approximately 1 to 20 μm . At elevated temperatures of 150-400°C the glass exhibits an increased permeability to hydrogen, which permits the microspheres to be pressurized by immersion in high-pressure hydrogen for a certain period of time. The hydrogen diffuses through the microsphere membranes, equilibrating the internal and external pressures and filling the spheres. Once filled, cooling the spheres to room temperature reduces the permeability trapping the hydrogen within the spheres. After transport and storage at room temperature, the hydrogen is released from the microspheres by reheating the bed to increase the permeability. The empty microspheres can then be cycled and refilled.

The fill rate is a function of glass properties, permeating gas, temperature and pressure differential. As in any pressure vessel, the burst pressure of the container and an applied safety factor limits the storage capacity of a microsphere.

The burst pressure of the sphere P_b is given by [Rambach, 1995]:

$$P_b = 4\pi\sigma_{\max} \frac{\Delta r}{d_s} \quad (4.5.1)$$

Where σ_{\max} is the biaxial tensile (hoop) stress in the sphere membrane at failure Δr is the membrane thickness and d_s is the sphere outer diameter like shown in the figure 4.5.1.

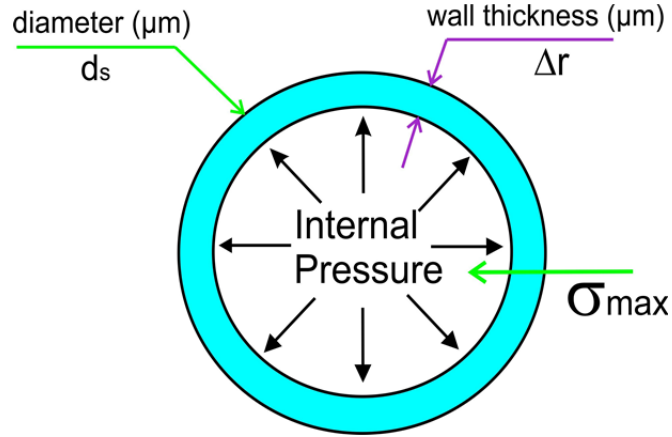


Figure 4.5.1 The geometry and dimensions of glass microsphere for hydrogen storage.

The energy needed to fill a bed of the microspheres is the sum of the energy used to pressurize the hydrogen to the filling pressure and the heat used to raise the bed temperature for a suitable increase in permeability. For glasses, the permeability K can be expressed as referring to [Rambach, 1995], [Sherif, 2014]:

$$K = K_0 T \exp\left(-\frac{\theta}{T}\right) \quad (4.5.2)$$

where T is the temperature of the glass and K_0 , and θ are constants that are functions of the mole percent of network modifiers (M) in the glass.

For a given pressure differential ΔP across the glass microsphere membrane, the internal pressure P_i at any time during the fill or release of hydrogen is:

$$P_i = P_{io} \pm \Delta P \left\{ 1 - \exp\left(-\frac{t}{\tau}\right) \right\} \quad (4.5.3)$$

where P_{io} , is the original internal pressure and t is time. The “+” sign applies to filling and the “-” sign applies to releasing. The term τ is the fill or release time constant (diffusion coefficient), which can be expressed as:

$$\tau = \frac{w \cdot d_s}{6KRT} \quad (4.5.4)$$

The diffusion parameter as a function of temperature T , width of the glass hull w , diameter of the sphere d_s , the permeability K , and R is the universal gas constant [Rambach, 1995].

4.6 Filling HGM with Hydrogen

Hydrogen diffuses through the glass wall and after reaching the desired pressure, the spheres are cooled down and diffusion stops (or is drastically reduced) [Rambach, 1995], [Sherif, 2014]. Although the

diffusion process through glass is well understood, measurements of diffusion rates are still difficult to handle. This is mainly due to the small size of the spheres and the required long-term stability of the measurement. In cooperation with FOTEC Company, we present a method for pressure and diffusion rate measurements at high accuracy and the potential for the spatial resolution of diffusion processes for hydrogen filled microspheres [Dyrnjaja, 2014]. The method is based on neutron radiography (NR) as described below.

For this experiment we used S38HS microspheres from company 3M™ with an average diameter of approximately 15 μm like (figure 4.6.1). The FOTEC Company is concentrating on different hydrogen storage technologies, especially on complex metal hydrides and the above-mentioned hollow glass microspheres. While for metal hydrides, storing of hydrogen is achieved by chemical bonding to the hydride (NaAlH_4 , LiBH_4 , etc.), hollow micro-spheres allow for gaseous storage of hydrogen (along with some other light elements). This is achieved by heating up the spheres within a hydrogen atmosphere at a constant pressure. Within a closed steel cylinder, constant hydrogen pressures (20, 25, 40 bar) were applied at a temperature of 190°C . The final pressure was measured using thermos-gravimetric analysis (TGA) [Bichler, 2013], [Schmid, 2012], [Nelson, 2013]. In order to achieve a high throughput of samples, we fixed the filling time to a maximum of 3 days. After that, the microspheres were cooled down to room temperature and brought to the reactor. Special aluminum sample holders were used in order to reduce scattering of neutrons within the sample holder.

Transmission of neutrons through the sample was measured over several days for different initial pressures at room temperature. Since S38HS microspheres show a non-negligible diffusion rate at room temperature for a reasonable time interval (several days), we were able to follow the exponential decrease of the neutron attenuation, which actually proves the feasibility of the NR method.

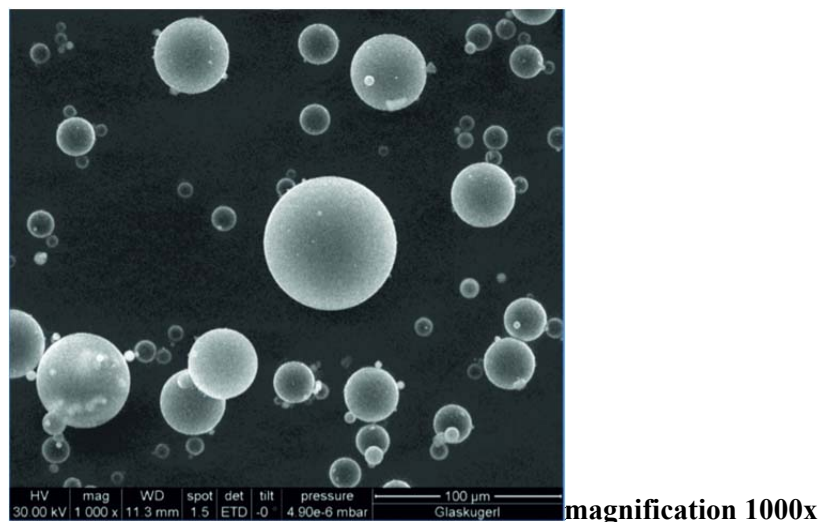


Figure 4.6.1 SEM image of S38HS Hydrogen filled microsphere [Schmid 2012].

4.7 The Neutron Radiography Method.

The application of neutron radiography for hydrogen studies has a long tradition at the Atominstitut. The transmission experiments were performed using a 100 μm thick ^6LiF scintillator layer with 150 μm spatial resolution. The detection process including a Maxwellian energy distribution of the thermal neutrons has been implemented in our MCNPX simulation program [Zawisky, 2008].

The hollow microspheres were filled with hydrogen gas at FOTEC Laboratory under different pressures 20, 25 and 40 bars. The high scattering cross-section of hydrogen yields high detection sensitivity by neutron radiography [Rauch, 1977], [Sears, 1983, 1992], [Lehmann, 2004], [Bacon, 1962]. Therefore the neutron attenuation is dominated by the hydrogen content in the sample while neutron absorption in glass is negligible. The neutron attenuation is characterized by the sample thickness d (in this case the thickness of the sample holder) and the total macroscopic cross section and can be approximated by an exponential law (T = transmission probability):

$$1 - T \cong 1 - e^{-\Sigma_{total} \cdot d} \quad (4.7.1)$$

It is convenient to use the total macroscopic cross section Σ :

$$\Sigma_{total} = N\sigma = \Sigma_s + \Sigma_a \quad (4.7.2)$$

(scattering + absorption) where N represents the number of nuclei per volume and d being the sample thickness; the scattering behavior of hydrogen as "free-gas" can be described by a simplified "pinball" model. The cross sections of hydrogen for thermal and cold neutrons are especially high in the low neutron energy range [Lehmann, 2004]. For hydrogen as a free gas, the cross section for the relevant energy range is taken from evaluated nuclear data file ENDF-VI extracted from MCNPX data libraries [MCNPX DATA, 2004].

In case of hollow microspheres, the macroscopic cross-section, is dominated by single and multiple scattering [Sears, 1989]. Multiple scattering occurs if the sample thickness d approaches the neutron's mean free path length [Lehmann, 2004], [Sears, 1989], [Smith, 2002], [Hassanein, 2005], [Grosse, 2006]:

$$L = \frac{1}{\Sigma_{total}} \quad (4.7.3)$$

where

$$\Sigma_{total} = \Sigma_H + \Sigma_{Glass} \quad (4.7.4)$$

From the measured Σ one derives a typical mean path length of $L = 18 \text{ cm}$ and $d/L = 0.05$ in the sample which indicates that multiple scattering is negligible. In a 10 cm sample-to-detector distance no scattering artefacts are detected, only a slight transmission enhancement of 0.1% at 1 cm sample distance.

4.7.1 Theoretical Considerations

The experimental transmission probability of neutrons is given by:

$$T_{\text{exp}} = \frac{I_s - I_b}{I_o - I_b} = e^{-\Sigma_{\text{total}} \cdot d} \quad (4.7.5)$$

I_s , I_b and I_o denote the intensity behind the sample, background intensity and open beam intensity respectively. All intensities are averaged in a selected area of interest (AOI). To quantify the hydrogen content in the micro spheres one has to measure the hydrogen loaded and the empty sample.

The density ρ_H can then be derived from:

$$T_H = \frac{I_{\text{filled}}}{I_{\text{empty}}} = e^{-\Sigma_H \cdot d} = e^{-\left(\frac{\rho_H \sigma_H N_A d}{M_H}\right)} \quad (4.7.6)$$

where N_A is Avogadro number; σ_H is neutron cross section of *hydrogen* as free gas (data are taken from ENDF-VI) [Lehmann, 2004], M_H is atomic weight of *hydrogen*, ρ_H is *hydrogen* density, d is thickness of the sample. From other side the statistical form of the ideal gas equation is:

$$pV = Nk_B T \quad (4.7.7)$$

p is the pressure, V is the volume, N is the number of molecules in 1 mol, k_B is the Boltzmann constant, T is the temperature.

From formula 4.7.2 where: $\Sigma_{\text{total}} = N\sigma$ where N is the number of atoms per volume:

$$N = \frac{\rho_H N_A}{M_H} \quad (4.7.8)$$

Therefore ρ becomes:
$$\rho_H = \frac{\Sigma M_H}{\sigma N_A} \quad (4.7.9)$$

Considering formula 4.7.9 ρ_H can be rewritten like:

$$\rho_H = \frac{\Sigma M_H}{\sigma_H N_A} = \frac{-\ln(T_H) M_H}{d N_A \sigma_H} \quad (4.7.10)$$

The density is directly coupled to the pressure inside the spheres (P is the pressure inside the spheres):

$$P = \frac{\rho_H}{M_H} k_B T \quad (4.7.11)$$

$$p_1 = N_1 k_B T \text{ where } N \text{ can be expressed: } N = \frac{\rho_H}{M_H}$$

by use of:

$$\frac{p_2}{p_1} = \frac{\rho_2}{\rho_1} \quad (4.7.12)$$

and using a reference density ρ_{ref} for hydrogen gas at 1 bar and 300K, equation (4.7.12) can be written as:

$$\frac{p}{\rho_{ref}} = \frac{\rho}{\rho_{ref}} \quad (4.7.13)$$

reference density ρ_{ref} for hydrogen gas at 1 bar and 300K is:

$$\rho_{ref} = \rho_{H \text{ ref}(1bar)} = 0.0832 \text{ kg} / \text{m}^3$$

Using equation (4.7.13), one directly derives the pressure by inserting the hydrogen density shown in figure 4.8.6 (right diagram). This yields a starting pressure on day 1 of approximately 24 bar for the red curve in figure 4.8.5 which is in good agreement with the applied pressure during the filling of the hydrogen (25 bar). According to equation (4.7.13) and figure 4.8.6 we derive an exponential decrease of

the pressure:

$$P(t) = P_o - \Delta P(1 - e^{-\frac{t}{\tau}}) \quad (4.7.14)$$

with P_o , $P(t)$ being the initial and actual pressure of the filled micro-spheres respectively, P_{ref} is the surrounding pressure (1 bar), ΔP is the pressure difference of $P(t)$ and P_{ref} , [Rambach, 1995].

Applying equation (4.7.13) and equation (4.7.14), one derives an average diffusion coefficient τ for both samples 20, 25 bars (see figure. 4.8.5) of 79 and 74 hours with a standard deviation of 15 and 17 hours respectively, therefore indicating τ as a pressure independent quantity. As would be expected from equation (4.5.4), τ is also expected to be a pressure independent quantity, which therefore is in good agreement with our measurements [Williams, 1922].

4.8 Experimental Data and Results

The radiography measurements were done at the Atomic Institute, using an exposure time of 120 seconds. The first microspheres with 25 bar and 40 bar pressure were investigated at room temperature using a 5.1 cm diameter aluminum can (cylindrical form), see figure 4.8.1. As a reference, empty microspheres were used. The transmission measurements were performed daily for a period of two weeks. As expected,

the hydrogen was released from the microspheres in the course of time like is shown in the diagrams in figure 4.8.2.

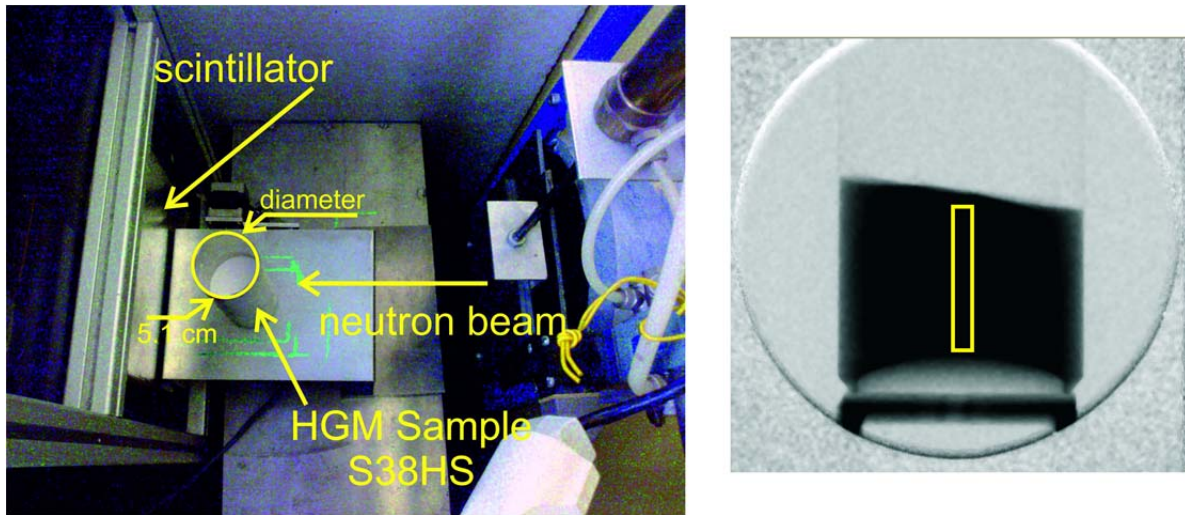


Figure 4.8.1 Left: Setup of the neutron transmission experiment. Right: Neutron radiography image of hydrogen at 40 bars and room temperature, according to Equation 4.7.5. The rectangular area shows an area of interest (AOI).

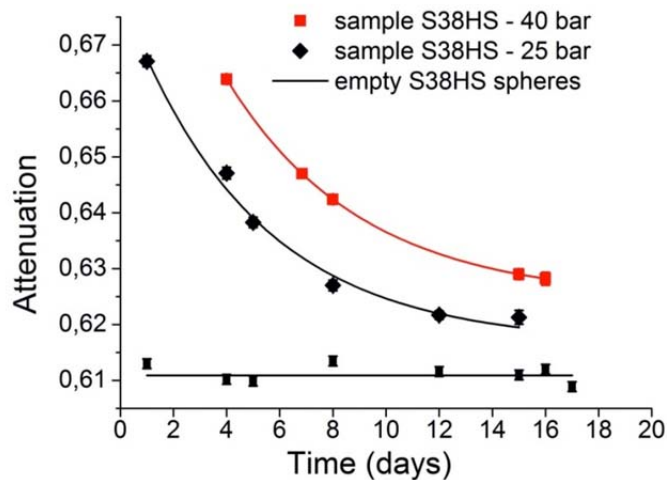


Figure 4.8.2 Neutron attenuation course of time for empty samples and for 25 and 40 bar applied pressure. The hydrogen content rises with the loading pressure [Dyrnjaja, 2014].

The aluminum can has a non-uniform thickness therefore the quantification of hydrogen was difficult and was not possible to have a large area of area of interest (AOI) during the radiography analysis. Thus the measurements were continued with spheres of 20 and 25 bar applied pressure filled into a rectangular aluminum holder $d = 1 \text{ cm}$ like shown in the figure 4.8.4.

Again a reference measurement with empty microspheres was performed (see figure 4.8.3). (The density resolution is $\rho = 0.00012 \text{ g/cm}^3$ for these measurements done with the scintillator).

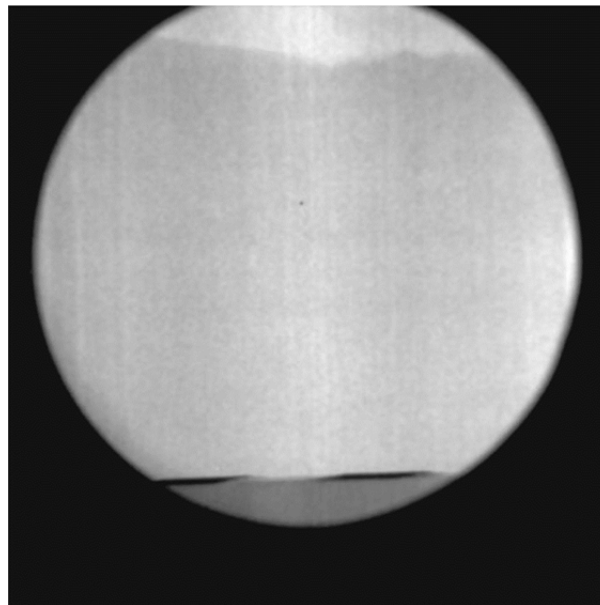


Figure 4.8.3 Image of the empty spheres inside a rectangular aluminum holder, 1cm thick. Contrast of the row image is enhanced only for presentation and doesn't affect the quantitative analysis.

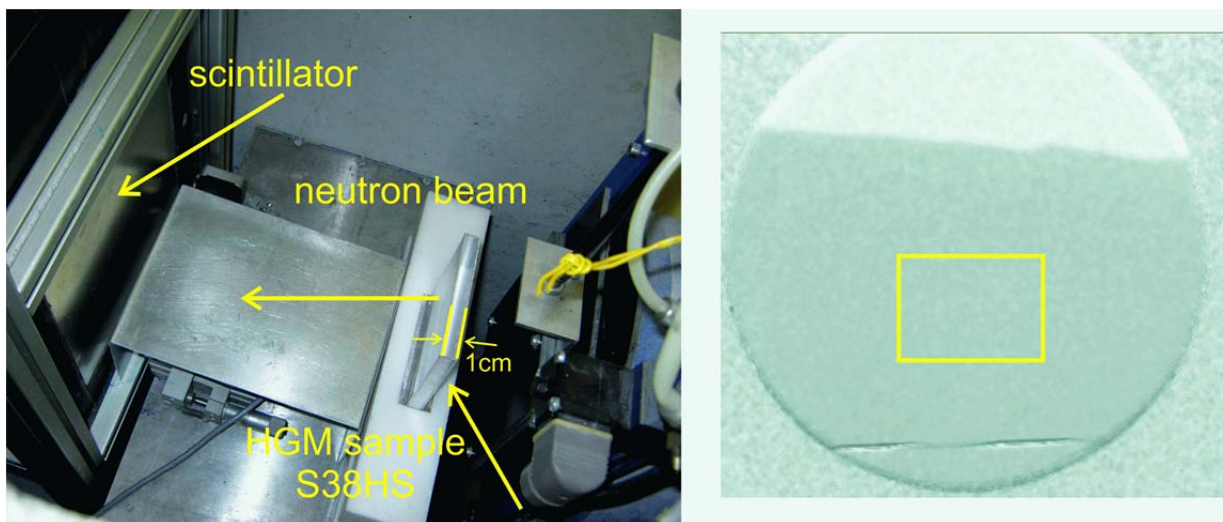


Figure 4.8.4 Left: Setup of the neutron transmission experiment. The distance between sample and detector is 10 cm, in order to avoid scattering artefacts. Right: Neutron radiography image of hydrogen at 20 bar and room temperature, according to equation 4.7.5. The rectangular area shows an area of interest (AOI) [Dyrnjaja, 2014].

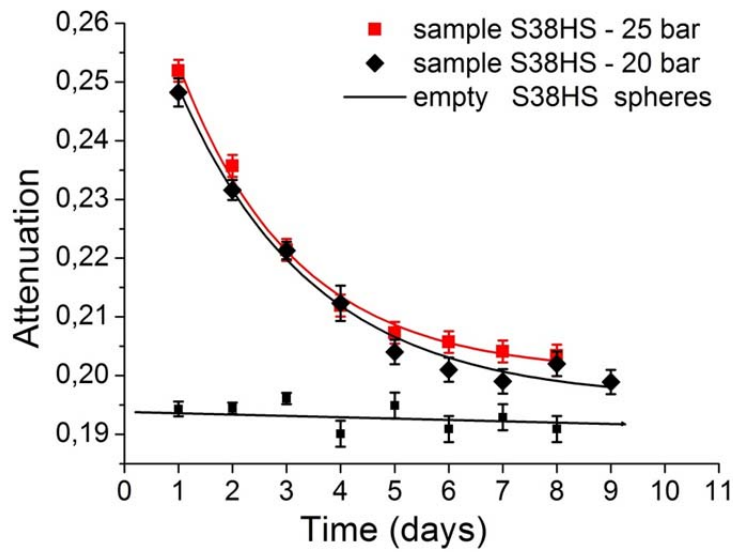


Figure 4.8.5 Neutron attenuation over course of time for empty spheres samples, 20 and 25 bar (applied pressure) spheres filled with hydrogen. The lines are least square fits to the experimental data. As expected, the hydrogen content rises with the loading pressure [Dyrnjaja, 2014].

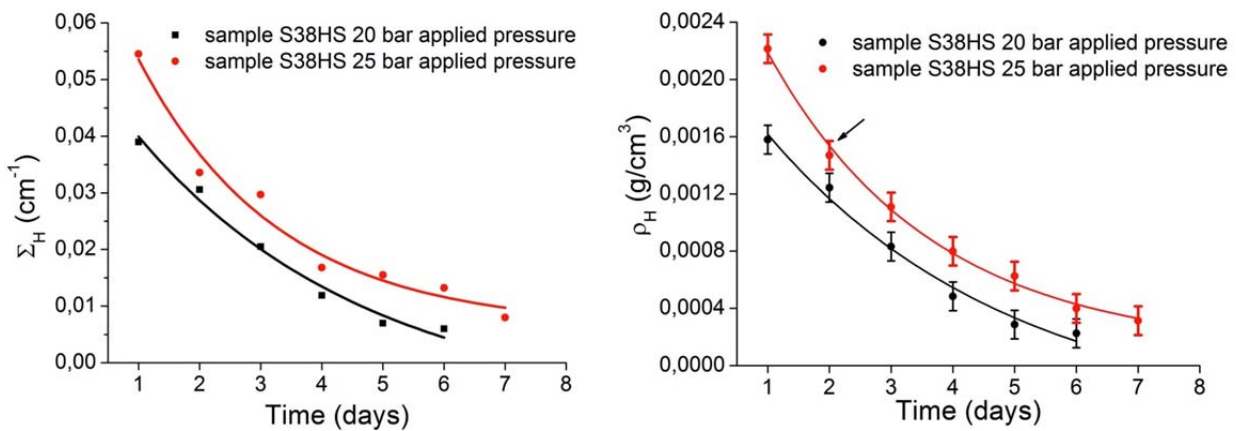


Figure 4.8.6 **Left:** Derived macroscopic cross sections and hydrogen densities ρ_H filling the spheres. **Right:** The lines are least square fits to the experimental data (the arrow indicates the data point relevant for comparison in figure 4.8.7) [Dyrnjaja, 2014].

We have also measured the neutron attenuation of a heated sample at 90°C as shown in figure 4.8.7. The diffusion coefficient rate value τ was calculated to 55 minutes (for heated sample). At 25 bars and room temperature the calculated density value is 0.00147 g/cm³ (the data point used is indicated by an arrow in

figure 4.8.6, right. One expects a density decrease of 0.00003 g/cm^3 after 60 minutes at room temperature (red dot in figure 4.8.7) which is one order of magnitude below the reported density change for the higher temperature case, where the hydrogen density decrease is 0.0006 g/cm^3 , when the sample is heated to 90°C as shown in figure 4.8.7 [Dyrnjaja, 2014].

One can see a strong enhancement of the diffusion rate, which, according to equation (4.5.4), is caused by a temperature dependent permeability of glass [Keding, 2009], [Keding, 2011], [Markovich, 2009]. In order to confirm this, measurements on different types of glass spheres, regarding their diameter and glass hull will be done in future experiments. Additionally, a systematic study of the temperature behavior could be very useful for the modeling of the diffusion of hydrogen through the spheres [Dyrnjaja, 2014].

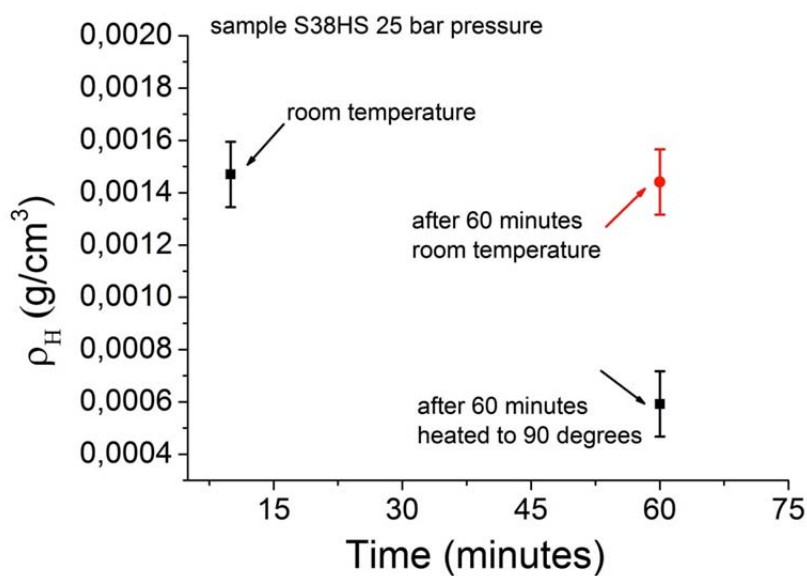


Figure 4.8.7 Hydrogen density inside the filled microspheres. We used microspheres filled at an initial pressure of 25 bar. The measurements were performed under constant temperature of 90°C for 1 hour interval [Dyrnjaja, 2014].

4.9 Summary

Neutron transmission measurements of hydrogen filled microspheres are the first step quantifying microspheres and their filling process. These data are necessary to optimize the complete system regarding storage pressure and long-term stability. The next steps are the optimization of the filling process and testing different types of microspheres. The outcome of this fundamental research can further be used to optimize hydrogen filled microspheres for energy related applications e.g. safety hydrogen storage system for fuel cells.

Chapter 5 Fuel Cell Radiography

Neutron imaging as a non-destructive method gives us the possibility to analyse the fuel cell during the operation. The source of the neutrons needed for the Neutron Radiography NR is a Triga Mark II reactor when the free neutrons are produced. Neutrons as particle are very sensitive to some materials, which contains hydrogen element like water. These properties make them very important since water visualization is very important for the good performance of a fuel cell device. The accumulations of the liquid water in proton exchange membrane PEM fuel during the operation limit their performance significantly.

5.1 Introduction

A fuel cell is an electrochemical device that combines hydrogen and oxygen to produce electricity, with water and heat as its by-product. The simplest form of a fuel cell consists of: an anode and a cathode with an electrolyte between them. At the anode, hydrogen reacts with a catalyst, creating a positively charged ion and a negatively charged electron. The proton then passes through the electrolyte, while the electron travels through a circuit, creating a current. At the cathode, oxygen reacts with the ion and electron, forming water and useful heat. This single cell generates about 0.7 volts, just about enough to power a single light bulb. When cells are stacked in series the output increases, resulting in fuel cells anywhere from several watts to multiple megawatts [https://en.wikipedia.org/wiki/Fuel_cell].

The first fuel cell was built in 1839. The first commercial use of fuel cells was in NASA space programs to generate power for probes, satellites and space capsules. Since then, fuel cells have been used in many other applications. The energy efficiency of a fuel cell is generally between 40-60%, if waste heat is captured for use [https://en.wikipedia.org/wiki/Fuel_cell].

5.1.1 Design of Fuel Cells

Fuel cells are made up of three adjacent segments: the anode, the electrolyte, and the cathode (figure 5.1.1). The most important basic parts in a fuel cell are [https://en.wikipedia.org/wiki/Fuel_cell]:

- The electrolyte substance usually defines the type of fuel cell
- The fuel that is used. The most common fuel is hydrogen.
- The anode catalyst, which breaks down the fuel into electrons and ions.
- The cathode catalyst, which turns the ions into the waste chemicals like water or carbon dioxide [https://en.wikipedia.org/wiki/Fuel_cell].

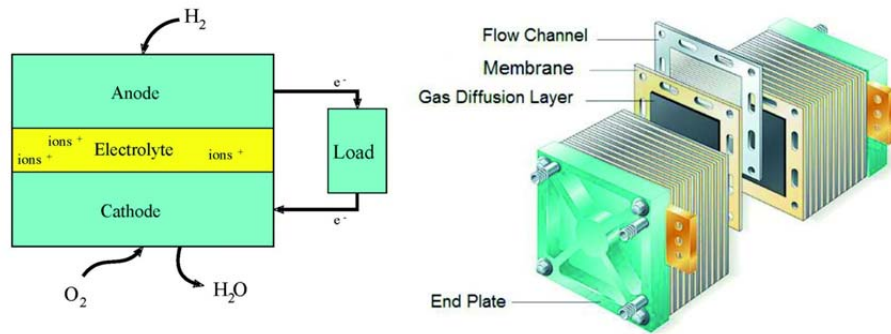


Figure 5.1.1 A diagram of a fuel cell [https://en.wikipedia.org/wiki/Fuel_cell].

5.1.2 Proton Exchange Membrane Fuel Cells

The proton exchange membrane fuel cell (PEMFC) is a proton-conducting polymer membrane, which separates the anode and cathode sides [https://en.wikipedia.org/wiki/Fuel_cell].

On the anode side, hydrogen diffuses to the anode catalyst where it later dissociates into protons and electrons. The protons are conducted through the membrane to the cathode, but the electrons are forced to travel in an external circuit (supplying power) because the membrane is electrically insulating. On the cathode catalyst, oxygen molecules react with the electrons (which have traveled through the external circuit) and protons to form water - the only waste product. In addition to this pure hydrogen type, there are hydrocarbon fuels for fuel cells, including diesel, methanol. The waste products with these types of fuel are carbon dioxide and water.

Anode: The electrode at which oxidation (a loss of electrons) takes place. For fuel cells and other galvanic cells, the anode is the negative terminal; for electrolytic cells (where electrolysis occurs), the anode is the positive terminal.

Cathode: The electrode at which reduction (a gain of electrons) occurs. For fuel cells and other galvanic cells, the cathode is the positive terminal; for electrolytic cells (where electrolysis occurs), the cathode is the negative terminal.

Membrane: The separating layer in a fuel cell that acts as electrolyte (an ion-exchanger) as well as a barrier film separating the gases in the anode and cathode compartments of the fuel cell.

Catalyst: A chemical substance that increases the rate of a reaction without being consumed; after the reaction, it can potentially be recovered from the reaction mixture and is chemically unchanged. The catalyst lowers the activation energy required, allowing the reaction to proceed more quickly or at a lower temperature.

In a fuel cell, the catalyst facilitates the reaction of oxygen and hydrogen. It is usually made of platinum powder very thinly coated onto carbon paper or cloth. The catalyst is rough and porous so the maximum

surface area of the platinum can be exposed to the hydrogen or oxygen. The platinum-coated side of the catalyst faces the membrane in the fuel cell.

Proton exchange membrane (PEM) fuel cells works with a polymer electrolyte. It has a form of a thin, permeable sheet. This membrane is small and light, and it works at low temperatures (about 80°C). In our experiments the PEM was heated at about 70°C. Figure 5.1.2 shows the principle how the fuel cell works.

The fuel for the PEMFC is hydrogen and the charge carrier is the hydrogen ion (proton). At the anode, the hydrogen molecule is split into hydrogen ions (protons) and electrons. The hydrogen ions permeate across the electrolyte to the cathode while the electrons flow through an external circuit and produce electric power. Oxygen, usually in the form of air, is supplied to the cathode and combines with the electrons and the hydrogen ions to produce water [https://en.wikipedia.org/wiki/Proton_exchange_membrane].

The reactions at the electrodes are as follows (see figures 5.1.3 and 5.1.4):

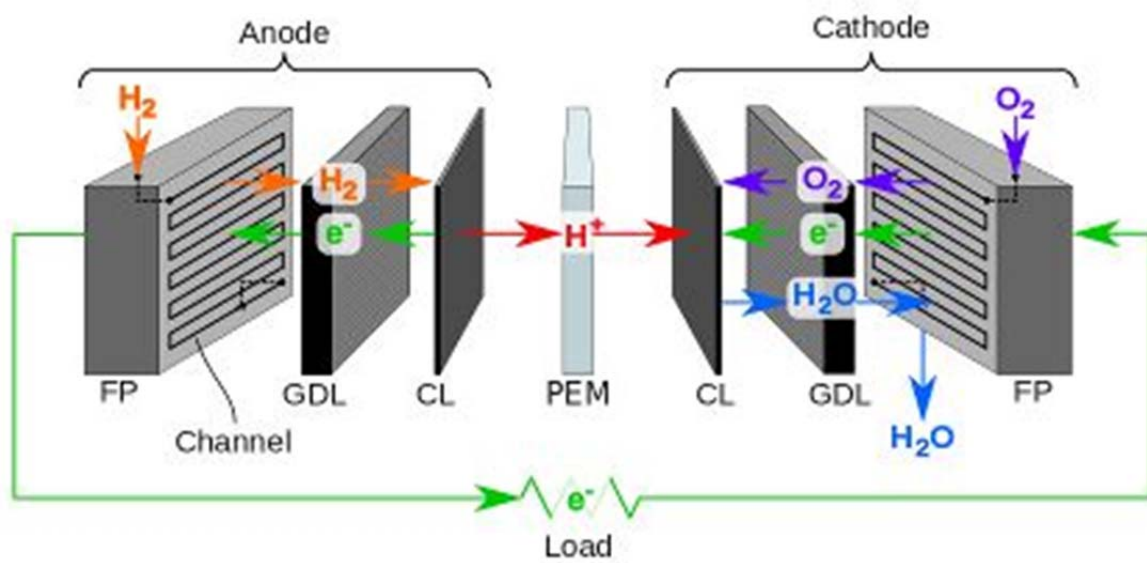
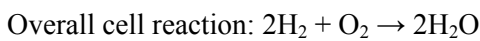
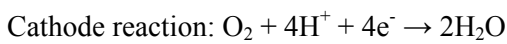
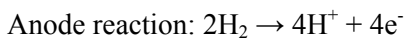


Figure 5.1.2 Layers and primary flows of a PEMFC, which are also the components of the fuel cell. Fluid enters and exits the cell through channels in the flow plates FP [Modelica, 2014].

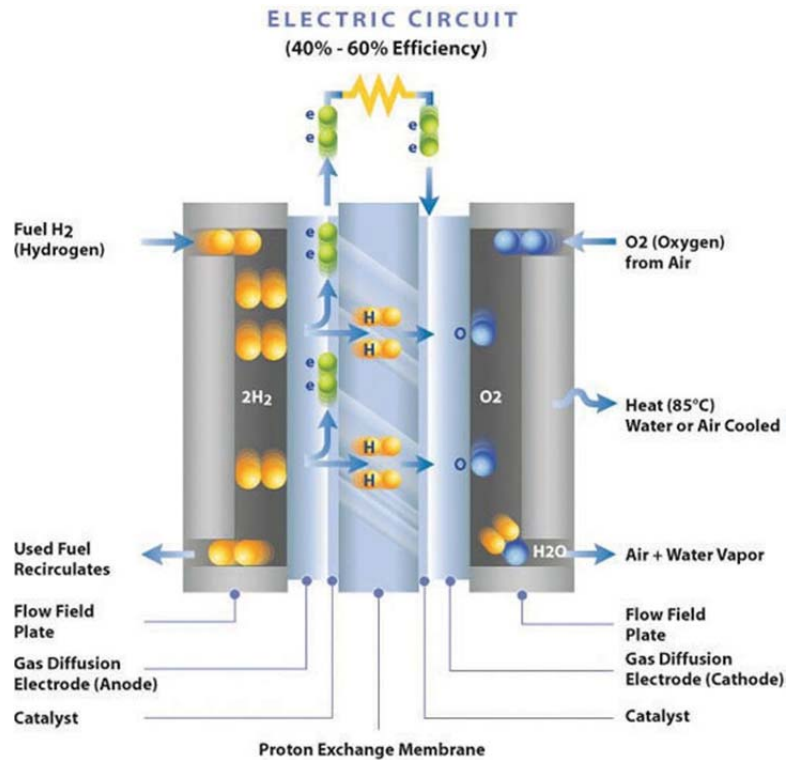


Figure 5.1.3 The structure of a PEM fuel cell. The catalyst at the anode facilitates the ionization of hydrogen, giving electrons to the external circuit. Protons are allowed to pass through a series of membranes to the cathode. The catalyst at the cathode facilitates the reaction of protons, oxygen atoms and electrons into water molecule [Bazylak, 2012].

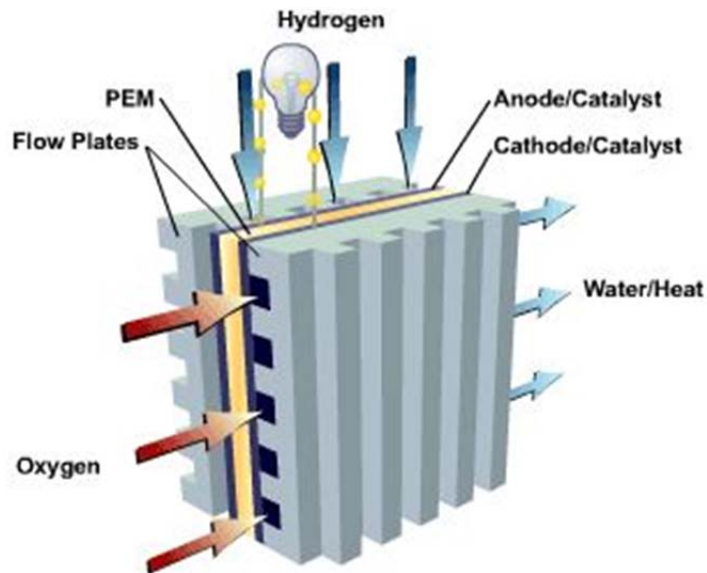


Figure 5.1.4 Schematic view of current production in fuel cell. The energy from the chemical reaction is converted directly into electricity [Bazylak, 2012].

5.1.3 Gas Diffusion Electrodes (GDE)

Referring to [bazylak.mie.utoronto.ca/research/] the gas diffusion electrodes (GDE) are electrodes with a conjunction of a solid, liquid and gaseous interface, and an electrical conducting catalyst supporting an electrochemical reaction between the liquid and the gaseous phase.

In the polymer electrolyte membrane fuel cell (PEMFC), it is crucial for the gas diffusion layer (GDL) to remain free of water in order to provide a pathway for gaseous fuel transport. The GDL is a porous material composed of a dense array of carbon fibers, which also provides an electrically conductive pathway for current collection (see figure 5.1.5). The GDL must also provide a pathway for excess water removal. Excess water commonly leads to flooding, where liquid water accumulates in the GDL and gas channels resulting in fuel starvation. Although the GDL is commonly made hydrophobic to enhance water removal, in practice, flooding is still a major cause of PEMFC performance degradation [bazylak.mie.utoronto.ca/research/].

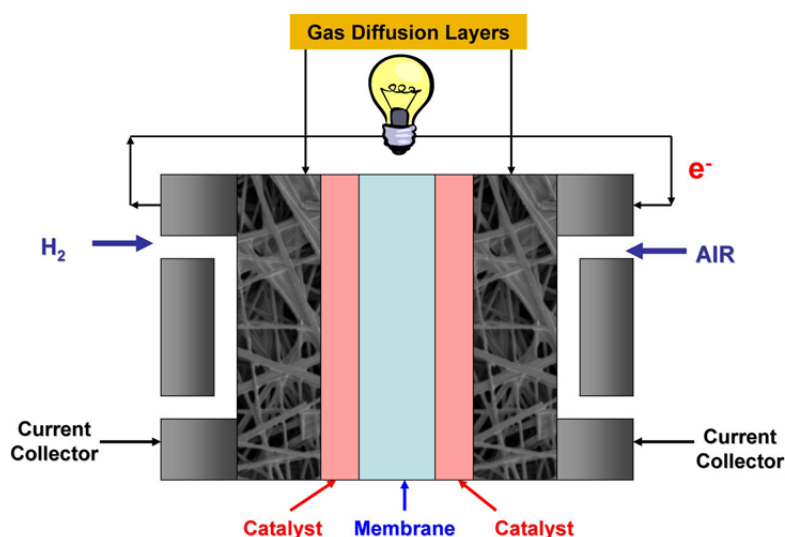


Figure 5.1.5 The gas diffusion layer (GDL) in the fuel cell [bazylak.mie.utoronto.ca/research/].

5.1.4 Theoretical Maximum Efficiency

The energy efficiency of a system or device that converts energy is measured by the ratio of the amount of useful energy put out by the system ("output energy") to the total amount of energy that is put in ("input energy") [https://en.wikipedia.org/wiki/Fuel_cell].

In the case of fuel cells, useful output energy is measured in electrical energy produced by the system. Input energy is the energy stored in the fuel. According to the U.S. Department of Energy, fuel cells are generally between 40-60% energy efficient.

This is higher than some other systems for energy generation. For example, the typical internal combustion engine of a car is about 25% energy efficient.

The maximum theoretical energy efficiency of a fuel cell is 83%, operating at low power density and using pure hydrogen and oxygen as reactants (assuming no heat recapture). According to the World Energy Council, this compares with a maximum theoretical efficiency of 58% for internal combustion engines. While these efficiencies are not approached in most real world applications, high temperature fuel cells (solid oxide fuel cells or molten carbonate fuel cells) can theoretically be combined with gas turbines to allow stationary fuel cells to come closer to the theoretical limit. A gas turbine would capture heat from the fuel cell and turn it into mechanical energy to increase the fuel cell's operational efficiency. This solution has been predicted to increase total efficiency to as much as 70% [https://en.wikipedia.org/wiki/Fuel_cell].

5.1.5 Basics and Motivation

The operating performance of a PEM fuel cell depends on a huge number of operating parameters:

Water balance (product water and humidification water)

- Temperature
- Load current
- Gas supply
- Type and condition (age, pinholes...) of MEA
- Type of gas diffusion layer GDL
- Channel design of flow field plates
- Force of which backing layers were pushed together

When current is drawn, water is produced on the cathode side of the fuel cell. A dry-out of the cell has to be avoided and a highly saturated membrane has to be guaranteed. On the other hand the accumulation of liquid water in PEM fuel cells during operation limits their performance significantly because of the access of reactant gases to the catalyst is retarded or avoided by water drops in the porous gas diffusion layer (GDL). Moreover, water blocks the channels in the flow field of the fuel cell and the cell is flooded. This effect leads to fuel starvation at higher power densities and accelerates the degradation by a variety of locally acting mechanisms. Improved water management can only achieve high power densities for fuel cell stacks in transport applications. A better understanding of the liquid water transport inside a fuel is expected to enhance the lifetime and performance of each cell.

However, most of the regions of PEM fuel cells in which liquid water transport occurs are inaccessible to in-

situ measurements. Computational methods are still limited by the lack of fundamental understanding of two-phase flow in porous media in particular when considering hydrophobic GDLs. So the balance between water productions and water removal has to be investigated for optimization [Hacker, 2010], [Strasser, 2010]. This is the aim of the present work.

5.2 Neutron Imaging System

NR (Neutron radiography) method provides a powerful and effective tool to visualize and quantify water transport inside the operating fuel cell. Although the fuel cell principle is has been known since many years, still researches are needed to make this technology competing and costs efficiency. In 1996, Mosdale reported the first use of neutron imaging to measure the water profile across the membrane in a PEM fuel cell [Mosdale, 1996]. Belows used neutron radiography to measure water transport profiles across a membrane in a working cell [Belows, 1999]. In 2004 Satija employed in-plane neutron imaging to an operating PEM fuel cell and produced a time series of images to evaluate the water management of a fuel cell system [Satija, 2004]. Hickner and co-workers investigated the water content in the PEM fuel cell as a function of current density and temperature [Hickner, 2006]. Recently Kim and Mench employed neutron imaging to visualize the phase-change-induced flow of liquid water in a PEM fuel cell [Kim, 2009], [Mench, 2003]. Li employed neutron imaging in the through plane to evaluate flow channels design [Li, 2007]. Chen employed neutron imaging to measure the liquid water content at four places in an operating PEM fuel cell [Chen, 2007]. Park employed neutron imaging to measure the water content in a PEM fuel cell with a single serpentine channel. Several authors have also employed neutron imaging to specially focus on measuring the liquid water distribution in GDL: [Okada, 1996], [Tüber, 2003], [Pasagullari, 2004], [Dong, 2005], [Litser, 2006], [Kumbur, 2006], [Weng, 2006], [Spernjak, 2007], [Chen, 2008], [Kim, 2008], [Park, 2008], [Zhang, 2004], [Arif, 2008]. Kramer as author employed neutron imaging to investigate the liquid water accumulation in a direct methanol fuel cell [Kramer, 2005]. The work published by Owejan and Trabold employed neutron imaging to a PEM fuel cell with an interdigitated flow field to investigate the accumulation of liquid water in the cathode [Owejan, 2006], [Trabold, 2006]. Author Turhan visualized water in the channels and GDL, and observed the tendency for water to accumulate under the land areas in a PEM fuel cell [Turhan, 2006]. Ludlow extended the use of neutron imaging from quantifying liquid water accumulation in the gas flow channels to isolating the water content in the MEA and membrane alone by analysing images before and after purging flooded gas channels [Ludlow, 2006]. Siegel employed neutron imaging over four continuous days PEM fuel cell testing as they explored the accumulation of liquid water in both the anode and cathode gas channels [Siegel, 2008]. Recently Turhan employed neutron imaging to a 50 cm² active area PEM fuel cell to investigate the effect of varying the channel size, landing size and land to channel ratio [Turhan, 2008]. Dong describes the results of a newly developed real-time technique for in situ

measurement of water vapor, nitrogen and oxygen distributions within the reactant flow channels of an operating PEMFC [Dong, 2005].

5.3 Water Visualization

For neutron transmission experiments usually thermal neutrons are used. The transmission experiments have been carried out at the Radiography Station NR II, using a 100 μm thin plate scintillator in combination with CCD camera.

According to [Zhang, 2004] the major obstacle that prevents a fuel cell from realizing its theoretical current density is most probable the accumulation of water produced inside the channels in the membrane electrode assembly (MEA), (figure 5.3.1). Therefore, the knowledge about the amount of liquid water inside the fuel cell is of great interest.

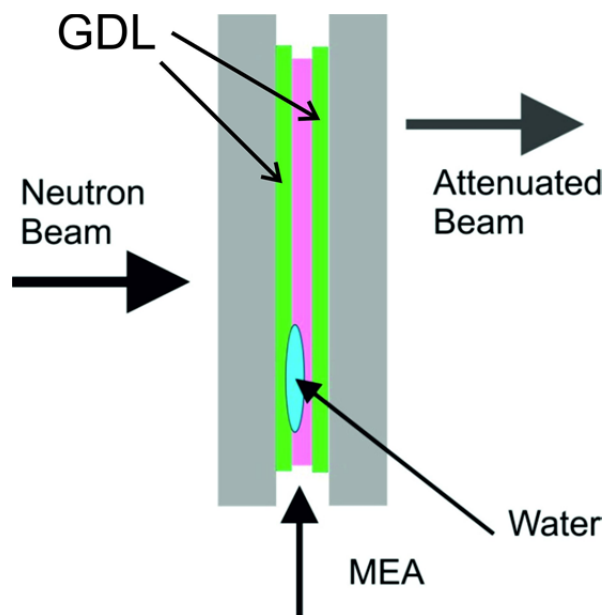


Figure 5.3.1 Schematic visualization principle of water creation inside the fuel cell.

In the middle of the fuel cell there are 3 layers: see figure 5.3.1 and figure 5.1.5.

The first layer is the gas diffusion layer, (GDL) which has a thickness of 330 μm . *The second layer*, which is in the middle, is the membrane electrode assembly MEA, (we use MEA 5620 from www.gore.com) which has a total thickness of 60 μm [Strasser, 2010].

The third layer is once more the gas diffusion (GDL) layer with a thickness 330 μm . All three layers together have a thickness of 720 μm .

The gas diffusions layers function is to dispense the gases (H_2 on the anode side and air on the cathode side). The MEAs function is to conduct the hydrogen H_2 ions from the anode side to the cathode side and to catalyze the chemical reaction: $2H_2 + O_2 \rightarrow 2H_2O$

The water content in the membrane varies with operating conditions. Here one of the most important operating parameters is the water balance. Liquid water comes into the fuel cell by humidification of the supplied gases. This has to be done, because the MEA has to be humid. Only with a humid membrane, the proton conductivity of the membrane works - (which is essential for the function of a PEMFC) - is warranted.

5.4 Image Normalization; Quantification Analysis

Neutrons are extremely sensitive to small amounts of water [Ludlow, 2006], [Kramer, 2005], [Lehmann, 2009]. It is convenient to normalized data images to a reference image (in our case using a dry fuel cell). In this way data are corrected for the presence of hydrogen containing structure of the MEA. Figure 5.4.1 represents an illustration of the quantification principle of transmitted neutron intensity. According to [Trabold, 2006] to isolate the water in the fuel cell, the “wet” images are normalized using a dry fuel cell image instead of the direct attenuated beam image.

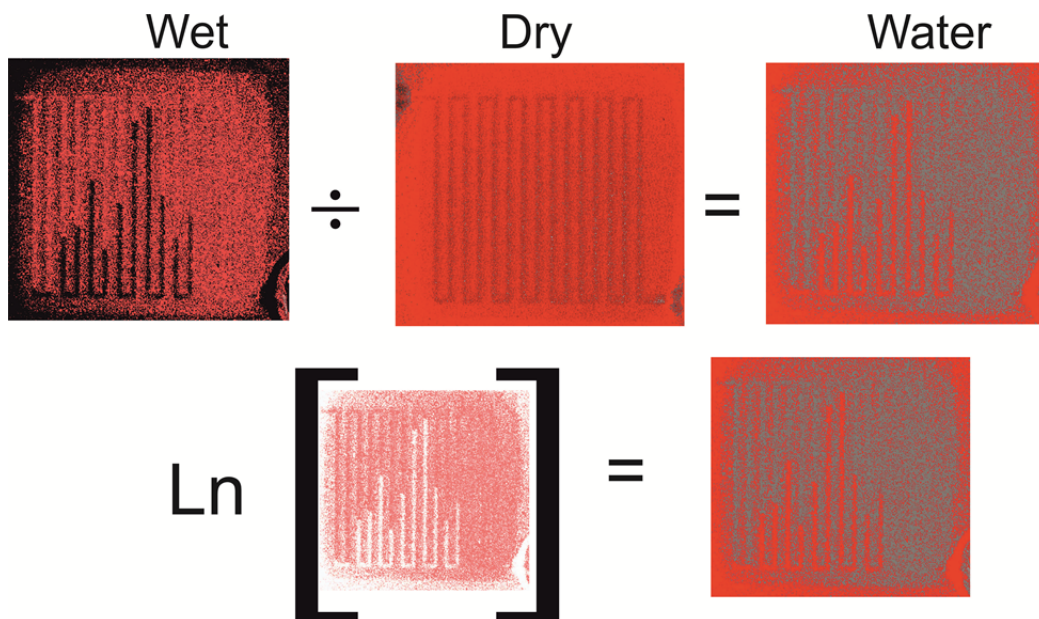


Figure 5.4.1 The image normalization using the dry image of the fuel cell. The values of the fuel cell humid membrane are divided pixel by pixel by the image value of the dry membrane leaving the “wet image”. Finally the negative natural log of each obtained pixel value (divided by the thickness of the membrane) yields the density of water distributed inside the membrane (these images were obtained using IP-ND at NR station II at Atominstitut). Dark red regions colour (low intensities) indicate liquid water, high intensities indicate dry regions.

In this case I_{dry} is the intensity of the dried sample at 70°C and I_{wet} describes the attenuation through fuel cell under humidified conditions. By dividing I_{wet} by I_{dry} we get the corrected normalized transmission through the fuel cell:

$$T_{water} \cong \frac{I_{wet}}{I_{dry}} = \exp(-\Sigma_{water} \cdot d) \quad (5.4.1)$$

where Σ_{water} is the macroscopic cross-section and d is membrane thickness. From Σ_{water} the absolute water density ρ_{water} in g/cm³ can be evaluated.

$$\Sigma_{water} = \frac{N_A \sigma}{A} \rho_{water} \quad (5.4.1a)$$

where A is the atomic weight, N_A is the Avogadro number, σ is the microscopic cross section in cm².

One has to normalize the intensities behind the wet sample to the dry sample in order to determine the transmission T:

$$T_{water} \cong \frac{I_{wet, 20^\circ C}}{I_{wet, 70^\circ C}} = \exp(-\Sigma_{water} \cdot d) \quad (5.4.2)$$

The density is calculated from the formula: $\rho_{water} \cong \frac{\Sigma_{water} A}{\sigma \cdot N_A}$ (5.4.3)

$$T_{water} \cong \frac{I_{wet}}{I_{dry}} = \exp(-\Sigma_{water} d) = \exp\left(-\frac{N_A \sigma}{A} \cdot \rho_{water} \cdot d\right) \quad (5.4.4)$$

$$\Delta\rho \geq \sqrt{\left(\frac{\delta I_{wet}}{I_{wet}}\right)^2 + \left(\frac{\delta I_{dry}}{I_{dry}}\right)^2} \cdot \frac{A}{N_A \sigma d} \quad (5.4.5)$$

5.5 Radiography Measurements with Scintillator

The first set of the transmission experiments had been performed with 100 μm scintillator's thick layer with 200 μm spatial resolution (and having a 10 x 15 cm² detection area) and with IP-ND (see detector characteristics in Chapter 2). The sample plates were exposed with 1.3 x 10⁵ n/(cm²s) neutron flux with a L/D ratio of 130. Figure 5.5.1 shows the components of the NR II station facility.

The fuel cell sample was placed as close as possible to the scintillator screen. To minimize the dark current the CCD camera was cooled to -130°C with liquid nitrogen. The cooling process was checked every 30 or 45 min. Exposure time was 500 seconds, and “no black removal” and “whole CCD camera” option with format 16 bit (dynamic range) was chosen for every image. The images were saved in the TIF-file format and

processed with Image-Pro Plus 6 (Media Cybernetics) software. (The measurements started usually at 10 a.m. and continued until the reactor regime was shut down (usually at 15.45 p.m.).

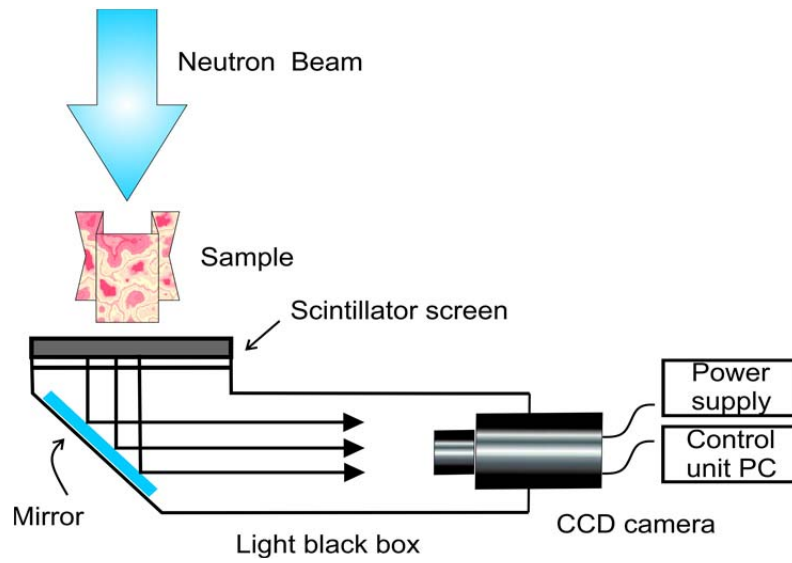


Figure 5.5.1 Schematic view of the scintillation process used for fuel cell in NR II station at ATI.

The stationary fuel cell is mounted in front of the neutron beam and resolution is maximized by placing the fuel cell as close as possible to the scintillator screen like is shown in the figure 5.5.2.

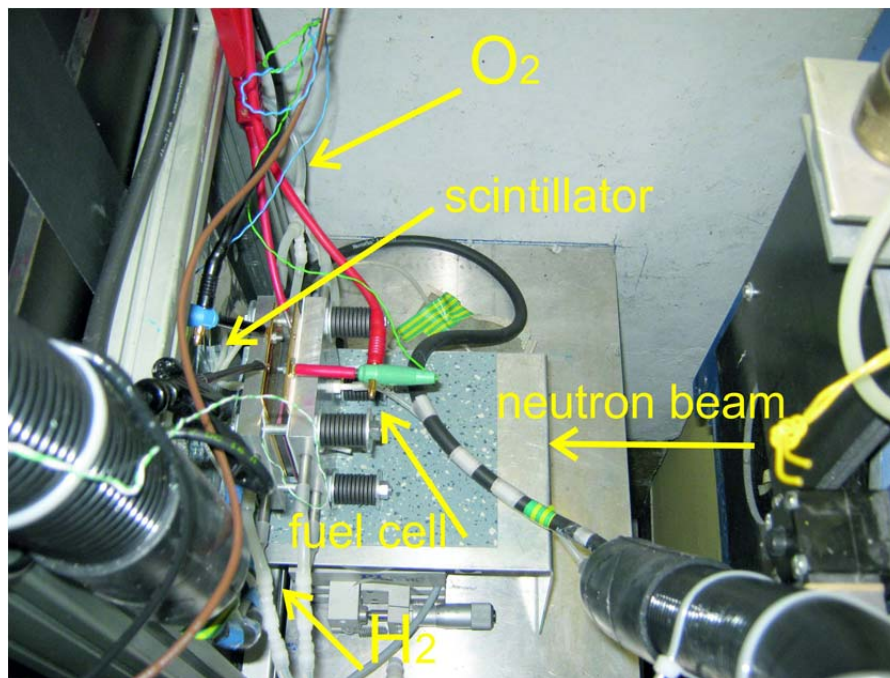


Figure 5.5.2 Setup of the neutron transmission experiment with ⁶Li (100 μm) scintillator at NR II station.



Figure 5.5.3 *View of the stationary fuel cell used in radiography measurements at NR II station.*

The PEM fuel cell is constructed (TU- Graz) with thick aluminum compression plates to the outermost ends of the assembly like is shown in figure 5.5.3. The anode and the cathode flow field channels are machined within an area of 10.2 cm^2 . Between the anode and the cathode flow fields are the membrane-electrode assemblies (MEA) and gas diffusion layers.

The fuel cell was controlled by a fuel-cell test station that was built near radiography station like is shown in figure 5.5.4. This fuel cell station provides accurate flows of hydrogen and oxygen as well as dry nitrogen. The cell was purged with dry nitrogen for 10-15 min to dry membrane. The gas passes through channels as shown in figure 5.5.4.

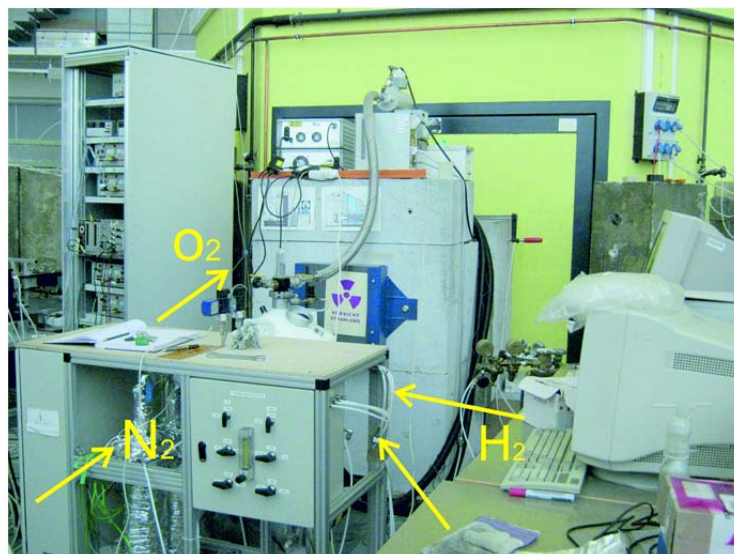


Figure 5.5.4 *The fuel cell test station set-up.*

5.6 Image Processing and Analysis - Results

The raw image in figure 5.6.1 represents the light intensity emitted from the scintillating screen. The sample image was rescaled. After applying a median filter and the correction, line profiles were chosen as shown in the figure 5.6.3 (see yellow lines). Line profiles were taken along the width of the MEA to extract intensity values. (In a line profile the X-axis represents the spatial scale and the Y-axis measures the intensity value). High relative humidity 30%-90% and operating temperatures around 70°C are preferred for stationary fuel cell. These parameters were adjusted to maintain proper cell hydration.

During operation the cell was supplied with humidified water at 70°C and applying different currents of 2 and 6 A. PEM fuel cell operating conditions include: humidity, cell temperature, operating current density.

First measurements were done with dried fuel cell and no current applied, at 70°C, (figure 5.6.2 left). A few images were made under these conditions.

After some images of the dried cell at 70°C the fuel cell was supplied with 30% humidity, (figure 5.6.2 right). Only with a humid membrane the proton conductivity inside the membrane is possible, which is essential for the function of a PEMFC. When current is applied, water is found or produced on the cathode side of the MEA via oxygen reaction and is transported through the GDL. The water then is removed from the cell by the gas flow and gravity [Trabold, 2006].

The more humidity and more current are applied more the water is created inside the channels of the PEM.

Figure 5.6.1 shows the raw image taken with ^6Li scintillator. Figure 5.6.2 shows the processed image of the fuel cell taken with a ^6Li scintillator, while figure 5.6.3 shows the processed neutron image of the inner membrane MEA of the fuel cell. The diagram in the figure 5.6.4 shows the intensity (in counts) histogram for the whole width of the membrane. Dry and wet regions are resolved in both detectors, but the better spatial resolution of the image plate allows a more precise density analysis. The different gray levels correspond to different amounts of water. The darker the gray level of the pixel, the more water is present. However, water is only slightly visible in the raw image with a very careful inspection. Color mapped images are only used, to enhance qualitative analysis and do not affect, quantitative analysis, therefore the images were colored.

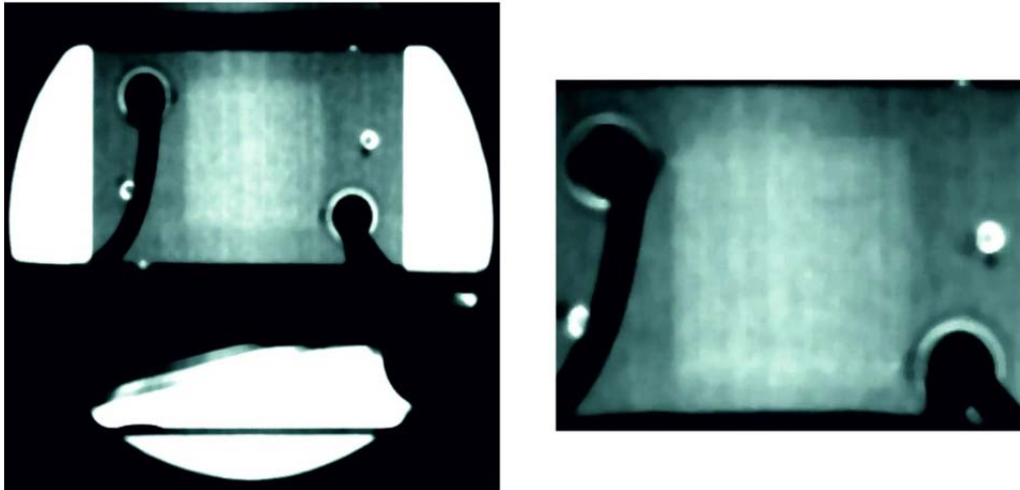
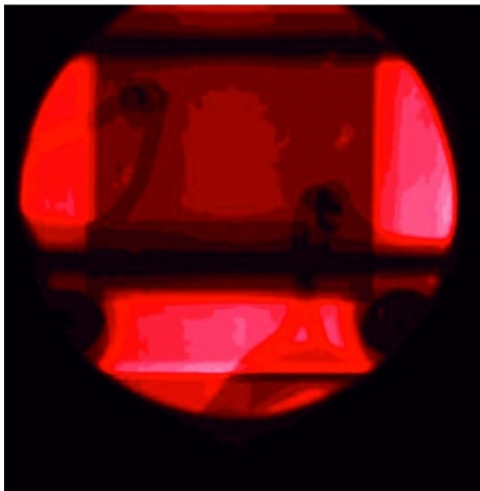


Figure 5.6.1 *Left:* Raw image of the fuel cell, radiography image of an operating fuel cell done with a 100 μm thin plate scintillator with $200 \times 200 \mu\text{m}^2$ readout resolution. The MEA is located in the centre of the image. The outer parts of the image contain coolant tubes, load connections, etc. **Right:** Magnification of central part MEA.

Dry Cell, at 70°C



Wet Cell, 30% humidity at 70°C



Figure 5.6.2 *Left:* Processed image from scintillator detector dried at 70°C with N_2 to purge water from the channels. **Right:** Processed image of the cell with 30% humidity. The MEA is located in the square region in the middle of the image. High intensities indicate thicker water regions (red color). The color mapping helps to show changes in water content, not easily resolved in gray scale images of the human eye just as in the figure 5.6.1.

fuel cell dried at 70°C

fuel cell 30% humid at 70°C

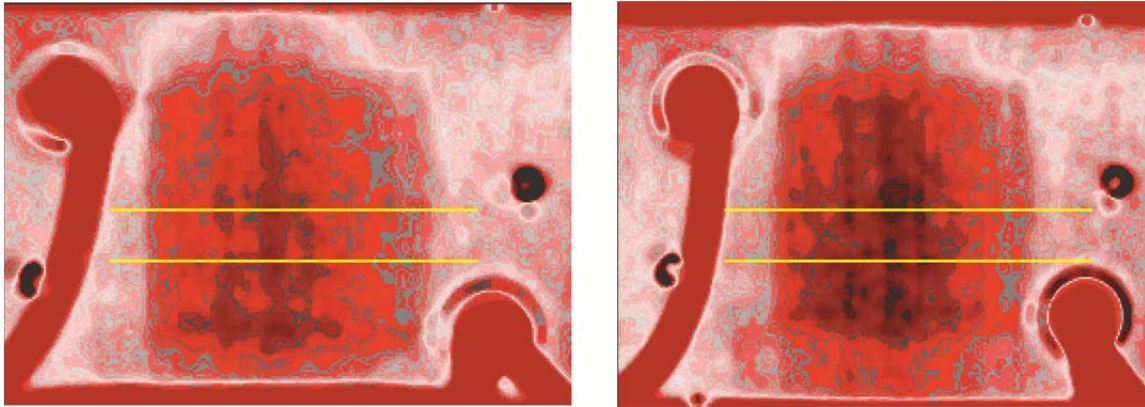


Figure 5.6.3 *Left: Processed image of MEA applying 0 current density dried at 70°C. Right: Processed image of MEA with 30% humidity at 70°C. There is a difference in images, which are clearly visible. Bright areas represent high neutron fluxes and dark areas low. Areas of high water concentration create a darker region in the image. The yellow line represents the line profiles along the width of the MEA to extract intensity value.*

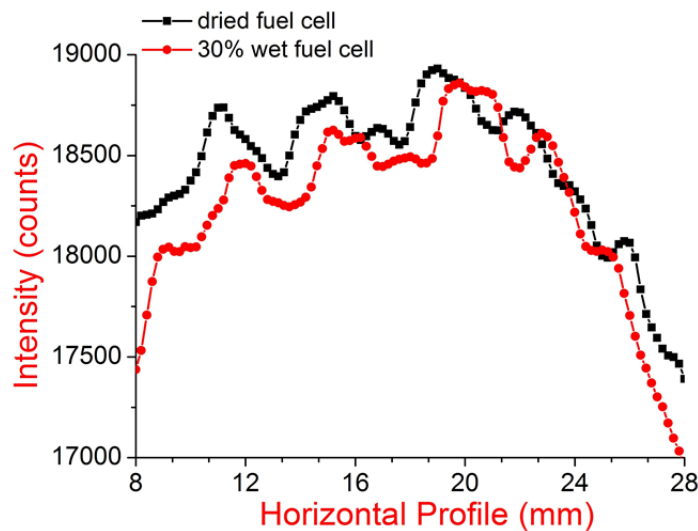


Figure 5.6.4 *A comparison of intensities versus the line-profile between the dry fuel cell sample, at 70°C and 30% humidified both at 70°C applying 0A current.*

5.7 Fuel Cell - humidity 90% (2A und 6A applied current)

Measurements continued systematically next day under different conditions for the stationary fuel cell. The fuel cell was supplied with 90% humidity, applying 2A current at 70°C to the inner membrane of MEA, applying 6A current under the same humidity and temperature conditions. The fuel cell station could provide accurate flow rates of hydrogen and oxygen as well as humidity values inside the fuel cell membrane

for this experiment. Before images were taken, the fuel cell was operated under the given conditions for 2 hours to stabilize.

By choosing the area along yellow line profiles in figure 5.7.1 for density analysis one integrates 5 x 5 pixels in the imaging plate (200 μm resolution). Water starts to accumulate down in the lower channels (see the marked area).

The diagrams in figure 5.7.2 represent intensities for 2A and 6A density respectively current for 90% relative humidity applied inside the fuel cell membrane (left) and the water density created inside under these conditions (right).

Water density is calculated applying the formulas (5.4.1), (5.4.2) and (5.4.3); $\Delta\rho$ is calculated applying formula (5.4.5), (for the region defined from the yellow lines); $\Delta\rho$ is calculated applying formula (5.4.5), where intensity values for 2A applied current, 90% applied humidity (inside membrane of the fuel cell) are taken as I_{dry} . Thus the reference intensity is: $I_{dry,2A,90\%wet}$

$$T_{water} = \frac{I_{wet,6A,90\%wet}}{I_{dry,2A,90\%wet}}$$

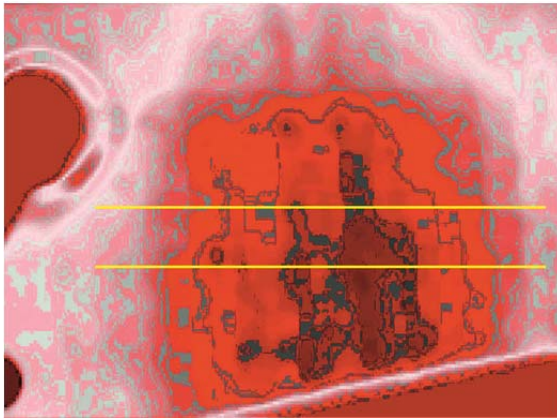
The average water density created inside the MEA is: $\langle\rho\rangle = 0.01143 \text{ g/cm}^3 \pm \Delta\rho \approx 0.00376 \text{ g/cm}^3$. A change of water is present in MEA; the water flows into the channels of the MEA. The images and their analyses are given below:

Table 5.7 summarizes the water density value of PEM fuel cell with 90% humidity applying 2A, 6A current density.

Cell Humidity (%)	Current density (A)	Water density $\langle\rho\rangle$ (g/cm ³)	Uncertainty $\Delta\rho$ (g/cm ³)
90	2		
90	6	0.01143	0.00376

Table 5.7 Summary of water density values created inside the PEM fuel cell.

2A current, 90% humid fuel cell



6A current, 90% humid fuel cell

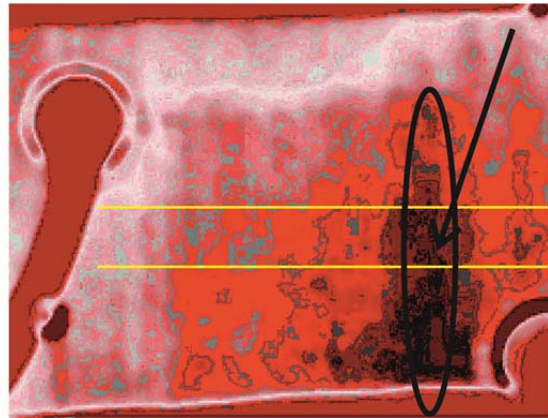


Figure 5.7.1 *Left:* Processed image of fuel cell applying 2A current with 90% humidity at 70° C. **Right:** Processed image of fuel cell applying 6A current density with 90% humidity at 70°C. There is a difference in water content. Bright areas represent high neutron fluxes and dark areas low. Areas of high water concentration create a dark region in the image. Water starts to accumulate on the cathode side of the MEA, right side of the cathode inlet (e.g. see the marked area). The contrast and colors of the raw images were enhanced only for presentation and doesn't affect the quantitative analysis.

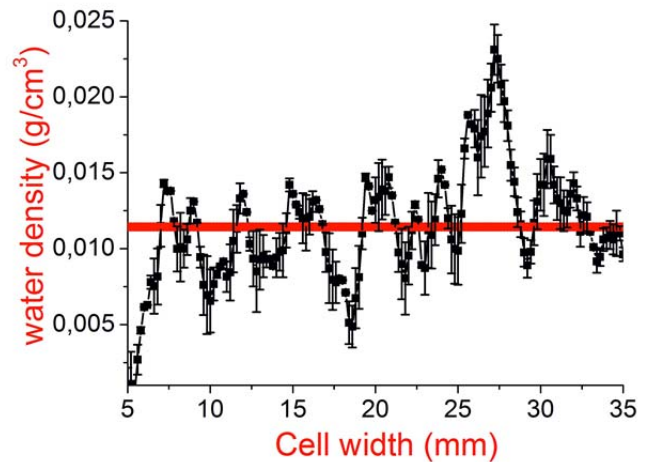
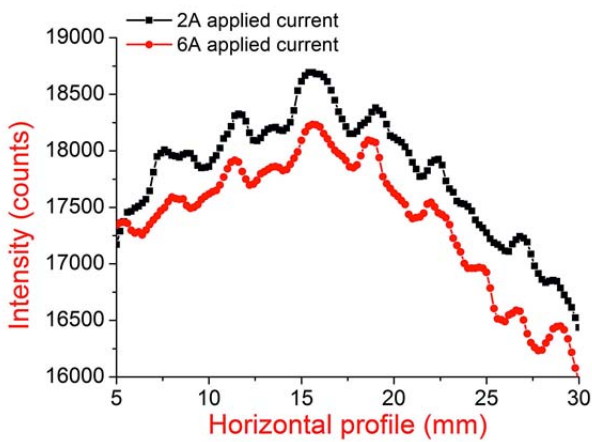


Figure 5.7.2 *Left:* A comparison of intensity counts versus horizontal line profile of the fuel cell membrane with 90% humidity, applying 2A (black line) and 6A (red line) current at 70°C. **Right:** Water density inside the fuel cell for 6A applied current density supplied with 90% humidity (where 2A intensity counts are taken as I_{dry}). Error bars for each density values in the diagram are calculated using (5.4.5) formula. Applying T-test distribution, the red line (center region) indicates the average water density created inside the MEA: $\langle \rho \rangle \approx 0.01143 \text{ g/cm}^3 \pm 0.00376 \text{ g/cm}^3$.

5.8 Fuel Cell - humidity 30% (2 and 6 A applied current)

A new stationary fuel cell was prepared by TU Graz team and measured at NR II station at Atominstitut. The cell was operated at different current densities 2A and 6A and for each current density the test was done at 30% relative humidity value. Exposure time was 500 seconds. The processed images are presented in figure 5.8.1. By choosing the area between yellow lines we could plot intensity counts like shown in figure 5.8.2 (left) and the water density created inside a fuel cell for 6A applied current density at 30% humidity (black points, right).

Because we couldn't have a totally dry membrane of MEA, water density is calculated applying the formulas (5.4.1), (5.4.2) and (5.4.3); $\Delta\rho$ is calculated applying formula (5.4.5), where intensity values for 2A applied

current, 30% applied humidity (inside membrane of the fuel cell) are taken as $I_{dry}: T_{water} = \frac{I_{wet,6A,30\%wet}}{I_{dry,2A,30\%wet}}$

The water density data sets were tested for T-test distribution.

The red line (center region, figure 5.8.2) indicates the average water density created inside the MEA: $\langle\rho\rangle = 0.01099 \text{ g/cm}^3 \pm 0.00535 \text{ g/cm}^3$.

A T-test distribution of water density values was performed and a significant difference between 2A and 6A was found.

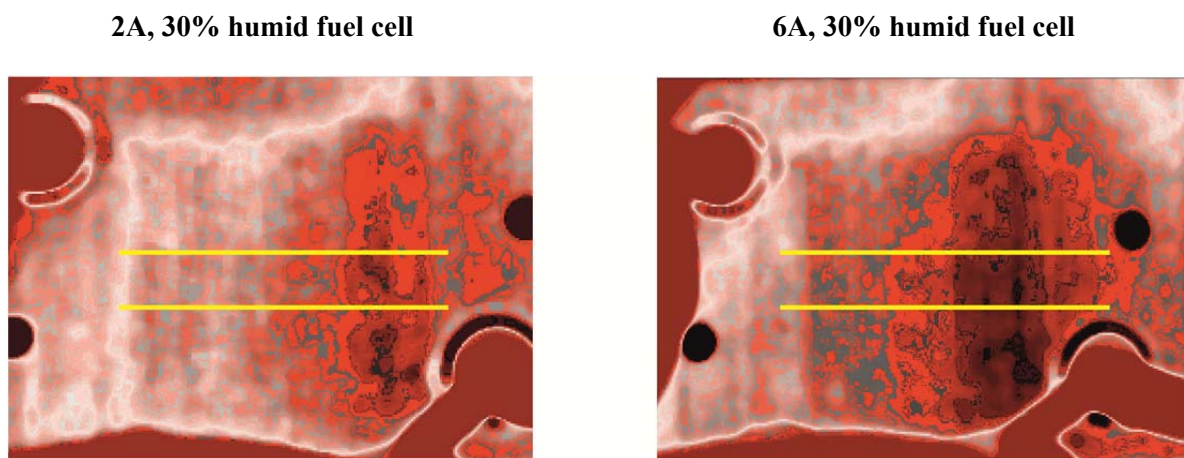


Figure 5.8.1 **Left:** Processed images from fuel cell applying 2A current. **Right:** Processed images from fuel cell applying 6A current with 30% humidity at 70°C. There is a difference in water content. Bright areas represent high neutron fluxes and dark areas low. Areas of high water concentration create a dark region in the image.

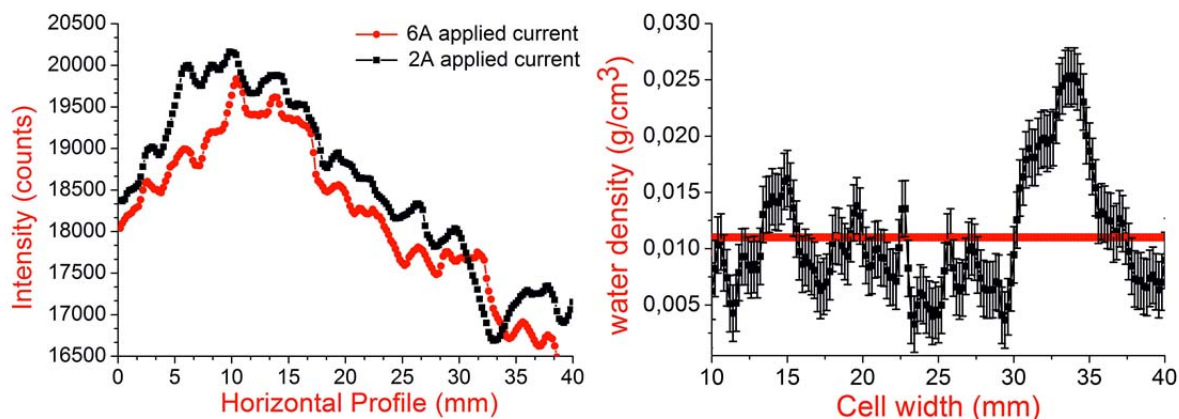


Figure 5.8.2 **Left:** A comparison of intensity counts versus horizontal line profile of the fuel cell membrane with 30% humidity, applying 2A (black line) and 6A (red line) current at 70°C. **Right:** Water density present inside the fuel cell membrane for 6A applied density current supplied with 30% humidity (where 2A intensity counts are taken as I_{dry}). Error bars for each density values in the diagram are calculated using (5.4.5) formula. Applying T-test distribution, the red line (center region) indicates the average water density created inside the MEA: $\langle \rho \rangle = 0.01099 \text{ g/cm}^3 \pm 0.00535 \text{ g/cm}^3$.

5.9 Fuel Cell - humidity 30% (2 and 8.5A applied current)

New measurements were performed by increasing the density current from 6A to 8.5A for 30% humidity applied inside the fuel cell. The processed images are shown in the figure 5.9.1. The diagram in figure 5.9.2 represents the intensity for 2A and 8.5A density current (left). The next diagram represents and water density created inside under these conditions (black points, right).

In figure 5.9.3 the intensities for all measured current densities (humidity 30%) are put together for comparison.

In figure 5.9.4 water densities values for 6A and 8.5A (humidity 30%) are put together for comparison.

The water density is calculated applying the formulas (5.4.1), (5.4.2) and (5.4.3); $\Delta\rho$ is calculated applying formula (5.4.5), where intensity values for 2A applied current, 30% applied humidity (inside membrane of

$$\text{the fuel cell) are taken as } I_{dry}: T_{water} = \frac{I_{wet,8.5A,30\%wet}}{I_{dry,2A,30\%wet}}.$$

The red line (center region) indicates the average water density created inside the MEA $\langle \rho \rangle = 0.03473 \text{ g/cm}^3 \pm 0.01021 \text{ g/cm}^3$ referring to the diagram in figure 5.9.2.

2A, 30% humid fuel cell

8.5A, 30% humid fuel cell

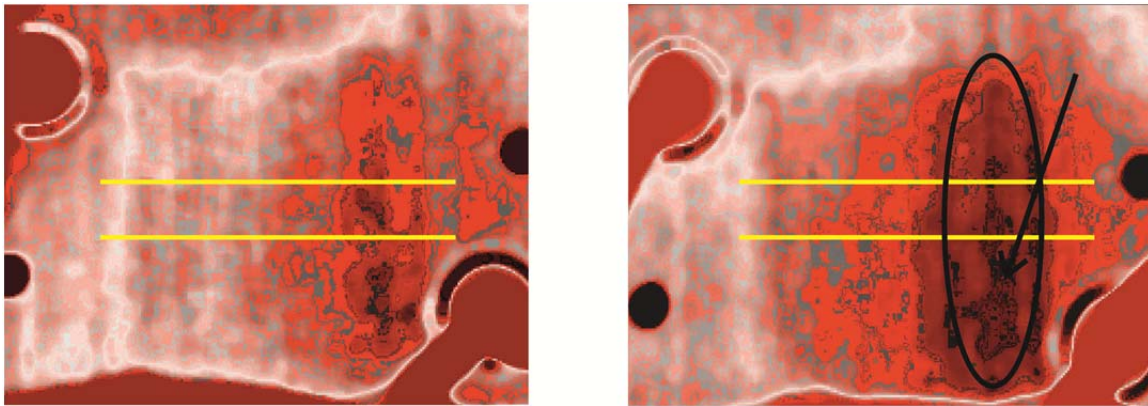


Figure 5.9.1 *Left:* Processed images from fuel cell applying 2A current. *Right:* The processed images from fuel cell applying 8.5A current with 30% humidity at 70°C. There is a significance difference in water content. Bright areas represent high neutron fluxes and dark areas low. Areas of high water concentration create a dark region in the image. Water starts to accumulate on the cathode side of the MEA.

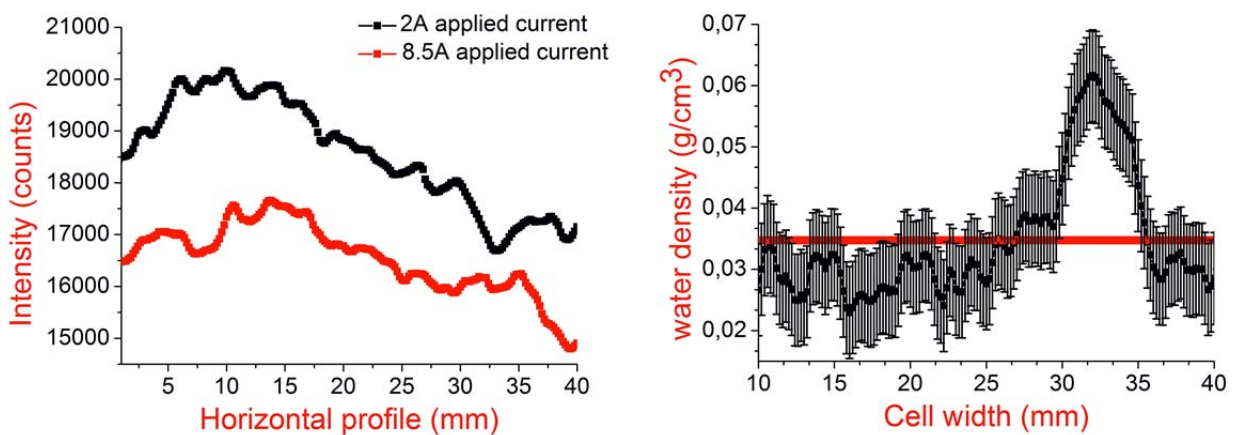


Figure 5.9.2 *Left:* A comparison of intensity counts versus horizontal line profile of the fuel cell membrane with 30% humidity, applying 2A (black line) and 8.5A (red line) current at 70°C. *Right:* Water density present inside the fuel cell membrane for 8.5A applied density current supplied with 30% humidity (where 2A intensity counts are taken as I_{dry}). Error bars for each density values in the diagram are calculated using (5.4.5) formula. Applying T-test distribution the red line (center region) indicates the average water density created inside the MEA: $\langle \rho \rangle = 0.03473 \text{ g/cm}^3 \pm 0.01021 \text{ g/cm}^3$.

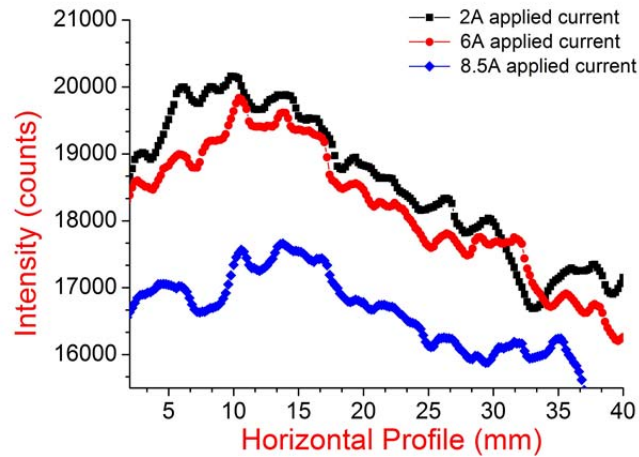


Figure 5.9.3 A comparison of intensity the horizontal line profile between the fuel cell sample with 30% humidity applying 2A (black line), 6A (red line) and 8.5A (blue line) current at 70°C.

From all analysis done with ^6Li scintillator water starts to accumulate in the right side of the image to the cathode inlet, which is clearly visible in the marked area like is shown in figure 5.9.1 and in the water density plot, figure 5.9.4.

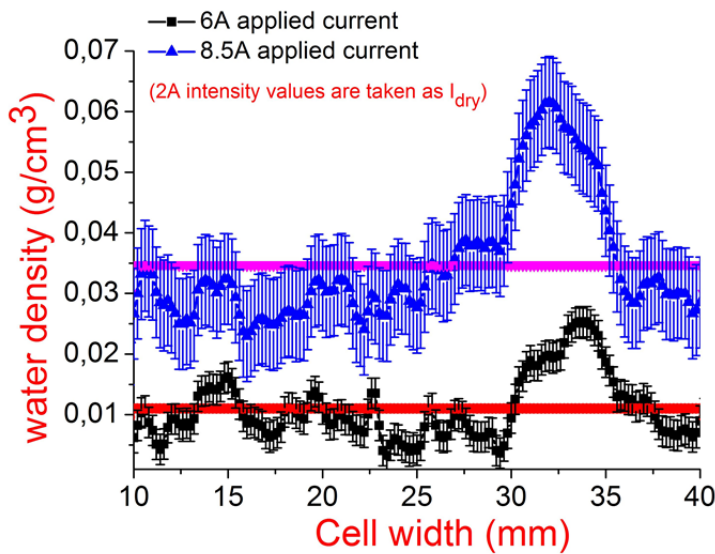


Figure 5.9.4 Water density inside fuel cell. Black data points represent the water density for 6A, 30% wet fuel cell membrane (where 2A intensity counts values are taken as I_{dry}). Applying the T-test distribution, the red line indicate the average water density: $\langle \rho \rangle_{6A, 90\% \text{ wet}} \approx 0.01099 \text{ g/cm}^3 \pm 0.00535 \text{ g/cm}^3$. Blue data points represent the water density for 8.5A, 30% wet fuel cell membrane (where 2A intensity counts values are taken as I_{dry}). Applying the T-test distribution, the pink line indicates the average water density: $\langle \rho \rangle_{8.5A, 90\% \text{ wet}} \approx 0.03473 \text{ g/cm}^3 \pm 0.01021 \text{ g/cm}^3$ (at level 0.05, the difference between the averages of the water densities populations differs significantly from the test difference).

The diagram in figure 5.9.5 represents the water difference created inside the fuel cell for 30% humidity while applied current is increased from 6A to 8.5A, (where 2A intensity counts values are taken as I_{dry}). The error for each water density value is calculated from the formula:

$$\delta\rho = \sqrt{(\Delta\rho_{2A})^2 + (\Delta\rho_{8.5A})^2} \quad (5.4.6)$$

Where: $\Delta\rho_{2A}$ $\Delta\rho_{8.5A}$ are the error values for water density values: ρ_{2A} and $\Delta\rho_{8.5A}$ calculated from the formulas (5.4.4) and (5.4.5) respectively and 3σ is the tolerance interval (three standard deviations account).

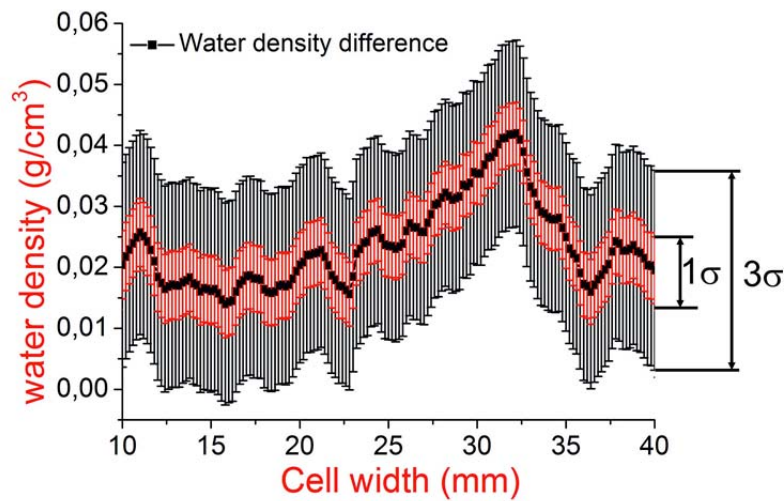


Figure 5.9.5 Water difference created inside the fuel when the current density is increased from 2A to 8.5A for constant humidity of 30%. Error bars are calculated using the formula (5.4.6) where uncertainty is given with 3σ standard deviation interval.

If we take 6A current intensity counts as I_{dry} value, applying: $T_{water} = \frac{I_{wet,8.5A,30\%wet}}{I_{dry,6A,30\%wet}}$, than we obtain the

water density value of: $\langle\rho\rangle = 0.02374 \text{ g/cm}^3 \pm 0.00712 \text{ g/cm}^3$ as it is shown in figure 5.9.6, black points (red line, center region). Applying the T-test distribution for this given data at 0.05 level, the difference between the averages of the water density population differs significantly from the test difference).

The diagram in figure 5.9.7 represents the water difference created inside the fuel cell for 30% humidity applying 8.5A current density, where 2A and 6A intensities counts are taken as I_{dry} . The error for each water density value is calculated from (5.4.6) formula, Where: $\Delta\rho_{2A}$, $\Delta\rho_{6A}$, $\Delta\rho_{8.5A}$ are the error values for water density values: ρ_{2A} , ρ_{6A} and $\Delta\rho_{8.5A}$, which are calculated from the formulas (5.4.4) and (5.4.5) respectively and 3σ is the tolerance interval (three standard deviations account).

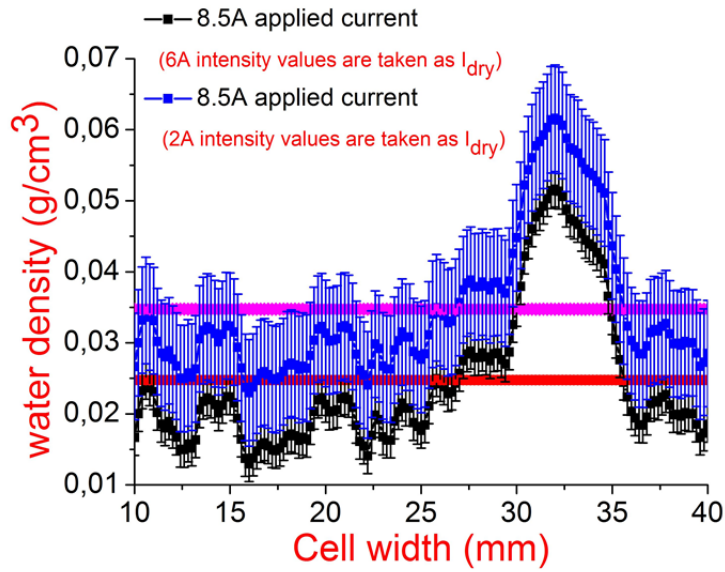


Figure 5.9.6 Water density inside fuel cell. Black data points represent the water density for 8.5A, 30% wet fuel cell membrane where $\underline{6A}$ intensity counts values are taken as I_{dry} . Applying the T-test distribution, the red data points (central region) represent the average water density: $\langle \rho \rangle_{6A, 90\% \text{ wet}} \approx 0.02374 \text{ g/cm}^3 \pm 0.00712 \text{ g/cm}^3$. The blue data points represent water density where $\underline{2A}$ intensity counts are taken as I_{dry} . Applying the T-test distribution, the pink data points (central region) indicate the average water density: $\langle \rho \rangle_{8.5A, 90\% \text{ wet}} \approx 0.03473 \text{ g/cm}^3 \pm 0.01021 \text{ g/cm}^3$

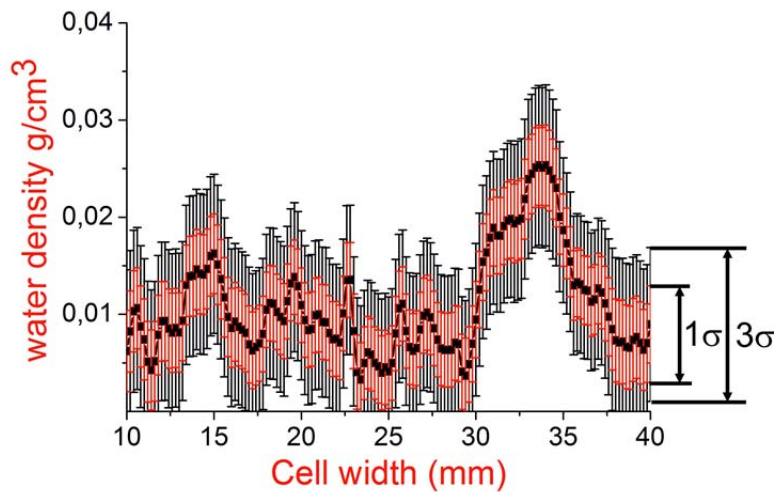


Figure 5.9.7 Water difference created inside the fuel cell membrane for the applied current density of 8.5A for constant humidity value of 30% where, $\underline{6A}$ intensity counts values are taken as I_{dry} , $\underline{2A}$ intensity counts values are taken as I_{dry} . Error bars are calculated using the formula (5.4.6) where uncertainty is given with 3σ standard deviation interval.

Table 5.9 summarizes the water densities values of PEM fuel cell with 30% humidity applying 2A, 6A and 8.5A current density and the diagram in figure 5.9.7 shows the water density increase versus applied current density.

Cell Humidity (%)	Current density (A)	Water density $\langle\rho\rangle$ (g/cm ³)	Uncertainty $\Delta\rho$ (g/cm ³)
30	2	0.01099	0.00535
30	6	0.02374	0.00712
30	8.5	0.03473	0.01021

Table 5.9 Summary of water density values created inside the PEM fuel cell.

If we consider only the current density factor clearly is seen that more water is created when we increase current density inside MEA in the fuel cell membrane, where, the humidity value is kept constant like is shown in figure 5.9.8.

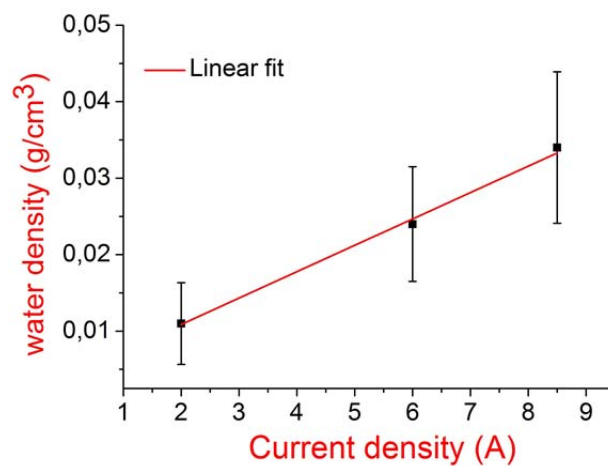


Figure 5.9.8 The water density versus current density. From the fitting data we expect a water density increase of $0.00375 \pm 1.80623 \cdot 10^{-4} \text{g/cm}^3$ increasing the current density from 2A to 6A and to 8.5A.

Using this method water can be detected and quantified. From intensity and water density profile diagrams in figures presented above it is clearly visible that water starts to accumulate in the right side of the image of the cathode inlet.

Water visualization and in PEM fuel cells provides detailed information about water transport in the gas flow channels.

5.10 Fuel Cell - humidity 90% (0 and 2 A applied current)

A new set of measurements was performed by increasing the humidity inside the MEA in fuel cell, operated at different current densities 0A, and 2A. For each current density the test was done at 90% relative humidity value. The processed images are shown in the figure 5.10.1.

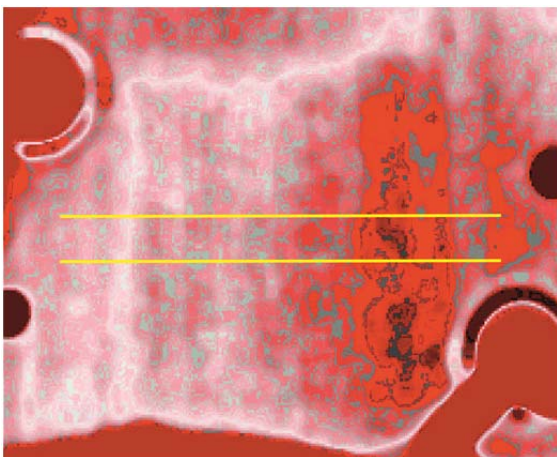
The diagram in figure 5.10.2 represents intensity for 0A and 2A density current (left). The next diagram represents the water density created inside under these conditions (black points, right).

Water density is calculated applying the formulas (5.4.1), (5.4.2) and (5.4.3); $\Delta\rho$ is calculated applying formula (5.4.5), where intensity values for 0A applied current, 90% applied humidity (inside membrane of

the fuel cell) are taken as I_{dry} : $T_{water} = \frac{I_{wet,2A,90\%wet}}{I_{dry,0A,90\%wet}}$

The average water density created inside the MEA: $\langle\rho\rangle \approx 0.00597 \text{ g/cm}^3 \pm 0.00467 \text{ g/cm}^3$ referring to the diagram in figure 5.10.2.

0A, 90% humid fuel cell



2A, 90% humid fuel cell

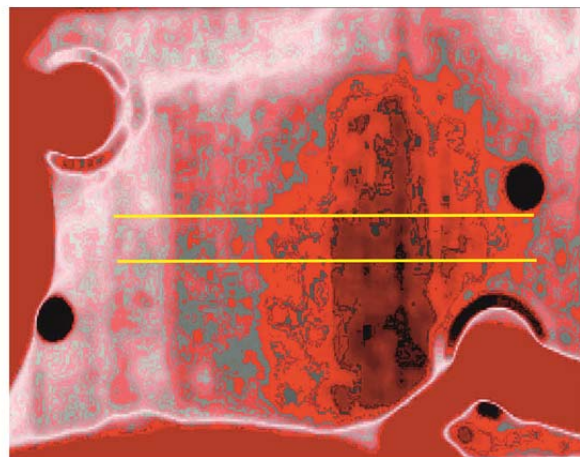


Figure 5.10.1 *Left:* Processed images from fuel cell applying 0A current. *Right:* Processed images from fuel cell applying 2A current with 90% humidity at 70°C. There is a difference in water content. Bright areas represent high neutron fluxes and dark areas low. Areas of high water concentration create a dark region in the image.

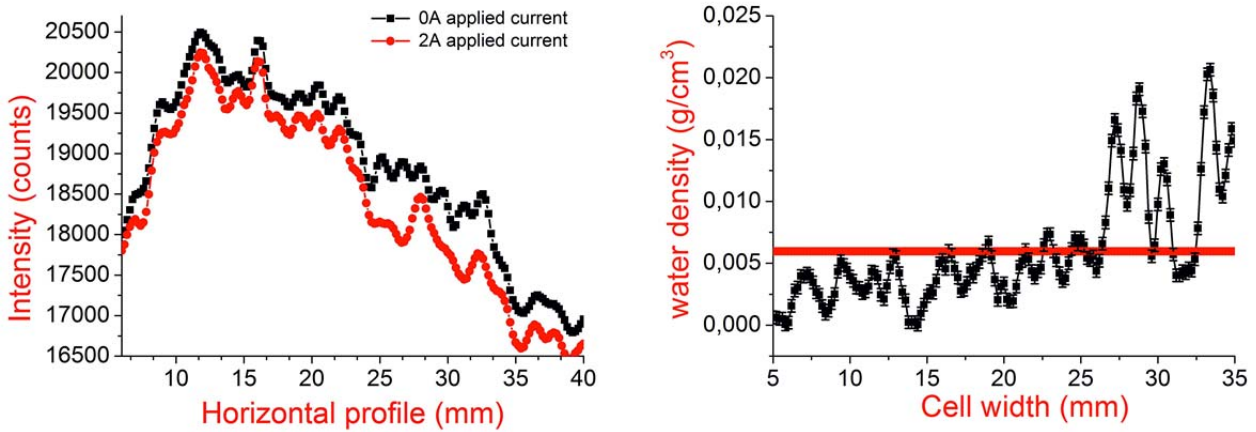


Figure 5.10.2 *Left:* A comparison of intensity counts versus horizontal line profile of the fuel cell membrane with 90% humidity, applying 0A (black line) and 2A (red line) current at 70°C. *Right:* Water density present inside the fuel cell membrane for 2A applied density current supplied with 90% humidity (where 0A intensity counts are taken as I_{dry}). Error bars for each density values in the diagram are calculated using (5.4.5) formula. Applying T-test distribution the red line (center region) indicates the average water density created inside the MEA: $\langle \rho \rangle_{2A, 90\% \text{ wet}} = 0.00597 \text{ g/cm}^3 \pm 0.00467 \text{ g/cm}^3$.

5.11 Fuel Cell - humidity 90% (0 and 6 A applied current)

The neutron images performed with ^6Li scintillator for 6A applied density current for 90% humidity inside fuel cell are presented below. The processed images are shown in the figure 5.11.1. The diagram in figure 5.11.2 represents intensity for 0A and 6A density current for 90% relative humidity applied inside the fuel cell (left). The next diagram represents and water density created inside under these conditions (black points, right).

Water density is calculated applying the formulas (5.4.1), (5.4.2) and (5.4.3); $\Delta\rho$ is calculated applying formula (5.4.5), where intensity values for 0A applied current, 90% applied humidity (inside membrane of

the fuel cell) are taken as I_{dry} :
$$T_{water} = \frac{I_{wet, 6A, 90\% \text{ wet}}}{I_{dry, 0A, 90\% \text{ wet}}}$$

The average water density created inside the MEA $\langle \rho \rangle = 0.03251 \text{ g/cm}^3 \pm 0.00987 \text{ g/cm}^3$ referring to the diagram in figure 5.11.2.

In figure 5.11.3 the intensities for all measured current densities (humidity 90%) are put together for comparison.

0A, 90% humid fuel cell

6A, 90% humid fuel cell

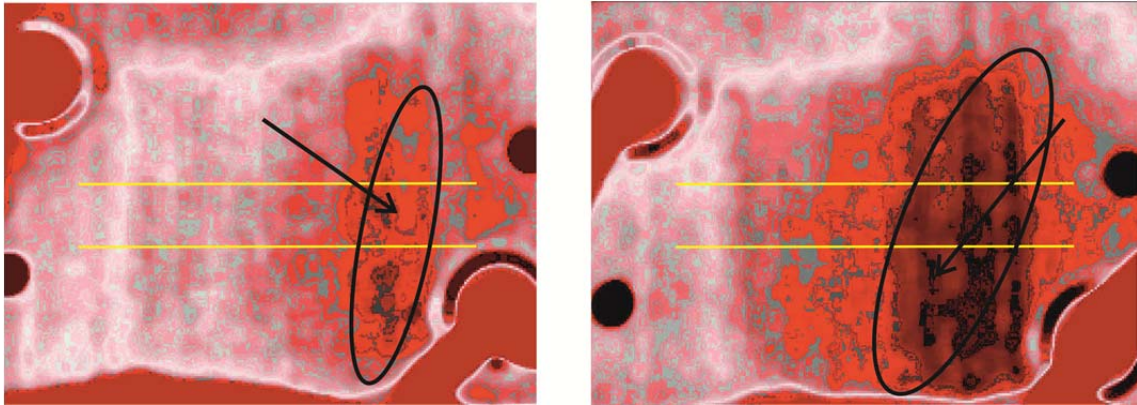


Figure 5.11.1 Left: Processed images from fuel cell applying 0A current. Right: Processed images from fuel cell applying 6A current with 90% humidity at 70°C. There is a difference in water content which is clearly visible. Bright areas represent high neutron fluxes and dark areas low. Areas of high water concentration create a dark region in the image in the marked area. Water starts to accumulate on the cathode side of the MEA.

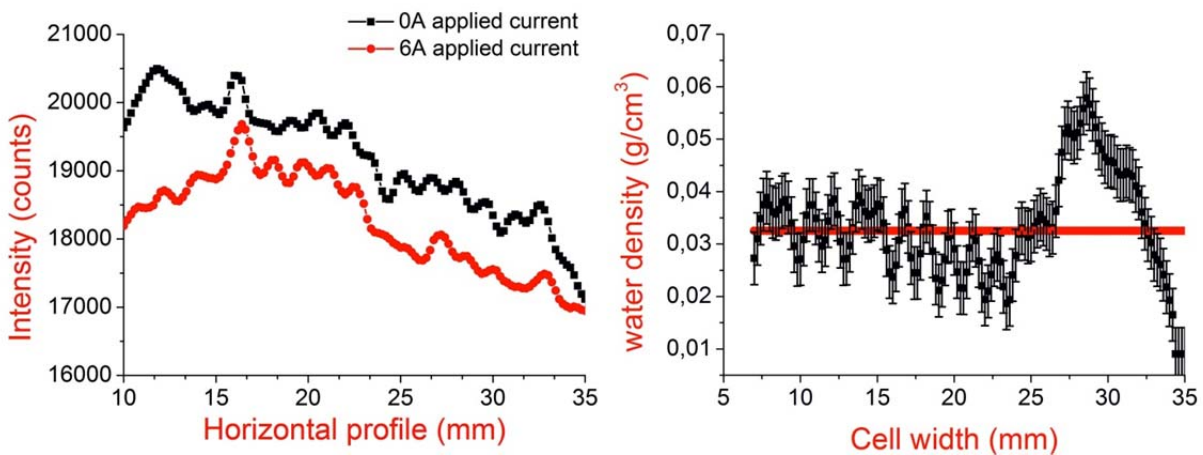


Figure 5.11.2 Left: A comparison of intensity counts versus horizontal line profile of the fuel cell membrane with 90% humidity, applying 0A (black line) and 6A (red line) current at 70°C. Right: Water density present inside the fuel cell membrane for 6A applied density current supplied with 90% humidity (where 0A intensity counts are taken as I_{dry}). Error bars for each density values in the diagram are calculated using (5.4.5) formula. Applying T-test distribution the red line (center region) indicates the average water density created inside the MEA: $\langle \rho \rangle = 0.03251 \text{ g/cm}^3 \pm 0.00987 \text{ g/cm}^3$.

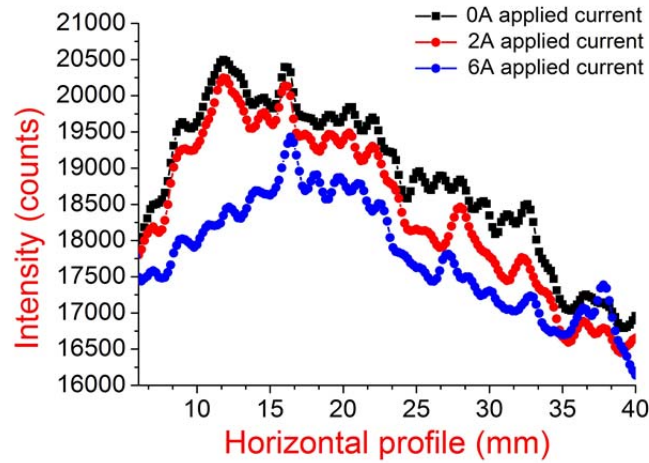


Figure 5.11.3 Comparison of intensity versus the horizontal line profile between the fuel cell sample with 90% humidity applying 0A (black line), 2A (red line) and 6A (blue line) current at 70°C.

In figure 5.11.4 the water density values for 2A and 6A applied current density under 90% humid membrane are put together for comparison. Figure 5.11.5 represents water density difference under these conditions (referring to the diagram 5.11.4). At level 0.05, the difference between the averages of the water densities population differs significantly from the test difference.

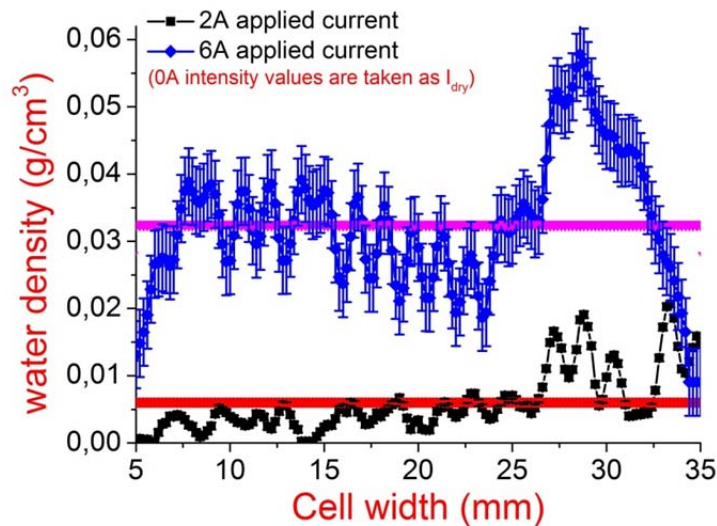


Figure 5.11.4 Water density inside fuel cell. Black data points represent the water density for 2A for 90% wet fuel cell membrane (where 0A intensity counts values are taken as I_{dry}). Applying the T-test distribution, the red line indicates the average water density: $\langle \rho \rangle_{2A, 90\% \text{ wet}} \approx 0.00597 \text{ g/cm}^3 \pm 0.00467 \text{ g/cm}^3$. Blue data points represent the water density for 6A for 90% wet fuel cell membrane (where 0A intensity counts values are taken as I_{dry}). Applying the T-test distribution, the pink line indicates the average water density: $\langle \rho \rangle_{6A, 90\% \text{ wet}} \approx 0.03251 \text{ g/cm}^3 \pm 0.00987 \text{ g/cm}^3$.

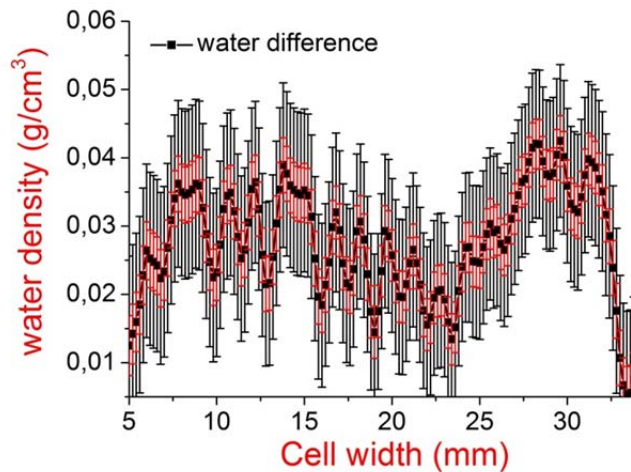


Figure 5.11.5 Water difference created inside the fuel when the current density is increased from 0A to 6A for constant humidity of 90%. Error bars are calculated using the formula (5.4.6) where uncertainty is given with 3σ standard deviation interval.

If we take 2A current intensity counts as I_{dry} value, applying: $T_{water} = \frac{I_{wet,6A,90\%wet}}{I_{dry,2A,90\%wet}}$, than we obtain the water density value of: $\langle\rho\rangle = 0.01757 \text{ g/cm}^3 \pm 0.01043 \text{ g/cm}^3$ as it is shown in figure 5.11.6, black points (red line, center region). Applying the T- test distribution for this given data at 0.05 level, the difference between the averages of the water density population differs significantly from the test difference).

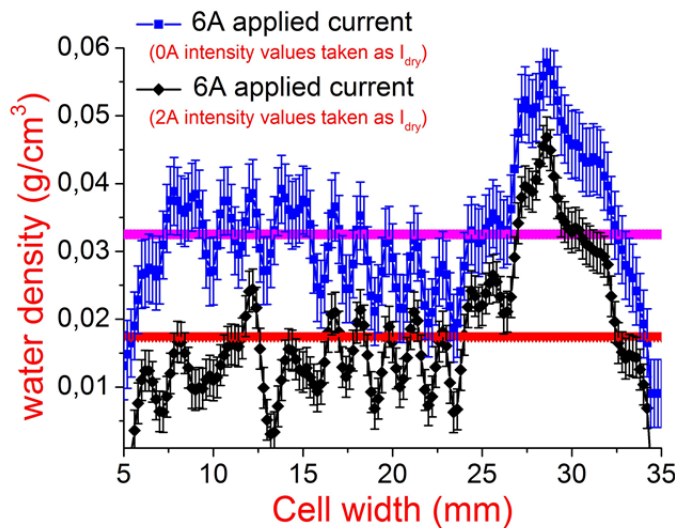


Figure 5.11.6 Water density calculated created in fuel cell for 6A applied density current for 90% humidity. The black data points represent the average water density where I_{dry} is taken for 0A applied current. Applying the T test distribution, the red line indicate the average water density: $\langle\rho\rangle_{6A, 90\% wet} \approx 0.03251 \text{ g/cm}^3 \pm 0.00987$.

Applying the T-test distribution, the pink data points represent the average water density where I_{dry} is taken for 2A applied current blue data points: $\langle \rho \rangle_{6A, 90\% \text{ wet}} \approx 0.01757 \text{ g/cm}^3 \pm 0.01043 \text{ g/cm}^3$.

The diagram in figure 5.11.7 represents the water difference created inside the fuel cell for 90% humidity applied current for applying 2A and 6A current density. The error for each water density value is calculated from the formula (5.4.6), where I_{dry} is taken for 0A and 2A applied current.

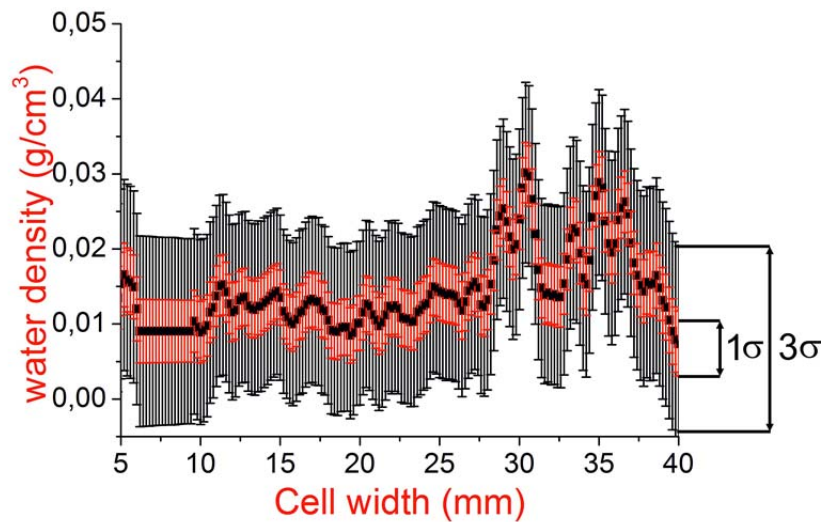


Figure 5.11.7 Water difference created inside the fuel when the current density is increased from 2A to 6A for constant humidity value of 90% (where I_{dry} is taken for 0A and 2A applied current). Error bars are calculated using the formula (5.4.6) where uncertainty is given with 3σ standard deviation interval.

Table 5.10 summarizes the water densities values of PEM fuel cell with 90% humidity applying 0A, 2A and 6A current density. These values are derived from neutron images performed with ^6Li scintillator with 200 μm resolution. If we consider only the current density factor is seen that more water is created when we increase current density inside MEA in the fuel cell where the humidity value is kept constant.

Cell Humidity (%)	Current density (A)	Water density $\langle \rho \rangle$ (g/cm ³)	Uncertainty $\Delta \rho$ (g/cm ³)
90	0	0.00597	0.00467
90	2	0.01757	0.01043
90	6	0.03251	0.00987

Table 5.10 Summary of water density values created inside the PEM fuel cell (the red color corresponds to the water density measurement value represents in 5.7 section).

The data from table 5.11 are plotted in the diagram like is shown in figure 5.11.8.

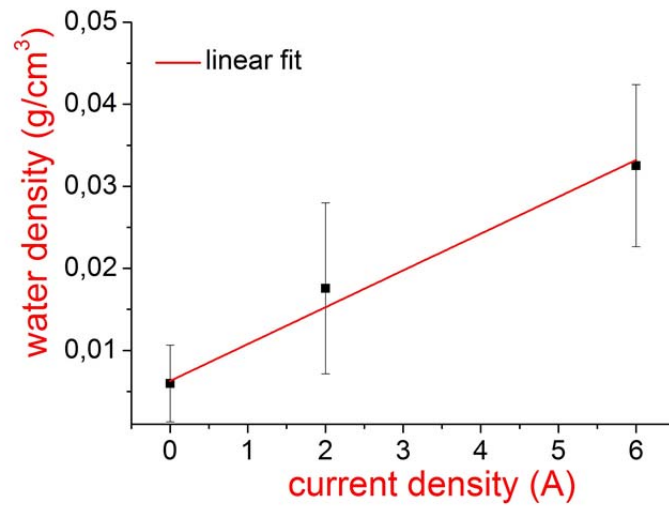


Figure 5.11.8 The water density increase versus current density. From the fitting data we expect a water density increase of 0.00449 g/cm^3 (red dot) increasing the current density from 0A to 2A to 6A.

Table 5.11 summarizes the water density value for 6A applied current under different humidity values 30% and 90% applied inside the PEM fuel cell. If we consider only the humidity factor clearly is seen that more water is created when we increase the humidity inside MEA in the fuel cell where the current density is constant.

Cell Humidity (%)	Current density (A)	Water density ρ (g/cm ³)	Uncertainty $\Delta\rho$ (g/cm ³)
30	6	0.01099	0.00535
90	6	0.01757	0.01043

Table 5.11 Summary of water density values created inside the PEM fuel cell.

The diagram in figure 5.11.9 shows the plotted data of the water density created inside MEA versus applied current for 30% and 90% applied humidity.

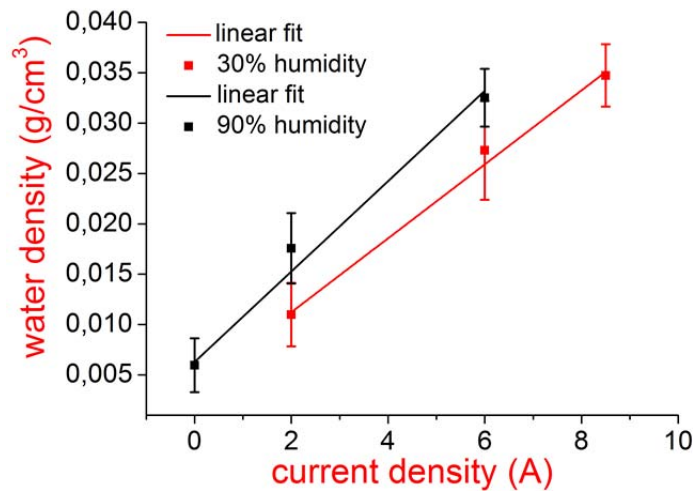


Figure 5.11.9 The water density versus current density. From the fitting data we expect a water density increase of $0.00375 \pm 1.80623 \cdot 10^{-4} \text{g/cm}^3$ for 30% humidity and $0.00449 \text{ g/cm}^3 \pm 4.36026 \cdot 10^{-4}$ for 90% humidity.

From all analysis done with ^6Li scintillator water starts to accumulate to the lower part of the channels on the cathode side of the MEA like is shown in figure 5.11.1 (see marked area) and from the density profile like is shown figure 5.11.4.

5.12 Quantification and Visualization with IP-ND Detector.

The first transmission measurements of the stationary fuel cell sample were done with Imagine Plate–Neutron Detector (IP-ND). This detector offers us a much better resolution compared with scintillator detector. The measurement lasted for 50 min exposure time, at full 250 kW reactor power. The fuel cell was not completely dried and was measured at room temperature. After having an image of the fuel cell at room temperature we started the drying process of the sample with N_2 while heating the fuel cell up to 70°C . The IP-ND was placed 30 cm from the neutron beam like is shown in figure 5.5.2, which has a diameter of 9 cm. Exposure time of 50 min was followed by 10 min scanning time ($25 \mu\text{m}$ pixel size) and 30 min erasing time. As scanning parameters with best signal-to-noise ratio at $25 \mu\text{m}$ resolution we chose the highest gradation (16 bit) and sensitivity S4000 at level L5. The scanned images were stored as Fuji-img file format and then further processed with Image-Pro Plus 6 (Media Cybernetics). The logarithm of the detected PSL signals is converted to unsigned 16 bit data yielding a full image size of 160 Mb.

The IP-ND images (the figures 5.12.1) provide a much sharper picture with higher sensitivity, compared with ^6Li scintillator images. The better spatial resolution of the imaging plates allows us to have more precise

density values. Figure 5.12.2 represents processed images. The diagrams from figure 5.12.3 represent intensity per pixel for the whole width of the MEA membrane for humid and dry case.

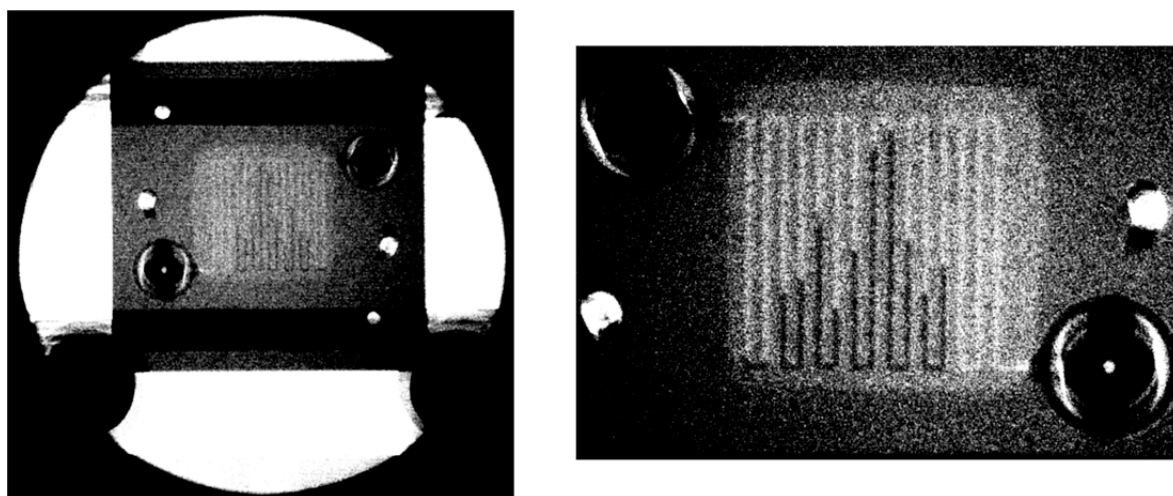


Figure 5.12.1 *Left: Raw image of the fuel cell, radiography image of an operating fuel cell done with IP-ND ($25 \times 25 \mu\text{m}^2$ resolution). The MEA is located in the centre of the image. The outer parts of the image contain coolant tubes, load connections, etc. Right: Processed image of the MEA. Water is easily seen in lower flow channels. Low intensities (dark regions) indicate thicker water regions. The different gray levels correspond to different amounts of water. The darker the gray level of the pixel, the more water is present.*

humid fuel cell

dry fuel cell

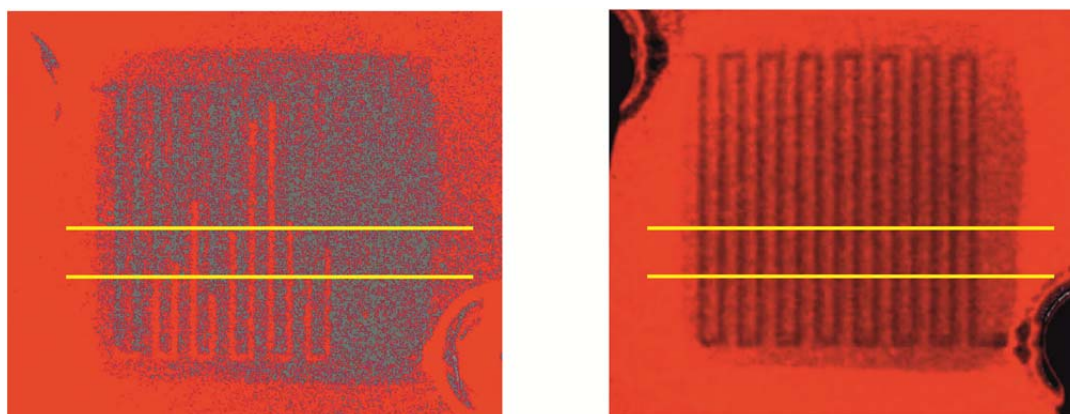


Figure 5.12.2 *Left: The processed wet image of the fuel cell done with IP-ND detector. Low intensities indicate thicker water regions (red color). Right: Processed image of the fuel cell dried at 70°C with N_2 , which helps to purge water from channels. Color mapped images are only used to enhanced qualitative analysis and do not affect quantitative analysis.*

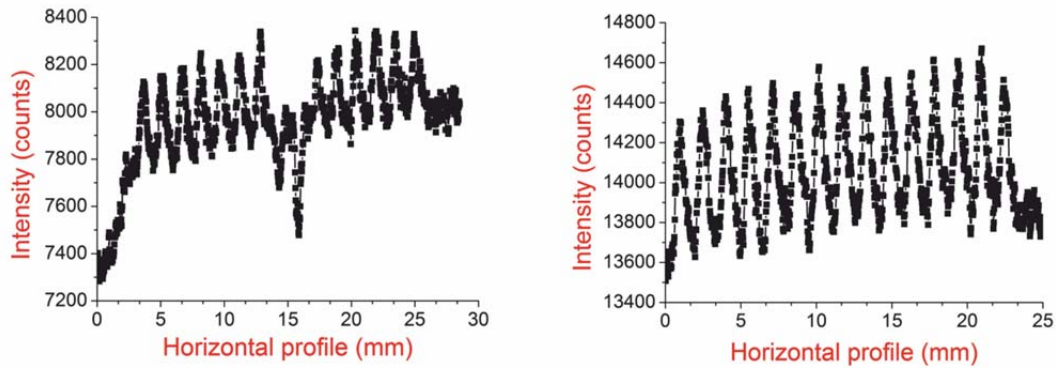


Figure 5.12.3 *Link:* This diagram shows the intensity for stationary fuel cell versus horizontal line-profile at room temperature. **Right:** This diagram shows the intensity versus horizontal line-profile of the membrane MEA for dried fuel cell at 70°C. If we compare intensity counts left/right clearly, we see water loss after drying process with nitrogen gas.

5.13 Fuel Cell - humidity 90% (6 and 8.5 A applied current)

The last series of neutrons radiography images were done applying 6A and 8.5A current. During operation the cell was supplied with 90% humidity at 70°C like is shown in figure 5.13.1. Figure 5.13.2 shows the processed images: water starts to accumulate to the low part of the channels (see marked area pink color). The fuel cell sample was placed as close as possible to the imaging plate. The diagram in figure 5.13.3 represents intensity for 6A and 8.5A density current respectively for 90% relative humidity. The diagram in the figure 5.13.4 represents and water density created inside under these conditions.

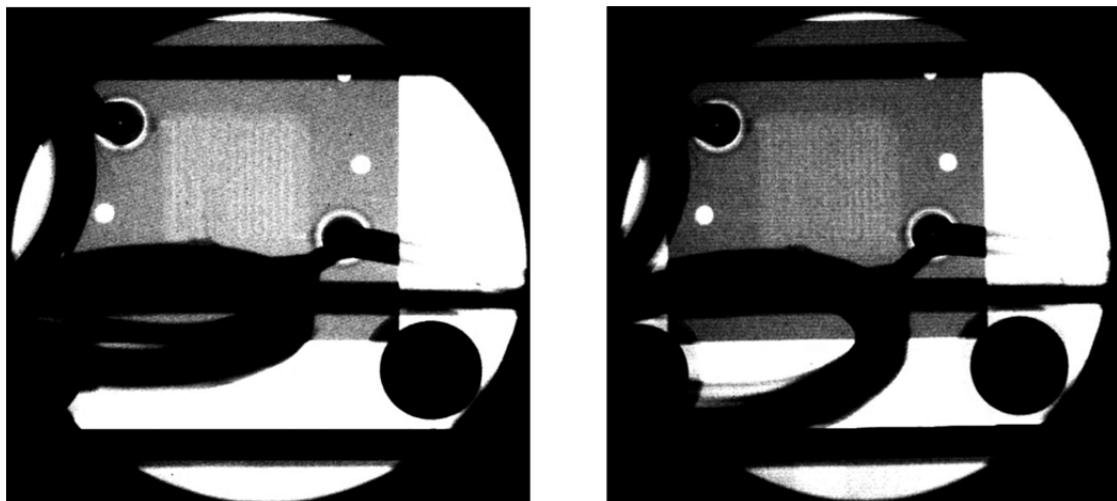


Figure 5.13.1 *Left:* Raw image of the stationary fuel cell by applying 6A current with 90% humidity of the inner membrane. **Right:** Raw image fuel cell sample by applying 8.5A current with 90% humidity of the MEA.

The water density is calculated applying the formulas (5.4.1), (5.4.2) and (5.4.3) where intensity values for the fuel cell 90% humid applying 6A current are taken as I_{dry} : $T_{water} = \frac{I_{wet,8.5A,90\%wet}}{I_{dry,6A,90\%wet}}$. The average water density created inside the MEA is: $\langle \rho \rangle = 0.0303 \text{ g/cm}^3 \pm 0.0025 \text{ g/cm}^3$.

applying 6A, 90% humid cell

applying 8.5A, 90% humid cell

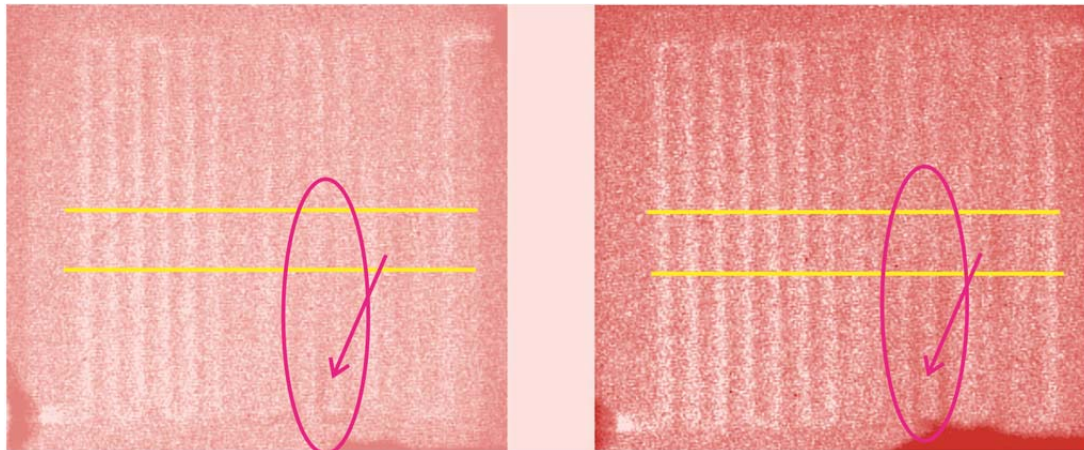


Figure 5.13.2 *Left:* Processed images from MEA of fuel cell applying 6A current. *Right:* Processed images from fuel cell applying 8.5A current with 90% humidity at 70°C. Bright areas represent high neutron fluxes and dark areas low. Areas of high water concentration create a dark region in the image. Water starts to accumulate on the cathode side of the MEA. There is a difference in water content is clearly visible (marked area).

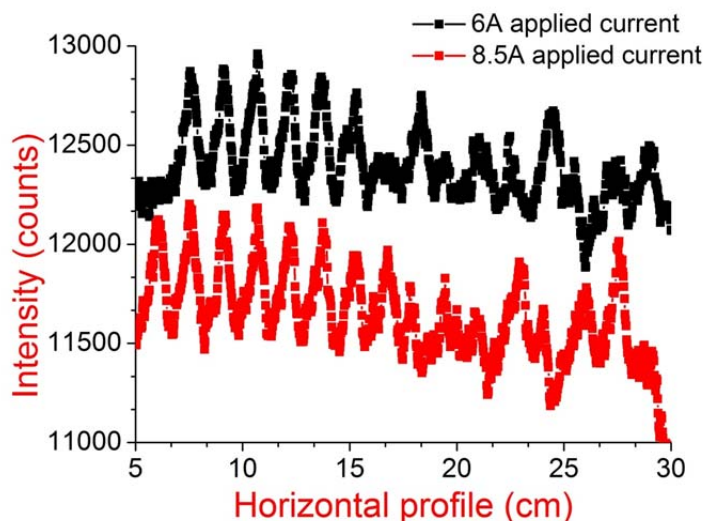


Figure 5.13.3 *A comparison of intensity versus the horizontal line profile between the fuel cell sample (yellow lines, figure 5.13.2) with 90% humidity applying 6A and 8.5A current at 70°C.*

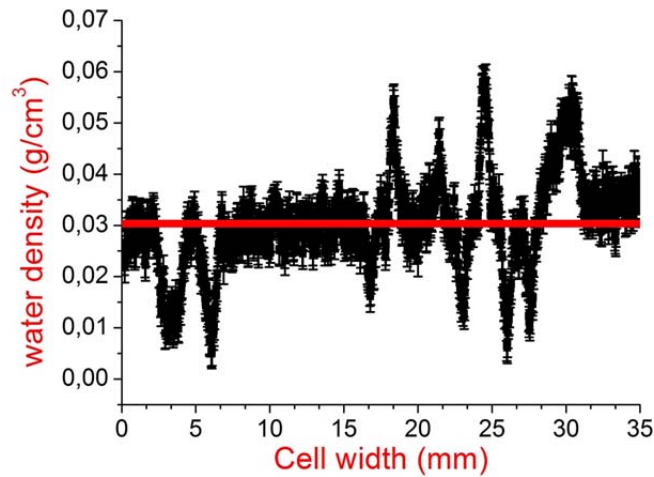


Figure 5.13.4 Water density inside the fuel cell for 8.5A applied current density supplied with 90% humidity. Applying T-test distribution the red line (center region) indicates the average water density created inside the MEA: $\langle \rho \rangle = 0.0303 \text{ g/cm}^3 \pm 0.0025 \text{ g/cm}^3$.

Table 5.13 summarizes the water density value of PEM fuel cell with 90% humidity applying 6A, 8.5A current density. This value is derived from measurements done with IP-ND.

Cell Humidity (%)	Current density (A)	Water density ρ (g/cm ³)	Uncertainty $\Delta\rho_{\text{rel}}$ ()
90	6		
90	8.5	0.0303	0.0025

Table 5.12 Summary of water density values created inside the PEM fuel cell for measurements done with IP-ND.

As mentioned above the fuel cell station could provide accurate flows of hydrogen and oxygen and humidity as well inside the fuel cell. For this experiment usual this process took at least about 2 hours to have a stable regime, but often the fuel cells were not showing the proper values and due to very long exposure time in case of using IP-ND a lot of measurements were lost. Other factors are the limited operation time of the reactor provided for these kinds of measurements.

5.14 Summary

Neutron imaging has proven to be a valuable tool to visualize operating stationary fuel cell. Neutron radiography is a useful technique to detect and quantify the water content inside a membrane electrode assembly (MEA). The NR II station at ATI in Vienna has provided images which spatial resolution 200 μm for ^6Li scintillator with CCD camera and 50 μm for IP-ND that are useful to quantify water distribution during fuel cell operation. Experiments were done for three different applied current values 2A, 6A and 8.5A and two relative humidity values: 30% and 90% necessary for cathode inlet. It was observed that for 90% fully humidified conditions the water content is increased with increasing current density.

These experiments and NR images technique provide a way to investigate liquid water created in anode and the cathode and will provide new prediction and control in water management in fuel cells. Knowing where water accumulates with more certainty helps us to understand the water transport in PEMFC.

From all the graphs it can be seen that current and humidity have a detectable influence on water quantity created inside of MEA. The higher the applied current for a given level humidity membrane, the higher is the water content and therefore the lower is the transmission. The analysis of the water density was done in applying different current relative to humidity of the fuel cell. A line profile was taken along the width of the MEA (yellow line) to extract intensity values. The water density was calculated and plotted relative to the cell width. Higher water density values correspond to lower intensity values and therefore higher absorption.

Fuel cell neutron experiments were performed with scintillator detector at selected relative humidity 30% under different applied current densities: 2A, 6A and 8.5A. From our experiment the obtained data for 6A applied current at 30% humidity value, the average water density is: $\langle\rho\rangle \approx 0.01099 \text{ g/cm}^3$ and for 8.5A applied current, at 30% humidity the average density is: $\langle\rho\rangle \approx 0.03473 \text{ g/cm}^3$. Clearly we see that for a constant humidity value of 30%, the current density significantly influences the water content and water distribution inside MEA referring to Table 5.9.

Results we also obtained for measurements performed at 90% humidity under 0A, 2A and 6A applied current densities. For 0A and 2A applied current at 90% humidity value the average density are: $\langle\rho\rangle \approx 0.00597 \text{ g/cm}^3$, $\langle\rho\rangle \approx 0.01757$ and for 6A applied current at 90% humidity the average density is $\langle\rho\rangle \approx 0.03251 \text{ g/cm}^3$ referring to Table 5.10.

Humidity also plays an important role and more humidity we applied more water flows inside the channels of the MEA. I_o is not I_{dry} because we couldn't have a totally dry membrane of MEA; for example we have

taken the ratio: $T_{water} = \frac{I_{wet, \max \text{ current}, 90\% \text{ wet}}}{I_{dry, \min \text{ current}, 90\% \text{ wet}}}$ where I_{dry} represents the intensity of the minimum applied current at a given humidity value (high intensity counts). From the intensity counts, we could calculate the (average) value of the water density ρ_{water} .

If we consider humidity only, we clearly see that more humidity we apply to the MEA more water is created inside the membrane. If we compare the density values for 30% humidity values for 6A applied density current we have average density: $\langle \rho \rangle_{30\%, 6A} \approx 0.01099 \text{ g/cm}^3$ and for 90% humidity values for 6A applied density current: $\langle \rho \rangle_{90\%, 6A} \approx 0.01757 \text{ g/cm}^3$ referring to Table 5.11. The results indicate that humidity plays a significant role in water distribution and density created inside MEA.

The average water density for measurements done with IP-ND, for 6A and 8.5A applied density current with 90% relative humidity applied inside the fuel cell is: $\langle \rho \rangle = 0.0303 \text{ g/cm}^3$ (see Table 5.12).

In all measurements and from all graphs it can be seen that more current we applied for a constant humidity more water is created, referring to figures 5.9.8, 5.11.8 and 5.11.9. Increasing the current density with 1A we expect a water density increase of $0.00375 \pm 1.80623 \cdot 10^{-4} \text{ g/cm}^3$ for 30% humidity and $0.00449 \text{ g/cm}^3 \pm 4.36026 \cdot 10^{-4} \text{ g/cm}^3$ for 90% humidity.

The best image of the inner structure of the MEA was acquired with neutron imaging plate (see figure 5.12.1) in which the spatial resolution cannot compete with scintillator detector. Although IP-ND detector offers us a better resolution and higher efficiency to localize water, the poor reproducibility of the IP-ND we lost a lot of measurements. The Triga reactor offers us not a high neutron flux, which is was another drawback for these kinds of measurements.

Another problem that we faced during measurements was fuel cell itself. Often the applied current was not showing the expected values, consequently such values, so the fuel was not working in the proper way.

These experiments and NR images technique provide a way to investigate liquid water created in anode and the cathode and will provide new prediction and control in water management in fuel cells. Knowing where water accumulates with more certainty helps us to understand the water transport in PEMFC.

Chapter 6

Heat Exchanger Radiography

6.1 Introduction

A **heat exchanger** is a piece of equipment built for efficient heat transfer from one medium to another. A solid wall to prevent mixing may separate the media or they may be in direct contact. They are widely used in space heating, refrigeration, air conditioning, power plants, chemical plants, petrochemical plants, petroleum refineries, natural gas processing, and sewage treatment. The classic example of a heat exchanger is found in an internal combustion engine in which a circulating fluid known as engine coolant flows through radiator coils and air flows past the coils, which cools the coolant and heats the incoming air. Another type of heat exchanger is the plate heat exchanger. One is composed of multiple, thin, slightly separated plates that have very large surface areas and fluid flow passages for heat transfer. This stacked-plate arrangement can be more effective, in a given space, than the shell and tube heat exchanger. Advances in gasket and brazing technology have made the plate-type heat exchanger increasingly practical. In HVAC applications, large heat exchangers of this type are called *plate-and-frame*; when used in open loops; these heat exchangers are normally of the gasket type to allow periodic disassembly, cleaning, and inspection. There are many types of permanently bonded plate heat exchangers, such as dip-brazed, vacuum-brazed, and welded plate varieties, and they are often specified for closed-loop applications such as refrigeration. Plate heat exchangers also differ in the types of plates that are used, and in the configurations of those plates. Some plates may be stamped with "chevron", dimpled, or other patterns, where others may have machined fins and/or grooves [wikipedia.org/wiki/Plate_heat_exchanger].

6.2 Design of Plate and Frame Heat Exchangers

The plate heat exchanger (PHE) is a specialized design well suited to transferring heat between medium- and low-pressure fluids [www.lifetime-reliability.com]. Welded, semi-welded and brazed heat exchangers are used for heat exchange between high-pressure fluids or where a more compact product is required. In place of a pipe passing through a chamber, there are instead two alternating chambers, usually thin in depth, separated at their largest surface by a corrugated metal plate. The plates used in a plate and frame heat exchanger are obtained by one piece pressing of metal plates. Stainless steel is a commonly used metal for the plates because of its ability to withstand high temperatures, its strength, and its corrosion resistance. The plates are often spaced by rubber sealing gaskets, which are cemented into a section around the edge of the plates. The plates are pressed to form troughs at right angles to the direction of flow of the liquid, which runs through the channels in the heat exchanger. These troughs are arranged so that they interlink with the other plates, which, forms the channel with gaps of 1.3-1.5 mm between the plates. The plates produce an extremely large surface area, which allows for the fastest possible transfer. Making each

chamber thin ensures that the majority of the volume of the liquid contacts the plate, again aiding exchange. The troughs also create and maintain a turbulent flow in the liquid to maximize heat transfer in the exchanger. A high degree of turbulence can be obtained at low flow rates and high heat transfer coefficient can then be achieved. A plate heat exchanger consists of a series of thin, corrugated plates, which are mentioned above and is shown in the figure 6.2.1.

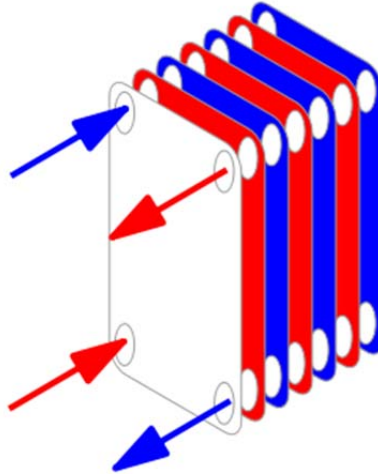


Figure 6.2.1 Conceptual diagram of a plate heat exchanger.

These plates are gasketed, welded or brazed together depending on the application of the heat exchanger. The plates are compressed together in a rigid frame to form an arrangement of parallel flow channels with alternating hot and cold fluids. As compared to shell and tube heat exchangers, the temperature approach in a plate heat exchangers may be as low as 1°C whereas shell and tube heat exchangers require an approach of 5°C or more. For the same amount of heat exchanged, the size of the plate heat exchanger is smaller, because of the large heat transfer area afforded by the plates (the large area through which heat can travel). Increase and reduction of the heat transfer area is simple in a plate heat-exchanger, through the addition or removal of plates from the stack [Paulos, 2013], [www.gea-phe.com].

Figure 6.2.2 shows how a plate heat exchanger PHE works. The heat energy transfer across the plate acts to change the temperatures of the two media. The hotter one becomes cooler, and the colder one becomes hotter.

One media (red color) enters at a top flows through every other channel, than leaves at the bottom; The other media enters at the bottom, flows through remaining channel then leaves at the top. Plate heat exchangers use the thin plates to keep two media of different temperatures apart while allowing heat energy to flow between them through the plate [www.gea-phe.com].

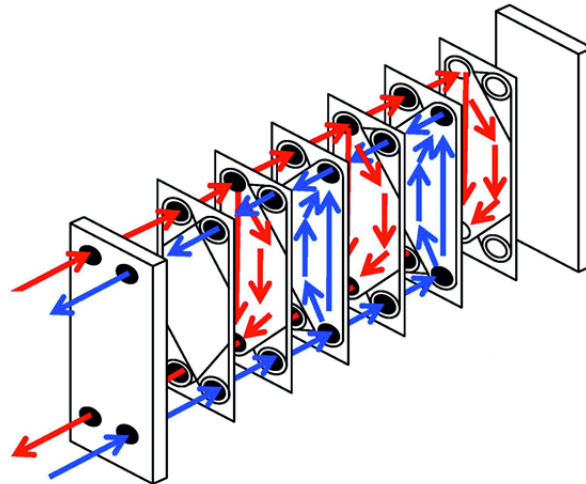


Figure 6.2.1 The heat exchanger that uses multiple layers of plates [www.gea-phe.com].

Figure 6.2.3 (left) shows a cross section of the plates. Because of plate thinness, a plate heat exchanger can work with a much closer temperature difference between the two media than other heat exchangers and still get a good heat transfer at lower flow rates, thereby saving pumping and operational costs. It is possible to cool a liquid down to nearly 1°C of the hot medium. Heat recovery of up to 85% to 90% is quite common, making the plate heat exchanger the most efficient heat exchanger for heat recovery, particularly for applications where the temperature difference between the media is small.



Figure 6.2.2 The heat transfer plate where plates are used to transfer the heat from the media on one side of the media to the media on the other side [www.gea-phe.com].

6.3 Heat Pump

A **heat pump** is a device that transfers heat energy from a heat source to a heat sink against a temperature gradient [wikipedia.org/wiki/Plate_heat_exchanger]. Heat pumps are designed to move thermal energy opposite the direction of spontaneous heat flow. A heat pump uses some amount of external high-grade energy to accomplish the desired transfer of thermal energy from heat source to heat sink. While compressor-driven air conditioners and freezers are familiar examples of heat pumps, the term “heat pump” is more general and applies to HVAC devices used for space heating or space cooling. When a heat pump is used for heating, it employs the same basic refrigeration-type cycle used by an air conditioner or a refrigerator but in the opposite direction, releasing heat into the conditioned space rather than the surrounding environment. In this use, heat pumps generally draw heat from the cooler external air or from the ground.

Heat Pumps and absorption heat pumps are an important and promising technology to decrease energy consumption regarding heating and cooling and increase overall efficiencies of industrial processes. To further develop these technologies it is important to understand two-phase flow regimes in heat exchangers, in particular plate heat exchangers. For that an experiment was set up at the Vienna University of Technology, where a small plate heat exchanger was analysed by neutron radiography to visualize two-phase regimes inside.

6.4 Neutron Radiography of a Plate Heat Exchange

The heat exchanger is commercially available at Alpha Laval Company and consisted of 20 sheets of metal with about 20 cm height and 7 cm width see figure 6.4.1. Plate heat exchangers provide efficient heat transfer with a small footprint. They are maintenance free, provide a long service lifetime and can withstand high temperatures and extremely high design pressures. They are used in a range of duties including cooling, heating, and evaporation and condensing [www.alfalaval.de].

The material of the heat exchanger was stainless steel brazed with nickel and working fluids flow through the gaps between plates. A commercial plate heat exchanger was visualized by thermal neutron radiography as a non-destructive method. Flow visualization images were conducted at NR II station at TRIGA reactor in Atominstitut ATI using 100 μm thick scintillator with cooled CCD camera with exposure time 300 seconds. Neutron beam was directed at the front face (perpendicularly) of the heat exchanger. White spots due to the direct irradiation were removed using median filters. The heat exchanger was put into the neutron beam with its connectors facing the beam, so the captured images always show a total value over all 20 plates. Since the whole setup was only designed as feasibility study there was no measurement of flow rates or temperatures. The neutron beam consisted of well-thermalized neutrons and had a diameter of 9 cm and a neutron flux of $1.3 \times 10^5 \text{ n/cm}^2\text{s}$. Three continuous frames with the interval of 2/30 s are shown for each figure.



Figure 6.4.1 *The heat plate exchanger used in the experiment at NR II station at ATI produced from Alpha Laval Company.*

6.5 Results and Discussion

Water and air are used as the working fluids. The difference of a water filled or air filled heat exchanger is clearly visible as well as the inner structure of the heat exchanger. Water in the channels is clearly visualized by neutron radiography. Water flow along both sides was also observed. Figures below show images of the PHE filled with air, whereas the images are realized with ^6Li scintillator with 300 sec exposure time. Figure 6.5.1 shows the inner structure of the dry heat exchanger (only air is flowing). Figure 6.5.2 shows the plate heat exchanger PHE, filled with water. Water in the channels is clearly visualized by this detector. Figure 6.5.3 shows the inner structure and clearly we can see that water is not flowing in a uniform way inside plate heat exchanger (see marked area). Non homogeneous liquid distribution was clearly shown (see figure 6.5.3). Only one side (primary) of the heat exchanger was connected and filled with water, whereas the other (secondary) side was left unconnected and thus dry. A few centimetres away from the connector there was a T piece to mix water with air to generate two-phase regimes (water/air) in the heat exchanger (see figure 6.4.1)

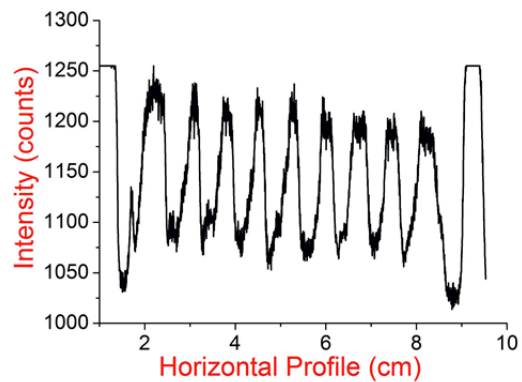
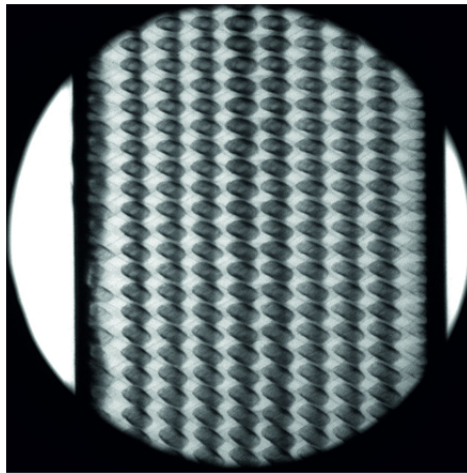


Figure 6.5.1 *Left:* Dry heat exchanger image; the visualized image is made using ${}^6\text{Li}$ scintillator with cooled CCD camera. **Right:** The inner structure of the plate heat exchanger made by brazing sheets of stainless steel.

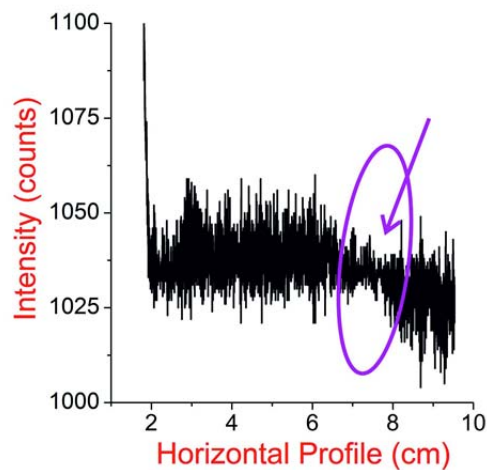
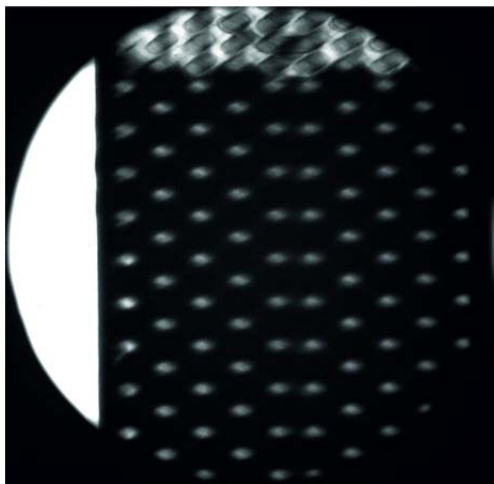


Figure 6.5.2 *Left:* The heat exchange filled with water. Water and air were used as fluids. Darker parts show thicker liquid thickness. **Left:** Intensity versus horizontal line profile of the PHE where water flows inside the marked area shows a non-homogeneous water distribution inside the PHE.

In the application for gas–liquid two- phase mixture the dynamic flow behaviours may strongly affect the heat transfer performance [Baba, 2009], [Furui, 2004], [Ozawa, 2004]. Water and air are used as the working fluids. The plate configuration is shown in figure 6.5.3 (left). Figure 6.5.3 (right) shows the inner structure of the heat exchanger where water and air is flowing simultaneously.

In such a case, flow visualization is very efficient to know and clarify the conditions of the two-phase flow behaviours [Aasano, 2005].

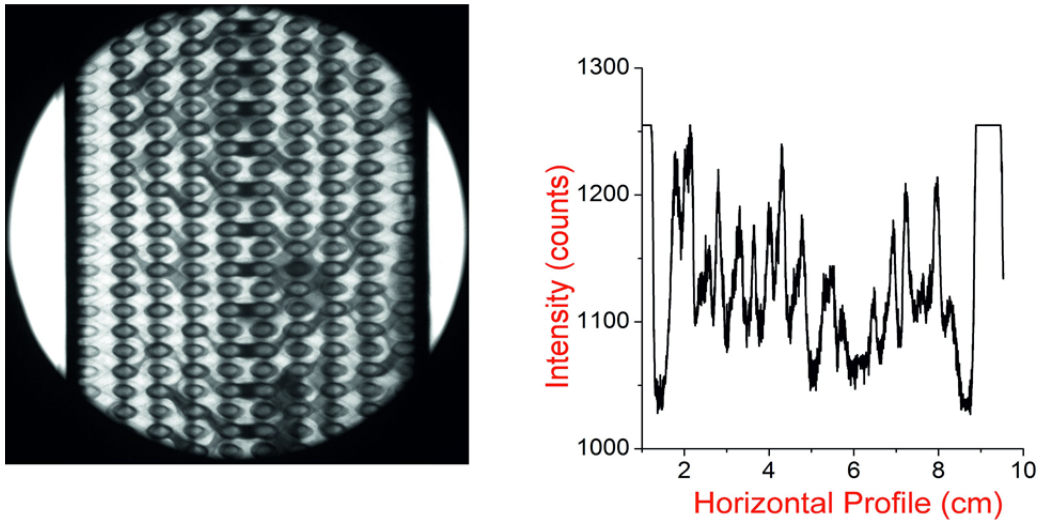


Figure 6.5.3 *Left:* Water in the channels is clearly visualized by neutron radiography. Water flow along both sides is observed. **Right:** Intensity versus horizontal line profile of the PHE where working fluids water and air flow as two phase mixture.

6.6 Summary

It has been shown that Neutron Radiography NR method can be applied to flow visualization of water-air which is difficult using other methods. This was a non-destructive test of water-air flows in a plate heat exchanger and was clearly visualised by this method.

To increase the efficiency of absorption heat pumps it is essential to understand the two-phase regime in heat exchangers. Furthermore the concentration of solutions which are used in absorption processes, e.g. $\text{NH}_3/\text{H}_2\text{O}$ or $\text{H}_2\text{O}/\text{LiBr}$, can be determined as a time mean value at a certain point of such a heat exchanger. With this method it is possible to map the mass transfer, (gas to liquid absorption, liquid to gas evaporation) which is most important to improve state of the art plate heat exchangers with regard to the absorption and the evaporation process. Of great interest in the future experiments, it will be using a portable neutron source which is a very useful system for routine material investigations.

Chapter 7 Conclusions

Wide ranges of radiograph experiments in various scientific disciplines based on neutron interaction (mainly absorption) with matter were performed. It has been shown that neutron radiography is a very efficient, non-destructive method to obtain information about the inner structure of materials of elements of interest and the presence of inhomogeneities within the sample, Hydrogen quantification and water distribution. All neutron transmission experiments were carried out at NR II station at ATI.

Detection system at NR II station at Atominstitut is mainly based on ^6Li - detector in combination with CCD camera and IP-ND.

By improving the resolution from 340 μm to 100 μm for the ^6Li detector also the efficiency and sensitivity for these type of detectors was positively influenced. These are important parameters to improve the quality of radiograph images. With the IP-ND with high resolution (50 μm) visualization had been successfully performed at low neutron flux. The IP-ND offers a much better resolution compared to the ^6Li scintillator detector and a higher sensitivity but this set-up does not permit repetitive imaging, which became evident during neutron radiography experiments with fuel cell samples.

The strong absorbing element like ^{10}B present in steel alloyed sample plates is not homogeneously distributed as boron steel materials are used in neutron shielding, this is a very important feature. The sample plates (which were produced from Böhler Bleche company) were exposed at a low neutron flux of $1.3 \times 10^5 \text{ n/cm}^2\text{s}$ and the transmission through plates was measured. Carrying out the neutron transmission experiments of boron steel alloyed plates gave us the possibility to study: the transmission through strong absorbing materials, the size and the distribution of boron element inside steel matrix, to estimate and correct secondary effects like background factor. The estimation and correction of background factor was done and analyzed with help of neutron transmission experiments through boron polyethylene plates. The size and distribution of boron present in steel samples was done with help of Monte Carlo simulation method. The good agreement between transmission experiments through boron steel plates and simulated data allowed us to make a good estimation: of background contribution and scattering effects, micro inhomogeneity in range of 20 μm . These factors have a strong influence on transmission measurements results.

The neutron imaging method was applied to hollow micro spheres filled with hydrogen, which can be used in the future for hydrogen storage. The data on the hydrogen content obtained for these kinds of sample are needed to understand better the diffusion process of hydrogen through micro hollow sphere walls, which depend on several influence factors, like pressure, temperature and glass material.

Neutron imaging, as a non-destructive method, allowed us to analyse fuel cells during the operation. This method was successfully used to visualize and quantify the water distribution inside fuel cells under different conditions. As neutrons are sensitive to small amounts of water, one can obtain information the amount of liquid water inside fuel cells in order to have deeper understanding of fuel cell performance.

Further measurements were performed to study the inner structure of *plate* of heat exchangers. The air-water phase was clearly and successfully visualized using the NR method. The characteristics of heat exchangers heavily depend on the water movement inside, where with the NR method it was possible to visualize the two-phase regime. Liquid water distribution depends on the inner structure of the plate heat exchangers which can be very good visualized as well with Neutron Radiography method.

Chapter 8 References

- Abbasi, N.: “The application of Fourier Analysis in Solving the Computed Tomography CT problem” July 3, 2010.
- Anderson, I. S., R. L. McGreevy, H. Z. Bilheux: “Neutron Imaging and Applications” A reference to the Imaging Community. ISBN 978-0-387-78692-6, Springer 2009.
- Arif, M., D.L. Jacobson, D.S. Hussey: “Neutron imaging study of the water transport in operating fuel cells” FY 2008 Annual Progress Report.
- Asano, H., N. Takenaka, T. Wakabayashi, T. Fujii: “Visualization and void fraction distribution of downward gas–liquid two-phase flow in a plate heat exchanger by neutron radiography” Nuclear Instruments and Methods in Physics Research A 542 (2005) 154-160.
- Asano, H.: “Visualization and void fraction measurements of gas–liquid two-phase flow in a commercial plate heat exchange by thermal neutron radiography” IEEE Transactions on nuclear science Vol. 52, No. 1, February 2005.
- Baba, T., S. Harada, H. Asano, K. Sugimoto, N. Takenaka, K. Mochiki: “Nondestructive inspection for boiling flow in plate heat exchanger by Neutron radiography” Nuclear Instruments and Methods in Physics Research A, 2009.
- Bacon, G. E.: “Neutron Diffraction 2nd edition” 1962, Oxford University Press.
- Barmakov, J. N., E.P. Bogolubov, A.P. Koshelev, V.I. Mikerov, V.I. Ryzhkov: “Neutron radiography; Proceedings of the 7th World Conference” Rome, Italy, 2002, p. 207.
- Bastürk, M., J. Arzmann, W. Jerlich, N. Kardjilov, E. Lehmann, M. Zawisky: “Analysis of neutron attenuation in boron-alloyed stainless steel with neutron radiography and JEN-3 gauge“ Journal of Nuclear Materials 2005, 341, 189-192.
- Bastürk, M., N. Kardjilov, E. Lehmann, M. Zawisky. “Monte Carlo simulation of neutron transmission of boron alloyed steel” IEEE transactions on nuclear science, 2005, Vol. 52(2), 394-399.
- Bastürk, M.: “Material Inspections with low Energy neutrons and 3D Image Reconstruction” PhD thesis TU-Wien (2003).
- Bazylak, A.: “Liquid water visualization in PEM fuel cells: “A review” International Journal of Hydrogen Energy 2009, 34, 3845-3857.
- Bellows, R. J., M. Y. Lin, M. Arif, A. K. Thompson, D. Jacobson: “Neutron Imaging Technique for In Situ Measurement of Water Transport Gradients within Nafion in Polymer Electrolyte Fuel Cells” Journal of the Electrochemical Society 1999, 146(3), 1099-1103.
- Berger, H., F. Iddings: “Neutron Radiography“ Louisiana State University, August 1998.
- Bichler, D.: “Entwicklung eines Helium speicher systems basierend auf Mikrogaskugeln“ Diplomarbeit TU-Wien 2013.
- Böhler-Bleche GmbH, NEUTRONIT Archives, AV4/0281/77 (1997), natural boron-alloyed stainless steel sheets (UNS S30467 – Type 304B7),
- Boillat, P., D. Kramer, B.C. Seyfang, G. Frei, E. Lehmann, G.G. Scherer, A. Wokaun, Y. Ichikawa, Y. Tasaki,

- K. Shinohara: "In situ observation of the water distribution across a PEFC using high resolution neutron radiography" *Electrochemistry Communications* 2008, 10, 546 – 550.
- Bruckner, G.: "Position sensitive detection of thermal neutrons with solid state detectors (Gd Si planar detectors)" *Nuclear Instruments and Methods in Physics Research A* 424, 183 1999.
 - Buchberger, Th.: "Neutronenradiographische Untersuchungen an Tantal-Tritium-Helium-Systemen" PhD thesis TU- Wien (1986).
 - Carpenter, J. M.: "Detectors for slow neutrons" 10th National School on Neutron and X-ray Scattering" Sept 2008.
 - Chen, Y.S., H. Peng.: "A segmented model for studying water transport in a PEMFC" *Journal of Power Sources* 2008, 185, 1179-1192.
 - Chen, Y.S., H. Peng, Daniel S. Hussey, David L. Jacobson, D.T. Tran, T. Abdel-Baset, M. Biernacki: "Water distribution measurement for a PEMFC through neutron radiography" *Journal of Power Sources*, 2007, Vol.170, issue 2, 376-386.
 - Cheng, Y.T., D.F.R. Mildner: "A sensitive high resolution neutron imaging detector" *Nuclear Instruments and Methods in Physics Research A* 454 (2000) 452-459.
 - Domanus, J. C.: "Practical Neutron Radiography" Kluwer Academic Publishers Dordrecht/Boston/London, 1992.
 - Dong, Q., J. Kull, M.M. Mench: "Real-time water distribution in a polymer electrolyte fuel cell" *Journal of Power Sources* 2005, 139, 106-114.
 - Dubus, F., U. Bonse, M. Zawisky, M. Baron, and R. Loidl: "First Phase Contrast Tomography with Thermal Neutrons" *IEEE Transactions on Nuclear Science*, Vol. 52, No. 1, February 2005.
 - Dyrnjaja, E., M. Zawisky:" The influence of boron micro-inhomogeneities on neutron transmission" *Nuclear Instruments and Methods in Physics Research B* 347 (2015) 47-51.
 - Dyrnjaja, E., S. Hummel, M. Keding, M. Th. Smolle, J. Gerger, M. Zawisky: "Neutron transmission measurements on hydrogen filled microspheres" *Instrumental and Method B* 318 (2014) 241-244.
 - Eijk, van C. W. E.: "Inorganic scintillators in medical imaging detectors" *Nuclear Instruments and Methods in Physics Research A* 509 pp.17-25, 2003.
 - Feigl, B., H. Rauch: "Performance of the Gd-Neutron Detector" *Nuclear Instruments and Methods in Physics Research* 61, 349, 1968.
 - Fornasiero, P., Graziani, M.: "Renewable Resources and Renewable Energy: A Global Challenge" 2007 by Taylor & Francis Group, LLC ISBN-10: 0-8493-9689-1, 2007.
 - Fujine, Sh., K. Yoneda, M. Kamata, M. Etoh: "Application of imaging plate neutron detector to neutron radiography" *Nuclear Instruments and Method in Physics Research* 1999, A 424, 200-208.
 - Furua, S., H. Umekawaa, M. Tsuzukia, M. Okuraa, M. Ozawaa, N. Takenaka: "Visualization of fluidized-bed heat exchanger in upward/downward flow condition by neutron radiography" *Nuclear Instruments and Methods in Physics Research A* 542 (2005) 161–167.
 - Grosse, M., E.H. Lehmann, P. Vontobel, M. Steinbrueck: "Quantitative determination of absorbed hydrogen in oxidized zircaloy by means of neutron radiography" *Nuclear Instruments and Methods in Physics Research A*, 2006 (566), 739 – 745.

- Grünzweig, C., G. Frei, E. Lehmann, G. Kühne, C. David: “Highly absorbing gadolinium test device to characterize the performance of neutron imaging detector systems” *Review of Scientific Instruments* 78(5):053708, 2007.
- Hacker, V.: “Fuel Cell Activities at TU Graz” Institute of Chemical Engineering and Environmental Technology, Graz University of Technology, IEA Workshop TU Graz September 1st, 2010.
- Haga, Y. K., S. Kumazawa, N. Niimura: “The optimization and g-ray effects of the neutron imaging plate” *Journal of Physics and Chemistry of Solids* 60 (1999) 1619–1621.
- Hajek, M., W. Schöner: “Spectral distribution of neutron fluence at the thermal column of the Triga Mark-II research reactor” Atomic Institute of the Austrian Universities AIAU 21313 2001.
- Hameed, F.: ”Upgrading and new applications of a neutron imaging facility” PhD thesis TU-Wien (2009).
- Hamnett, A.: “Handbook of Fuel Cells – Fundamentals, Technology and Applications” University of Strathclyde, Glasgow, UK, 2010 John Wiley & Sons, Ltd. ISBN: 978-0-470-97400-1.
- Harms, A., A. B. K., Garside, P. S. Chan: “Edge-spread function in neutron radiography” *Journal of Applied Physics* Vol 43, Issue 9 pp 3863-3867, 1972.
- Hassanein, R. K., E. Lehmann, P. Vontobel: “Methods of scattering corrections for quantitative neutron radiography” *Nuclear Instruments and Methods in Physics Research A* 542, 353–360, 2005.
- Hassanein, R. K., F. de Beer, N. Kardjilov, E. Lehmann: “Scattering correction algorithm for neutron radiography and tomography tested at facilities with different beam characteristics” *Physica B* 385–386, 1194–1196, 2006.
- Hassanein, R. K., H. O. Meyer, A. Carminat, M. Estermann, E. Lehmann, P. Vontobel: “Investigation of water imbibition in porous stone by thermal neutron radiography” *Journal of Physics D: Applied Physics* 39 4284–4291, 2006.
- Hassanein, R. K., PhD Thesis: “Correction methods for the quantitative evaluation of thermal neutron tomography” ETH No. 16809, (2006).
- Hickner, M. A., N.P. Siegel, K.S. Chen, D.N. McBrayer, D.S. Hussey, D.L. Jacobson, M. Arif: ”Real-Time Imaging of Liquid Water in an Operating Proton Exchange Membrane Fuel Cell” *Journal of the Electrochemical Society* 2006, 153(5), A902-A908.
- <http://bazylak.mie.utoronto.ca/research/>
- <http://de.wikipedia.org/wiki/Brennstoffzelle>
- http://dspace.dial.pipex.com/johncaunt/neutron_shielding
- http://en.wikipedia.org/wiki/Plate_heat_exchanger
- <http://pdg.lbl.gov/2015/listings/rpp2015-list-n.pdf>
- <http://www.ati.ac.at/reactor/technischdaten/>.
- <http://www.fuelcellenergy.com>
- http://www.fujifilm.com/products/life_science_systems/science_imaging
- http://www.fujifilm.com/products/life_science_systems/science_imaging
- http://www.fujifilm.com/products/life_science_systems/science_imaging
- <http://www.gea-phe.com/>

- http://www.thermo.com/eThermo/CMA/PDFs/Product/productPDF_24116.pdf.
- Hussey, D. S., D.L. Jacobson, M. Arif, J.P. Owejan, J.J. Gagliardo, T.A. Trabold: "Neutron images of the through-plane water distribution of an operating PEM fuel cell" *Journal of Power* 2007, 172, 225-228.
- Kak, A., Slaney, M.: "Principles of Computerized Tomographic Imaging" ISBN-10 0-89871-494, 2001.
- Karasawa, Y., S. Kumazawa, N. Niimura: "Gammy-ray sensitivity and shielding of a neutron imaging plate" *Journal of Applied Crystallography*, 1999, Vol 32, 878-882.
- Karasawa, Y., S. Kumazawa, N. Niimura: "The character and application of neutron imaging plate" *Physica B* 241-243 pp 139-141, 1998.
- Kardjilov, N: "Further developments and applications of radiography and tomography with thermal and cold neutrons" PhD thesis TU-Münich 2003.
- Keding, M., A. Reissner, D. Bichler, M. Tajmar: "Novel hydrogen storage solutions for space and aerospace applications" In *Hydrogen and Fuel Cells*, 2011.
- Keding, M., G. Schmid, M. Tajmar: "Innovative hydrogen storage in hollow glass-microspheres" In *HFC 2009 Conference + Exhibition Conference Proceedings*, 2009.
- Kharfi, F., M. Bastürk, A. Boucenna: "Characterization of weak, fair and strong neutron absorbing materials by means of neutron transmission: Beam hardening effect" *Nucl. Instr. And Meth. A* 565 (2006) 416-422.
- Kharfi, F.: "Imaging and Radioanalytical Techniques in Interdisciplinary Research – Fundamentals and Cutting Edge Applications" March 2013. ISBN 978-953-51-1033-0.
- Kim, S., M.M. Mench: "Investigation of Temperature-Driven Water Transport in Polymer Electrolyte Fuel Cell: Phase-Change-Induced Flow" *Journal of the Electrochemical Society*, 2009, 156 B, 353-362.
- Kim, T. J., C.M. Sim, M.H. Kim: "Research on water discharge characteristics of PEM fuel cells by using neutron imaging technology at the NRF, HANARO" *Applied Radiation and Isotopes* 2008, 66, 593-605.
- Kobayashi, H., M. Satoh: "Basic performance of a neutron sensitive photo stimulated luminescence device for neutron radiography" *Nuclear Instruments and Methods in Physics Research A* 424 1-8, 1999.
- Koerner, S., B. Schillinger, P. Vontobel, H. Rauch: "A neutron tomography facility at a low power research reactor" *Nuclear Instruments and Methods in Physics Research A* 471 69–74, 2001.
- Koerner, S.: "Digital image processing in neutron radiography" PhD thesis TU-Wien (2000).
- Kramer, D., E. Lehmann, G. Frei, P. Vontobel, A. Wokaun, G.G. Scherer: "An on-line study of fuel cell behavior by thermal neutrons" *Nuclear instruments and Methods in Physics Research* 2005, A 542, 52-60.
- Kumbur, E. C., K.V. Sharp, M.M. Mench: "Liquid droplet behavior and instability in a polymer electrolyte fuel cell flow channel" *Journal of Power Sources* 2006, 161, 333-345.
- Lamarsh, J. R.: "Introduction to Nuclear Reactor Theory" New York University 1966
- Lefmann, K.: "Neutron Scattering: Theory, Instrumentation and Simulation" Department of Materials Research Riso National Laboratory Technical University of Denmark August 25, 2007
- Lehmann, E. H., Kardjilov, N., P. Vontobel: "Hydrogen distribution measurements by neutrons" *Applied Radiation and isotopes*, 2004 (61) 503 – 509.
- Lehmann, E. H., P. Boillat, G. Scherrer, G. Frei: "Fuel cell studies with neutrons at PSI's neutron imaging facilities" *Nuclear Instruments and Method in Physics Research* 2009, A 605, 123-126.

- Lehmann, E. H., P. Vontobel, G. Frei, C. Brönnimann: “Neutron imaging-detector options and practical results” *Nuclear Instruments and Methods in Physics Research A* 531 (2004) 228–237.
- Li, X. G., I. Sabir, J. Park: “A flow channel design procedure for PEM fuel cells with effective water removal”. *Journal of Power Sources* 2007, 163, 933-942.
- Lim, K. L., Kazemian, H., Yaakob, Z.: “Solid-state Materials and Methods for Hydrogen Storage: A Critical Review” *Chem. Eng. Technol.* 2010, 33, No. 2, 213–226, DOI: 10.1002/ceat.200900376,
- Lima, C. T. S., V. R. Crispim, W. M. S. Santos: “Gadolinium sheet converter for neutron radiography” *Applied Radiation and Isotope* 65 (2007), 1381-1385.
- Litser, S., D. Sinton, N. Djilali: “Ex situ visualization of liquid water transport in PEM fuel cell gas diffusion layers” *Journal of Power Sources* 2006, 154, 95-105.
- Litvin, V. S.: “ZnS (Ag)⁶LiF and LiI (Eu) scintillators and silicon photomultipliers for thermal neutron detectors with high space and time resolution” *Bulletin of the Russian Academy of Science; Physics*, 2009, Vol 73, No 2 pp. 219-221.
- Lu, Z., C. Rath, G. Zhang, Satish G. Kandlika: “Water management studies in PEM fuel cells, part IV: Effects of channel surface wet ability, geometry and orientation on the two-phase flow in parallel gas channels” *International Journal of Hydrogen Energy*, 2011, Volume 36, Issue 16, 9864–9875.
- Ludlow, D.J., C.M. Calebrese, S.H. Yu, C.S. Dannehy, D.L. Jacobson, D.S. Hussey, M. Arif, M.K. Jensen, G.A. Eisman: “PEM fuel cell membrane hydration measurement by neutron imaging” *Journal of Power Sources* 2006, 162, 271-278.
- Markovic, A., D. Stoltenberg, D. Enke, E.U. Schluender, A. S. Morgenstern: “Gas permeation through porous glass membranes” *Journal of Membrane Science*, 2009 (336), 17-31.
- Masalovich, S., A. Ioffea, M. Schlappa, H. von Seggern, E. Kussela, Th. Bruckela: “Optimization of a neutron image plate detector with low g-sensitivity” *Nuclear Instruments and Methods in Physics Research A* 539 pp 236–249, 2005.
- Mench, M.M., Q.L. Dong, C.Y. Wang: ”In situ water distribution measurements in a polymer electrolyte fuel cell“ *Journal of Power Sources* 2003, 124, 90-98.
- Modelica fuel cell library- Fuel Cell System 2014.
- Mohtadi, R., Matsunaga. T.: ”Hollow Glass Microspheres as Micro Media for Complex Metal Hydrides Hydrogen Storage Compounds”
- Monte Carlo Particle: “MCNPX 2.4.0 version” Transport Code System for Multiparticle and High Energy Applications OAK Ridge, National Laboratory (2004).
- Monte Carlo particle: “MCNPX version 2.4.0, MCNPX-DATA” Oak ridge National Laboratory, 2004.
- Mosdale, R., G. Gebel, M. Pineri: “Water profile determination in a running proton exchange membrane fuel cell using SANS” *Journal of science* 118(1996) 269-277.
- Nice, K., J. Strickland: “<http://auto.howstuffworks.com/fuel-efficiency/alternative-fuels/fuel-cell2.htm>”.
- Okada, T. A., G. Xie, Y. Tanabe: “Theory of water management at the anode side of polymer electrolyte fuel cell membranes” *Journal of Electro analytical Chemistry* 1996, 413, 49-65.
- Owejan, J. P., T.A. Trabold, D.L. Jacobson, D.R. Baker, D.S. Hussey, M. Arif: “In situ investigation of water

- transport in a operating PEM fuel cell using neutron radiography”: Part 2 “Transient water accumulation in an interdigitated cathode flow field”, *International Journal of Heat and Mass Transfer* 2006, 49, 4721-4731.
- Ozawaa, M., H. Umekawa, S. Furuia, K. Hayashia, N. Takenaka: “Quantitative flow visualization of fluidized-bed heat exchanger by neutron radiography” *Applied Radiation and Isotopes* 61 (2004) 715–724.
 - Park, J., X. Li, D. Tran, T. Abdel-Baset, D.S. Hussey, D.L. Jacobson M. Arif: “Neutron imaging investigation of a PEM fuel cell” *International Journal of Hydrogen Energy* 2008, 33, 3373-3384.
 - Pasagullari, U., C.Y. Wang: “Liquid Water Transport in Gas Diffusion Layer of Polymer Electrolyte Fuel Cells” *Journal of the Electrochemical Society* 2004, 151, A399-A406.
 - Paulos, J.: “Anatomy and Function of a Plate Heat Exchanger” *GEA Heat Exchangers*, December 2013.
 - Peters, T.: “CT Image Reconstruction” Robarts Research Institute, London Canada <http://www.robarts.ca/terry-peters>
 - Pleinert, H., E. Lehmann, S. Korner: “Design of a new CCD-camera neutron radiography detector” *Nuclear Instruments and Methods in Physics Research A*, 399, pp. 382–390, 1997.
 - Rambach, G. D.: “Hydrogen Transport and Storage in Engineered Glass Microspheres” DOE Hydrogen Program Contractor’s Review Meeting Coral Gables, 1995 FL April 1&21.
 - Rauch, H., A. Zeilinger: ”Hydrogen transport studies using neutron radiography“ 1977 *Atomic Energy Review*, 15(2).
 - Rauch, H., M. Zawisky, Ch. Stellmach, P. Geltenport: “Giant Absorption cross section of ultracold neutrons in gadolinium“ *Physical Review Letters*, 1999, 83, 4955-4958.
 - Rehacek, J., Z. Hradil, M. Zawisky, W. Treimer, M. Strobl: “Maximum-likelihood absorption tomography” *Europhysics Letters* 59 (5), pp. 694-700 (2002).
 - Satija, R., D.L. Jacobson, M. Arif, S.A. Werner: “In situ neutron imaging technique for evaluation of water management systems in operating PEM fuel cells” *Journal of Power Sources* 2004, 129, 238-245.
 - Schillinger, G., E. Lehmann: “Detectors for Neutron Imaging” *Neutron News* 17 (1) 19, 2006.
 - Schmid, G.: ”Beschichten von Mikrogaskugeln zur Wasserstoffspeicherung in Verbindung mit NaBH4“ Diplomarbeit TU-Wien 2012.
 - Schröder, A., K. Wippermann, W. Lehnerta, D. Stoltena, T. Sanders, T. Baumhöferb, N. Kardjilovc, A. Hilgerc, J. Banhartc, I. Mankec: “The influence of gas diffusion layer wettability on direct methanol fuel cell performance: A combined local current distribution and high resolution neutron radiography study” *Journal of Power Sources* 2010, 195, 765 – 4771.
 - Sears, V. F.: “Neutron Optics” Oxford University Press, 1989.
 - Sears, V. F.: “Neutron scattering length and cross sections” *Neutron News*, 1992, Vol. 3, No 3.
 - Sears, V. F.: “Optimum sample thickness for total cross section measurements” *Nuclear Instruments and Methods in Physics Research*, 1983, 213:561.
 - Sears, V. F.:”*Advances in Physics*” Vol. 24, No. 1 (1975) 1.
 - Shelby, J. E., M. Hall: “Glass Microspheres for Hydrogen Storage” Alfred University 2005
 - Shelby, J. E., M. M. Hall, F. C. Raszewski: “A Radically New Method for Hydrogen Storage in Hollow Glass Microspheres” DE-FG26-04NT42170, New York State College of Ceramics, Alfred University, Alfred, NY

14802, June 7, 2006.

- Sherif, S. A., Goswami, D. Yogi, Stefanakos E., K. Steinfeld: “Handbook of Hydrogen Energy” 2014 by Taylor & Francis Group, LLC, ISBN-13: 978-1-4200-5450-7.
- Shultis, J. K., R.E. Faw: “An MCPN Primer” Department of Mechanical and Nuclear Engineering, Kansas State University Manhattan, KS 66506
- Siegel, J. B., D.A. McKay, A.G. Stefanopoulous, D.S. Hussey, D.L. Jacobson: “Measurement of Liquid Water Accumulation in a PEMFC with Dead-Ended Anode” Journal of The Electrochemical Society 2008, 155, 11, B 1168-1178.
- Smith, G. C.: “Neutron Imaging, Radiography and Tomography” Encyclopaedia of Imaging Science & Technology Brookhaven national Laboratory Uptown, NY 11973-5000, March 2002.
- Smith, S: “Digital Signal Processing: A Practical Guide for Engineers and Scientists” 2003. ISBN: 0-750674-44-.
- Spornjak, D., A.K. Prasad, S.G. Advani: “Experimental investigation of liquid water formation and transport in a transparent single-serpentine PEM fuel cell” Journal of Power Sources 2007, 170, 334-344.
- Storbl, M.: “New Alternative Contrast Methods in Neutron Computer Tomography” PhD-Thesis” TU-Wien 2002.
- Strasser, R.: “Flashing basics about fuel cells, Short introduction into water management” Report 2010 TU – Graz.
- Stummer, T.: “Comparison of two neutron collimator geometries for neutron radiography using Monte Carlo methods” (2005), Atomic Institute of the Austrian Universities AIAU 21313.
- Takenaka, N., T. Fujii, A. O. Motomura, A. Turuno: “Flow visualization of liquid metals by neutron radiography” Fusion Engineering and Design 27 (1995) 607-613.
- Thoms, M.: “Neutron detection with imaging plates Part I. Image storage and readout” Nuclear Instruments and Methods in Physics Research A, 424, 1999, pp 33-39.
- Thoms, M.: “Neutron detection with imaging plates Part II. Detector characteristics” Nuclear Instruments and Methods in Physics Research A, 424, 1999, 26-33.
- Tillman, D. A., Sarkanen K. V., Anderson, L. L.: “Fuels and Energy from Renewable Resource” ISBN 0-12-691250-5, 1977.
- Trabold, T. A., J.P. Owejan, D.L. Jacobson, M. Arif, P.R. Huffmann: “In situ investigation of water transport in a operating PEM fuel cell using neutron radiography”: Part 1 “Experimental method and serpentine flow field results”, International Journal of Heat and Mass Transfer 2006, 49, 4712-4720.
- Tüber, K., D. Pöcza, C. Hebling: ”Visualization of water buildup in the cathode of a transparent PEM fuel cell“ Journal of Power Sources 2003, 124, 403-414.
- Turhan, A., K. Heller, J.S. Brenizer, M.M. Mench: “Passive control of liquid water storage and distribution in a PEFC through flow-field design” Journal of Power Sources 2008, 180, 773-783.
- Turhan, A., K. Heller, J.S. Brenizer, M.M. Mench: “Quantification of liquid water accumulation and distribution in a polymer electrolyte fuel cell using neutron imaging” Journal of Power Sources 2006, 160, 1195-1203.
- Vontobel, P., E. H. Lehmann, R. Hassanein, G. Frei: “Neutron tomography: Method and applications” Physica B 385–386 (2006) 475–480.

- Wallin, L.: “MCNPX simulations for evaluation of high-energy neutron tomography of canisters for spent nuclear fuel” Uppsala University: Neutron Physics Report, (2005) UUNF 05/#02.
- Weng, F. B., A. Chun-Ying Hsu, Chi-Yuan Lee: “Study of water-flooding behavior in cathode channel of a transparent proton-exchange membrane fuel cell” Journal of Power Sources 2006, 157, 674-680.
- Williams, G., J. Ferguson: “The diffusion of hydrogen and helium through silica glass and other glasses” Journal of the American Chemical Society, 1922 (44) 2160 – 2167.
- Williams, S. H., A. Hilger, N. Kardjilov, I. Manke, M. Strobl, P.A. Douissard, T. Martin, H. Rieseemeier and J. Banhart: “Detection system for micro-imaging with neutrons” Published By IOP-Publishing For SISSA 2012.
- www.boehler-bleche.at
- www.boehler-bleche.at
- www.fuelcells.org
- www.fujifilm.com/products/life_science_system/science_imaging
- www.lifetime-reliability.com
- Zawisky, M., E. Dyrnjaja, F. Hameed, J. Springer: “Digitized neutron imaging with high spatial resolution at low power research reactor; Analysis of detector performance” Nuclear Instruments and Methods in Physics Research A, 2008, (578), 342 – 349.
- Zawisky, M., E. Dyrnjaja; F. Hameed; J. Springer: “Digitized neutron imaging with high spatial resolution at low power research reactor: Applications to steel and rock samples” Nuclear Instruments and Methods in Physics Research B, 2010 (268), 2446 – 2450.
- Zawisky, M., H. Rauch, Ch. Stellmach, P. Geltenport: “Giant Absorption cross section of ultracold neutrons in gadolinium“ Physical Review Letters, 1999, 83, 4955-4958.
- Zawisky, M., M. Bastürk, J. Rehacek, Z. Hradil: ”Neutron tomographic investigations of boron-alloyed steels” Journal of Nuclear Materials 2004, 327, 188-193.
- Zawisky, M., M. Bastürk, R. Derntl, F. Dubus, E. Lehmann, P. Vontobel: “Non-destructive ^{10}B analysis in neutron transmission experiments“ Applied Radiation and Isotopes 2004, 61, 517-523.
- Zawisky, M.: “Neutronenoptik und Tomographie“ TU-Wien Special Vorlesung SV 141.158, TU-Wien 2006.
- Zeitelhack K.: “Search for alternative techniques to helium-3 based detectors for neutron scattering applications” 2012, Volume 23, Issue 4.
- Zhang, J., R. Shimoj, K. Shinoara, D. Kramer, E.H. Lehmann, G. Scherrer: “Visualization and quantification of the water distribution inside an operating fuel cell by neutron radiography” 14-th International Conference on the Properties of Water and Steam in Kyoto, held in Kyoto, Japan, August 29 – September 3, 2004.

Chapter 9 Appendix A

A-1 MCNPX 2.4.0 version

Cell Cards

An input file has the structure as:

Problem title card

Cell card

Surface card

Data card

Tallies

A-2 Cell Card

The Cell card contains information about the material in the cells, the density of the material used and the geometry of the cell. This card contains also the information about which particle in the cell is of importance.

Cell Card has the form:

j m d geom params

where: **j** – cell number

m – material number

d – material density (a negative entry is interpreted as the mass density in units of g/cm^3).

geom – specification of the geometry of the cell

params – specification of cell parameters

All the surfaces of the geometry problem are defined in *Surface Card*.

A-3 Surface Card

Surface card has the form:

j n a list

where: **j** – surface number

n – absent or 0 for no coordinate transformation

a – equation

list – 1 to 10, as required

A-4 Data Card

The Data Card contains information about the source (position, energy, direction etc.) how to detect and what particles to detect, the material composition of the cell, number of the particles to be simulated and the appearance of the output file.

A-5 SDEF – General Source Card

This card has the form:

SDEF source variable – specification

<u>Variable</u>	<u>Meaning</u>
ERG	Energy
PAR	Particle type source will emit
POS	Reference point for position sampling
RAD	Radius of the source
VEC	Direction of the particles
DIR	Direction of flight
SIn	Source information card
SPn	Source probability card
SBn	Source bias card
DSn	Dependent Source Distribution card

A-6 Tallies

The user needs to specify the *Tallies*, which are used to specify what type of information the user wants to gain from Monte Carlo calculation. There exist seven basic neutron tally types; tally specifications:

<u>Tally</u>	<u>Tally Description</u>	<u>Units</u>
F1:n	Number of n particles crossing a surface	particles
F2:n	Flux averaged over a surface	particles/cm ²
F4:n	Flux averaged over a cell	particles/cm ²
F5:n	Flux at a point or ring detector	particles/cm ²
F6:n	Energy deposition averaged over a cell	MeV/g
F7:n	Fission energy deposition	MeV/g

Thus MCNPX is able to simulate (tally) the particle flux, the particle current and the energy deposition over surfaces, or cells, in the geometry. This information is gained by combination of sub-tallies like: En (tally energy), Cn (tally cosine), TMn (tally multiplier), FSn (tally segment), etc.

A-7 Material Specification

The Material card **Mm** specifies both isotopic composition of the material and the cross-section evaluation to be used in the cells. The **Mm** card has the form:

Mm ZAID₁ fraction₁ ZAID₂ fraction₂

Where: **m** on the material card corresponds to the material number on the cells card:

ZAID - nuclide identification number

Z - atomic number of the element or nuclide

A - mass number of the nuclide

Nn - the library identifier

x - class of data fraction – a negative entry is interpreted as weight fraction of the *i* material.

The units used are:

1. lengths in centimetres (cm)
2. energies in MeV
3. temperatures in MeV (kT)
4. atomic densities in units of atoms (barn/cm)
5. mass densities in g/cm³
6. cross sections in barns (10⁻²⁴ cm²)

A-8 How to Run MCNPX

The MCNPX execution line has the following form:

mcnp file options (file's name is i=inp.txt).

For plotting, the command is:

mcnp ip i=inp.txt ixrz print

To run only MCNPLOT and plot tallies after running, the command is: **mcnp z i=inp.txt print**

The most common way to plot cross-section data, the command is: **mcnp i=inp.txt ixz print**

For geometry visualization it is necessary to install the X-ServerDeep/32 program [MCNPX, 2004]; with such tool the user is able to see the geometry plot of the problem and plot tallies (see figure 3.3.2).

A-9 Detector Modelling

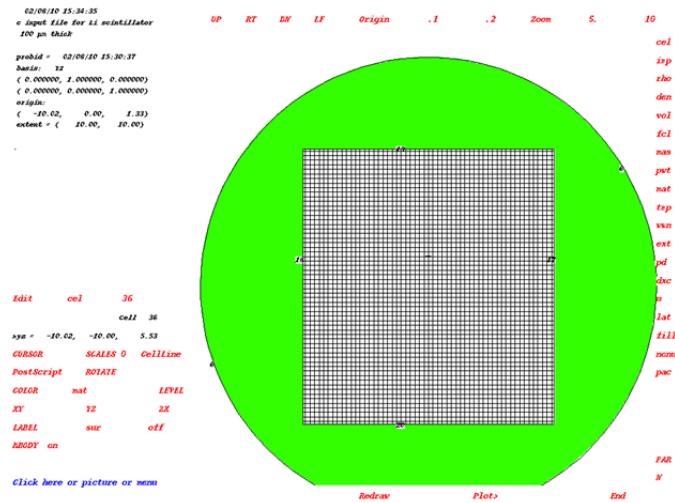


Figure A-1 Geometry configuration of the simulated detector.

All the graphs and geometry were plotted installing X- Deep/32 program.

Input file of the detector

The detector is designed as the box with a given volume and the pixel size is 100 μm and is modelled by the data cards:

Input file

Cell cards

34 0 15 -16 18 -17 20 -19 fill=1 imp:n=1 \$ detector

35 0 -23 fill=2 lat=1 u=1 imp:n=1

36 0 22 -21 lat=1 u=2 imp:n=1

Surface cards

15 px -10.01

16 px -10

17 py 5.51

18 py -5.51

19 pz 6

20 pz -6

21 py 0.01

22 py -0.01

23 box -10.04 -10.0 5.51 0.01 0 0 0 0.01 0 0 0 0.01

Tallies

f04:n (35<35[-25:25 0:0 0:0]<34)t \$ flux in detector cells

de4 &

1.020e-10 1.530e-10 2.110e-10 3.150e-10 4.340e-10 &
5.520e-10 6.480e-10 7.610e-10 8.250e-10 9.680e-10 &
1.050e-09 1.570e-09 2.163e-09 3.220e-09 4.440e-09 &
5.650e-09 6.640e-09 7.780e-09 8.430e-09 9.910e-09 &
1.070e-08 2.210e-08 3.220e-08 4.440e-08 5.650e-08 &
6.620e-08 7.790e-08 8.440e-08 9.900e-08 1.070e-07 &
1.480e-07 2.210e-07 3.270e-07 4.540e-07 5.340e-07 &
6.760e-07 7.360e-07 8.630e-07 9.360e-07 1.010e-06

df4 &

9.999e-01 9.999e-01 9.999e-01 9.997e-01 9.993e-01 &
9.880e-01 9.830e-01 9.770e-01 9.730e-01 9.640e-01 &
9.590e-01 9.260e-01 8.900e-01 8.330e-01 7.780e-01 &
7.320e-01 7.010e-01 6.690e-01 6.520e-01 6.190e-01 &
6.030e-01 4.610e-01 3.960e-01 3.470e-01 3.140e-01 &
2.940e-01 2.750e-01 2.660e-01 2.480e-01 2.390e-01 &
2.080e-01 1.740e-02 1.450e-02 1.250e-02 1.150e-02 &
1.030e-02 9.990e-02 9.920e-02 8.890e-02 8.560e-02.

The DE and DF cards are the multipliers for the ${}^6\text{Li}$ detector with 100 μm thick layer. These absorption coefficients are calculated including all the detector characteristics (the ${}^6\text{Li}$ density, energy spectra and ecc). They represent the absorption rates A_{det} (DF) for the energies DE (in MeV). They are interpolated for the energy of an incident neutron.

A-10 Collimator Modelling

The conical and the cylindrical part of the thermal column.

Input file of the collimator

Collimator geometry modelling.

Input file for Li scintillator 100 μm thick.

Cell cards

20 1 -8.65 1 -2 -3 4 5 imp:n=1 \$ collimator 1
21 2 -0.0014 1 -2 -5 imp:n=1
22 3 -2.34 1 -2 -4 5 imp:n=1
23 4 -0.984 2 -6 8 -7 imp:n=1 \$ collimator 2
24 1 -8.65 2 -7 -8 9 imp:n=1
25 3 -2.34 2 -7 10 -9 imp:n=1

26 2 -0.0014 2 -7 -10 imp:n=1
 27 0 -1 -5 -10 -11 -6 imp:n=0
 28 6 -2.267 -6 3 1 -2 8 -11 imp:n=1
 29 0 6 imp:n=0
 30 2 -0.0014 -6 -11 7 #34 imp:n=1
 31 0 -6 -1 5 imp:n=0
 32 5 -0.983 1 -8 3 -2 imp:n=1
 33 0 -6 11 imp:n=0

Surfaces Cards

1 px -254 \$ collimator 1
 2 px -127
 3 kx -400 2.3668e-4 1
 4 kx -398 2.3668e-4 1
 5 kx -397 2.3668e-4 1
 c
 6 cx 10
 7 px -27 \$ cylinder collimator 2
 8 cx 4.8
 9 cx 4.6
 10 cx 4.1
 11 px 0

```

03/30/06 14:17:17
c input file for 1 mm thick
boron-steel plate

probid = 03/30/06 14:13:09
basis: XY
( 1.000000, 0.000000, 0.000000)
( 0.000000, 1.000000, 0.000000)
origin:
( -33.56, 1.24, 0.00)
extent = ( 40.00, 40.00)
  
```

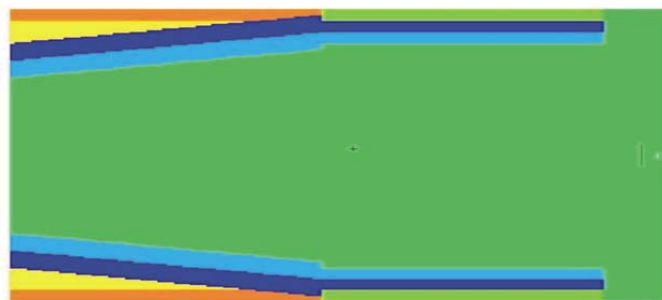


Figure A-2 The geometry of the neutron beam plotted with X-Deep/32 program.

A-11 Boron Steel in-Homogeneity Modelling

Hexagonal lattice modelling for the material (steel and boron steel).

The geometry is modelling from the cells cards:

Input file for model 1

Cells cards

37 0 -44 lat=2 u=2 imp:n=1 fill=3 \$ lattice

38 8 -7.682 -55 u=3 imp:n=1

39 7 -7.80 55 u=3 imp:n=1

Surface cards

44 rhp 0 0 -0.0010 0 0 0.002 0.0010 0 0

55 so 0.00120

77 rpp -17 -16.863 -2 2.1 -6 6

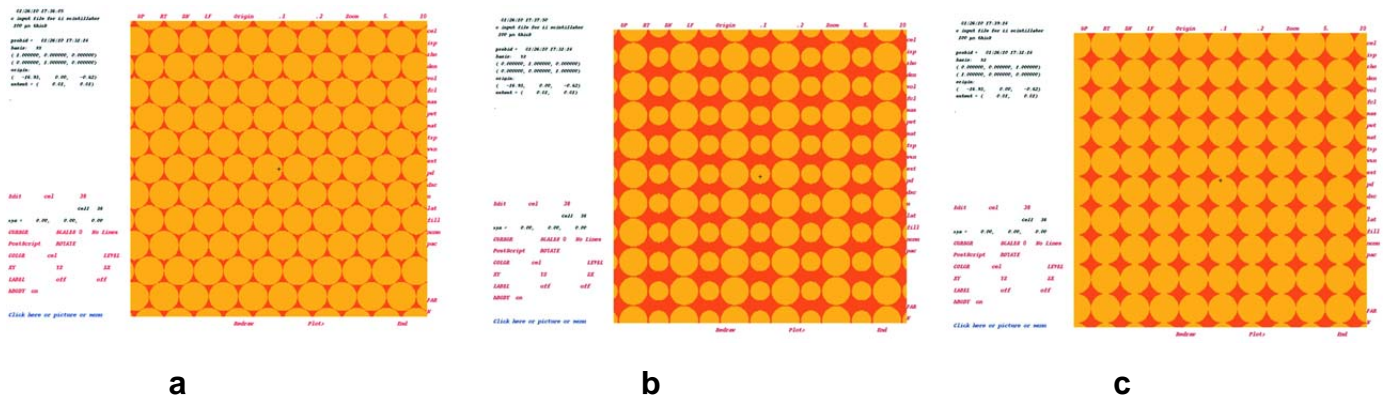


Figure A-11 *a*: geometry configuration of sample. (cut through XY plane). *b*: geometry configuration of sample. (cut through YZ plane). *c*: geometry configuration of sample. (cut through XZ plane).

Input file for model 3

Cells cards

37 0 -44 lat=2 u=2 imp:n=1 fill=3 \$ lattice

38 8 -7.682 -55 u=3 imp:n=1

39 7 -7.80 55 u=3 imp:n=1

Surface cards

44 rpp -0.0105 0.0105 -0.0105 0.0105 -0.0105 0.0105

55 rpp -0.010245 0.010245 -0.010245 0.010245 -0.010245 0.010245

77 rpp -17 -16.25 -5 5.1 -6 6

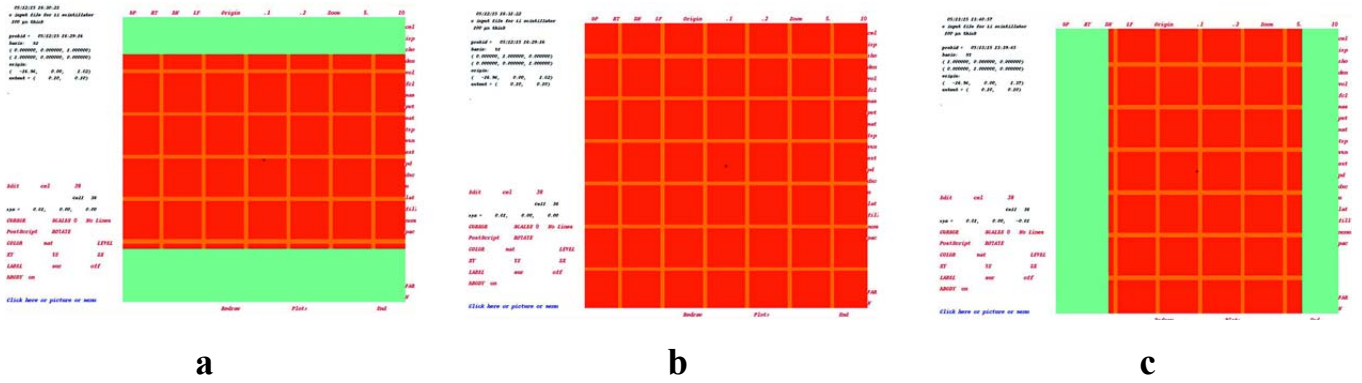


Figure A-12 a: Geometry configuration of sample. (cut through XZ plane). b: Geometry configuration of sample. (cut through YZ plane). c: Geometry configuration of sample. (cut through XY plane).

Input file for model 4

Cells cards

37 0 -44 lat=1 u=2 imp:n=1 fill=3 \$ lattice

38 8 -7.661 -55 u=3 imp:n=1

39 7 -7.80 55 u=3 imp:n=1

Surface cards

44 rpp -0.015 0.015 -0.015 0.015 -0.015 0.015

55 rpp -0.0135 0.0135 -0.0135 0.0135 -0.0135 0.0135

77 rpp -17 -16.863 -5 5.1 -6 6

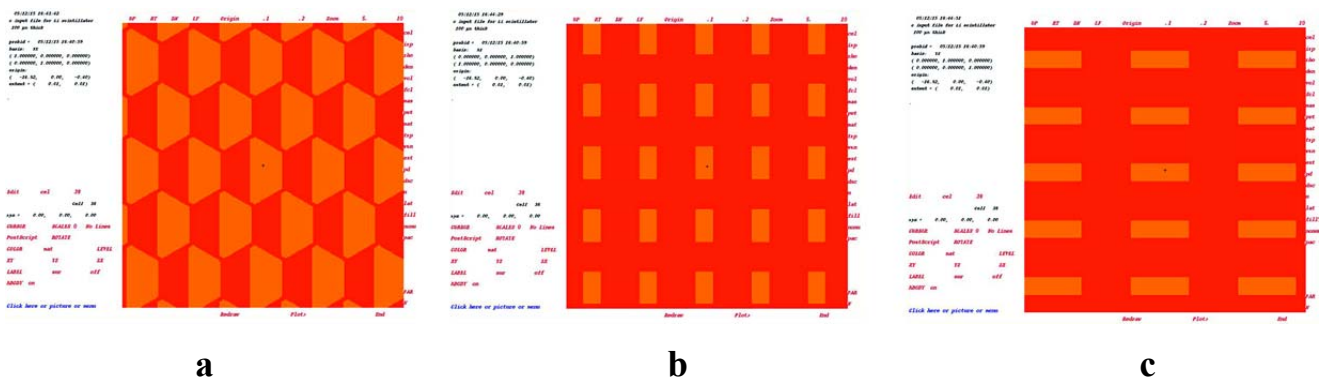


Figure A-13 a: Geometry configuration of sample. (cut through XZ plane). b: Geometry configuration of sample. (cut through YZ plane). c: Geometry configuration of sample. (cut through XY plane).

A-12 Neutron Source design in simulations.

The simulated neutron source at the z=-300 cm is modelled by the data cards:

Input file mode n

SDEF par=1 pos=-300 0 0 sur=1 erg=d1 rad=d2 vec=1 0 0

sp1 -2.53e-08

si2 0 1

sp2 -21 1

The distribution D1 contains Maxwellian spectrum for 2.53^8 MeV energy which has a syntax: $\exp(-e/a)$ which correspond to Maxwell fission spectrum.SDEF is the general source

A-13 Material Modelling

Material composition input file is given from materials cards. The concentration is given in weight percent.

Input file

Materials cards

m7 26000.55c -0.66116 \$Fe

6000.50c -0.0004835 \$C

14000.50c -0.004835 \$Si

25055.50c -0.017406 \$Mn

6000.60c -0.001934 \$S

24000.50c -0.1720293 \$Cr

42000.50c -0.026109 \$Mo

28000.50c -0.11604 \$Ni

m8 26000.55c -0.63449655 \$Fe

6000.50c -0.00048845 \$C

14000.50c -0.0048845 \$Si

25055.50c -0.0175842 \$Mn

16000.60c -0.0019538 \$S

24000.50c -0.1738882 \$Cr

42000.50c -0.0263763 \$Mo

28000.50c -0.117228 \$Ni

5010.50c -0.003743 \$B-10

5011.50c -0.014972 \$B-11

Chapter 10 Appendix B

B-1 Transmission Experiments with Monochromatic Beam

The Hahn-Meitner Institute HMI in Berlin operates a 10 MW thermal research reactor. It is a light water cooled and moderated type reactor based on 24 fuel elements of low enriched uranium. It provides

both thermal and cold neutron sources. Our experiment was located at the V-hall along six neutron guides supplied by a cold neutron source CNS. The CNS is placed at another conical beam tube close to the core. It is operated with hypercritical hydrogen at temperatures between 25 and 35 K at a pressure of 14-17 bars. At the V12 hall are placed the double crystal diffractometers V12a and V12b. It is based on the angular resolution of the Bragg reflection at perfect crystal planes.

$$n \cdot \lambda = 2d \cdot \sin \theta$$

When the neutron beam hit a crystal multilayer with grazing incident angle θ and single wavelength λ , the Bragg reflection of the beam occurs. The wavelength of the neutron reflected by the multilayer is decided by the grazing angle θ and the period of the multilayer d . A pyrolytic graphite monochromator (002) is located in the beam of NL3B some 1.5 m downstream from the V12a monochromator and deflects at 5.244 Å wavelength diffraction toward the sample position. This beam is split by an additional perfect Si single crystal, (111) which acts as the monochromator crystal of high flux density used for high resolution in neutron radiography and in USANS. The beam size is $50 \times 50 \text{ mm}^2$ with a spatial resolution of approximately 250 μm and a monochromatic flux density of approximately $3 \times 10^5 \text{ n/cm}^2\text{s}$ without additional collimation. The detector system in use is 2D $^6\text{Li}/\text{CCD}$ camera of 400 μm thick layer. The divergence of the beam in the instrument is connected by the Bragg condition with the ratio $\Delta\lambda/\lambda$ i.e. the degree of monochromatisation, for a (111) reflection, a wavelength of 5.5 Å ones calculates $\Delta\lambda/\lambda \sim 10^{-2}$.

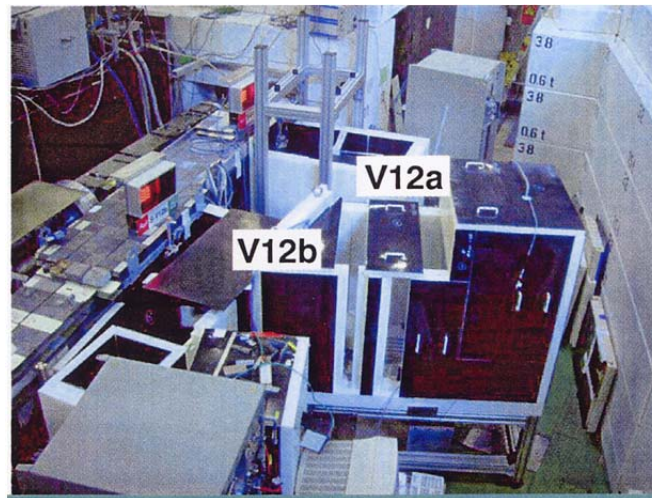


Figure B-1 High resolution double crystal diffractometer and monochromatic tomography at V12 set-up instrument at HMI Berlin.

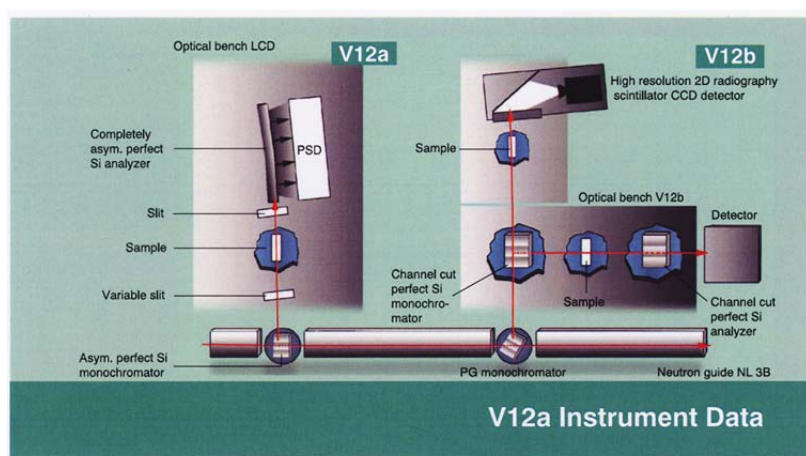


Figure B-2 Schematic view of double crystal diffractometer.

The V12 is a multiple purpose instrument with two beams at the NL3B beam guide. The first one provides 4.76 Å. The second port provides 5.244 Å neutrons for the V12b which is further divided by a perfect single crystal monochromator to a high double crystal diffractometer for special fundamental and high resolution applications and an attenuation radiography and tomography instrument for high instrument investigations with monochromatic neutrons.

	V12b I	V12b II
Neutron guide	NL3B, curved R = 500	NL3B, curved R = 500
Monochromator crystals	PG (002)	perfect Si single crystal (111) edged, variable geometries
Wavelength	0.52(1) nm	0.524(1) nm
Diffract. analyser crystals		perfect Si single crystal (111) edged, variable geometries
Neutron flux	3×10^9 n/cm ² s	5×10^9 n/cm ² s
Resolution	250 μm	5×10^{-5} nm ⁻¹
Total range	5 x 5 x 5 cm ³	$5 \times 10^{-5} - 10^{-1}$ nm ⁻¹
Detectors	2D scintillator/CCD system	³ He counter
Instrument responsible	M. Strobl, strobl@hmi.de W. Treimer, treimer@hmi.de	

Figure B-3 Instrument Data.

The neutron transmission of boron steel alloy plates was measured at V12b set-up instrument. The distance between the monochromatic neutron source and scintillator detector was 2 m and the sample plate was placed 10 cm from the detector. The exposure time was 1300 sec and for each plate three projections were taken. The image files were saved in TIF format and processed with Image-Pro Plus 6 (MediaCybernetics) program at ATI in Vienna. According to the formula:

$$E_{th} = k_B T = \frac{m v_{th}^2}{2} = \frac{h^2}{2m\lambda_{th}^2}$$

to the neutron wavelength of 5.244 Å it corresponds the 2.972⁻⁰⁹ MeV energy value.

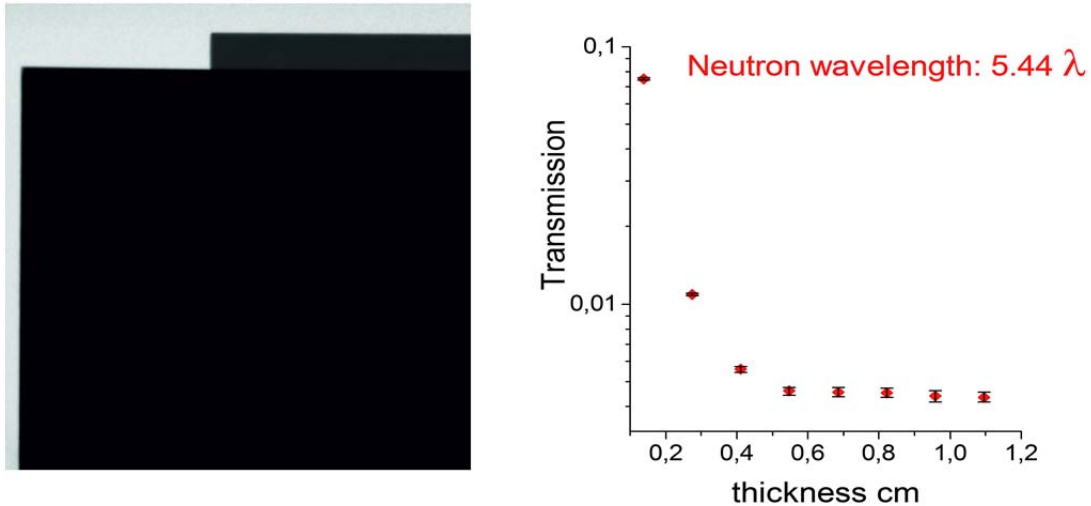


Figure B-4 **Left:** The image of the boron steel plates done with V12b instrument, which provides 5.244 Å neutron wavelength. **Right:** The transmission of boron steel alloy plates for monochromatic neutron beam 5.244 Å wavelength.

During these measurements the background contribution is very high. Indeed the exposure time was very long; another reason we assume since that the absorption is very high the error automatically is very high. The uncertainty of the transmission is very high. Correcting the beam hardening effect the background contribution becomes so high that we cannot really estimate the transmission.

At HMI – Berlin we had possibilities to measure the transmission of the samples using also the V7 Cold Neutron Radiography and Tomography CONRAD instrument. This beam line is located at the end of the curved neutron guide NL1b, facing the cold source of the BER II reactor. The existence of a neutron guide helps to achieve an enormously high cold neutron flux of the order approximately 2×10^8 n/cm²s at the end of the guide with negligible background of gamma radiation and fast neutrons.

Actually the transmission is so low that you cannot distinguish between 9, 10, 11 and 12 mm plate thickness referring to the diagram in figure B-5.

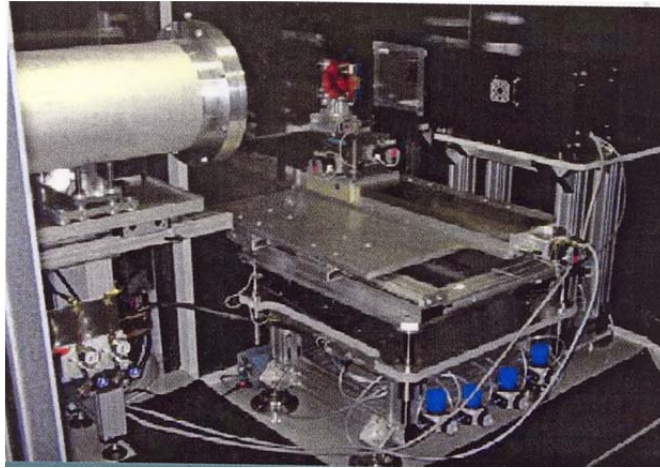


Figure B-5 Cold Neutron Radiography and Tomography V7 (CONRAD) set-up instrument.

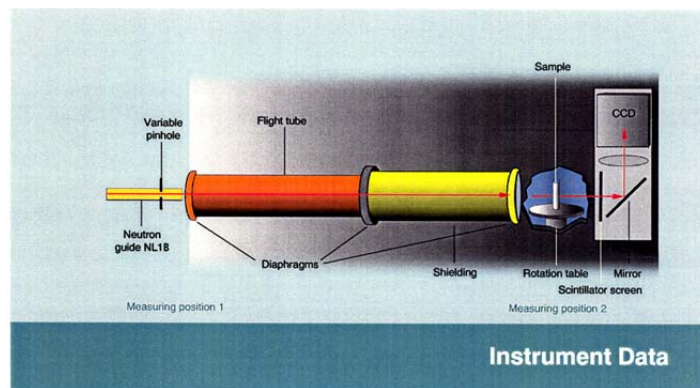


Figure B-6 Schematic view of CONRAD set-up.

Spectrum	0.2 – 1.2 nm (Maxwellian distribution with a maximum at 0.35 nm)
Sample environment	Cooling water, air pressure, N-, He- and H- gas lines
Measuring positions	Two (the parameters are listed below)
Detectors	CMOS camera (Position I) – PCO 1200hs - 1280 x 1024 pixel CCD camera (Andor DW436N-BV) 2048x2048 pixel (Position II)
Instrument responsible	N. Kardjilov, kardjilov@hmi.de direct dialling -2298

Figure B-7 Instrument Data.

At CONRAD instrument it is possible to investigate the inner structure of large samples with a spatial resolution of up to 100 μm . Eight different thickness plates were placed in front of the neutron beam and the transmission for eight plates with 2.5 \AA neutron wavelength was measured. The exposure time was 120 seconds and the experiment was carried out from Dr. N. Kardjilov.

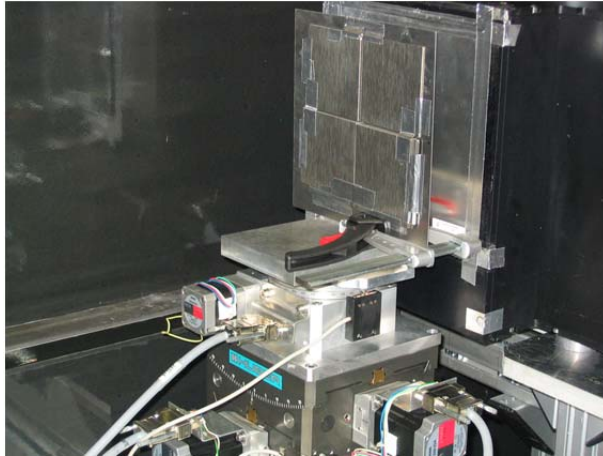


Figure B-8 The radiograph set-up at CONRAD instrument.

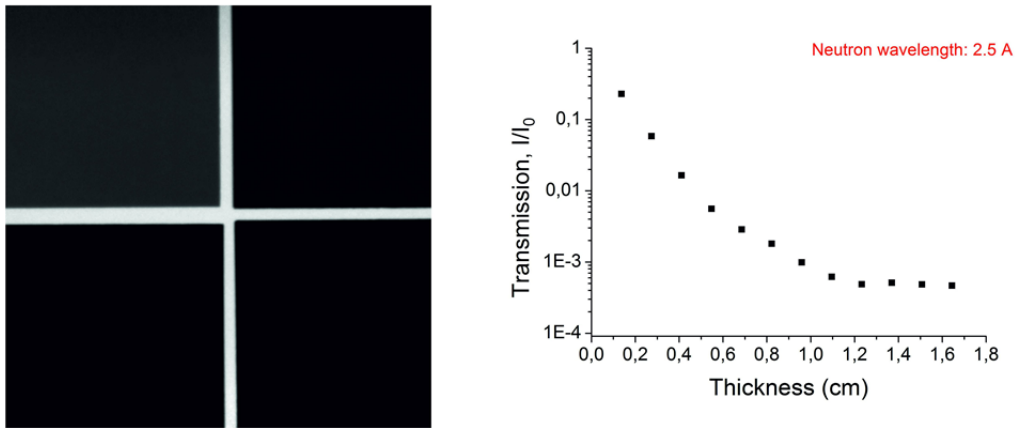


Figure B-9 **Left:** The radiograph image of the boron steel plates at CONRAD instrument. **Right:** The transmission of boron steel alloy plates for monochromatic neutron beam 2.5 \AA at CONRAD instrument set-up.

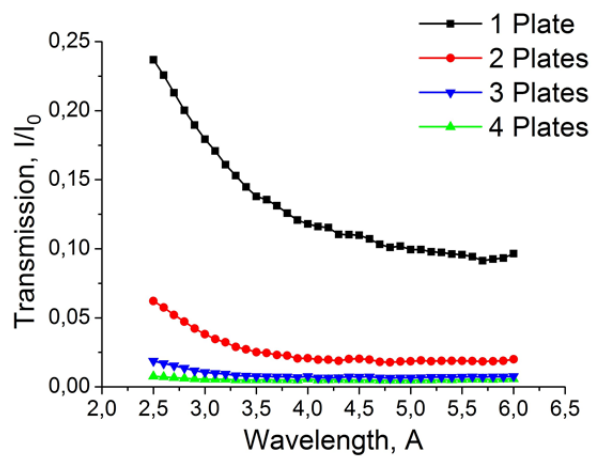


Figure B-5 The transmission of boron steel alloy plates scanned with cold neutron interval spectra with from 2.0 to 6.5 \AA at CONRAD instrument set-up.

The physicist Leo Szilard once announced to his friend Hans Bethe that he was thinking of keeping a diary:

"I don't intend to publish. I am merely going to record the facts for the information of God."

"Don't you think God knows the facts?" Bethe asked.

"Yes," said Szilard.

"He knows the facts, but He does not know this version of the facts."